

Low Temperature Physics

Edited by A. S. BOROVIK-ROMANOV

Advances
in
Science
and
Technology
in
the USSR



Physics Series
Mir Publishers
Moscow

Advances
in
Science
and
Technology
in
the USSR

Physics Series



Low Temperature Physics

Edited by

A. S. BOROVIK-ROMANOV,
Mem. USSR Acad. Sc.

Translated from the Russian by
Valerii Ilyushchenko,
Cand. Sc. (Phys. and Math.)

MIR Publishers
Moscow

Физика низких температур
Под редакцией акад. А. С. Боровика-Романова
Издательство «Мир» Москва

First Published 1985

© Издательство «Мир», 1985
© English translation, Mir Publishers, 1985

*Dedicated to the Memory of
P.L. KAPITZA
One of the Greatest Physicists
of Modern Time*

Foreword

Research in low temperature physics as a rule always uses liquid helium. Until the beginning of the 1950's liquid helium was obtained in two scientific centres in the USSR, that is the Cryogenic Laboratory at the Ukrainian Physicotechnical Institute and the Institute for Physical Problems. The latter was founded by P. L. Kapitza in 1934. Low temperature physics has always been an important part of the Institute's activities and has made it world famous.

This collection consists of six articles written by scientists at the Institute for Physical Problems and covers experimental work in to new areas of low temperature physics.

We, the authors of this collection, all worked for many years under the leadership of P. L. Kapitza, who exerted an important influence on each of us. We timed this collection for Kapitza's ninetieth birthday as a token of our heartfelt gratitude and deep respect. Unfortunately, he did not live to see his jubilee and so this collection is devoted to his memory, the memory of a great modern physicist and outstanding personality, Pyotr Leonidovich Kapitza.

Academician A.S. Borovik-Romanov

Contents

Foreword by A. S. Borovik-Romanov	6
Preface by A. S. Borovik-Romanov	11

1. GRYSTALLIZATION WAVES IN ${}^4\text{He}$, by A. Ya. Parshin 15

1.1. Introduction	15
1.2. Surface of a Classical Crystal	16
1.2.1. Surface Energy and Equilibrium Shape of Crystal	16
1.2.2. Surface Structure at $T = 0$	17
1.2.3. Surface Structure at $T \neq 0$	22
1.2.4. Some Problems of Growth Kinetics	24
1.3. Surface of a Quantum Crystal	27
1.3.1. Quantum-Rough State	27
1.3.2. Coherent Crystallization	36
1.3.3. Crystallization Waves	38
1.3.4. Sound Transmission Through a Quantum-Rough Surface	41
1.4. Experimental Investigation of Coherent Crystallization and Crystallization Waves	45
1.4.1. On the possibility of Direct Observation of Capillary Phenomena in Crystals	45
1.4.2. Optical Cryostat	47
1.4.3. Features of the Low Temperature Growth Kinetics of ${}^4\text{He}$ Crystals	49
1.4.4. Techniques to Excite Crystallization Waves	55
1.4.5. Visual Observations of Crystallization Waves	60
1.4.6. Spectrum and Damping of Crystallization Waves	62
1.5. Conclusion	74
References	75

2. SOUND PROPAGATION THROUGH A LIQUID-METAL INTERFACE, by K. N. Zinov'eva 78

2.1. Introduction	78
2.2. Acoustic Phenomena at a Liquid-Solid Interface	79
2.2.1. Reflection and Transmission Coefficients of the Acoustic Energy According to the Classical Acoustic Theory [2.6]	79
2.2.2. The Khalatnikov Theory of Liquid Helium-Solid Heat Transfer. Kapitza Resistance [2.2]	82

Contents

8

2.2.3.	The Andreev Theory of Resonance Absorption of Sound by a Metal Surface	83
2.2.4.	The Generalized Acoustic Theory	85
2.2.5.	Rayleigh Surface Waves	89
2.2.6.	First Experiments on Reflection and Transmission Coefficients of Thermal Phonons Passing Across a Liquid Helium-Solid Interface	92
2.3.	Experimental Investigations of Sound Transmission from Liquid ^4He into a Metal	94
2.3.1.	Experimental Procedure	94
2.3.2.	Apparatus	96
2.3.3.	Experiment	103
2.3.4.	Results of Measurements at $T \geq 0.2$ K	104
2.3.5.	Results of Measurements at $T < 0.2$ K	112
2.3.6.	Discussion of Experimental Curves. Evaluation of Errors	115
2.3.7.	Calculations Using the Generalized Acoustic Theory	116
2.3.8.	Comparison of Experimental Data with the Generalized Acoustic Theory	121
2.3.9.	Comparison with the Andreev Theory	128
2.4.	Conclusion	129
	References	130

3. INVESTIGATIONS OF ^3HE SUPERFLUID PHASES BY PULSED NMR TECHNIQUE, *by Yu. M. Bun'kov* 132

3.1.	Introduction	132
3.2.	The Equipment for Producing Ultralow Temperatures	134
3.2.1.	Operating Conditions	134
3.2.2.	The Dilution Refrigerator	135
3.2.3.	The Nuclear Demagnetization Refrigerator	141
3.3.	Instability of Homogeneous Precession in $^3\text{He-A}$ and Its Effect on Relaxation Processes	143
3.3.1.	Basic Properties of the ^3He Superfluid Phases	143
3.3.2.	"Intrinsic" Relaxation Mechanism in Superfluid ^3He	146
3.3.3.	A Study of the $^3\text{He-A}$ Free Induction Signal	149
3.3.4.	Instability of Homogeneous Precession in $^3\text{He-A}$	156
3.3.5.	Experimental Studies of an Instability in the Homogeneous Precession in $^3\text{He-A}$	161
3.4.	A Texture Transition in $^3\text{He-B}$ Induced by a Radio Frequency Field	164
3.4.1.	Threshold Effect in Pulsed $^3\text{He-B}$ NMR	164
3.4.2.	A Texture Transition in $^3\text{He-B}$	167
3.4.3.	Studies of the Brinkman-Smith Relaxation Mode with Parallel Plate Geometry	169
3.5.	Conclusion	171
	References	172

4.	EXPERIMENTAL INVESTIGATIONS OF COHERENT MAGNETIC BREAKDOWN, by N. E. Alekseevskii and V. I. Nizhankovskii	174
4.1.	Introduction	174
4.2.	Beryllium	175
4.3.	Aluminium	191
4.4.	Niobium	198
4.5.	Ruthenium Dioxide RuO_2	212
4.6.	Conclusion	218
	References	218
5.	WEAK ELECTRON LOCALIZATION AND MAGNETORESISTANCE OSCILLATIONS OF CYLINDRICAL NORMAL METAL FILMS, by Yu. V. Sharvin and D. Yu. Sharvin	221
5.1.	Introduction	221
5.2.	An Experiment with Lithium Film	226
5.2.1.	Experimental Technique	226
5.2.2.	Experiments at 1.1 K	227
5.3.	Experimental Observations of the Longitudinal Magnetoresistance Oscillations of Cylindrical Films of Different Metals, and the AAS Effect	230
5.3.1.	Magnesium	234
5.3.2.	Cadmium	236
5.3.3.	Lithium	237
5.4.	Conclusion	239
	References	239
6.	BRILLOUIN-MANDELSHTAM SCATTERING IN MAGNETIC MATERIALS, by A. S. Borovik-Romanov and N. M. Kreines	241
6.1.	Introduction	241
6.2.	Magnetooptical Effects and the Mechanism of Light Scattering in Magnetic Materials	243
6.3.	Apparatus and Samples	248
6.3.1.	Apparatus	248
6.3.2.	Samples	250
6.4.	Spectra of Thermal Magnons in CoCO_3	251
6.5.	Modulation of Light by Magnetic Resonance in Magnetic Materials	255
6.5.1.	General Remarks	255
6.5.2.	CoCO_3	257

6.5.3.	K_2CuF_4	259
6.5.4.	$RbNiF_3$ [6.23]	261
6.5.5.	$Nd_3Ga_5O_{12}$ [6.24]	265
6.6.	Magnon "Bottle-Neck" Under AFMR and FMR	266
6.7.	Light Scattering from Parametrically Excited Quasiparticles (Magnons and Phonons) in $CoCO_3$	275
6.7.1.	Parametrical Magnons in $CoCO_3$	276
6.7.2.	Parametrical Phonons in $CoCO_3$	286
	References	

Author index**Subject index**

Preface

This collection of articles is devoted to three important branches of low temperature physics: studies of solid and liquid helium, free electron motion in metals, and low temperature magnetism. The discovery of superfluidity and the subsequent works by P. L. Kapitza and L. D. Landau commenced a new branch of physics—physics of quantum liquids. During the last decade physics of quantum crystals also entered this branch, started by theoretical works by A. F. Andreev and I. M. Lifshitz.

The first article concerns quantum crystals and liquids. It is devoted to a new phenomenon discovered by A. F. Andreev, K. K. Keshishev, and A. Ya. Parshin, viz. crystallization waves in helium. Andreev et al theoretically predicted and experimentally observed waves with macroscopic amplitude moving along the surface of solid helium crystal in equilibrium with superfluid helium. The crystallization waves are caused by alternate melting and crystallization. The phenomenon is a spectacular macroscopic manifestation of the quantum laws in condensed media at low temperatures.

The second article covers investigations of the temperature jump discovered by P. L. Kapitza. This jump originates at a solid-liquid interface in the presence of a heat flux through the interface. This is only observed at low temperatures (in liquid helium), since its magnitude is inversely proportional to the temperature cubed. The theoretical interpretation given by I. M. Khalatnikov stresses that due to the big difference in acoustic velocities the interface is only transmitted by a small fraction of the phonons from the helium incident on the solid surface at angles smaller than that of total internal reflection ($\sim 10^\circ$). Andreev demonstrated that for the phonons incident on a metallic surface at the Rayleigh angle, viz. for phonons transforming into surface waves, there should be an anomalously strong resonance absorption (for the angle of incidence). The article by K. N. Zinov'eva describes the skilled experiments she undertook

to study ultrasonic transmission across a liquid helium-metal interface. These experiments vindicated the theoretical predictions.

The third article, by Yu. M. Bun'kov, is also devoted to investigations of liquid helium, but of its lighter isotope, helium-3. As was predicted by L. P. Pitayevskii and experimentally discovered by Lee, Richardson, and Osheroff, helium-3 passes to a superfluid state that is substantially different from that of helium-4. The main difference is that after the Fermi particles, the helium-3 atoms, have paired (this process is necessary for superfluidity), the pairs possess nonzero orbital moment and their spin equals 1. As a result, helium-3 below the phase transition point ($T_c = 2.7$ mK) combines the properties of superfluidity, liquid crystal, and antiferromagnet. Bun'kov's article describes the refrigerator designed and constructed at the Institute for Physical Problems to produce temperatures down to 0.5 mK, as well as the results of studies using pulsed NMR on the two superfluid phases, ${}^3\text{He-A}$ and ${}^3\text{He-B}$. The main new result is the observation of an instability in the homogeneous spin precession in ${}^3\text{He-A}$. At the angles of deviation larger than 50° the decay into spin waves rises exponentially. This explains why the relaxation time of the free induction signal appears to be an order of magnitude smaller than that predicted by the simple relaxation theory of homogeneous precession.

The next two articles are devoted to the behaviour of conduction electrons in metals. The development of this important branch over the last 50 years can be divided tentatively in two. During the first stage very pure single crystal samples of metals were investigated. The low temperatures and the crystal perfection yielded very large electron free paths that were comparable to the dimensions of the samples or the electron orbits in the magnetic fields applied to the samples. Using a variety of magnetic, galvanomagnetic, and microwave techniques the Fermi surfaces of many metals were investigated and some completely unexpected topologies were discovered. The scientists at the Institute for Physical Problems have contributed heavily to these studies. The article by N. E. Alekseevskii and V. I. Nizhankovskii is devoted to the effect of a strong magnetic field on the motion of electrons, when the individual sheets of the Fermi surface are separated by small energy gaps. The phenomenon of magnetic breakdown might therefore arise in a strong magnetic field with elec-

trons tunnelling from one orbit to another. N. E. Alekseevskii and V. S. Egorov discovered that during magnetic breakdown in beryllium the resistance becomes oscillatory function of the inverse magnetic field. These oscillations occur for certain orientations while possessing a giant amplitude and a very short period. A. A. Slutskii explained this phenomenon by saying that the tunnelling proceeds efficiently only if the phases of the wave functions of the tunnelling electrons change by $2\pi n$ tracing the orbits. For this reason the observed phenomenon was called coherent magnetic breakdown. In the article N. E. Alekseevskii and V. I. Nizhankovskii describe in great detail their experimental studies of coherent magnetic breakdown in beryllium, aluminium, niobium, and ruthenium dioxide.

The second stage of studying the motion of electrons in metals is related to samples with comparatively large disorder in the form of impurities, vacancies, or dislocations. The free paths of electrons for such samples become comparable with interatomic distances. It was shown that theory can predict a number of relationships concerning the behaviour of such disordered systems. This theory, whose foundations were laid down by P. W. Anderson and G. Mott in the late sixties, was called the localization theory. A number of its predictions were corroborated experimentally, especially, for systems of low dimensionality. A very elegant effect was forecasted on the basis of this theory by Altshuler, Aronov, and Spivak in 1981. They predicted that resistance of a cylindrical, disordered metallic film should oscillate as a function of a magnetic field oriented along the cylinder's axis. The period of the oscillations corresponds to the change in the magnetic flux through the cylinder by the value of the flux quantum, $hc/2e$. The article by Yu. V. Sharvin and D. Yu. Sharvin describes their experiments in which for the first time this interesting phenomenon was observed and they compare quantitatively theory and experiment.

The sixth article in the collection was written by A. S. Borovik-Romanov and N. M. Kreines and is devoted to low temperature magnetism. At the Institute for Physical Problems an extended series of investigations on antiferromagnets has been undertaken. Most paramagnets pass to antiferromagnetic state at temperatures below 100 K. During the last decade Brillouin-Mandelshtam scattering (BMS) of light from spin waves in ferromagnets and antiferromagn-

nets has been observed at several laboratories in the world (including the Institute for Physical Problems). At the Institute for Physical Problems light scattering from spin waves excited by microwave power was observed for the first time. This article describes the results of this and other experimental work in which the BMS from excited spin systems was studied. These experiments provided new data on the spectra of spin waves and their relaxation.

Academician A. S. Borovik-Romanov

A. Ya. Parshin, D.Sc. (Phys. and Math.)

1.1. INTRODUCTION

In the last few years the phenomena taking place at the liquid-solid interface in helium have aroused a considerable interest. The unique feature of such an interface consists in its ultrahigh mobility and this due to a practically nondissipative nature of growth and melting of helium crystals at temperatures near absolute zero. This feature, first predicted theoretically [1.1] and then observed experimentally in different laboratories, ensures a unique possibility of direct experimental studies of capillary phenomena in crystals. Among the phenomena closely connected with ultrafast helium crystallization, such as crystallization waves [1.1-3], anomalous sound transmission and anomalous Kapitza resistance [1.4-9], and surface phase transitions [1.3, 1.10-13], perhaps the most unusual and easily observable seem to be crystallization waves.

The physical nature of the ultrafast crystallization phenomenon can be understood using the concept of quantum-mechanical delocalization of point defects in quantum crystals [1.14]. Actually a strictly nondissipative crystallization can be obtained only with a special type of coherent motion present in a two-phase system, as opposed to the classical situation, where the crystallization process results from random transitions of individual particles between two phases. In this review we shall try to give a complete picture of the status of modern theoretical and experimental studies on ultrafast helium crystallization and crystallization waves. The body of the review is made up by three sections. Sec. 1.2 contains the modern concepts, essential for further exposition, of the general thermodynamic surface properties of conventional classical crystals and their growth mechanism. The exposition is laid out so that the introduced concepts could be directly transferred to the quantum case. The basic ideas of the current theory of surface phenomena in quantum crystals are presented in Sec. 1.3. In Sec. 1.4 one finds the results of experimental investigations of helium crystallization processes at low temperatures and crystallization waves.

1.2. SURFACE OF A CLASSICAL CRYSTAL

1.2.1. Surface Energy and Equilibrium Shape of Crystal

In crystals, as in liquids, the quantity that characterizes thermodynamic properties of a surface is the free energy of the unit surface area α which is numerically equal to the minimum work needed to form this unit surface element [1.15]. For a crystal that is immersed in a liquid or gas phase and is in complete thermodynamic equilibrium with the latter, the quantity α is a function of both temperature and the two angles φ_1 and φ_2 . These angles control the orientation of the surface versus crystallographic axes. In these circumstances, the equilibrium shape is determined by minimizing of the crystal's surface free energy while volume is kept fixed:

$$\oint_S \alpha \, dS = \text{minimum} \quad (1.1)$$

The solution of this variational problem in the general case, viz. for an arbitrary function α (φ_1, φ_2), is given by the known Wulff construction (see, e.g. [1.15]). To obtain an equilibrium shape one needs to draw a straight line segment from a certain point (as if from a center) along every direction characterized by the angles φ_1 and φ_2 whose length is proportional to the value of α for a given direction. A plane perpendicular to the segment is drawn at its endpoint. The envelope of the derived family of planes defines the equilibrium crystal shape. Therefore the requirement of positiveness of the second variation in (1.1) leads to the condition $\alpha + \frac{\partial^2 \alpha}{\partial \varphi_{1,2}^2} > 0$ which ensures the stability of a given surface point (see [1.16]).

When solving concrete problems it might be more convenient to use a differential equation of a surface instead of Wulff's construction. Such equation is the Euler one for the variational problem (1.1) with an indefinite Lagrange constant incorporated. An equivalent equation, yet without indefinite constants, can be obtained from the condition of phase equilibrium [1.17, 1.18]. Aiming at subsequent applications, let us write down this equation in a suitable form with the gravitational field also included:

$$F + P + \left(\alpha + \frac{\partial^2 \alpha}{\partial \varphi_1^2} \right) \frac{1}{R_1} + \left(\alpha + \frac{\partial^2 \alpha}{\partial \varphi_2^2} \right) \frac{1}{R_2} = \frac{\rho_1}{m} \mu \quad (1.2)$$

Here F is the free energy of the crystal unit volume, ρ_1 the crystal density, m atomic mass, P the pressure inside the liquid near the surface (including the additional hydrostatic term), μ chemical potential of liquid, R_1 and R_2 the major surface curvature radii, φ_1 , and φ_2 the angles read off within the planes of principal normal sections.

One of the specific properties of crystals which distinguishes them from liquids is a specific faceting, viz, strictly plane portions of a surface. As was first demonstrated by Landau [1.19], the faceting is caused by nonanalyticity of α versus the angles φ_1 and φ_2 . Namely, to produce a plane portion of a surface needs the derivative, $\frac{\partial\alpha}{\partial\varphi}$, for a given orientation to experience a finite jump (such surface used to be called singular ones [1.20]). And it is the linear size of the plane portion that is proportional to this jump value. In Eq. (1.2) this situation corresponds to the quantities $\alpha + \frac{\partial^2\alpha}{\partial\varphi_1^2}$ and, respectively, to the curvature radii of surfaces going to infinity. In the same article Landau has demonstrated that such unusual properties of the function α (under reasonably general assumptions, the jump $\frac{\partial\alpha}{\partial\varphi}$ appears to take place for a surface of any integer Miller indices) are eventually due to the presence of the translation symmetry of particle positions in crystal. Leaving the analysis of the microscopic picture that leads to such a conclusion aside to the next Section, let us only note here that from the general thermodynamic viewpoint this conclusion seems to be quite natural*: Really, as for any thermodynamic quantity, the properties of surface energy considered as a function of a surface state are primarily governed by its full symmetry group. Therefore, an analytical dependence of α on external parameters is to be expected only in the cases when the symmetry group parameters are changing in a continuous way. On the other hand, considering the angles φ_1 and φ_2 as external parameters, we see that in their continuous variation the surface translation symmetry is changed in a very complicated, nonanalytical manner. Thus, the lengths of elementary vectors of translation along the surface are, to be rigorous, everywhere discontinuous functions of the angles φ_1 and φ_2 . From this viewpoint, the existence of non-singular surfaces characterized by an analytical dependence of α on φ_1 and φ_2 within a certain region of their variation seems more impressive. The conditions necessary for the singular and nonsingular surfaces to exist are considered in the next Section.

1.2.2. Surface Structure at $T=0$

In a microscopic description of a classical crystal surface structure one usually uses some surface model. This is most commonly done by using a version of Kossel's model which is perhaps

* The assumption that $\frac{\partial\alpha}{\partial\varphi}$ is the discontinuous function in crystals was long ago suggested by Gibbs [1.17].

the most effective method to describe surface microstructure (see the review by Voronkov [1.21] which contains Kossel's model and its closest generalizations, the review of different microscopic models of crystal surface in the monograph by Lodies and Parker [1.22], and also, reviews by Burton, Cabrera, Frank [1.23], and by Chernov [1.16]). Since in this section we aim at giving the most general representation of the notions concerned, the content of this model will not be presented in any detail. Instead we shall try to avoid any notions of a model at all using symmetry considerations as the background.

An assumption essentially always used in models of the Kossel type to describe a two-phase interface is that it is possible to assign unambiguously every particle of a substance to a particular phase. Such an assumption cannot always be substantiated in a reasonable way, for example in the case of a crystal-liquid interface, due to the complicated character of particle motion within the near-surface layer. The only case where such an association raises no doubts is the equilibrium state at $T = 0$, when the surface of a classical crystal is interface with vacuum. We shall start with considering just such surfaces, and unless otherwise specified, in all further cases the point in question will be the surface of an ideal crystal without any defects apart from those found in thermodynamic equilibrium.

Any macroscopically uniform surface has a definite orientation relative to the crystalline axes and is specified by a set of integers, viz. Miller indices. Two cases are possible. The surface symmetry group can match the symmetry group of the corresponding crystalline plane, one of whose sides is considered to be "external". In the other case of a substructure, there is a subgroup of this group. For the sake of simplicity we assume that no so-called incommensurate structures originate on the surface (studying this special class of structures, which is of a great interest, would take us too far away from basic aim). We shall consider a surface in the ground state, one in a minimum energy state. Any fault in translational symmetry of the ground state will be called a surface defect. The energy of any defect is evidently a positive quantity. For us, naturally, of the utmost interest are the defects whose origins are connected with a change in the number of particles belonging to a crystal, viz. with elementary processes of crystal growth. The energy of formation of such an isolated defect, evidently, cannot be infinitely small simply because, if only one particle was added, the surface state will at once be changed in a stepwise manner. Let ε_0 be the minimum energy of the isolated defect on the surface of a given orientation. Then, in equilibrium, at $T \ll \varepsilon_0$ the concentration of defects will decrease exponentially. The surfaces with such a property are generally called atomically smooth. Clearly, at sufficiently low temperatures, the equilibrium surface of any classical crystal is in the atomically smooth state.

Of surface defects, those that change the topological structure of the surface (i.e., steps and kinks-on-steps) are of a vital importance (Fig. 1.1). The step is a linear surface defect that causes surface positions on both sides of the defect to differ at infinity by an elementary vector of crystal translation not lying within the surface plane. The ground state of the step is governed by minimizing the total energy under these conditions and by a given step orientation which is characterized by the normal vector that lies in the surface plane (or

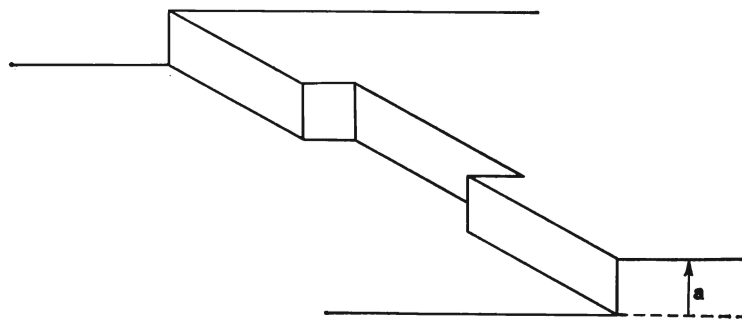


Fig. 1.1. A step with two kinks on the atomically smooth surface.

by the appropriate two-dimensional Miller indices). With a step in the ground state, the rigorous translational symmetry of the surface is conserved, yet now only in a single direction, along the step. Similarly, the kink is a point defect on a step. It occurs when the step positions differ at infinity by an elementary vector of crystal translation, which is noncollinear with the step, and the energy has a minimum value. On the step of a given orientation two types of kinks are feasible differing in "signs" (Fig. 1.1).

The topological meaning of steps and kinks so defined lies in the impossibility of their production (or annihilation) by adding finite number of particles to a crystal. In fact, to produce a defect of the adsorbed atom type it suffices for one particle to be added to the crystal, whereas adding one particle to a kink results only in its displacement by an elementary translational vector along the step (the kink is assumed to be always in the ground state). Thus, the only way to destroy an isolated kink-on-step is by "taking it away" to infinity (the step itself does possess the property like this). With kinks of both signs presented on a step, it is possible to annihilate two kinks of opposite signs. This means that the behaviour of the "kink gas" on a step is regulated by the conservation law of topological charge, viz. to an algebraic sum of kink numbers with a due account for their

signs (also, for steps, the conserved topological charge is a two-dimensional vector quantity following the vector summation law).

The specific role of the "topologically charged" defects when they are produced with a finite concentration (viz. with a finite density of topological charge) is to change the step (alias, surface) orientation. The ground state energy of the new step (surface) may be either higher or lower than that of the initial state. Therefore, the statement concerning the defect energy positiveness is valid only in respect to topo-

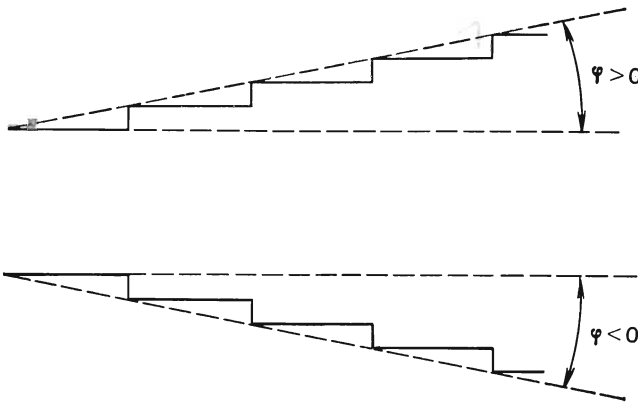


Fig. 1.2. A stepwise surface.

logically neutral defects, particularly, to pairs of kinks or steps having opposite signs, whereas an isolated kink or step can have both positive and negative energy values.

The concepts of step and kink are indispensable in any theoretical description of classical crystal surface structure. Certainly, to quantitatively compare theory to experiment a further detailization of these concepts by introducing concrete assumptions about the microstructure of these objects and character of interatomic bonds is needed. Significant progress was made in this way (see reviews [1.16, 1.21-25]). However, here we would like to draw attention to the fact that the concepts of step and kink, with all their qualitative features incorporated, can be introduced by means of symmetry reasoning alone which will ensure possibility of their extension to include the quantum case.

Now we shall demonstrate, according to Landau [1.19] (see also [1.26]), that an atomically smooth surface is sure to be singular. To do this, let us first consider the concrete case of the (001) plane in a cubic crystal. The surface energy of the plane is a certain quantity α_0 . The planes are inclined to the initial one at a small angle φ , viz. the family of planes $(01N)$, where $N = \frac{1}{\varphi}$ (Fig. 1.2), at a suffi-

ciently large N can be considered as steplike ones. Actually, according to the definition, the step has a finite width that is an effective size along its normal (this size is, generally speaking, of the order of an elementary translation vector on the surface). By taking into account that the energy of interaction between steps decreases with distance as r^{-2} [1.27, 28], it is possible to neglect this interaction. Therefore, at a sufficiently small φ , the surface energy, $\alpha(\varphi)$, with due regard for the linear term in φ , is simply a sum of the initial surface energy α_0 and of the step energy per unit area:

$$\alpha = \alpha_0 + \varepsilon_s \frac{\varphi}{a}$$

where ε_s is the energy of unit length of one step and a the step height. Eventually, noting that the “negative” steps produced in changing the sign of φ have the same energy ε_s as the above “positive” ones, we arrive at

$$\alpha = \alpha_0 + \varepsilon_s \frac{|\varphi|}{a} \quad (1.3)$$

from which it is seen that the derivative $\frac{\partial \alpha}{\partial \varphi}$ at $\varphi = 0$ does undergo a finite jump $\Delta \frac{\partial \alpha}{\partial \varphi} = \frac{2\varepsilon_s}{a}$. Next, according to the paper cited above, it could be possible to demonstrate, with due regard for the step interaction, that the jump, $\frac{\partial \alpha}{\partial \varphi}$, takes place on any facet (01N), too. Yet it is clear that to establish that there is discontinuity in the derivative $\frac{\partial \alpha}{\partial \varphi}$ is now quite superfluous. Actually, if one starts with the above definition alone, rather than using any pictorial presentation of the step structure, the last conclusion will remain valid provided a facet of any integer Miller indices in a crystal of arbitrary symmetry is chosen as the “initial” one. The only thing required to make the proof valid is finiteness of the step width and positivity of the energy of a pair of steps with opposite signs which are defined on the given “initial” surface. In other words, the proof is valid if the step exists as a linear defect of an atomically smooth surface. Naturally, in the general case, the symmetry of the “positive” and “negative” steps vanishes, so that in an expression for $\Delta \frac{\partial \alpha}{\partial \varphi}$, instead of $2\varepsilon_s$, one has to write a sum of the energies of the “positive” and “negative” steps. In addition, it should be remembered that the energy of a step is essentially a nonanalytical function of the initial surface orientation.

1.2.3. Surface Structure at $T \neq 0$

At finite temperatures, the structure of an atomically smooth surface becomes complicated because of the surface defects in the thermodynamic equilibrium. It is clear that at sufficiently high temperatures, when the defect concentration is close to the atomic one, such concepts as step and kink will largely lose their meaning. The surface structure under these conditions came to be an object of numerous studies (see the reviews [1.16, 1.21-25]). We shall try to give the answer to this question by essentially following the article by Burton and Cabrera [1.29] but by avoiding, as before, any model assumptions.

Let us first note that the proof of the singularity of an atomically smooth surface can be extended without any major changes to the case of an isolated step. The only point needed to make the proof is the introduction of the concept of a kink as a point defect on the given step being in the ground state. Let $\varepsilon_s(0)$ be the energy per unit length of such step at $T = 0$. Then for the steps inclined to the initial one by the angle φ , we have

$$\varepsilon_s(\varphi) = \varepsilon_s(0) + \begin{cases} \frac{\varepsilon_+}{a} \varphi, & \varphi > 0 \\ -\frac{\varepsilon_-}{a} \varphi, & \varphi < 0 \end{cases} \quad (1.4)$$

where ε_+ and ε_- are the energies for “positive” and “negative” kinks, respectively, and a the kink height, so that $\Delta \frac{\partial \varepsilon_s}{\partial \varphi} = (\varepsilon_+ + \varepsilon_-) a^{-1}$. Now, by considering ε_s as a function of the kink concentration, we have

$$\varepsilon_s = \varepsilon_s(0) + \varepsilon_+ n_+ + \varepsilon_- n_-$$

By introducing the concentration of kink pairs $n = \frac{n_+ + n_-}{2}$, and allowing for $\varphi = a(n_+ - n_-)$, we arrive at

$$d\varepsilon_s = (\varepsilon_+ + \varepsilon_-) dn + \frac{\varepsilon_+ - \varepsilon_-}{2a} d\varphi \quad (1.5)$$

whence it is seen that the quantity $\varepsilon_+ + \varepsilon_- = \frac{\partial \varepsilon_s}{\partial n} \Big|_{\varphi} = \mu_0$ is the chemical potential of a pair. This quantity, and, consequently, the jump $\Delta \frac{\partial \varepsilon_s}{\partial \varphi}$ proportional to it, are positive. This fact ensures a minimum value for the energy of the step ground state when pairs are by definition absent.

Now let $T > 0$. Here ε_s should be taken to mean the free energy per unit length of a step (at $T = 0$ the distinction between energy and free energy has been meaningless). Furthermore, at the given T

and φ the concentration of the equilibrium pairs is now nonzero ($n \approx \approx \exp\left(-\frac{\mu_0}{T}\right)$ at $T \ll \mu_0$) and the condition of equilibrium boils down to the quantity $\frac{\partial \epsilon_s}{\partial n}\Big|_{T,\varphi}$, that is the pair's chemical potential has vanished. The jump $\Delta \frac{\partial \epsilon_s}{\partial \varphi}$ taken along an equilibrium curve also vanishes together with this potential. Thus, the step is nonsingular at finite temperatures. As will be shown the surface can also become nonsingular at rather high temperatures. The surface (or step) states, for which there are no singularities, are called atomically rough.

The production energy of a kink pair is, as it has been shown, a very essential feature of the step state: vanishing of this quantity will produce an atomically rough state. Concerning a surface, an analogous role is played by the production energy of a pair of steps, since zeroing this quantity ensures vanishing the singularity of the surface energy α . The difference is caused by the fact that, for linear defects like steps, this can only occur at a sufficiently high temperature. Indeed, kinks, like any other point defects, emerge with a finite small concentration even at low temperatures (this means the production energy of such defects is zero at an arbitrary finite temperature). Also, for steps, as for all other linear defects whose energy is proportional to its length L , their equilibrium number [$\approx \exp(-\epsilon_s L/T)$] is zero at any positive value of ϵ_s , since the exponent contains a macroscopically large length.

Now let us follow the temperature dependence of the production energy. This is the free energy of a steps' pair (it will be noted, as before, by ϵ_s) located on an atomically smooth surface. Let us neglect point defects except for the kinks on the very steps. The equilibrium kink concentration builds up with temperature. Along with it, the number of statistically significant kink configurations on every step and hence the pair entropy S_s are rapidly increased. Noting that $S_s = -\frac{\partial \epsilon_s}{\partial T}$ we see the pair free energy ϵ_s to be reduced with the temperature increase and to be zero at a certain temperature T_R^* . Taking into account the interaction between the steps and point defects like adsorbed atoms and surface vacancies (closed steps of a finite length whose equilibrium concentration near T_R are also rapidly increased) does not qualitatively change this conclusion. Instead, it strongly hampers both the calculation of T_R and studies of the temperature dependence of ϵ_s near T_R .

Producing an isolated pair of steps at $T > T_R$ decreases the surface free energy. Therefore, in equilibrium the pairs exist on a surface and their number is found from the equilibrium condition which is

* This is the "roughening transition" temperature as will be seen at the end of the subsection.

derived from the vanishing derivative of the total surface free energy with respect to the number of pairs. In other words, the pair production energy ϵ_s with a due regard for interaction of this pair with other pairs and point defects, vanishes at $T > T_R$ (similar to the chemical potential of a kinks' pair on a step at $T > 0$) and the surface itself becomes, as a result, atomically rough.

From the topological point of view, vanishing of singularity in the angular dependence of surface energy is connected with breakdown in the long-range order. Indeed, on an atomically smooth surface without any steps, the long-range order is conserved even with point defects available (similar to a conventional three-dimensional crystal where the long-range order is conserved with available vacancies). The steps, viz. defects of topological significance, destroy the long-range order (as in the analogy with the three-dimensional crystal one can say that the emergence of steps plays the same role as the initiation of a plastic deformation in a crystal). An atomically rough state might be said to emerge as a result of averaging over orientation adjacent to those of the initial atomically smooth surface. The vanishing of a singularity is a natural outcome of such averaging. It is necessary to note, however, that the term "atomically rough state" does not uniquely correspond to the surface topological type. In fact, as was demonstrated by Marchenko [1.30], on the given atomically rough surface several different types of topological order can occur that replace one another, when the temperature is changing.

The transition from an atomically smooth state into the atomically rough one, insofar as it is connected with the vanishing of a mathematical singularity of the function $\alpha(\varphi_1, \varphi_2)$, must proceed as a phase transition. This is usually called a "roughening transition" following Burton and Cabrera [1.29] who were first to study such transitions (Andreev [1.31] proposed a phenomenological approach to the problem and introduced the term "faceting transition"). A vast amount of works, especially in the last few years (see reviews [1.32-33]), are dedicated to the problem of roughening transition, which has proved to be intimately connected with that of two-dimensional phase transitions. Presently, the question of greatest interest is the role played in the roughening transitions by quantum effects [1.13, 1.34-36].

1.2.4. Some Problems of Growth Kinetics

Now we shall very briefly outline the question of growth kinetics in a classical crystal influenced by surface structure. More precisely, the only item we shall be interested in is the behavior of the growth kinetic coefficient under a small oversaturation. This is

represented by the quantity $K = \frac{V}{\delta\mu}$ at $\delta\mu \rightarrow 0$, where V is the displacement rate of an interface with a given orientation, and $\delta\mu$ is the difference in chemical potentials between the crystal and medium. No substantially novel ideas are required to elucidate this question. Unless otherwise specified, let us stress that the point in question concerns the surface of an ideal crystal. Hence we shall not consider the growth processes due to the presence of dislocations.

Let us start with an initial atomically smooth surface at a certain finite temperature. To be specific, the crystal will be assumed to have grown from a gas phase. In equilibrium the surface contains a certain number of point defects of the type of adatoms and surface vacancies. The process of continuous crystal growth can be imagined as the result of a gradual build up of particles on the crystal that is caused by the increase in the number of adatoms and the decrease in the number of vacancies. However, such a process on an atomically smooth surface is always accompanied by an increase in the surface energy in proportion to the surface area. It is easy to check this fact because the surface remains atomically smooth even at very low temperatures when the equilibrium number of defects is exponentially small. In this case, when the excess number of defects, N_s , becomes much greater than their equilibrium number the change in the surface energy will be equal to $\varepsilon_0 N_s$, where ε_0 is the energy of one defect (the difference between free energy and energy can be neglected owing to the smallness of temperature). The change in the surface energy will increase with N_s up to values of the order of the atomic concentration, when the interaction between defects should be considered. When the temperature is increasing this surface property cannot vanish other than via a phase transition. Such a transition will be shown to become nothing other than the "roughening transition", only specified in other terms. When microscopic surface "displacements" take place, an increase in the surface energy in proportion to the surface area means it is impossible for a crystal having an atomically smooth surface to grow continuously. Having produced the small oversaturation, $\delta\mu$, the two-phase system, together with the surface, will fall into a certain metastable state. The presence of the latter is an additional indication that enables an atomically smooth surface to be discriminated from an atomically rough one.

The growth of a crystal with an atomically smooth surface can proceed via formation of nuclei of new atomic layers. Given $\delta\mu$, there exist a definite critical size of nucleus which ensures its further growth. This size is determined by the vanishing of the variation in the system's total free energy when a small number of particles, δN , passes from one phase to another. If this size is large compared

to the lattice constant, a_0 , the nucleus energy will be that of the nucleus boundary (the boundary in this case is a closed step with the length L) $\varepsilon_s L$, where ε_s is the free energy per unit step averaged over all orientations.

Equating the variation of this quantity to that of the volume free energy, $\delta\mu \delta N$, and taking into account $\delta L \sim \frac{1}{a_0 n_0 L} \delta N$ (n_0 is the number of particles per unit crystal volume), we shall obtain

$$L_{\text{cr}} \sim \frac{\varepsilon_s}{a_0 n_0} \frac{1}{\delta\mu} \quad (1.6)$$

viz. the critical size grows infinitely at $\delta\mu \rightarrow 0$. On the other hand, the probability of producing a critical nucleus per unit time, viz. the growth rate, V , is proportional to $\exp(-\varepsilon_s L_{\text{cr}}/T)$. So, it is seen that for such a process the kinetic growth coefficient, K , vanishes. Moreover, the growth rate remains practically zero up to very large values of the $\delta\mu$ (about $\varepsilon_s^2/a_0 n_0 T$), thus making it possible for metastable states to exist.

Consider the case when the surface is atomically rough. Now $\varepsilon_s = 0$, the critical size according to (1.6), will also vanish. In other words, even atomically sized "nuclei", at however small $\delta\mu$, are critical (let us remember that the production energy of any defect including point defects, is zero in an atomically rough state of surface). It is clear that in this situation no metastable state will take place. Similarly the dependence of surface energy on surface "displacement" will also have no sense.

Thus, a continuous normal growth of a crystal with an atomically rough surface is possible. The kinetic growth coefficient has a finite magnitude which is defined by the probability of one particle attaching to the crystal per unit time. A rough estimate of K (of its classical upper limit, to be more precise) can be obtained in the following way. Let $\delta\mu$ be very large, i.e. of the order of thermal energy, mV_t^2 . The maximum possible velocity of interface motion, V , will be obtained if we assume a particle in a gaseous (or liquid) phase is to be attached to a crystal in every collision with the surface while reverse processes do not occur. In this case $V \sim V_t$. If we also assume that the linear dependence $V = K \cdot \delta\mu$ is conserved down to the smallest $\delta\mu$, we obtain the estimate:

$$K \sim \frac{1}{mV_t} \quad (1.7)$$

viz. the classical upper limit for the quantity K is just equal to the characteristic inverse momentum of particle.

1.3. SURFACE OF A QUANTUM CRYSTAL

1.3.1. Quantum-Rough State

It is well-known that in conventional crystals the quantum-mechanical indistinguishability of the molecules (or atoms) that form a crystal does by no means influence its properties. The low temperature heat capacity of a crystalline lattice, for example, is controlled by the Debye law irrespective of the molecules' intrinsic statistics. The reason is that in a conventional crystal one can take each molecule apart by its link with a certain site of the lattice. Quantum effects manifest themselves only through the presence of zero oscillations whose amplitude is small compared to the interatomic distance. Zero oscillations do not disorder positions of the crystal particles since the exponential probability of two adjacent particles exchanging sites can be neglected. According to Andreev and Lifshitz [1.14], the quantum crystal is a crystal, in which, owing to the comparatively large amplitude of zero oscillations, this probability can not be negligible. A quantum crystal is specified, first of all, by the character of motion of the point defects. In conventional crystals the motion of point defects just like vacancies, is a diffusion process because of the possibility that these defects may make thermoactivation jumps into an adjacent site. In a quantum crystal such processes occur via quantum tunnelling, even at zero temperature. Furthermore, during thermoactivation diffusion the successive jumps are quite random and have no intercorrelation while in quantum diffusion they represent, on the contrary, a unified coherent process being exactly analogous to the motion of an electron in a periodic potential. Here the so-called quantum-mechanical delocalization of point defects takes place, viz. each defect transforms into a quasiparticle whose state is specified by the definite magnitude of quasimomentum (and of energy). It is clear that in studying the surface processes in a quantum crystal the coherent character of the motion of the point defects has to be accounted for in a proper way. It is this fact that served as a starting point for the theory presented here [1.1].

As it already has been noted classical theory is faced with tremendous difficulties when describing the microscopic structure of a crystal-liquid interface because an unambiguous identification of each particle with a particular phase is impossible owing to the complicated character of particle motion near the interface. Only at fairly low temperatures, when the second phase is a rarified gas can such an identification of particles become feasible. The need for explicit accounting of quantum-mechanical indistinguishability of identical particles at an interface between a quantum liquid and a quantum crystal makes their individualization impossible at any temperature. In the microscopical description of the surface structure one would

have to use a density function which is periodic in the crystal bulk and particular constant in the liquid bulk. Transition region between these two asymptotics has a width which is the effective thickness of a boundary and equal to several interatomic distances. Thereby many concepts generally used in models like Kossel's appear to be devoid of any immediate physical sense. The concept of point defect of the adatom type, for example, cannot be generally formulated in any clearcut fashion in the quantum case.

The foregoing does not, of course, mean that the quantum surface is not a physically well-defined two-dimensional object. First of all, for the position of the surface to be unambiguously defined it is sufficient to have a conventional condition of the absence of particle surface density [1.15]. Also such concepts as step and kink-on-step can be introduced in the quantum case in a perfect analogy the classical atomically smooth surface introduced in Section 1.2.2. For example, a step on a surface corresponds to the state of the interface when its positions at infinity (to the left and to the right) in Fig. 1.1 are displaced by an elementary vector \mathbf{a} of crystal translation not lying on the surface plane. Owing to crystal periodicity and liquid homogeneity, the displacement by the translation vector transforms the interface into an equivalent position. Hence, the step is a linear defect on the surface and, essentially, only this property of the surface is vital for the subsequent discussion. Here we repeat that the concept of step and, analogously, that of kink-on-step located on a surface of arbitrary integer Miller indices can be introduced in this way.

The state of a step is governed by the configuration of kinks located on it. Each kink can be considered as a point defect-on-step. Assume that in an equilibrium state at $T = 0$ the surface has an oriented step with a kink over it. Displacing the kink by an elementary translation vector along the step means a particle transition (here a helium atom*) from one phase to another. The probability of such transitions are finite even at $T = 0$ due to processes which are similar to quantum tunnelling. The kink energy is not changed under such displacements, since the chemical potentials of phases in equilibrium are the same. This means that the kink, similar to other point defects in a quantum crystal, behaves under these conditions like a delocalized quasi-particle whose state is controlled by the quasimomentum.

The kink energy, ϵ_s , is a function of the kink quasimomentum, p (see Fig. 1.3), with the energy band width, Δ , proportional to the probability, w , of one atom tunnelling per unit time, viz. $\Delta \sim \hbar w$.

* To be precise, we consider the interface between solid and liquid helium, even though the exposed reasons have, undoubtedly, a more general meaning.

Here this probability is apparently not less than the corresponding probability which defines the width of a vacancion band in ${}^4\text{He}$, viz. the magnitude of Δ is expected to be about 1 K.

Let p_0 be the value of quasimomentum corresponding to the energy band bottom. For an isolated kink, this state at $T = 0$ is stationary (and ground). The stationary states closely spaced in energy correspond to nonzero kink velocities and thereby to a continuous flux of matter from one phase to another. In other words, the transition

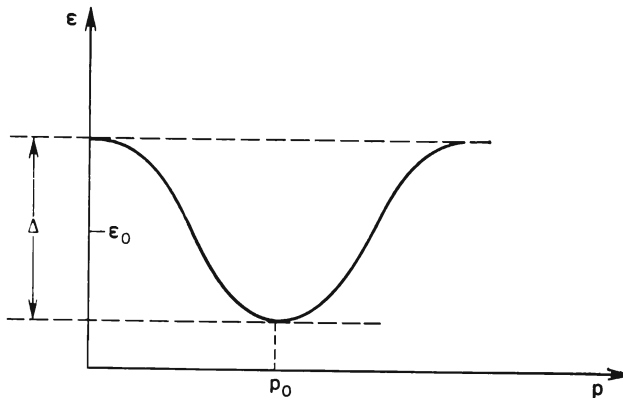


Fig. 1.3. Energy band of an isolated kink.

of matter from one phase to another is a coherent process not related to any energy dissipation. In fact, a violation of the coherency could take place only owing to collisions between kink and phonons or to an emission of the latter. At $T = 0$, however, there are no thermal excitations and the processes of phonon emission at low kink velocities are forbidden by the conservation laws of energy and momentum. Let us also emphasize that the states are not separated from the ground state by a finite energy gap. Thus, the isolated kink exemplifies a system with stationary states infinitely close in energy to the ground state and is specified by the presence of a continuous flux of matter from one phase to another.

As for any classical defect, the energy of an isolated kink, ϵ_0 , is a positive quantity*. On the other hand, the localized kink is a "packet" composed of states with arbitrary values of p . Therefore, the value of ϵ_0 lies approximately in the middle of the energy band. If the energy corresponding to the band bottom, $\epsilon(p_0)$, is positive, then there are no kinks in the step ground state, viz. the step at

* More precisely, this is the total (summed) energy of two kinks with opposite signs (see Sec. 1.2.2).

$T = 0$ is atomically smooth. If the value of Δ is adequately large (roughly speaking, $2\Delta > \varepsilon_0$), then $\varepsilon(p_0) < 0$, viz. the step energy decreases when producing kinks with $p = p_0$. In other words, the atomically smooth state appears to be unstable in regard to kink production (more precisely, in regard to the production of opposite sign kink pairs since under the fixed mean orientation of a step the

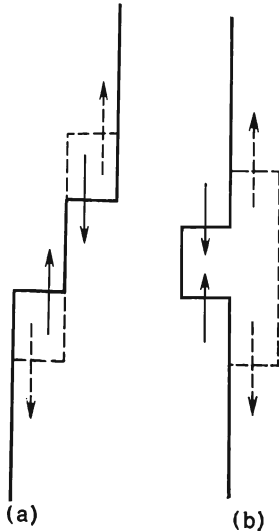


Fig. 1.4. Possible types of kink collisions.

production of kinks with only one sign is impossible). To elucidate the structure of the step ground state allowance need to be made for the interaction between kinks.

When colliding, two kinks of the same sign can exchange their quasi-momenta (Fig. 1.4a). If kink signs are opposite, besides this kind of collision it is possible for a collision to be accompanied by a "flip-over" into an adjacent row (Fig. 1.4b), generally speaking, the probability of this process being not so low. In fact, at distances longer than the interatomic distance, the interaction between kinks is generally effected by the elastic deformation field inside a crystal [1.27]. In this case we have

$$U(r) \sim \frac{\varepsilon_0^2}{E} \frac{1}{r^3} \quad (1.8)$$

where E is the Young's modulus (under Van der Waals interaction $U \sim r^{-4}$ [1.19]). On the other hand, at a distance comparable to the interatomic distance we evidently have $U(r) \sim \varepsilon_0$. The probability of the "flip-over" is the same as the probability of a particle tunnelling

through the potential barrier. The barrier is specified by the function $U(r)$ and under these conditions the probability may range up to about unity. If the energy $\epsilon(p_0)$ is not too close to zero, viz. if $|\epsilon(p_0)| \sim \Delta$, sizable interaction between kinks will only be at distances of the order of interatomic separations.

Thus, in increasing the kink concentration on a step the latter's energy will be decreased until it will reach a minimum at a particular concentration (which is, generally speaking, of the order of the atomic concentration). Such a step may be called "quantum-rough" since it involves a large number of kinks even in the ground state. An essential property of this step is the presence of states that are infinitely close to ground state energy and correspond to a step's continuous motion accompanied by particle transitions from one phase to another. The availability of such states is guaranteed by the processes of flip-over into an adjacent row. Thus, the quantum-rough step seems to be totally delocalized when on crystal surface.

The total energy of a quantum-rough step, ϵ_s , (calculated per length of elementary translation vector along the step) may prove either positive or negative depending on whether the positive energy of a "bare" atomically smooth step*, ϵ_{s0} , compensates for the negative energy of the delocalized kinks with their interaction incorporated. If $\epsilon_s > 0$ for all possible orientations of a step on the surface at hand, then the surface ground state will have no steps, and at $T = 0$ the surface will remain in a classical atomically smooth state. If $\epsilon_s < 0$, even for only a pair of opposite orientations of the step, then the atomically smooth surface will prove to be unstable for producing such steps. Thus, a surface in equilibrium will represent a specific two-dimensional liquid consisting of delocalized steps of different configurations. The number of each sort of step is evidently not fixed and is determined by the minimum total energy. With this property in mind, such a surface will be called "quantum-rough".

Since the quantum-rough surface is in equilibrium at $T = 0$, its entropy must vanish. In connection with this, it will be useful to note the following. The entropy of a classical atomically rough surface is due to the presence of a large number of microscopic configurations corresponding to the same macroscopic state (configurational entropy). Therefore it is not zero and this is why the classical atomically rough surface cannot exist as a surface in equilibrium. Therefore, this brings into question the very possibility of the existence of a surface state which differs from the classical atomically smooth one, at absolute zero. A simple example demonstrates whether this is possible in practice. Consider a step with a single kink. The localized kink states are degenerated with the multiple $\frac{L}{a_t}$,

*

The case at hand are again two kinks with opposite signs.

where L is the step length and a_t the translational vector length along the step. Therefore, the configurational entropy of such a system is $\ln(L/a_t)$. The quantum delocalization resulting in the band $\varepsilon(p)$ removes this degeneration thus eliminating configurational entropy.

The general information in Sec. 1.2 relative to an equilibrium crystal shape and, in particular, to its connection with the character of the angular dependence of α , still remains valid in the quantum case. However, in contrast to the classical crystal surface, the surface in the quantum case could be nonsingular even at $T = 0$. Indeed, we have already seen that in a quantum-rough state, the number of steps is nonzero even at zero temperature and is in turn determined by the condition of minimum surface energy. In other words, the energy production of a pair and along with it the quantity $\Delta\partial\alpha/\partial\varphi$ also vanish just as in the case of a classical atomically rough state. It goes without saying that the same crystal may have both quantum-rough and atomically smooth parts of the surface. An equilibrium facet pattern of such a crystal has a number of flat facets encircled by rounded-off parts.

As we have seen, the possibility of producing a quantum-rough state is determined by the "strength" of the quantum effects. As can be seen from the experimental data, we deal with a most interesting situation in the case of the ${}^4\text{He}$ crystal. In this crystal the quantum delocalization effects are not too strong so that at least three nonequivalent facets remain atomically smooth. It is possible in this case to further detail the properties of surfaces oriented close to the atomically smooth facets, i.e. of the surfaces with very large Miller indices, since these "singular" facets have the most dense packing (the last feature, as will be seen later on, is perfectly natural).

This possibility was already indicated by Landau [1.19]. Indeed let us again consider a facet (001) of a cubic crystal as an initial "singular" facet. Then $(01N)$ type facets can be considered as stepwise provided N is adequately large. The steps on the facets $(01N)$ can be treated as "faults" in the periodic arrangement of the initial steps (Fig. 1.5). The energy of a pair of such "secondary" steps, $\varepsilon_s(N)$, can be calculated if the long-range interaction of initial steps is known. In the work [1.19], the energy $\varepsilon_s(N)$ (to be exact, the quantity $\Delta\partial\alpha/\partial\varphi$ which is unambiguously connected with the energy) was calculated assuming that the long-range interaction between steps is the Van der Waals type ($U \propto r^{-3}$). If we recognize that the elastic interaction ($U \propto r^{-2}$) is stronger, then we shall obtain

$$\varepsilon_s(N) = \frac{12\zeta(3)}{\pi} \frac{1-\sigma^2}{E} (f^2 + \beta^2 a_s^2) \frac{1}{N^4} \quad (1.9)$$

where σ is Poisson's ratio, E is Young's modulus, ζ is Riemann's zeta function, f and β are the interaction parameters of the initial steps

(see [1.27]). Accordingly, $\Delta\partial\alpha/\partial\varphi = a_N^{-1} \varepsilon_s(N) \propto N^{-3}$ (the height of the “secondary” step, a_N , is evidently equal to a_s/N). In a perfectly analogous manner, it is possible to calculate the energy of a pair of “secondary” kinks, viz. of the kinks on atomically smooth $(1N)$ steps which are slightly inclined relative to the (01) step. In this case, obviously, we have $\varepsilon(N) \propto N^{-5}$.

Consider now in more detail the $(1N)$ steps while allowing for the effects of quantum delocalization. The role of the quantum effects

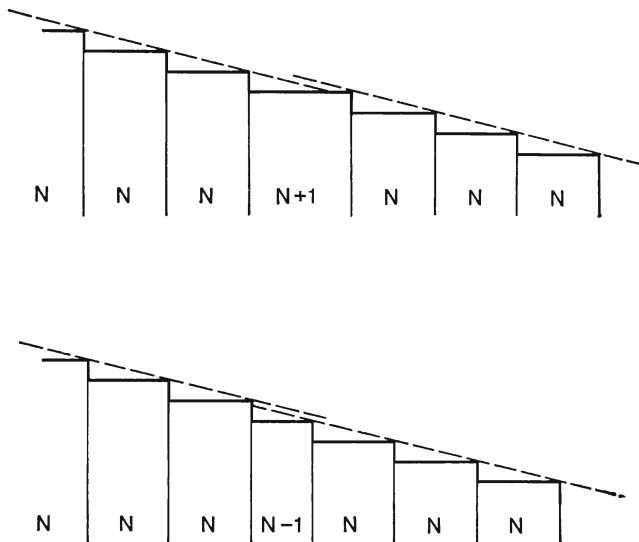


Fig. 1.5. “Positive” and “negative” steps on the $(01N)$ facet.

grows with Δ , the width of the energy band of a kink on the initial (01) step. Initially, let Δ be small as compared to the energy of a localized kink, ε_0 (due to symmetry of the initial step the energies of the “positive” and “negative” kinks are the same). In this case, the $(1N)$ steps will consist of kinks of only one sign. Such a system at large N can be studied in great detail (including at finite temperatures provided that the number of thermally produced pairs is not so large, viz. at $T \ll \varepsilon_0$). Let us consider the basic properties of this system. Let us take $T = 0$. If N is not too large then the interaction between steps will result in their localization. To do this requires that when one kink is shifted by interatomic distance, a_0 , the energy U_{int} of its interaction with all remaining kinks would change by a quantity larger than Δ . Assuming for simplicity that $U_{\text{int}} \approx \varepsilon_0 (a_0/r)^3$ (for the step itself to be stable requires a repulsive

interaction), we obtain the localization condition:

$$N \leq \left(\frac{\epsilon_0}{\Delta} \right)^{1/5} \quad (1.10)$$

Localizing the steps means that the quantum effects can be neglected and this, in turn, automatically leads to the conclusion that the step, like any classical step at $T = 0$, is in an atomically smooth state. It should be noted that the condition for the conservation of the atomically smooth state can be obtained directly by comparing the energy of a localized "secondary" kink, $\epsilon(N)$, with the band width, Δ_N , that occurs due to kink delocalization. Noting that $\epsilon(N) \approx \epsilon_0 N^{-5}$ and that at large N the value of Δ_N is practically the same as Δ (each is controlled, essentially, by the same probability of attaching one atom to a crystal per unit time), we see that this condition is exactly equivalent to that of (1.10).

In the opposite limiting case of large N , the kink-on-step represents a one-dimensional "gas" of quasiparticles and at $T = 0$ this gas, certainly, cannot be thought of as an ideal gas. The peculiar feature of this gas is that its particles being identical in their characteristics are distinctive because each kink belongs to a definite crystalline row. When moving along a step, the kinks cannot exchange their sites, i.e. they are mutually impenetrable. With long-range interaction neglected, such a gas is equivalent to a one-dimensional gas of solid spheres. The energy spectrum of the latter is known [1.37] to exactly match the energy spectrum of a one-dimensional ideal gas of spin-polarized fermions. The criterion for the ideal state of such a Fermi-gas is the smallness of the elastic interaction energy ($\epsilon_0 N^{-3}$) compared to the Fermi-energy (ΔN^{-2}), viz.

$$N \gg \frac{\epsilon_0}{\Delta} \quad (1.11)$$

Finally, notice that in analyzing the collective oscillations in a kink gas one has to take into account a specific interaction of kinks "via liquid". This is due to the fact that kink motion is always accompanied by a liquid phase motion. Therefore, when two kinks are moving at the velocities of V_1 and V_2 , the kinetic energy of the liquid is augmented by a term proportional to the product $V_1 V_2$. The corresponding interaction energy is

$$U = \frac{a_0^4}{2\pi} \frac{(\rho_1 - \rho_2)^2}{\rho_2} \frac{V_1 V_2}{r} \quad (1.12)$$

where ρ_1 and ρ_2 are the densities of crystal and liquid, respectively, r is the interkink spacing (the corresponding Hermitian operator looks much more complicated). This interaction must be accounted for because its long-range character leads to a logarithmic divergence in energy when the kink gas moves as a whole (essentially, it is

this interaction that is incorporated macroscopically when the crystallization wave spectrum is calculated, see Sec. 1.3.3).

Now let us return to consider the possible states of surfaces with large Miller indices at $T = 0$. The state of the $(01N)$ surface, adjacent to the initial atomically smooth (001) surface, is governed by the state of its constituent steps, viz. the (01) ones. If an isolated (01) step is quantum-rough, then at a sufficiently large N the $(01N)$ surface will also be quantum-rough. In fact, a step's quantum-rough state means that it is delocalized, which in turn makes it impossible to form substructures in the steps system such that correspond to topological defects of the “secondary” step type. Step delocalization, however, can become disadvantageous from the energy standpoint if its interaction with other steps is sufficiently strong. The corresponding condition (this can be obtained essentially from the same reasoning as in the kink-on-step case) is

$$N \leq \left(\frac{a_0 \epsilon_s}{\Delta} \right)^{1/4} \quad (1.13)$$

Next, if the (01) step is atomically smooth, the adjacent $(1M)$ steps must be quantum-rough [see condition (1.10)]. Accordingly, the $(1, M, MN)$ surfaces also appear to be quantum-rough at a sufficiently large M and N . Here the criterion to localize primary kinks, and therefore, steps, boils down, like (1.10), to requiring that the quantity Δ is small compared to a change in the interaction energy of a given kink with the remaining ones (when this kink is displaced by an interatomic spacing). The corresponding condition is, evidently, governed by concrete parameters of the two-dimensional lattice produced by kinks.

Thus, we see that, given that the quantity Δ characterizing the “strength” of quantum effects is small, surfaces with sufficiently large Miller indices always turn out to be quantum-rough. Therefore, surfaces with the smallest Miller indices, viz. the most densely packed ones have the highest “chance” to retain an atomically smooth state. Such a situation is similar to that in a classical crystal at finite temperatures. There is, however, an appreciable difference. At finite temperatures each step turns out to be rough, whereas the most densely packed steps can, generally speaking, remain atomically smooth when quantum effects are present and $T = 0$. Hence, at $T = 0$ the $(01N)$ facets can remain atomically smooth at infinitely large N , whereas at $T > 0$ these facets are rough.

When considering the properties of surfaces (and steps) with large Miller indices, we, naturally, assumed these surfaces (steps) to exist at $T = 0$. In connection with this the following should be noted. As was demonstrated by Marchenko [1.38], in equilibrium crystal edges, viz. common boundaries of two planes converging at a finite angle cannot exist on the surface of any crystal with sufficient-

ly large dimensions. Thus, surfaces of arbitrary orientation must be presented in the equilibrium facet pattern of a crystal. The proof is based on the fact that, with due regard for striction effects, the crystal edge energy becomes negative making a substructure without macroscopic edges advantageous from the energy standpoint. The analogous proof is not valid, however, if applied to a step. Hence, there is, in principle, a conceivable situation when steps lacking all orientations exist on a given atomically smooth surface. For example, $(1N)$ steps cannot exist in the case of attractive interaction between the kinks of the same sign, which is possible [1.27]). In this circumstance, the statement that surfaces of sufficiently large Miller indices must always be quantum-rough is invalid.

1.3.2. Coherent Crystallization

A crystal with a quantum-rough surface can grow (or melt) either by extending the surface confined by each step or by producing new atomic layers during the collisions of two steps (this process is analogous to flip-over to adjacent rows during collisions between two kinks). These and their reverse processes are responsible for the existence of a system's stationary states being infinitely close to the ground state. A continuous growth and melting occurs in these stationary states. Under such conditions the growth and melting of a crystal present a coherent process which does not pertain in principle to any kind of energy dissipation. Thus, the motion of the interface at $T = 0$ occurs without disturbing phase equilibrium. In other words, the kinetic growth coefficient of a crystal with a quantum-rough surface becomes infinite at zero temperature.

The situation with atomically smooth surfaces is reversed. Indeed, at $T = 0$ an atomically smooth surface in equilibrium contains no defects. Therefore, the growth of a crystal having such a surface can only occur via producing nuclei of new atomic layers, i.e. closed steps of a finite length whose energies as defined above are positive. With a finite interphase difference in chemical potentials, $\delta\mu$, it is possible for a critical size nucleus to be produced in a quantum under-barrier way [1.39]. At $\delta\mu \rightarrow 0$ the critical dimension increases infinitely and the probability of this process rapidly (exponentially) approaches zero so that $\lim V/\delta\mu = 0$. Consequently, the kinetic growth coefficient of a crystal with an atomically smooth surface vanishes even with quantum effects added. This result is valid at finite temperatures, as we have seen in Sec. 1.2.4, and when nuclei are produced via thermoactivation the growth coefficient also vanishes.

The presence of stationary states that fit to the continuous growth and melting of a crystal provides a new property with which to identify quantum-rough surface states. Since crystal growth occurs with-

out any equilibrium violations, the growth rate must be viewed as a thermodynamic variable. To be exact, the phase equilibrium condition (1.2) is supplemented by additional terms which are related to the kinetic energy of bulk phases. In addition, surface energy becomes dependent on both the growth rate and the velocity of the tangential component of the liquid phase velocity relative to crystal phase. Accordingly, the form of the surface tension tensor that controls capillary crystal forces will also be changed [1.27-28, 1.40]. These items greatly complicate the problem of setting out a complete system of equations for surface motion. As yet, this problem has not been solved. However, to find the surface small oscillation spectrum in the long-wave limit (see the next Sec.) all these speculations are immaterial. Their incorporation leads either to nonlinear (in velocity) effects or to additional terms that appear in the spectrum and contain higher (as compared to the principal ones) powers of wave vector.

At finite temperatures, the growth of a crystal with a quantum-rough surface is accompanied by energy dissipation caused by the interaction between bulk thermal excitations and the moving surface. Let us evaluate the dissipation due to phonons. When falling onto the interface as viewed from the liquid phase phonons produce the pressure $P_{\text{ph}} \sim E_{\text{ph}} \sim nT^4/\theta^3$, where n is the number of atoms per unit volume, θ the Debye temperature, E_{ph} the phonon energy per unit volume. Under equilibrium that is with a fixed interface, this pressure is compensated for by the solid phase pressure. If the interface moves with the velocity V , then a pressure drop $\delta P_{\text{ph}} \sim \frac{V}{c}E_{\text{ph}}$ (c is sound velocity) due to Doppler effect is directed by the interface against the motion. As a result, energy of the order of $\frac{V^2}{c}E_{\text{ph}}$ is dissipated per unit time and per unit area. On the other hand, the same energy dissipation is equal to $\delta\mu \cdot \dot{N}$, where $\dot{N} \sim nV$ is the number of atoms passing per unit time from one phase into another. Therefore we find:

$$K \sim \frac{c\theta^3}{T^4} \quad (1.14)$$

Thus, the growth coefficient tends to infinity as $T \rightarrow 0$.

Phonons are the principal thermal excitations in the liquid ${}^4\text{He}$ at temperatures below about 0.5K. At higher temperatures, the more essential excitation might be the roton contribution to the total energy dissipation for which an approximate dependence of the type $K \propto \exp(\Delta_r/T)$, where Δ_r is the roton gap width, is expected to be valid.

These estimates indicate only the temperature dependence of the growth coefficient in one or another temperature ranges. For a

quantitative comparison with experimental data these estimates are, of course, quite insufficient. Besides, strictly speaking, these estimates are valid only in the “ballistic” case when free path lengths of phonons and rotons are sufficiently large (the surface wavelength serves as a characteristic dimension, see the next Sec.). Andreev and Knizhnik [1.41] (see also [1.42]) calculated the growth coefficient limits for both the “ballistic” and “hydrodynamic” cases. Further discussion of this question is in Sec. 1.4.

The preceding has related to ${}^4\text{He}$ crystals. As for ${}^3\text{He}$ crystals, a formula analogous to that of (1.14) can be applied to them only at extremely low temperatures. Temperatures must be much less than that needed for the transition into a superfluid state and, of course, with the condition that the crystal surface remains in a quantum-rough state. Yet here the principal type of thermal excitations both in liquid and solid phase is represented by spin waves with a linear dispersion law [1.43, 44], as for phonons. The main contribution into energy dissipation is produced by the crystal spin waves since their velocity is lower. Therefore, the quantity c in (1.14) stands for the spin wave velocity inside the antiferromagnetic solid ${}^3\text{He}$ and θ the Neel temperature. At higher temperatures, where liquid ${}^3\text{He}$ behaves as a normal Fermi liquid, the basic dissipation mechanism is the interaction of the moving interface with Fermi excitations. Energy dissipation is, of the order of magnitude, $p_F n V^2$, where p_F is Fermi momentum. The estimate corresponds to the temperature independent growth coefficient $K \sim 1/p_F$. An analogous estimate could be made also for a crystal growing from a dilute solution of ${}^3\text{He}$ - ${}^4\text{He}$ (with a concentration $n_3/n \ll 1$) [1.45, 46]. Here the energy dissipation due to interaction between a moving interface and impurities of ${}^3\text{He}$ is, of the order of magnitude, $n_3 p_3 V^2$, this corresponds to the growth coefficient $K \sim \frac{n}{n_3} \cdot \frac{1}{p_3}$, where p_3 is the characteristic momentum of an impurity atom. By comparing to (1.14), we see that at low temperatures the ${}^3\text{He}$ impurities can substantially influence growth kinetics of ${}^4\text{He}$ crystals even at extremely low concentrations.

1.3.3. Crystallization Waves

We have seen in the previous Section how the quantum rough surface state provides a possibility for strictly nondissipative crystallization and melting of a crystal at $T = 0$. This means that at rather low temperatures the process of establishing an equilibrium crystal shape with the quantum-rough surface is of an oscillatory character. In fact, any deviation of the crystal shape from equilibrium results in increasing its surface energy. Therefore, any non-equilibrium crystal shape will change towards decreasing the surface

energy via crystallization or melting. On the other hand, because of the difference in density of the two phases, crystal growth and melting will lead to a liquid phase motion, viz. to an increase in system's kinetic energy. It is clear that given a small energy dissipation, the surface will be subjected to weakly damped oscillations similar to conventional capillary waves on a liquid phase surface. The spectrum of these oscillations, viz. of crystallization waves, can be easily found in the limit of long waves, when the compressibility of both phases can be neglected. It is essential that no model concepts about surface microscopic structure are introduced to do this.

In deriving the crystallization wave spectrum we shall allow for the gravitational field and damping caused by the finiteness of the kinetic growth coefficient. To do this, first of all we shall note that with capillary effects included Eq. (1.2) will replace the conventional condition of phase equilibrium, $\mu_1 = \mu_2$. Therefore, in describing weakly nonequilibrium situations, e.g. a crystal growth in the absence of any thermal flux, the right-hand side of Eq. (1.2) must be augmented by the term $\frac{\rho_1 V}{mK}$, where V is the growth rate at the given point and K the kinetic growth coefficient. Let us consider a flat surface, $z = 0$, undergoing a displacement $\zeta(x, t) = \zeta_0 \exp(ikx - i\omega t)$ along its normal. A motion resulting in a noncompressible liquid is described by the potential ψ that satisfies the Laplace equation, $\Delta\psi = 0$, viz. $\psi = \psi_0 \exp(ikx - i\omega t - kz)$. Mass conservation during phase transition yields a boundary condition for the z -component of liquid phase velocity:

$$V_z = \frac{\rho_2 - \rho_1}{\rho_2} \dot{\zeta} \quad \text{at} \quad z = 0 \quad (1.15)$$

Instead of the phase equilibrium condition (1.2) in this case we have:

$$\left(\frac{1}{\rho_2} - \frac{1}{\rho_1} \right) (P' - \rho_2 g \zeta) + \frac{1}{\rho_1} \tilde{\alpha} \frac{\partial^2 \zeta}{\partial x^2} = \frac{1}{mK} \dot{\zeta} \quad (1.16)$$

where $\tilde{\alpha} = \alpha + \partial^2 \alpha / \partial \varphi^2$, φ is the angle between the normal to a displaced surface and the z -axis, P' the alternating part of pressure in liquid (here we have taken into account $\partial \mu_2 / \partial P = m / \rho_2$). Further allowing for

$$P' = -\rho_2 \dot{\psi}, \mathbf{V} = \nabla \psi \quad (1.17)$$

we find the spectrum of plane waves:

$$\omega^2 - \frac{\tilde{\alpha} \rho_2}{(\rho_1 - \rho_2)^2} k^3 - \frac{\rho_2 g}{\rho_1 - \rho_2} k + \frac{\rho_1 \rho_2}{(\rho_1 - \rho_2)^2} \frac{i\omega k}{mK} = 0 \quad (1.18)$$

As can be seen from (1.18), the propagation velocity of these oscillations is much lower than that of sound, thus justifying the neglect

of compressibility in both phases. The gravitational term in (1.18), as with conventional capillary waves, must be allowed for only at the lowest frequencies, when wavelength is of the order of or lower than the capillary constant (about 1 mm).

Much like capillary waves, crystallization waves are unstable to decay from one to two quanta which have lower energy. Therefore, strictly speaking, these waves have a finite damping even at $T = 0$, when $K \rightarrow \infty$. The order of magnitude of this damping (being inversely proportional to lifetime), γ , is determined by the formula,

$\gamma \sim \frac{\hbar k^5}{\rho}$ (see [1.47], where the corresponding problem is solved for conventional capillary waves). For low-frequency oscillations, at finite temperature, the damping mechanism caused by the finiteness of the growth coefficient is the most important. From (1.18), assuming weak damping, we find:

$$\gamma = \frac{\rho_1 \rho_2 k}{2m K(\rho_1 - \rho_2)^2} \quad (1.19)$$

For ${}^3\text{He}$, where the Fermi-liquid theory applies, using the estimate of K from Sec. 1.3.2. one can demonstrate that the oscillations are strongly damped at all frequencies. The same conclusion also follows from the estimate of this quantity for a classical crystal with an atomically rough surface [see (1.7)]. It is evident that linear oscillations like crystallization waves cannot exist on a classical atomically smooth surface. Thus, the existence of weakly damping crystallization-melting waves is an essentially quantum effect.

As has already been noted, the surface in a quantum-rough state represents a two-dimensional quantum "liquid". Certainly, the concepts of step and kink in their original sense are now insufficient for a microscopic description of such a liquid to be adequate. In fact, steps and kinks remain well defined objects only so long as their concentrations are low. On the other hand, in an advanced quantum-rough state, viz. in the absence of special small parameters the kink and step concentrations are far from being small. Their interaction cannot be taken as weak; besides, the number of "particles" of each sort does not conserve in this liquid. In this situation the principal property of the quantum-rough surface, viz. the presence of stationary states corresponding to a continuous crystal growth and melting, essentially can only be postulated (the same with the existence of a quantum-rough surface). Consequently, the speculations set forth in Section 1.3.1 are to be taken not as a proof but rather as an indication to the very possibility that such states exist. In this situation a real problem can be solved when testing the self-consistency of the concept of coherent crystallization, together with all the implications that follow from it. Thereby a decisive corroboration of the concepts' physical foundation can only be provided by experiment.

For describing a quantum-rough surface at finite temperatures one should know its spectrum of elementary excitations, viz. collective excitations in a system of strongly interacting kinks and steps. The calculation of this spectrum over the whole wavelength range is, of course, impossible. However, in the long wavelength limit, as we have seen just now, such collective excitations are crystallization waves. The knowledge of their spectrum enables the temperature dependence of the surface energy, α , to be calculated at low temperatures. We shall not give the derivation, since it is analogous to that of Atkins [1.48] for capillary waves on superfluid helium surface, but shall only give the result:

$$\alpha(T) = \alpha_0 - \frac{1}{4\pi} \Gamma(7/3) \zeta(7/3) \cdot \frac{(\rho_1 - \rho_2)^{4/3}}{\alpha_0^{2/3} \rho_2^{2/3}} \frac{T^{7/3}}{\hbar^{4/3}} \quad (1.20)$$

(here we neglect anisotropy of α_0).

Besides crystallization waves, there exists one additional branch of surface elementary excitations, viz. elastic oscillations of the Rayleigh wave type with a linear dispersion law [1.6] (see the next Sec.). The contribution of these oscillations to surface energy is proportional to the higher degree of temperature (T^3), hence at low temperatures it can be neglected.

1.3.4. Sound Transmission Through a Quantum-Rough Surface

Usually when studying the reflection and refraction of sound at a crystal-liquid interface, one only assumes that the conditions of surface mechanical equilibrium rather than phase equilibrium are satisfied. For conventional classical crystals, such an approach is well justified, since the times for establishing a phase equilibrium are extremely long as compared with those for a sound wave period. As was first noted by Castaing and Nozieres [1.4], the character of sound reflection changes abruptly when the kinetic growth coefficient is sufficiently large. Consider a quantum-rough interface at $T = 0$. At this interface the phase equilibrium condition, $\mu_1 = \mu_2$, being equivalent here to the constant pressure condition is always fulfilled. This means that, when a sound wave falls at such the interface, the alternating pressure part vanishes at the interface, viz. the latter succeeds in "adjusting" via recrystallization to meet this condition. The constant pressure at the interface means, in turn, the transmitted wave amplitude will vanish, too. At finite temperatures, thermal excitations slow down the interface motion, the phase equilibrium is violated more and more as the growth coefficient reduces, and sound penetrates from one phase into another.

However, it turns out that due to capillary effects sound can pass through a quantum-rough surface even at $T = 0$ [1.6], and the transmitted wave amplitude being proportional to sound frequency. We shall consider this problem as it is exemplified by an elastic isotropic crystal.

Let a plane sound wave with the frequency ω and the wave vector \mathbf{k} be incident on the surface ($z = 0$) as viewed from the liquid phase. Now let \mathbf{v} be the liquid phase velocity and \mathbf{u} the elastic deformation vector in the crystal. The resulting displacement of the interface is a sum of two terms, viz. the elastic displacement, u_z , and that caused by recrystallization, ζ . The condition of mass conservation during crystal growth is written:

$$(\rho_1 - \rho_2) (\dot{u}_z + \dot{\zeta}) = \rho_1 \dot{u}_z - \rho_2 v_z \quad (1.21)$$

In deriving the remaining boundary conditions relevant to both mechanic [see Eq. (1.4) in [1.27]] and phase equilibrium [Eq. (1.2)] one has to take into account that the "nondeformed" surface is $z = \zeta(x, y, t)$. By choosing the plane (x, z) as a plane of incidence so that $R_2^{-1} = 0$, $R_1^{-1} = -\partial^2 \zeta / \partial x^2$ (all displacements, of course, are small compared to a wavelength), and by denoting the alternating parts of pressure and of stress tensors with $\delta P = P - P_0$, $\delta \sigma_{ik} = \sigma_{ik} - \sigma_{ik}^0$ respectively, we shall obtain the conditions for the mechanic equilibrium in the form:

$$-\beta \frac{\partial^2 \zeta}{\partial x^2} + \delta \sigma_{zz} + \delta P = 0 \quad (1.22)$$

$$\delta \sigma_{vz} = 0, \quad v = x, y$$

where β is the surface tension coefficient, which in the isotropic case the relevant tensor is reduced to [1.27]. The quantities entering (1.2) will be transformed in the following way:

$$\delta F = F - F_0 = \frac{\partial F}{\partial \rho_1} \delta \rho_1 = \frac{P_0 + F_0}{\rho_1} \delta \rho_1 = \frac{\mu_0}{m} \delta \rho_1$$

$$\delta \mu = \mu - \mu_0 = \frac{\partial \mu}{\partial P} \delta P = \frac{m}{\rho_2} \delta P,$$

whence

$$\left(1 - \frac{\rho_1}{\rho_2}\right) \delta P - \alpha \frac{\partial^2 \zeta}{\partial x^2} = 0 \quad (1.23)$$

Equations (1.21)-(1.23) form a complete system of linearized boundary conditions for a quantum-rough surface at $T = 0$. Neglecting the capillary effects, viz. the terms containing α and β , the boundary conditions are reduced to $\delta P = 0$, $\delta \sigma_{iz} = 0$. The variables that describe each of the two media are seen to be separable in such a way that the boundary conditions for both media are the

same as those at the interface with vacuum [here condition (1.21) determines just the total boundary displacement]. In other words, the sound incident at the interface from either side reflects totally. Besides, the spectrum of surface elastic oscillations (of the Rayleigh wave type) is precisely the same as that at an interface with vacuum, while on an atomically smooth surface it depends substantially on the properties of the liquid phase [1.49]. (In this case, instead of condition (1.23) one has to assume that recrystallization vanishes, viz. $\dot{\zeta} = 0$.)

When using boundary conditions (1.21)-(1.23) to solve dynamic problems one must remember that while being essentially static, these conditions do not as yet incorporate capillary effects caused by dynamic properties of the surface (see an analogous remark in Sec. 1.3.2). Generally, the quantities like surface mass flow, surface momentum, and surface kinetic energy do not vanish simultaneously with surface mass density (here we deal with a situation similar to that described by Andreev and Kompaneetz [1.50], where the exact equations of motion of a free surface of superfluid helium were found with a normal part present). In our case one can only state that the surface momentum is a linear function of the difference in velocities of the two phases at an interface, $v_i - \dot{u}_i$, where $i = x, y, z$, and that the surface kinetic energy is a quadratic form of the same variables. The exact form of these functions could be determined only by simultaneously finding the exact nonlinearized equations of surface motion (similar to the manner of deriving the hydrodynamic equations of a superfluid liquid [1.51], see also [1.40]). Correct accounting for these quantities will result in the linearized Eqs. (1.22), (1.23) having additional terms that contain second derivatives in time (e.g. like $\rho_s \ddot{\zeta}$, where $\rho_s \sim \rho a_0$), and also in Eq. (1.21) having e.g. terms like $\rho'_s \frac{\partial}{\partial x} (v_x - \dot{u}_x)$, where $\rho'_s \sim \rho_s$, whose sense is the divergence of surface mass flow.

All such terms can be neglected when determining the crystallization wave spectrum in the long wavelength limit. However, when determining high-frequency corrections to this spectrum and capillary corrections to the Rayleigh wave spectrum, as well as when solving the problem of capillary transmission of sound through surface, the terms not included in (1.21)-(1.23), generally speaking, introduce some corrections that are comparable with the principal terms. Therefore, from Eqs. (1.21)-(1.23) one can obtain only a qualitative estimate for transmitted sound amplitude (the corresponding interpretation is recommended for the results from [1.6]; see also [1.52, 53]). It is also clear that some attempts to apply a high-frequency corrections to the crystallization wave spectrum have been inconclusive. They are either based on the use of boundary conditions

(1.21)-(1.23) [1.54], or accounts for the surface kinetic energy yet neglecting the surface special elastic properties [1.53], or true for some semimicroscopic model [1.55]. Moreover, the applicability of macroscopic approximation seems to be doubtful, when the high-frequency corrections to surface wave spectra ($\omega \sim 10^{11}$ Hz, $k \sim 10^6$ or 10^7 cm $^{-1}$) become essential. In fact, the condition $ka_0 \ll 1$, where a_0 is the interatomic spacing is usually sufficient to apply macroscopic equations. It should be remembered, however, that crystallization waves exist on surfaces of arbitrary Miller indices, except a few of the most densely packed surfaces. This means the lengths of translational elementary vectors on the surfaces considered can be infinitely large. Therefore, to be precise, we can neglect the influence of Brillouin zone boundaries only at infinitely large wavelengths.

Finally, it should be noted that the coherence of the crystallization process necessary to satisfy condition (1.23) must be violated at sufficiently high frequencies. Indeed, if, for example, the frequency of an incident sound wave exceeds the value of Δ/\hbar , the behaviour of elementary kinks cannot be considered as a motion of delocalized quasi-particles; under these conditions the surface behaves itself rather like a classical, atomically rough one. This is the reason why crystallization waves cannot exist with frequencies exceeding Δ/\hbar .

Estimate of the ratio of transmitted wave amplitude, u_0 , to the incident wave amplitude, v_0 , can be easily obtained by noting that at low frequencies this ratio is small, i.e. $u_0/v_0 \ll 1$ (given the wave incident as viewed from the crystal, we would have, respectively, $v_0/u_0 \ll 1$). Therefore, in Eq. (1.21) one can neglect the term \dot{u}_z (the same can be done with the term like $\rho'_s \frac{\partial}{\partial x} (v_x - \dot{u}_x) \sim \rho'_s k v$).

Further for helium $\frac{\rho_2}{\rho_1 - \rho_2} \approx 10$, therefore in estimates we shall keep this ratio and denote it as $\frac{\rho}{\Delta\rho}$. Then $\dot{\zeta} \sim \frac{\rho}{\Delta\rho} v_0$; $\delta P \sim \frac{\rho}{\Delta\rho} \alpha k^2 \zeta \sim \sim \left(\frac{\rho}{\Delta\rho}\right)^2 \alpha k^2 \omega^{-1} v_0$, and (taking $\beta \sim \alpha$) $\delta\sigma_{zz} \sim \delta P$. Also, by considering $\dot{u} \sim \frac{1}{\rho c} \delta\sigma_{zz}$, $\omega \sim ck$ (since sound velocities in liquid and solid phases are of the same order of magnitude), we shall finally obtain:

$$\frac{\dot{u}_0}{v_0} \sim \left(\frac{\rho}{\Delta\rho}\right)^2 \frac{\alpha}{\rho c^3} \omega \quad (1.24)$$

It is clear that this estimate is valid both for transversal and longitudinal waves. Undoubtedly, this estimate is meaningful only for such angles of incidence, whenever a transmitted wave can exist, viz. in the absence of total internal reflection. In this connection let us note a peculiar feature of the Rayleigh waves on the surfaces at hand: their velocity is less than that of sound in the liquid since the velocity

of transversal sound waves in a crystal is less than that of sound in the liquid [1.56, 57]. Hence, the Rayleigh wave does not radiate sound into liquid even with capillary effects considered. Rayleigh waves damping at $T = 0$ is governed only by the process of their decay into crystallization waves.

According to (1.24), the probability of phonon transmission through a quantum-rough interface, viz. the amplitude ratio squared, is proportional to ω^2 . Knowing this probability it is possible, according to Khalatnikov [1.58], to calculate the Kapitza resistance on such surface. Here the resistance evidently appears to be proportional to T^{-5} at sufficiently low temperatures, when one can use the estimate (1.24). Whereas on atomically smooth surfaces it should usually be proportional to T^{-3} . The T^{-5} dependence was discovered experimentally [1.7-9, 1.59], and, in a perfect agreement with theory, on atomically smooth surfaces of helium crystals the conventional T^{-3} dependence was actually observed.

1.4. EXPERIMENTAL INVESTIGATION OF COHERENT CRYSTALLIZATION AND CRYSTALLIZATION WAVES

1.4.1. On the Possibility of Direct Observation of Capillary Phenomena in Crystals

The ability of retaining a definite shape is the obvious property with which to clearly distinguish a solid from a liquid. In a solid body under ordinary conditions there are no internal motions changing the mutual positions of its parts, viz. changing its entire shape. Therefore, capillary phenomena being characteristic for liquids are not generally observed in crystals.

In fact, the external shape of a body can be changed not only by internal motions. In melting or crystallization the crystal shape changes because of particle transition from one phase to another. It is essential that under conditions close to equilibrium these processes develop extremely slow, viz. in practice a crystal simply fails to acquire the equilibrium shape during tolerable times.

The physical reason responsible for the unacceptable slow crystal growth under ordinary conditions is the following. In crystallization, as in any other first-order phase transition, states of two phases are separated by a certain energy barrier that provides for the equilibrium of each phase. For a phase transition to proceed at a certain finite velocity it needs to disturb the phase equilibrium in one way or another. As a result, the phase transition is always accompanied by an energy dissipation that finally limits the rate of establishing the phase equilibrium and, in particular, the rate of relaxation towards the equilibrium shape.

The energy dissipation accompanying a phase transition is controlled by a specific crystallization mechanism which in turn is governed by interface structure, as we have seen in Sec. 1.2. Thus, for an atomically rough surface the growth rate, V , is linearly dependent on the chemical potential difference between the two phases, $\delta\mu$. A rough estimate of the minimum value of the shape relaxation for a classical crystal with an atomically rough surface can be made by following simple reasoning. Let the crystal shape be significantly different from equilibrium, then $\delta\mu \sim \frac{\alpha}{R} a_0^3$, where we can take $\alpha \sim T_{\text{melt}} \cdot a_0^{-2}$ (we specifically assume that the second phase is a liquid), where α is the surface energy, a_0 the interatomic separation distance, and R the characteristic crystal dimension. From this, by estimating the growth coefficient from Eq. (1.7), we obtain $\tau \sim \frac{R}{V} \gg$

$$\geq \frac{R^2}{a_0} \sqrt{\frac{m}{T_{\text{melt}}}}$$

for the time needed to establish the equilibrium shape. A more accurate estimate for τ which is valid even when the gravitational field is essential, is not difficult to obtain directly from Eq. (1.18). This equation determines the crystallization wave spectrum and is able to describe not only the oscillatory but also the aperiodic mode of surface motion (at sufficiently small K values).

Apart from the limitation caused by the finiteness of the kinetic coefficient, K , limitations are often no less significant which follow from analysis of the heat- and mass-transfer processes that accompany the phase transition. Provided that the latent heat is not abnormally small and thermal conductivity is not abnormally high, similar reasoning yields $\tau \sim \frac{R^3}{a_0^2} \sqrt{\frac{m}{T_{\text{melt}}}}$.

Finally, in order to get a true equilibrium crystal shape in a real experiment, an extraordinary high homogeneity of both temperature and internal stress distribution is needed in the crystal. Thus, given these assumptions, for the maximum admissible temperature difference δT in crystal we have $\delta T \ll \frac{a_0}{R} T_{\text{melt}}$. These reasonings clearly demonstrate that there are great experimental difficulties in producing a crystal with an equilibrium shape. In connection with this we note that the facet pattern of a classical crystal usually bears no relation to its equilibrium shape and is mainly due to anisotropy in growth kinetics. The shape relaxation time for a classical crystal with an atomically smooth surface is practically infinitely long.

The situation is radically different in quantum crystals, especially in those of helium isotopes. First of all, these crystals can be found in equilibrium with a liquid at temperatures down to absolute zero. Furthermore, at fairly low temperatures the melting heat is very small, while thermal conductivity is quite high. The situation where ${}^4\text{He}$ is in the region of superfluidity is especially favourable

[in ^3He this seems to be at the region near the minimum on the melting curve (0.3 K) and at temperatures of about 1 mK]. Here the major limiting factor in establishing an equilibrium shape is the kinetic growth coefficient, K . However, as we have seen in Sec. 1.3, it is in quantum crystals that as temperature decreases the value of K might grow unbounded. This means that in quantum crystals, especially in ^4He crystals, the conditions can, at least in principle, be satisfied so that an equilibrium crystal shape can quite rapidly be established. Such a situation offers vast possibilities for the investigation of crystal surface phenomena, even those which until now have been considered specific for liquids.

1.4.2. Optical Cryostat

Experimental observation of crystallization waves would be of primary importance in proving the theory presented above. Hence, the observation technique selected has to provide a direct and unambiguous demonstration of this phenomenon existence. From this point of view, an optical technique which enables direct visual observations of surface oscillations and measurements of all the basic characteristics of these oscillations has obvious advantages. In addition, it is essential that even the simplest optical instrument gives the orientation of a growing crystal, the state of its surface, and the availability of defects which are to be controlled.

When investigating helium with optical techniques, a number of difficulties have to be overcome due to helium's extremely low polarizability. Within the optical range, the helium refraction index satisfies the following relationship:

$$n - 1 = 0.20\rho$$

(ρ is density in g/cm^3). This holds true for all three states either condensed or gaseous (the birefringence of hcp-crystals is very small, $\frac{n_e - n_0}{n_0 - 1} = 7 \cdot 10^{-5}$ [1.60]). Since the densities of solid and liquid phases on the melting curve at $T < 1$ K are 0.191 and $0.173 \text{ g}/\text{cm}^3$, respectively, [1.61], the difference between the refraction indices of a crystal and liquid on the melting curve is $\Delta n = 0.0036$. Clearly, to obtain a sufficiently high-contrast picture of a helium crystal under these conditions is a rather difficult task. The crystal surface becomes visible, essentially, only at the angles of incidence close to 90° (within several degrees), viz. in a slipping illumination. Therefore, the cryostat design should provide for a wide range of variability in the illumination of the sample and the ability to observe the sample at different angles. These requirements are best met by an optical cryostat having flat windows and large aperture ratios. This creates,

however, the problem of eliminating the heat supplied to the experimental cell by external thermal radiation.

Note that direct observation is the simplest, yet not the most unique of available optical techniques. For example, in experiments done by J. Landau's group, the growth process of helium crystals was successfully studied using a holographic interferometer [1.10],

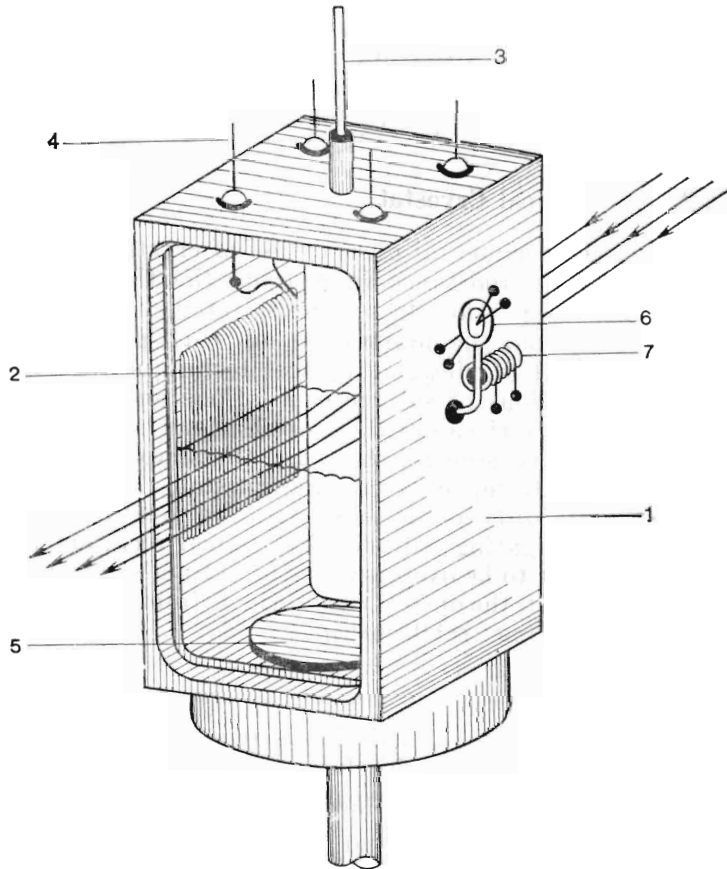


Fig. 1.6. Design of an experimental cell: 1—body, 2—capacitor, 3—filling capillary, 4—electrical lead, 5—heatlead, 6—thermometer, 7—cadmium reference mark.

1.62-63]. Such a technique, in principle, enables the reconstruction of the sample configuration without large aperture windows. However, this technique is incomparably more complicated in its practical application and requires an extremely high manufacturing quality of all optical parts of the setup. In addition, because of the small difference in refraction indices between two phases, interferometric

techniques have rather low resolution. Thus, for example, when using a He-Ne-laser for two rays passing through solid and liquid phases, a path difference of about one interference fringe is accumulated over the ray path $x \sim \frac{\lambda}{\Delta n} \approx 0.18$ mm. This practically nullifies all the advantages of the interferometric techniques.

In our experiments [1.2-3, 1.64] a somewhat modified version of a metallic cryostat was used, which was designed long ago by Shalnikov [1.65] to study the motion of charges inside crystalline helium. The temperatures required (down to 0.3 K) are produced by pumping ${}^3\text{He}$ vapor. The most essential modifications dealt with the windows and experimental cell. The total number of plane-parallel windows in our setup was 5 pairs (observations were carried out in the look-through mode). The main part of the heat which was caused by radiation from the windows was removed by using additional windows on an intermediate nitrogen screen. They were made from a monocrystalline sapphire 5 mm thick and reduced the heat supplied to the experimental cell to the value of $5 \cdot 10^{-5}$ W. To illuminate the experimental volume, a luminescent lamp was used that provided, at an appropriate aperture ratio, a light intense enough to photograph and film without a noticeable increase in the heat supply.

${}^4\text{He}$ crystals were grown in a metallic chamber with a rectangular cross-section, 12×15 mm² (Fig. 1.6), made from ferrochromium. The whole interior of the chamber can be observed through the two opposing walls made from chemical glass, $12 \times 28 \times 3$ mm³. Inside the chamber, on a side wall a capacitor was mounted to excite crystal surface oscillations via an ac electric field (for more detail of the capacitor design see Sec. 1.4.4). A capillary tube and four electrical leads were soldered into the top of the chamber, and a copper heatlead to the ${}^3\text{He}$ bath at the bottom. To reduce the heat supply to the chamber, a part of the capillary tube was put into thermal contact with the ${}^3\text{He}$ bath. A carbon thermometer calibrated against ${}^3\text{He}$ vapor pressure was mounted onto the heatlead which was soldered into the side chamber wall. Calibration was controlled by means of a cadmium reference ($T_0 = 0.515$ K) mounted on the same heatlead.

1.4.3. Features of the Low Temperature Growth Kinetics of ${}^4\text{He}$ Crystals

In our experiments, the crystals were grown from ${}^4\text{He}$ which was initially purified by thermomechanical (fountain) effect, and has a ${}^3\text{He}$ concentration no higher than 10^{-8} . The ${}^4\text{He}$ crystals were grown at a constant temperature, (from 0.4 to 1.3 K), and with a regulated helium flow into the chamber to control the crystallization rate. In fact, such a technique is clearly called for by the

very shape of helium phase diagram at low temperatures (the value of $\frac{dP}{dT}$ along the melting curve and, with it, the crystallization heat, are practically equal to zero). The chamber was filled with liquid helium pressurized at about 25 atm by means of an external compressor, then the latter was detached. Growth and melting of crystals were produced by changing the temperature of an external buffer vessel (300 cm³ in volume) that could be attached and detached as required by the experimental schedule. This method enables the growth rate to be varied over wide range, up to several mm/s. In fact, the crystals used to measure spectrum and crystallization wave damping were grown at much lower rates, at about 0.1 mm/min. And the estimated temperature gradient in a sample did not exceed 10⁻⁴ K/cm. If necessary (e.g. when some defect was detected in the course of growing) the crystal could be easily melted and then its growth continued. Once a crystal had been grown, the buffer vessel was detached and the position of interface could remain unchanged for many hours within about 0.1 mm.

In our experiments, visual control was the basic method to check the quality of growing crystals. Direct observation of a ⁴He crystal during its growing process at low temperatures not only allows its orientation to be fixed, but also enables an effective check to be made on the degree of its perfection since a crystal surface appears to be very sensitive to defects both during growth and, especially, in equilibrium. Note that the gravitational field substantially influences the growth dynamics and crystal shape through the entire temperature range studied. This fact alone shows that in our experiment crystallization processes occurred under the conditions very close to equilibrium.

At the temperatures below 1.2 K, as a rule, a crystal grows from one nucleus, and is always to some extent faceted. The faceting is more strongly pronounced at larger growth rates and at lower temperatures. The observed faceting always corresponded to a hexagonal prism represented by various number of facets which depended on the point of nucleus creation, crystal dimensions, and its orientation relative to the chamber walls (see Fig. 1.7). Crystal symmetry allows identifying the prism bases with the (0001) basal plane, and the side facets, being perpendicular to the latter, with the planes of either {1120} or {1010} type.

Figure 1.7 clearly shows all the specific features of the low temperature growth of ⁴He crystals: distinct faceting at relatively high growth rates (about 0.1 mm/s, a, b frames); appearance of rounding-off in the upper part of the surface when the growth rate is reduced (c), along with a transition to a specific meniscus (d). When melting, crystals generally have a droplike shape. The dependence of crystal shape on growth rate is naturally explained by anisotropy in the

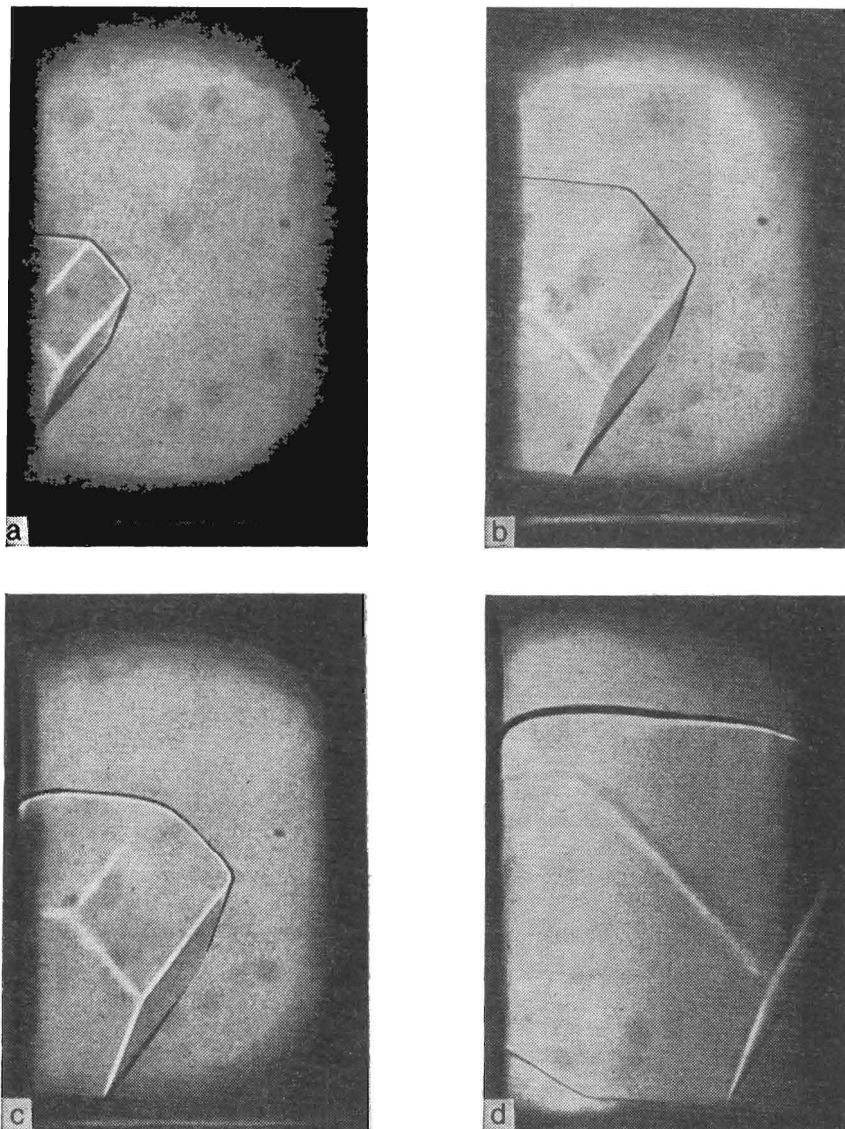


Fig. 1.7. Different growth stages of a crystal.

kinetic growth coefficient which takes minimum values for the directions controlled by facets of growth prism and having in these directions a singularity of the cusp type [1.66]. Therefore, the lower the tem-

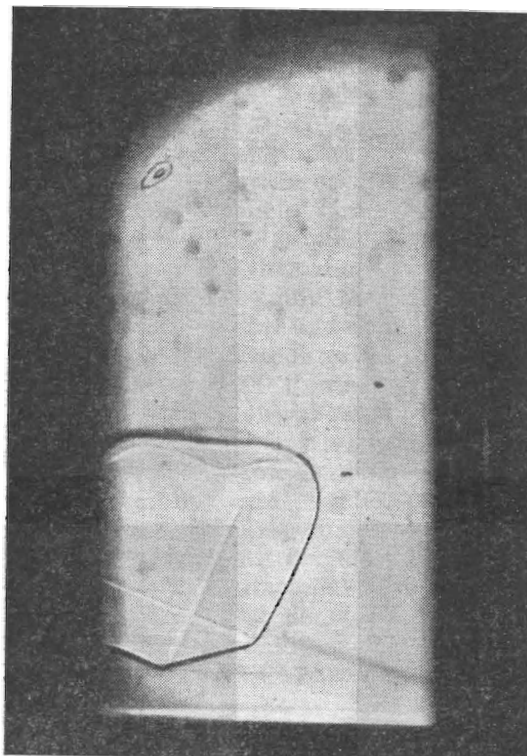


Fig. 1.8. The 2 mm helium crystal suspended from one of the chamber side walls at $T \approx 0.5$ K.

perature is the stronger the anisotropy becomes. These features of growth kinetics were also observed by J. Landau and co-workers [1.63].

Particularly low growth rates are specific for the (0001) facet. At the lowest temperatures (in the interval of 0.4-0.6 K) the typical growth rates in the [0001] direction are so low that, at a suitable orientation, a crystal can be suspended for several hours from one of the chamber's side walls while "resting" on the (0001) facet (Fig. 1.8). Under these conditions, the crystal growth along the [0001] direction proceeds, perhaps, only as a result of the creation of atomic layer nuclei at the points of contact between the (0001)

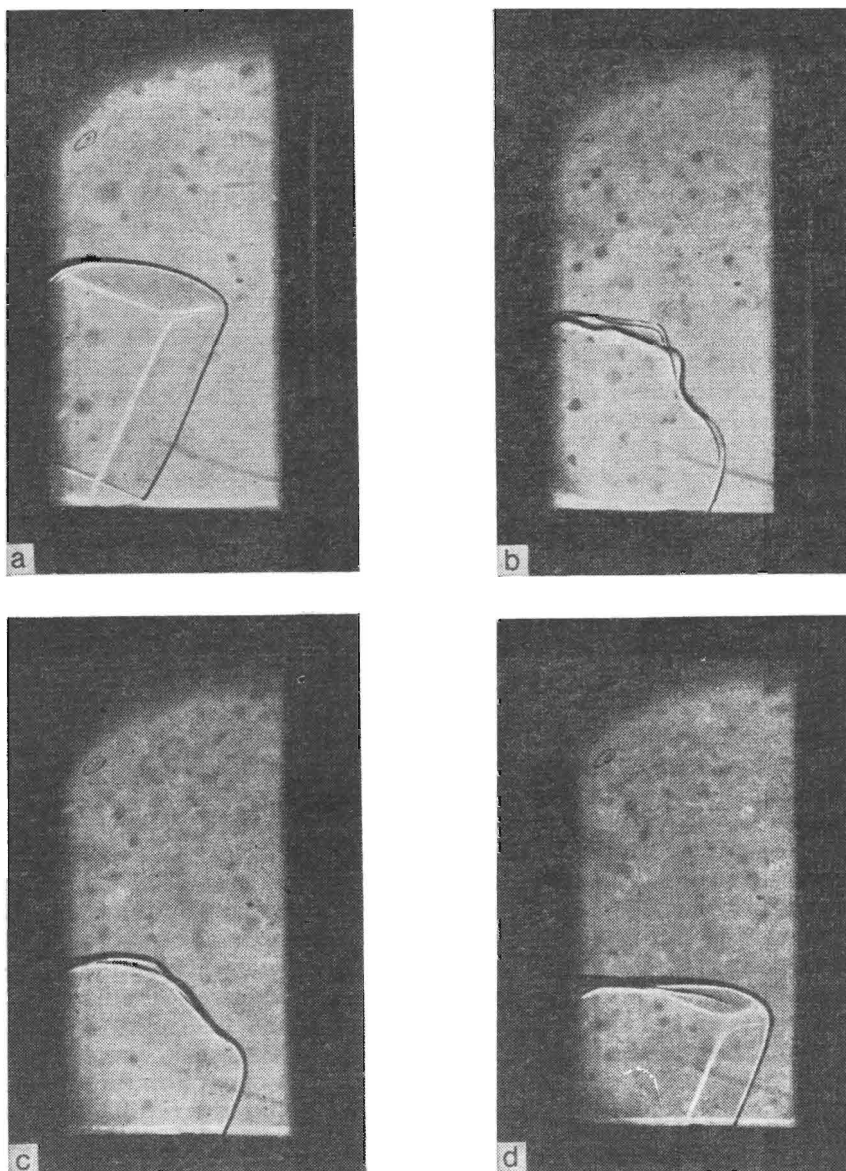


Fig. 1.9. Motion picture frames of the "release" of a crystal. The shooting rate is 24 frames per second.

facet and the chamber walls. In this case a very fast avalanche-like recrystallization often occurs (during less than 0.1 s). As a result the crystal that was, for example, on one of the side walls, "drops" down onto the chamber bottom, still conserving its primary orientation (Fig. 1.9). As a rule, this process is accompanied by the creation of one or more surface defects (most often arising in the (0001) plane). They are, perhaps, the stacking faults that have been thoroughly studied in conventional, closely packed structures (see, e.g. [1.67]).

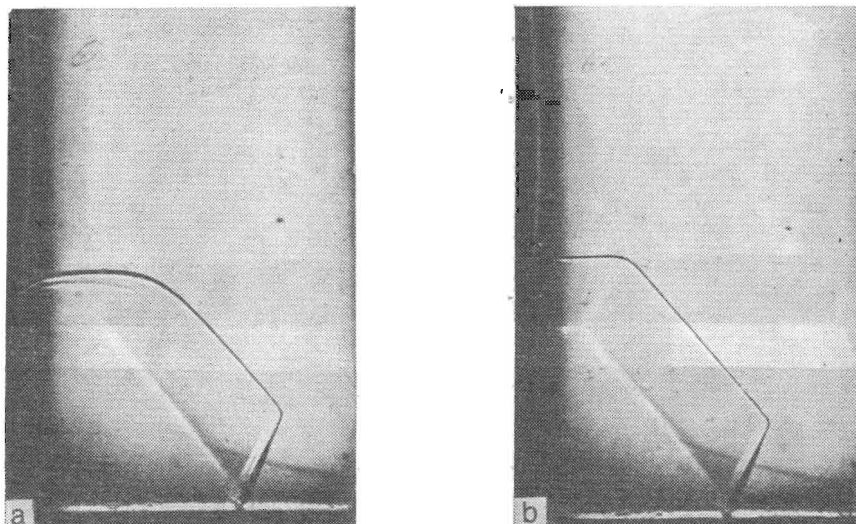


Fig. 1.10. The crystal with a stacking fault: a—under quasi-equilibrium conditions, b—during growth.

In equilibrium these defects show up as the "canyons" which are created where the defect plane outcrops (Fig. 1.10a). Clearly the excess energy of a defect which is proportional to the latter's area is responsible for the creation of the canyons. The observed depth of the canyons (about 0.5 mm) enables one to state that this energy is of the same order of magnitude as the crystal-liquid interface energy, viz. about 0.1 or 0.2 erg/cm². Resuming the growth of crystals with those defects cause the "canyons" to be healed so that the resulting facet pattern does not differ in any way from that of a defectless crystal (Fig. 1.10b). Let us stress that block orientations on both sides of the stacking faults are the same. Therefore, it would be very difficult to detect such defects by any other techniques (for example, the coefficient of sound reflection from a stacking fault, according to [1.28], is about $(a_0/\lambda)^2$, where a_0 is the interatomic distance, and λ the sound

wavelength; evidently, the same is valid when applied to light reflection).

Growing a large crystal without visible defects depends not only on temperature (the best results were obtained in the interval of 0.8-0.9 K), but also on nucleus orientation. As a rule, multiple recycling of the growing process during one experimental run produces nuclei having the same or a very similar orientation. In the overwhelming majority of experiments, the "singular" facets had a sizable (not less than 20°) inclination to the horizontal plane. In these cases, in order to avoid the "drops", one had to search thoroughly for the best growing conditions for each run. It should be noted that heating a sample (which has been grown, say, at 0.8 K) up to a temperature of 1.1 K or higher, as a rule, leads to an irreversible change in its surface shape. This change is possibly caused by a plastic crystal deformation which in turn is due to a variation in equilibrium pressure of about 0.1 atm, the latter exceeding the experimental value of the yield point of solid helium [1.68-69]. For this reason, crystals intended for measuring the spectrum and damping of crystallization waves, were grown at the lowest possible temperatures, where these "drops" could be completely avoided (usually, about 0.8 K). The measurements were carried out at the temperatures lower than 0.6 K, so that the pressure over a crystal during the measurement was differed from the pressure during growth by less than $5 \cdot 10^{-3}$ atm.

Concluding this Section, let us note that the technique developed is a version of that used by Shalnikov [1.65, 1.70] for helium crystal growth at constant pressure. Since the Shalnikov work was published, essentially all experimenters who endeavour to produce perfect helium crystals use a modified version of this technique [1.57, 1.60, 1.71-75]. As X-ray experiments [1.73] and measurements of heat conductivity [1.72] have shown, this technique succeeds in growing quite perfect helium crystals, as long as the growth rate is not too high (not higher than 0.5 mm/min). In our experiments, the growth rate was about 0.1 mm/min. Constant temperature and, especially, constant pressure, in conditions of our experiment (superfluid liquid helium, slopeless melting curve) were maintained during the growth process with an accuracy significantly higher than in experiments by Mezhov-Deglin [1.72], and Golub and Svatko [1.75] who detected extremely high values of heat conductivity of helium crystals grown by means of Shalnikov's technique. Direct visual observations support this conclusion concerning the high quality of these crystals.

1.4.4. Techniques to Excite Crystallization Waves

It is possible to suggest several techniques to excite crystallization waves. The most apparent one is mechanical, with a liquid set into motion by means of some vibrator. In this way, crystalli-

zation waves with fairly large amplitudes, over the most observable frequency range from several Hz to several kHz, can be excited. Another conceivable technique excites mechanical vibrations of the whole chamber. It is this technique that was used by us to excite high amplitude crystallization waves (see the next Section).

The mechanical excitation techniques suffer an essential disadvantage however, when measuring the spectrum and damping of crystallization waves. The problem was that the cryostat we used, just like a majority of cryostats producing temperatures below 1 K, possessed a very large number of natural mechanical frequencies falling precisely within the range we are interested in, and at these frequencies it has a high Q factor. As with any mechanical excitation technique, the presence of these natural frequencies leads usually to different beats and "ringing" that greatly complicate the analysis of surface oscillations. Therefore, we choose a technique essentially free of this disadvantage, namely, surface oscillation excitation by an ac electric field.

This technique is based on the well-known phenomenon of the "pulling-in" of medium having high dielectric constant into an electric field. In many ways it is analogous to the technique used by Boldarev and Peshkov [1.76] and Leiderer [1.77] to study the surface tension of ^3He - ^4He liquid solutions. As mentioned in the previous Section (see Fig. 1.6), a special capacitor is mounted on one of the side walls of the experimental cell. The capacitor is made of two copper wires each of 30 μm in diameter with nylon insulation (the outer diameter of about 40 μm) and wound bifilarly (150 turns) over the whole surface of the fiberglass plate of $12.5 \times 14.5 \times 1.5 \text{ mm}^3$ so that the average gap between adjacent wires was about 5 μm (practically, from 0 to 10 μm). The plate width (14.5 mm) was chosen so that the clearance between the capacitor and the chamber glass walls was minimal. Preliminary tests of the capacitor in He II demonstrated it was reliable up to voltages of 3.5 kV which correspond to maximum electric field strength up to $3 \cdot 10^6 \text{ V/cm}$.

In the absence of an electric field, an equilibrium surface is shaped like a convex meniscus (Fig. 1.11). Switching on the electric field induces a change in the effective wetting angle at the capacitor, and an accompanying rise of the meniscus edge that can attain 1 or 2 mm (see Fig. 1.12).

At low voltages, the displacement of meniscus edge is approximately proportional to the voltage squared, yet a fast saturation was observed at voltages higher than 500 or 600 V. This phenomenon is accounted for by the inhomogeneity of the capacitor surface which is due to unevenness in the isolation thickness and the gap between adjacent wires. At rather high voltages across the capacitor, small-sized crystallites, which are in no way related to the main crystal, are formed over the whole capacitor surface at sites of maximum

field strength. The corresponding "critical" voltage E_{cr} can be derived from the condition when the decrease in capacitor energy due to forming such crystallites will be of the order of its surface energy:

$$\frac{\epsilon_1 - \epsilon_2}{8\pi} E_{\text{cr}}^2 v \approx \alpha S \quad (1.25)$$

where v is the crystallite volume and S its surface area. Taking into account that the crystallite size is about $10 \mu\text{m}$, we shall determine the required voltage from 500 to 1000 V. This deduction is supported by direct observations. When applying voltage higher than 700 or

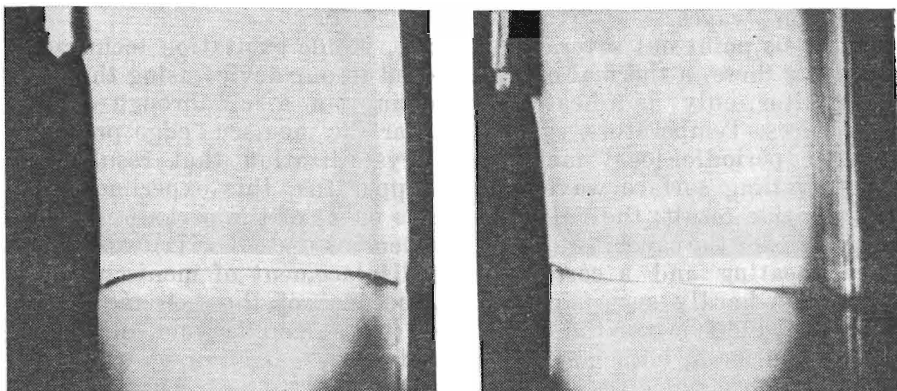


Fig. 1.11. Equilibrium meniscus (a crystal occupies the space below meniscus).

Fig. 1.12. A meniscus inside the capacitor electric field (the capacitor is located to the left).

800 V, the reflectance of the capacitor surface in slipping illumination is abruptly lowered. This demonstrates that a large number of scattering centers appear. These crystallites, evidently, having random orientations in relation to the main crystal reduce the efficiency of the electric field acting on the main crystal by inhibiting its contact with the regions of maximum electric field strength.

Applying an ac voltage of appropriate frequency to the capacitor can excite a plane crystallization wave with a wave front parallel to the capacitor surface. In measurements of the spectrum and damping of crystallization waves, the voltage across capacitor is composed of two parts: the dc one, U_1 , and the ac one, U_2 . The excitation efficiency of the principal mode is maximized when U_1 -voltage is over the range of (400-800) V. Dependence of the excitation efficiency on U_2 is approximately linear up to 200 V, except in the region of the lowest voltage (from 20 to 30 V) where very unstable wave am-

plitude is observed. The dc voltage was chosen so that the average wetting angle is close to $\frac{\pi}{2}$, so as to reduce measurement errors due to the curvature of crystal surface, and the voltage generally came within the range of (500-700)V. The ac voltage amplitude was typically about 100 V which provided a rather efficient excitation without too high a level of nonlinear distortions.

This technique becomes inefficient at high frequencies, when the wavelength is equal to (or less than) the diameter of the capacitor's wire winding. In our experiments, measurements were performed at wavelengths from 7 mm to 0.3 mm so as to provide an accurate test of the theoretical formulas for the spectrum and damping of crystallization waves.

Let us point out several additional, viable excitation techniques. Among these, a thermal one was tested in our device using the same capacitor, only as a heater by passing an a. c. through one of its wires. Temperature variations near the meniscus edge provoked either periodic local melting or crystallization that resulted in a travelling surface wave. In our apparatus, this experiment had a negative result: the only observable effect of the periodic heat release inside the capacitor (at the frequencies up to 1 kHz) was a general heating and a corresponding displacement of meniscus. This result is hardly surprising mainly because of the extremely high heat conductivity of the two phases (in fact, under our conditions, heat transfer in both phases occurs via propagation of second sound waves whose velocity is much higher than that of crystallization waves). Another possible mechanism of exciting crystallization waves is to some extent analogous to the generation of sea waves by wind. Namely, it is possible to demonstrate that, when a liquid flows along a crystal surface at a sufficiently high velocity, v_s (here we deal with the superfluid flow component), the surface becomes unstable for the initiation of crystallization waves. The corresponding minimum critical velocity is determined by the expression

$$v_{s0} = \left[\frac{4\tilde{\alpha}(\rho_1 - \rho_2)g}{\rho_2^2} \right]^{1/4} \quad (1.26)$$

Here $\tilde{\alpha}$ changes from 0.1 to 0.2 erg/cm², and v_{s0} from 4 to 5 cm/s; and the crystallization waves with $k = \sqrt{\frac{\rho_1 - \rho_2}{\tilde{\alpha}}} g$ start to be excited. If, in experimental conditions, only waves having k values such that $k > k_m$ can be excited, then the corresponding critical velocity is $\sqrt{\frac{\tilde{\alpha}}{\rho_2}} k_m$. Experimental observations of these critical velocities are, perhaps, worthy of independent study. However, to do this requires an apparatus substantially different from ours.

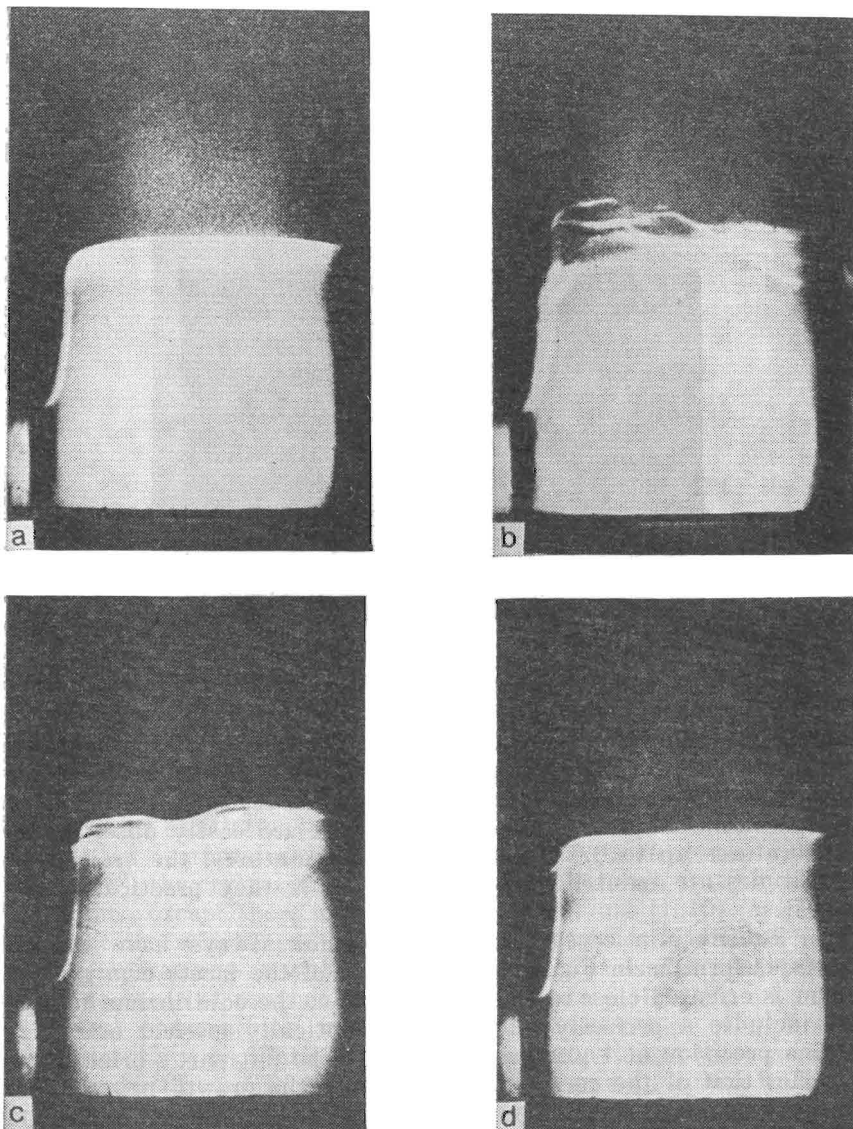


Fig. 1.13. Motion picture frames of excitation and damping of crystallization waves at $T \approx 0.5$ K.

1.4.5. Visual Observations of Crystallization Waves

Crystallization waves excited by an electric field have amplitudes generally do not exceed 0.1 mm, thus hampering visual observation. At the same time, even an insignificant vibration of the apparatus at the frequencies of about 10 Hz and higher is enough to excite visible surface oscillations. Gently tapping the outer wall of the cryostat wall causes oscillation amplitudes of several millimeters. Figure 1.13 exhibits a set of movie frames of exciting and



Fig. 1.14. The meniscus shape for (0001) horizontal plane crystal.

damping these oscillations. A resting liquid-solid interface is shown in the first frame. The subsequent frames demonstrate the interface behaviour after tapping the outer wall of the cryostat (the frames are spaced at about 1 s). Such oscillations are easily observed at temperatures up to 0.6 K. At higher temperatures, the oscillation amplitudes are reduced rapidly and at 0.8 K they practically disappear.

An equilibrium crystal surface does not always have convex meniscus form as in Fig. 1.11. When one of the facets of a growth prism is oriented close to a horizontal plane, the equilibrium meniscus includes a perfectly flat part (an optically perfect one, viz. with a precision of 1 μm), see Fig. 1.14. The flat part's orientation matches that of the corresponding facet of the growth prism. This is easily established in the process of the crystal's growth. The shape and size of the flat part are extremely sensitive to even insignificant inclinations to the horizontal plane. At angles of inclination of about 15-20°, this part is viewed as a tiny spot (1 mm in size) near one of the meniscus edges that can be easily mistaken as a surface defect. The flat part is reduced in size as temperature rises, and completely

disappears in the temperature range of 1.17-1.20 K for basal plane and about 0.9 K for lateral prism facets (similar data are also gained in [1.10, 1.13]). In the presence of a flat portion, surface oscillations persist to be excited on the rounded-off part of meniscus, while the flat portion remains perfectly at rest and only its boundary experiences the oscillations caused by those of the rounded-off parts. If oscillation amplitudes are very high, terraces can be found speedily moving across the flat part while their heights remain

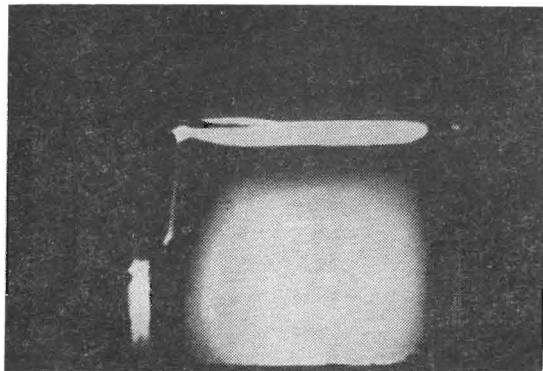


Fig. 1.15. A terrace on the basal plane.

unchanged (sometimes analogous terraces are observed during fast crystal growth, Fig. 1.15). Let us note that crystallization waves are observed, not only when the crystal fills the whole bottom part of the container, but also when a crystal is "suspended" from one of the lateral walls (Fig. 1.8). In this case, the rounded-off parts, and only these, show oscillations distinctly. All data clearly demonstrate that at the low temperatures (below 0.9 K and, at least, down to 0.4 K, see [1.13]) the crystal surface is in a quantum-rough state in all orientations, except those of two special, $\{0001\}$ and $\{10\bar{1}0\}$ (or $\{11\bar{2}0\}$) orientations which turn into a classical, atomically smooth state. The temperatures at which equilibrium flat parts disappear correspond to those of roughening transitions.

Visual observations enable successful detection of not only crystal surface oscillations, but also the behavior at the meniscus boundaries (the contact lines between meniscus and glass walls are especially clearly seen). If the surface oscillation amplitude is not too high ($\lesssim 0.5$ mm), the meniscus boundary remains practically motionless; at higher amplitudes, a separation occurs, viz. meniscus edges start to move together with the whole surface.

Both standing and travelling waves could be used to measure the spectrum of crystallization waves. The operating conditions of our

apparatus were not sufficiently favorable to excite standing waves. Firstly, in the temperature range studied, the crystallization waves are characterized by a rather sizable damping (see later on, in Sec. 1.4.6). This is why only the lowest frequency (from 10 to 100 Hz) resonances could have a somewhat significant Q-value. Also, a crystal surface limited by the chamber walls forms a "rectangular resonator", which is far from being ideal primarily because of an appreciable meniscus curvature near its edges. To find the natural frequen-

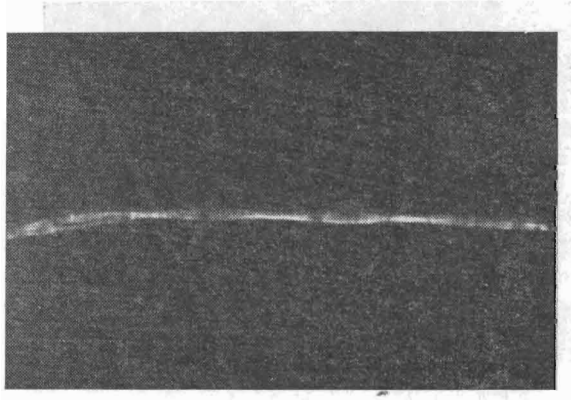


Fig. 1.16. Standing crystallization wave.

cies of this resonator is a very difficult task; the situation is still more aggravated by the fact that the conditions defining amplitude and phase of a reflected wave are, strictly speaking, unknown. Finally, the occurrence of natural mechanic resonances in the apparatus at the same frequency range as for the waves under study (dozens of Hz) which are characterized by Q-values much larger than those of the surface oscillations, results in the observed resonances (see Fig. 1.16) being complex electromechanical resonances of the whole apparatus. Therefore, to measure spectrum and damping of crystallization waves one needs higher frequencies and, respectively, more sensitive optical techniques.

1.4.6. Spectrum and Damping of Crystallization Waves

In our first experiments [1.2], the measurements of crystallization wavelength were performed by He-Ne-laser light diffracting from these waves. Such a technique had been used to study the surface tension of ${}^3\text{He}-{}^4\text{He}$ liquid solutions by Leiderer [1.77]. Thus measured at $T = 0.43$ K the spectrum for one of the crystals is presented in Fig. 1.17. In practice, this technique appears to be

inconvenient. Random surface oscillations caused by vibrations in the apparatus result in a sizable broadening of the diffraction picture; besides this, it does not allow direct measurement of the damping.

Another technique [1.3] was used, in which a narrow (having the width substantially less than the wavelength to be measured) beam

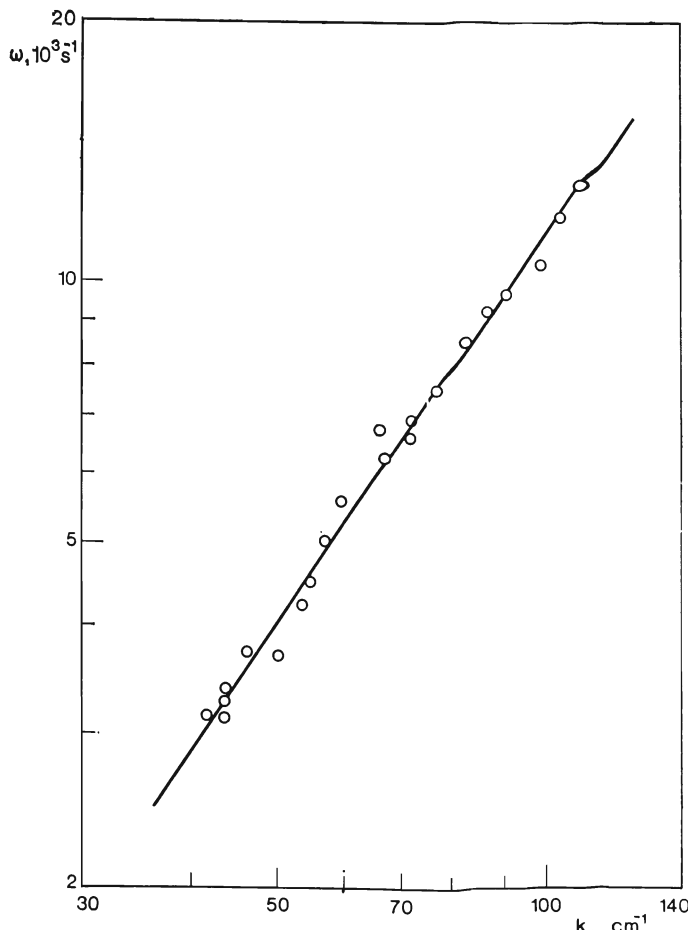


Fig. 1.17. The crystallization wave spectrum measured by diffraction technique.

of He-Ne-laser slowly scanned the oscillating surface and remained almost parallel to the wave front. This scanning was performed by rotating the optical bench, which contained all optical elements of

the setup, about the vertical axis located 1.5 m from the cryostat. The vertical beam size was about 2 mm, the wave amplitude, according to estimates, changed from 0.01 to 0.05 mm, and random oscillation amplitudes were the same or even somewhat larger. The lower part of the beam is refracted by a slightly curved surface being significantly deflected downwards, and the remaining light passes over the surface hitting a photodiode. Thus, the light intensity at

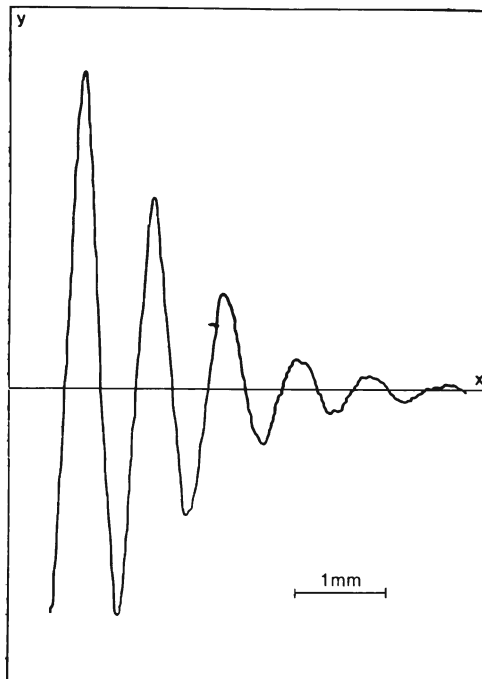


Fig. 1.18. An example of the detector signal record.

the photodiode contains an ac component proportional to the vertical displacement at a given point. The photodiode output signal was amplified by a band-pass unit tuned to the excitation frequency, and after passing through a lock-in detector (at a constant phaseshift between exciting and reference signals) was fed to the y -input of an xy -recorder. Simultaneously, a signal was fed across the x -input of the recorder from the multiturn potentiometer which was connected by a micrometer screw used to drive the scanning. Fig. 1.18 shows one of the records produced in this way.

The distance along the x -axis between signal zeros defines a crystallization wavelength, while the amplitude ratio for adjacent maxima

controls its damping. The adoption of lock-in detector at frequencies over 100 Hz enabled a substantial reduction in the noise level caused by random vibrations. However, between 80-120 Hz as well as below 60 Hz, the noise level is so high that the wavelength cannot be adequately measured. Note that measurements at such low frequencies, with wavelengths of several millimeters, are generally unreliable due to the need for introducing corrections for the chamber walls. As it has been stated, we have no adequate data accurately to solve this problem. Therefore, the basic measurements were performed at frequencies over 200 Hz, where these corrections can be neglected. Here the detected signal has the form $\exp(-\alpha x) \cos k_0 x$ (where k_0 and α are real and imaginary parts of the wave vector, respectively). This holds true if the reflected wave can be neglected and the process of recording starts at some distance from the point of wave excitation ($\lambda/2$ or larger). These conditions were fulfilled in all measurements. Figure 1.19 shows the results of measuring the spectra for one of our samples at two temperatures, 0.360 and 0.505 K. The dashed straight line follows the dependence $\omega \sim k^{3/2}$, while the solid line represents the theoretical dependence $\omega(k)$ according to Eq. (1.18) with the gravitational term included (the damping correction may be neglected), and $\tilde{\alpha} = 0.21 \text{ erg/cm}^2$. Thus, within the experimental error of (5%), $\tilde{\alpha}$ remains unchanged when temperature rises from 0.36 K to 0.50 K. The data for other samples are essentially the same, they differ from the latter only by a common insignificant shift of the whole curve due to a change in the value of $\tilde{\alpha}$. In addition to the previous one, the following $\tilde{\alpha}$ values were recorded: 0.18, 0.155, 0.15, and 0.097 erg/cm^2 (the last value corresponds to the dot-dashed straight line in Fig. 1.19). The spectrum given in Fig. 1.17 fits $\alpha = 0.23 \pm 0.04 \text{ erg/cm}^2$. These data suggest a sizable anisotropy of the surface energy, yet they do not, of course, give a complete idea as to the magnitude and character of this anisotropy, since all the surfaces investigated by this technique had a random orientation and formed an angle not less than 20° with any of the special surfaces.

Crystallization wave spectrum measurements using a single fitting parameter, $\tilde{\alpha}$, because of the excellent agreement between experimental and theoretical spectra, can be seen as one of the methods to measure surface energy. In practice, this method provides, perhaps, a much better accuracy as compared to e.g. the method based on direct investigation of equilibrium crystal shape (see [1.63-64, 1.78]). In our case, accuracy is mainly governed by that of wavelength measurements.

The main advantage of our technique is that it falls into the "zeroth" category, viz. it is not related to direct amplitude measurements of any signal. Therefore, its "response" does not involve any

characteristics of the measuring scheme like amplification factor, optical channel transmission, etc. The accuracy of measuring a displacement, which is the space between signal zeros, is effected by noise level. This was held to within 1%, except for the limiting

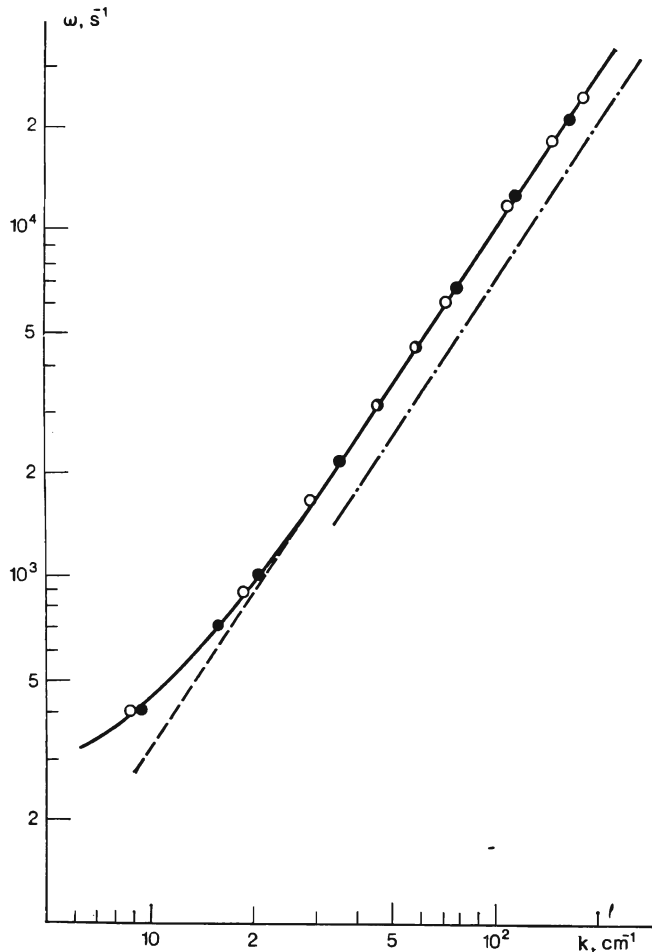


Fig. 1.19. The crystallization wave spectrum for a sample at two temperatures: $\bigcirc T = 0.360$ K, $\bullet T = 0.505$ K.

points of the frequency range investigated where the signal-to-noise ratio was substantially reduced. This ratio could be improved in two ways: either by increasing the time constant of the detector or by increasing the exciting signal amplitude. The first one is accompanied

by an exorbitant increase in measurement time (when the chosen time constant of our detector was 1 s, one experimental record required not less than 10 min.). The second way is unacceptable, also, since at high exciting voltages, as has been mentioned, crystallization occurs over all of the capacitor surface that is placed above the main meniscus. In this case the total liquid volume inside the container changes periodically, and the resulting surface oscillation consists of the wave under investigation, being superposed over a quasi-homogeneous oscillation of the same frequency. As a result, the signal record "drifts out" of the zero level, spacings between zeros cease to be the same and an accurate wavelength measurement becomes impossible. This effect can be substantially reduced by placing the meniscus as close to the upper edge of a capacitor as possible, however, it cannot be eliminated completely. Besides, at high exciting amplitudes, the damping measurement results become unrepeatable (in this process the spectrum does not change in an appreciable manner). This is, perhaps, related to the irreversible changes in a crystal caused by prolonged exposure to an ac electric field of high amplitude. Currently, the physical nature of these changes is open to speculation; it is felt that they are caused by the creation of some crystal defects.

Since measurements of damping, viz. of the α values, are related to amplitude measurements, an additional difficulty arises which is caused by imperfections in our optics. These are mainly due to glass contamination. The most unpleasant consequences of these contaminations are the depositing of particles of a fine-grained suspension of solidified gases on the windows of the helium Dewar vessel and vacuum jacket. These solidified gases are mainly air that is permanently trapped in cryogenic liquid helium. As a result, the intensity of the transmitted light becomes an extremely complicated function of the x -coordinate, and the amplitude distribution of the registered maxima no longer follows an exponential law. Since the amplitude of the detected oscillations is very small (much less than the total height of the lightbeam), calibrating the records against the total intensity of transmitted light, although eliminating large scale inhomogeneities, does not fully compensate for all inhomogeneities. When measuring the temperature dependence of damping, positions of maxima are not changed with temperature, viz. within the experimental error limits the spectrum is not temperature dependent and this alleviates the problem. But when measuring damping its values can contain small ($\leq 0.5 \text{ cm}^{-1}$) uncontrollable additional terms that stem from the fact that it is impossible to exactly calibrate the transmission. This is why temperature variations of damping can be measured more accurately than damping itself (e.g. at lowest temperatures). When measuring the frequency dependence of damping, the separations between maxima change with frequency. To improve

the experimental accuracy, the measurements at each fixed frequency were repeated several times for different values of the phaseshift between exciting and reference signals (in this case all maxima are shifted, the separation distance being fixed).

The magnitude of damping, as follows from Eq. (1.18), is determined by the relationship:

$$\kappa = \frac{1}{3} \rho_1 \rho_2^{1/3} (\rho_1 - \rho_2)^{-2/3} \tilde{\alpha}^{-2/3} (mK)^{-1} \omega^{1/3} \quad (1.27)$$

(in the frequency range investigated gravitational correction can be neglected). Figure 1.20 presents the results of the frequency depen-

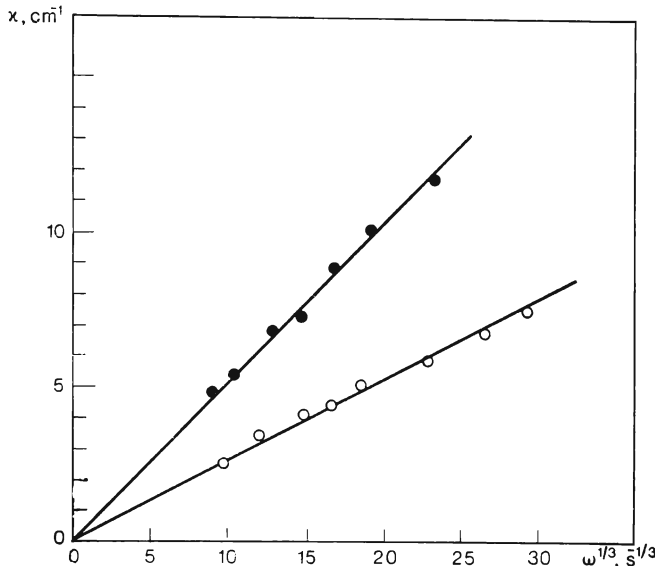


Fig. 1.20. The frequency dependence of crystallization wave damping at two temperatures: \circ $T = 0.360$ K, \bullet $T = 0.505$ K.

dence of κ at two different temperatures for a sample whose spectrum is shown in Fig. 1.19. The dependence $\kappa \sim \omega^{1/3}$ is seen to hold within the experimental error, viz. the damping is caused by the finiteness of the growth coefficient (the contributions from other possible damping mechanisms for this sample probably do not exceed 1 cm^{-1}).

According to Eq. (1.14), at low temperatures, when energy dissipation due to the motion of an interface is determined by the latter's collisions with phonons, the growth coefficient is dependent on temperature according to the law $K \propto T^{-4}$. At higher temperatures, when the number of rotons in liquid becomes sufficiently large, it mainly obeys the law $K \propto \exp(\Delta_r/T)$, where Δ_r is the roton gap

width. Figure 1.21 demonstrates the temperature dependence of the quantity $\frac{1}{mK}$ calculated from the ζ values measured for three different samples.

It can be stated that at low temperatures damping diminishes more slowly than if it were a purely phonon mechanism. When comparing experimental data with theory, it should be borne in mind that in a real experiment there are causes that lead to residual damping, viz. to finite damping at arbitrarily low temperature. This concerns different processes for scattering of crystallization waves from both crystal defects and surface oscillations caused by the apparatus vibrations, effects of radiation source geometry and meniscus curvature, and others. Such residual damping, evidently, can be greatly changed from one sample to another and, depending on the dominating scattering mechanism, is varied with frequency according to various laws. From this point of view one can easily explain the systematic discrepancy between the data sets pertaining to two different frequencies for the sample N°3 in Fig. 1.21 (in fact, the residual damping amounts to $\zeta_0 \simeq 2 \text{ cm}^{-1}$ for both frequencies). It seems likely that crystal defects exert the most pronounced influence on the results of damping measurements. This assumption is favored by the fact that damping is substantially intensified when the crystal is first heated up to 0.8-1.0 K, and then recooled again. An analogous result is observed after a crystal "shake-up" by an ac electric field of the high amplitude, of about 1 kV.

These reasons enable the data in Fig. 1.21 to be interpreted as follows. We shall assume that the measured damping is composed of three independent terms, viz. residual damping as well as phonon and roton ones:

$$\frac{1}{mK} = A(\omega) + BT^4 + Ce^{-\frac{\Delta_r}{T}} \quad (1.28)$$

Hence, according to the said above, the coefficient A can vary from one sample to another and, besides this, it can depend on frequency. The phonon damping terms, B , caused by a strong anisotropy of sound velocity in the crystalline ${}^4\text{He}$, can be notably changed by the sample's orientation. The roton contribution, C , which mainly depends on the characteristics of the liquid's rotons, probably has approximately equal values for all the samples.

The curves are drawn in Fig. 1.21 according to this interpretation, and demonstrate the contributions of the first two terms to Eq. (1.28). The roton contribution found by this method is depicted in Fig. 1.22. All data are seen to fit one dependence having the form, $\exp(-\Delta_r/T)$, which is essentially the most serious argument in favor of this interpretation. The obtained value $\Delta_r = 7.8 \text{ K}$ lies somewhat above the neutronographic and calorimetric data,

which range from 7.1 to 7.3 K [1.79]. This difference, however, can only be an apparent one, since the coefficient C may depend on temperature according to a power law, as do the majority of quantities which the roton spectrum defines (heat capacity, normal density, etc.)

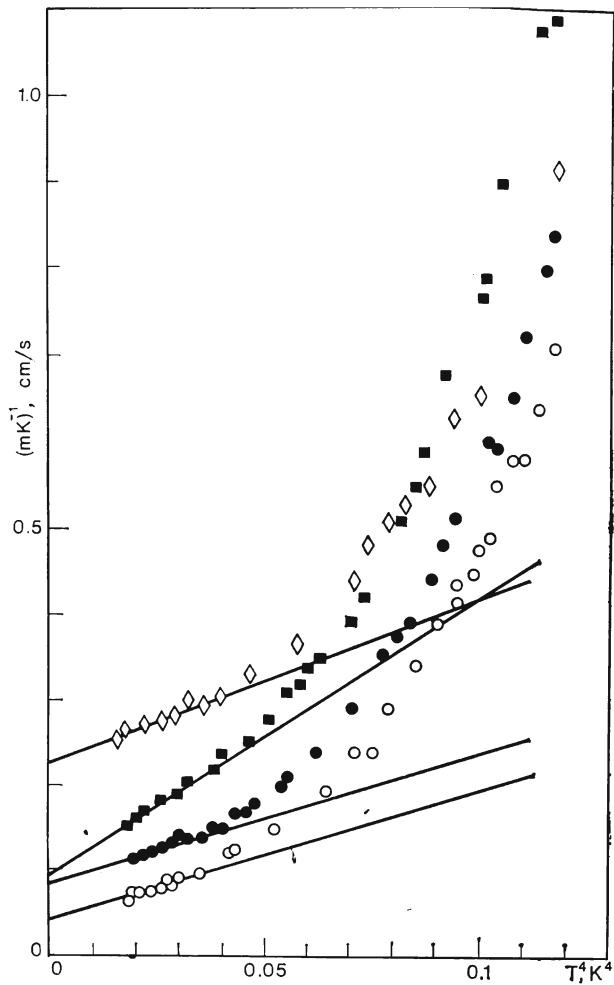


Fig. 1.21. The temperature dependence of crystallization wave damping for three samples: sample N°3, \circ 1113 Hz, \bullet 232 Hz; sample N°4, \square 827 Hz; sample N°5, \diamond 837 Hz.

It would be very interesting to compare these results with other experimental data concerning the kinetic growth coefficient of ${}^4\text{He}$ crystals. Presently, there are no such data in the phonon region. In the roton region, our data on both temperature dependence and

absolute value agree well with the results of Castaing [1.5] which he obtained by studying the anomalous transmission of sound through a quantum-rough interface, as well as with the results of Bodensohn [1.80] which he obtained in measuring the time needed to establish an equilibrium shape of ${}^4\text{He}$ crystals that had an electrically charged surface. As to the comparison of experimental data with

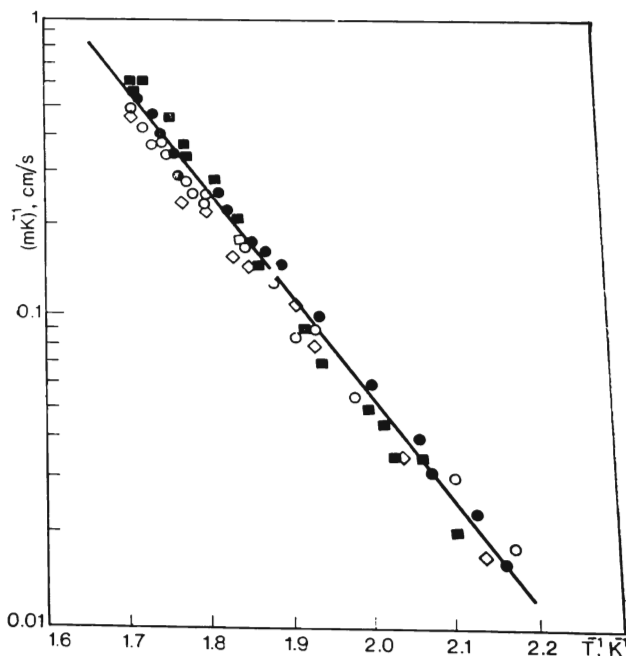


Fig. 1.22. The assumed roton contribution into damping. Notations are the same as in Fig. 1.21. The straight line corresponds to $\Delta_r = 7.8 \text{ K}$.

the quantitative theory [1.41-42], the case seems to be much less clear. In the phonon region, our data are within an order of magnitude of that predicted by the theory. Nevertheless, this agreement should not be taken too seriously due to the insufficiently reliable, in our opinion, identification of the phonon contribution to the crystallization wave damping. In the roton region, in addition to a true temperature dependence, the theory [1.41] predicts a damping 20-fold lower than the observed one. Besides, according to the same theory, this result is valid only in the ballistic regime, where the roton free-path is much longer than the crystallization wavelength. However, in our experiments and, even more so, in the experiments by Castaing

and Bodensohn, an opposite hydrodynamic regime of damping takes place.

According to Andreev and Knizhnik [1.41], in the hydrodynamic regime, crystallization wave damping is only due to dissipative processes in bulk of both the liquid and crystal, since the conditions at a moving interface correspond to a thermal equilibrium (even at finite temperatures). The last statement should be considered as an assumption that is even more strong than the assumption about the nondissipativity of crystallization at $T = 0$. According to this assumption, the growth coefficient in its primary sense appears to be infinite. To define damping one introduces an effective growth coefficient which is related to total damping by the same relation (1.19); for this we shall use the former notation, K . It is essential that the effective growth coefficient so defined turns out to be frequency (or wave vector) dependent; the actual form of this dependence is strongly influenced by a dominating dissipation mechanism type. The roton contribution to damping is described by the expression:

$$\frac{1}{mK} = \frac{2\eta_r k}{\rho_1} \quad (1.29)$$

where η_r is the roton viscosity. Within the temperature range we are interested in, the value of η_r is temperature independent and equals about $2 \cdot 10^{-5}$ P [1.81-82]; this value is too small to provide an appreciable contribution to the damping observed. Thus, the fast build up of damping at $T > 0.5$ K remains, essentially, unexplained.

In order to estimate the crystal phonons contribution to the total damping, let us take into account that for these phonons the condition $kl_N \ll 1$ can be taken as satisfied in our experiment, albeit by slightly stretching a point. If, in addition, one could neglect all processes not conserving quasimomentum, viz. when the following condition is valid,

$$kl_N \gg (l_N/l_U)^{1/2} \quad (1.30)$$

(l_N and l_U are the mean free paths of crystal phonons characterizing normal and Umklapp processes respectively), then the corresponding contribution will be described by an expression like (1.29), where the roton viscosity is replaced by the crystalline phonon viscosity. In sufficiently perfect crystals, at $T \simeq 0.5$ K one has $l_U \gg 1$ cm [1.75, 1.83], so that condition (1.30) is, perhaps, actually satisfied; yet, the observed temperature and frequency dependences of damping are not adequately described by expressions like (1.29) (the

phonon viscosity is proportional to T^{-1} [1.84]). In the opposite limiting case of a “very poor crystal” [1.41], the following expression was obtained:

$$\frac{1}{mK} = \frac{TS^2}{\rho_1 \kappa_s k} \quad (1.31)$$

where S is the entropy per unit volume, κ_s the thermal conductivity coefficient; “intermediate” cases are also possible. By using various assumptions about the number and character of crystal defects, one could try to “fit” formulas of the theory [1.41] to experiment. The fitting, however, would be inevitably of such a speculative character as to be of no interest at all. In any case, it is evident that for a sufficient understanding of the damping mechanisms of crystallization waves, a wealth of work must be done both in experiment and in theory. In connection with this, let us note a very interesting fact discovered by Bodensohn [1.80]: the kinetic growth coefficient is practically unchanged in passing from the hcp- to the bcc-phase of ${}^4\text{He}$. This point is difficult to understand from the viewpoint of current theory. Investigations of the effect of ${}^3\text{He}$ impurities on crystallization wave damping promise to be no less interesting. Let us now consider this question in more detail.

First, let us estimate a possible effect of the impurities in our experiments. With $T \simeq 0.5$ K and the concentrations $\sim 10^{-8}$, the ${}^3\text{He}$ impurities in a liquid are reduced to a nondegenerate gas. Then their contribution into damping (see Sec. 1.3.2) is, by order of magnitude:

$$\frac{1}{mK} \sim \frac{n_3}{n} \cdot \frac{p_3}{m} \sim \frac{n_3}{n} \frac{\sqrt{m^* k_B T}}{m} \approx 10^{-4} T^{1/2} \text{ (cm/s)}$$

(m^* is the effective impurity mass). The effect of the impurities on the mean free path of thermal excitations in both liquid and crystal at so low concentrations can be neglected. Consequently, in the temperature range investigated, the impurities can yield a sizable contribution to damping at concentrations of about 10^{-5} . This estimate, however, can be significantly changed, if impurity energy levels exist at a crystal-liquid interface, as is the case with the free surface of liquid helium [1.85]. Presently, there are no evidence on those levels; investigations of this question are important not only for understanding the damping mechanism of crystallization waves, but they are of a considerable interest on their own.

Recently, the concept of coherent crystallization has been independently corroborated in the experiments by Huber and Maris [1.7] (see also [1.8-9]). They measured the Kapitza resistance at a quantum-rough interface between solid and liquid helium. At low

temperatures (below 0.3 K), when the transmission coefficient of "thermal" phonons through the interface is small (according to the theory [1.6] based on these concepts), the Kapitza resistance was proven to vary as the (-5) power of temperature, just as the theory predicts. Thus, these experiments demonstrate the applicability of the concepts of quantum-rough state and coherent crystallization in analyzing the ultrahigh-frequency processes, at least up to 10^{10} Hz. In this connection let us remember that, from the viewpoint of the theory discussed in Sec. 1.3.2, the concept of coherent crystallization should be valid up to frequencies of about Δ/\hbar , viz. $(10^{10}-10^{11})$ Hz.

Finally, let us mention two very interesting and up to now completely unexplored questions. They are, first, the investigations of the spectrum and damping of crystallization waves for surface orientations close to the "singular" ones. Here most interesting is the character of singularities in angular dependences of spectrum and damping at $\varphi \rightarrow 0$. Therefore, in principle, a tempting possibility emerges to directly compare experimental data with microscopic theory (also as yet not created), using the model concepts envisaged in Sec. 1.3.1. Second is the question of crystallization waves in ${}^3\text{He}$ whose observation might be possible at temperatures below 1 mK. Here, due to spin degrees of freedom, it is possible to observe novel, interesting effects as compared to ${}^4\text{He}$ [1.86].

1.5. CONCLUSION

In our opinion, the experimental evidence indicates conclusively that the concepts of quantum-rough state and coherent crystallization have real meaning. In any case, the gigantic values of kinetic growth coefficient observed at the lower end of the investigated temperature range exceed its classical upper bound by 4-5 orders of magnitude, and cannot be explained in any reasonable way within the framework of known classical crystallization mechanisms. The experiments on the anomalous Kapitza resistance corroborate this conclusion, and, in addition, suggest that the concept of coherent crystallization is applicable to analyzing ultrahigh-frequency processes.

Until quite recently, Fisher and Weeks [1.34], and after them other authors (see, e.g. [1.35]), using various theoretical models of helium crystal surface, have called in question the very existence of the quantum-rough state. Leaving aside the strictly theoretical aspects of this problem, we would like to note that there is now no explanation for the existence of crystallization waves and the anomalous Kapitza resistance, except an explanation based on the concepts of quantum-rough state and coherent crystallization.

I would like to express here my gratitude to A.F. Andreev,

A. V. Babkin, K. O. Keshishev, V. I. Marchenko, and A. I. Shalnikov for participation in these investigations, and the fruitful discussions that to a considerable degree facilitated my understanding of surface phenomena in helium crystals.

References

- 1.1. A. F. Andreev, A. Ya. Parshin, *Sov. Phys. JETP*, **48**, 763 (1978).
- 1.2. K. O. Keshishev, A. Ya. Parshin, and A. V. Babkin, *JETP Lett.* **30**, 56 (1979).
- 1.3. K. O. Keshishev, A. Ya. Parshin, and A. V. Babkin, *Sov. Phys. JETP* **53**, 362 (1981). A. Ya. Parshin, *Sov. Phys. Usp.* **24**, 835 (1981).
- 1.4. B. Castaing and P. Nozieres, *J. Phys.* **41**, 701 (1980).
- 1.5. B. Castaing, S. Balibar, and C. Laroche, *J. Phys. Lett.* **41**, 897 (1980).
- 1.6. V. I. Marchenko, A. Ya. Parshin, *JETP Lett.* **31**, 724 (1980).
- 1.7. T. E. Huber, H. J. Maris, *Phys. Rev. Lett.* **47**, 1907 (1981).
- 1.8. L. Puech, B. Hebral, D. Thou louze, and B. Castaing, *J. Phys. Lett.* **43**, 809 (1982).
- 1.9. P. E. Wolf, D. O. Edwards, and S. Balibar, *J. Low Temp. Phys.* **51**, 489 (1983).
- 1.10. J. E. Avron, L. S. Balfour, C. G. Kuper, J. Landau, S. G. Lipson, and L. S. Schulman, *Phys. Rev. Lett.* **45**, 814 (1980).
- 1.11. S. Balibar and B. Castaing, *J. Phys. Lett.* **41**, 329 (1980).
- 1.12. S. Ramesh, G. D. Maynard, *Phys. Rev. Lett.* **49**, 47 (1982).
- 1.13. P. E. Wolf, S. Balibar, and F. Gallet, *Phys. Rev. Lett.* **51**, 1366 (1983).
- 1.14. A. F. Andreev and I. M. Lifshitz, *Sov. Phys. JETP* **29**, 1101 (1969).
- 1.15. L. D. Landau and E. M. Lifshitz, *Statistical Physics*, Part 1, Pergamon Press, Oxford, 1980, §§ 154, 155.
- 1.16. A. A. Chernov, *Sov. Phys. Usp.* **4**, 116 (1961).
- 1.17. J. W. Gibbs, *Collected Works*, Vol. 1, Longmans, Green & Co., New York 1928.
- 1.18. C. Herring, in: *Structure and Properties of Solid Surfaces*. Ed. R. Gomer, C. G. Smith, Chicago, 1953, p. 5.
- 1.19. L. D. Landau, *Collected Works*, Pergamon, London, 1971.
- 1.20. C. Herring, *The Physics of Powder Metallurgy*, McGraw Hill Book Co., New York, 1951, p. 143.
- 1.21. V. V. Voronkov, in: *Crystal Growth*, Ed. N. N. Sheftal, Vol. 8, Nauka, Moscow, 1974, p. 7 (in Russian).
- 1.22. R. Parker, *Solid State Physics*, Vol. 25, Academic Press, 1970, p. 152.
- 1.23. W. Burton, N. Cabrera, and F. Frank, *Phil. Trans. Roy Soc., London*, **243A**, 299 (1951).
- 1.24. A. A. Chernov, *Sov. Phys. Usp.* **13**, 127 (1970).
- 1.25. K. A. Jackson, *Crystal Growth and Characterization*, North Holland Co., Amsterdam, 1975.
- 1.26. C. Herring, *Phys. Rev.* **82**, 87 (1951).
- 1.27. V. I. Marchenko, A. Ya. Parshin, *Sov. Phys. JETP* **52**, 129 (1980).
- 1.28. A. F. Andreev, Yu. A. Kosevich, *Sov. Phys. JETP* **54**, 760 (1981).
- 1.29. W. K. Burton, N. Cabrera, *Disc. Farad. Soc.* **5**, 33 (1949).
- 1.30. V. I. Marchenko, *JETP Lett.* **35**, 407 (1982).
- 1.31. A. F. Andreev, *Sov. Phys. JETP* **53**, 1063 (1981).
- 1.32. H. Muller-Krumbhaar, in: *Crystal Growth and Materials*. Ed. E. Kaldius and H. J. Scheel, North Holland Co., Amsterdam, 1977.
- 1.33. J. D. Weeks, in: *Ordering in Strongly Fluctuating Condensed Matter Systems*. Ed. T. Riste, Plenum Press, New York, 1979.
- 1.34. D. S. Fisher, J. D. Weeks, *Phys. Rev. Lett.* **50**, 1077 (1983).

- 1.35. S. V. Iordanskii, S. E. Korshunov, *JETP Lett.* **38**, 655 (1983).
- 1.36. L. A. Bol'shov, V. L. Pokrovskii, and G. V. Uimin, *JETP Lett.* **39**, 128 (1984).
- 1.37. E. H. Lieb, W. Liniger, *Phys. Rev.* **130**, 1605 (1963).
- 1.38. V. I. Marchenko, *Sov. Phys. JETP* **54**, 605 (1981).
- 1.39. A. F. Andreev, in: *Progr. in Low Temp. Phys.*, Vol. 8. Ed. D. F. Brewer, North Holland Co., Amsterdam, 1982.
- 1.40. S. V. Iordanskii, S. E. Korshunov, and I. A. Larkin, *Sov. Phys. JETP* **56**, 1224 (1982).
- 1.41. A. F. Andreev, V. G. Knizhnik, *Sov. Phys. JETP* **56**, 226 (1982).
- 1.42. R. M. Bowley, D. O. Edwards, *J. Phys.* **44**, 623 (1983).
- 1.43. D. D. Osheroff, *Physica* **90B**, 20 (1977).
- 1.44. D. D. Osheroff, C. Yu., *Phys. Lett.* **77A**, 458 (1980).
- 1.45. A. Ya. Parshin, *Physica* **109 & 110B + C**, 1819 (1982).
- 1.46. B. Castaing, A. S. Greenberg, and M. Papoula, *J. Low Temp. Phys.* **47**, 191 (1982).
- 1.47. W. F. Saam, *Phys. Rev.* **48**, 1918 (1973).
- 1.48. K. R. Atkins, *Can. J. Phys.* **31**, 1165 (1953).
- 1.49. L. M. Brekhovskikh, *Waves in Layered Media*, Academic Press, 1960, § 4.
- 1.50. A. F. Andreev, D. A. Kompaneetz, *Sov. Phys. JETP* **34**, 1316 (1971).
- 1.51. L. D. Landau, E. M. Lifshitz, *Fluid Mechanics*, Pergamon Press, Oxford, 1959, § 129.
- 1.52. H. J. Maris, T. E. Huber, *J. Low Temp. Phys.* **48**, 99 (1982).
- 1.53. L. Puech, B. Castaing, *J. Phys. Lett.* **43**, 601 (1982).
- 1.54. M. Uwaga, G. Baym, *Phys. Rev.* **B26**, 4928 (1982).
- 1.55. A. M. Kosevich, Yu. A. Kosevich, *Physica* **108B**, 1195 (1981).
- 1.56. J. Wilks, *The Properties of Liquid and Solid Helium*, Clarendon Press, Oxford, 1967, § 84.
- 1.57. R. H. Crepeau, O. Heybey, D. M. Lee, and S. A. Strauss, *Phys. Rev.* **A3**, 1162 (1971).
- 1.58. I. M. Khalatnikov, *Introduction to the Theory of Superfluidity*, Benjamen, New York, 1965, Ch. XII.
- 1.59. T. E. Huber, H. J. Maris, *J. Low Temp. Phys.* **48**, 463 (1982).
- 1.60. J. E. Vos, B. S. Blaisse, D. A. E. Boon, W. J. van Scherpenseel, and R. Kingma, *Physica* **37**, 51 (1967).
- 1.61. E. R. Grilly, *J. Low Temp. Phys.* **11**, 33 (1973).
- 1.62. J. Pipman, S. G. Lipson, J. Landau, and N. Bocher, *J. Low Temp. Phys.* **31**, 419 (1978).
- 1.63. J. Landau, S. G. Lipson, L. M. Määttänen, L. S. Balfour, and D. O. Edwards, *Phys. Rev. Lett.* **45**, 31 (1980).
- 1.64. K. O. Keshishev, A. Ya. Parshin, and A. I. Shal'nikov, *Physics Reviews* **4**, Section A, 155 (1982).
- 1.65. A. I. Shal'nikov, *Sov. Phys. JETP* **20**, 1161 (1964).
- 1.66. A. A. Chernov, *Sov. Phys. Crystallography* **7**, 728 (1962).
- 1.67. W. T. Read, Jr., *Dislocations in Crystals*, McGraw-Hill, 1954, Ch. 7, §§ 3-7.
- 1.68. K. O. Keshishev, L. P. Mezhov-Deglin, and A. I. Shal'nikov, *JETP Lett.* **17**, 269 (1973).
- 1.69. V. L. Tsymbalenko, *Sov. Phys. JETP* **45**, 989 (1977).
- 1.70. A. I. Shal'nikov, *Sov. Phys. JETP* **14**, 755 (1961).
- 1.71. L. P. Mezhov-Deglin, *Sov. Phys. JETP* **19**, 1297 (1964).
- 1.72. L. P. Mezhov-Deglin, *Sov. Phys. JETP* **22**, 47 (1965).
- 1.73. D. S. Greywall, *Phys. Rev.* **A3**, 2106 (1971).
- 1.74. B. A. Fraass, S. M. Heald, and R. O. Simmons, *J. Crystal Growth* **42**, 370 (1977).
- 1.75. A. A. Golub, S. V. Svatko, *Physica* **107B**, 281 (1981).
- 1.76. S. T. Boldarev, V. P. Peshkov, *JETP Lett.* **17**, 297 (1973).

- 1.77. P. Leiderer, H. Poisel, and M. Wanner, *J. Low Temp. Phys.* **28**, 167 (1977).
- 1.78. S. Balibar, D. O. Edwards, and C. Laroche, *Phys. Rev. Lett.* **42**, 782 (1979).
- 1.79. D. S. Greywall, *Phys. Rev.* **B18**, 2127 (1978); **B21**, 1329 (1979).
- 1.80. J. Bodensohn, P. Leiderer, and D. Savignac, *Proc. IV Int. Conf. Phonon Scat. in Cond. Matter*, Stuttgart, 1983.
- 1.81. I. M. Khalatnikov, *Introduction to the Theory of Superfluidity*, Benjamin, New York, 1965, Ch. IV.
- 1.82. B. Castaing, A. Libchaber, *J. Low Temp. Phys.* **31**, 887 (1978).
- 1.83. L. P. Mezhov-Deglin, *Sov. Phys. JETP* **25**, 568 (1967).
- 1.84. E. M. Lifshitz, L. P. Pitaevskii, *Physical Kinetics*, Pergamon Press, Oxford, 1981, §§ 69, 70.
- 1.85. A. F. Andreev, *Sov. Phys. JETP* **23**, 939 (1966).
- 1.86. S. E. Korshunov, A. V. Smirnov, *Sov. Phys. JETP* **56**, 1234 (1982).

2

Sound Propagation Through a Liquid-Metal Interface

K. N. Zinov'eva *D.Sc. (Phys. and Math.)*

2.1. INTRODUCTION

Studies of the acoustic properties of an interface between liquid helium and solid began after Kapitza discovered [2.1] a fundamental phenomenon in low temperature physics, viz. the temperature jump which was called the "Kapitza temperature jump".

Kapitza established that when heat is being transferred from solid into liquid helium or vice versa, a temperature difference ΔT is observed at the interface which is proportional to the heat flux density, \dot{Q}/S . The interface's thermal resistance, $R_K = \frac{\Delta TS}{\dot{Q}}$, is therefore inversely dependent on the cube of the temperature.

Later, the Kapitza jump was observed at low temperatures at the interface between any two media at least one of which was dielectric and which differ in their acoustic resistance, $\rho_i c_i$ (ρ_i is the density of medium and c is the velocity of sound). The relationships found by Kapitza for the He-II solid interface have also been qualitatively confirmed in experiments with other substances.

A theory describing this phenomenon was suggested by Khalatnikov [2.2]. Since the elementary excitations in He-II are phonons and rotons, and the thermal excitations in the crystalline solid are crystal lattice oscillations, viz. phonons, heat transfer between the solid and liquid must take place via an energy transfer from the phonons in the liquid to those in the solid or vice versa. The rotons play an insignificant role in the heat transfer because the number of phonons in a solid with an energy higher than or equal to a roton's energy, $\Delta = 8.6$ K, is exponentially small.

Since the acoustic impedances of the media are mismatched ($\sim 10^3$) and the phonon critical angle in helium is small ($\leq 10^\circ$), the heat transfer is strongly limited. This results in the interface's thermal resistance, R_K , and overheating of one medium relative to the other.

The Kapitza jump is one of the most complicated phenomena in low temperature physics. Numerous experiments have demonstrated that the real heat transfer proceeds much more efficiently than that should be expected from the Khalatnikov acoustic theory. The discrepancy is especially large (up to two orders of magnitude) at $T \sim 1\text{-}2$ K. The predicted strong dependence of R_K on the elastic constants of the solid was not observed experimentally, with the theoretical T^{-3} law

being satisfied only at very low temperatures ($\lessdot 0.1$ K). The experiments also established a strong dependence of R_K on the properties of solid phase's surface: at low temperatures the Kapitza resistance depends mainly on the character of the mechanical and thermal processing of the surface and R_K is weakly dependent on the liquid phase's properties (^4He or ^3He).

During the past decade, an investigation of the angular and frequency dependences of the transmission and reflection coefficients of phonons crossing the boundary between liquid helium and a solid have been carried out in order to test the theoretical fundamentals experimentally and to find an explanation for those facts inconsistent with the theory.

This review contains the results of experimental low temperature studies of acoustic wave (acoustic phonons) incident from liquid ^4He on the surface of metal (tungsten or gold) [2.3-5]. The experimental apparatus, experimental data, and a discussion of them can be found in Sec. 2.3. The theories that explain physics of the phenomenon and that were used to analyze the data are briefly discussed in Sec. 2.2. Readers familiar with the acoustic theory of heat transfer can pass over this Section.

2.2. ACOUSTIC PHENOMENA AT A LIQUID-SOLID INTERFACE

2.2.1. Reflection and transmission coefficients of the acoustic energy according to the classical acoustic theory [2.6].

Let a plane wave be incident on the liquid-isotropic solid interface from a liquid that occupies the half-space $z > 0$ (see Fig. 2.1). The velocity \mathbf{V} of particles in the liquid is determined by the preset scalar potential φ , viz. $\mathbf{V} = \text{grad } \varphi$, and in the solid by the scalar potential Φ and vector potential ψ , so that $\mathbf{u} = \text{grad } \Phi + \text{rot } \psi$, where \mathbf{u} is the displacement vector. Let the wave vector \mathbf{k} of an incident wave lies within the xz -plane. We choose ψ so that $\psi_y = \psi$, $\psi_x = \psi_z = 0$. Then incident and reflected waves can be written in the form:

$$\varphi = A e^{ik(x \sin \theta - z \cos \theta)} e^{-i\omega t} \quad (2.1)$$

$$\varphi_r = A_r e^{ik(x \sin \theta + z \cos \theta)} e^{-i\omega t} \quad (2.2)$$

where A and A_r are amplitudes and ω is a frequency.

Longitudinal and transverse waves that arise in the solid are denoted by the subscripts l and t, respectively:

$$\Phi = A_l e^{ik_l(x \sin \theta_l - z \cos \theta_l)} e^{-i\omega t} \quad (2.3)$$

$$\psi = A_t e^{ik_t(x \sin \theta_t - z \cos \theta_t)} e^{-i\omega t} \quad (2.4)$$

Here θ , θ_1 , and θ_t are the angles between the z -axis and the corresponding directions of wave propagation, while k , k_1 , and k_t are the corresponding wave numbers: $k = \frac{\omega}{c}$, $k_1 = \frac{\omega}{c_1}$, $k_t = \frac{\omega}{c_t}$, where c , c_1 ,

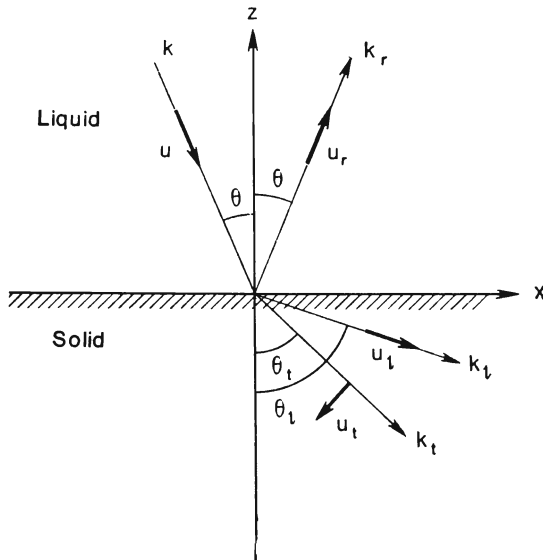


Fig. 2.1. The wave excited by a plane acoustic wave incident from the liquid ($z > 0$) on the surface of the solid ($z < 0$); θ are the angles of incidence and reflection of the incident wave in the liquid; θ_1 and θ_t are the angles of refraction of the longitudinal and transverse waves in the solid; u , u_r and k , k_r are, respectively, the displacements of particles and the wave vectors of the incident and reflected waves in the liquid; u_1 , u_t and k_1 , k_t are the displacements of the particles and the wave vectors of the refracted longitudinal and transverse waves in the solid.

and c_t are propagation velocities of waves. From Snell's law we have

$$k \sin \theta = k_1 \sin \theta_1 = k_t \sin \theta_t;$$

$$\frac{\sin \theta}{c} = \frac{\sin \theta_1}{c_1} = \frac{\sin \theta_t}{c_t} \quad (2.5)$$

The A_r , A_1 , and A_t coefficients are determined from the boundary conditions at $z = 0$ (normal displacements like normal stresses on both sides of the interface are equal to each other and a shear stress vanishes on the boundary).

By neglecting the effects of sound absorption in the solid and liquid, we obtain the known solutions [2.6]:

$$\frac{A_r}{A} = \frac{Z_l \cos^2 2\theta_t + Z_t \sin^2 2\theta_t - Z}{Z_l \cos^2 2\theta_t + Z_t \sin^2 2\theta_t + Z} \quad (2.6)$$

$$\frac{A_l}{A} = \frac{\rho}{D} \frac{2Z_l \cos 2\theta_t}{Z_l \cos^2 2\theta_t + Z_t \sin^2 2\theta_t + Z} \quad (2.7)$$

$$\frac{A_t}{A} = -\frac{\rho}{D} \frac{2Z_t \sin 2\theta_t}{Z_l \cos^2 2\theta_t + Z_t \sin^2 2\theta_t + Z} \quad (2.8)$$

$$Z = \frac{\rho c}{\cos \theta}, \quad Z_l = \frac{D c_l}{\cos \theta_l}, \quad Z_t = \frac{D c_t}{\cos \theta_t} \quad (2.9)$$

where ρ and D are the densities of liquid and solid phases.

Suppose J_0 , J_1 , and J_2 are the intensities (energies) of incident, reflected, and transmitted waves, respectively. Then the reflection coefficient of energy from the interface is

$$v(\theta, \omega) = \frac{J_1}{J_0} = \frac{A_r^2}{A^2} \quad (2.10)$$

and the transmission coefficient of energy into the solid is

$$w(\theta, \omega) = \frac{J_2}{J_0} = 1 - \frac{A_r^2}{A^2} \quad (2.11)$$

According to (2.11) and (2.6), for normal incidence we shall have

$$w(0) = \frac{4\rho c D c_l}{(\rho c + D c_l)^2} \quad (2.12)$$

For $\rho c \ll D c_l$,

$$w(0) \simeq \frac{4\rho c}{D c_l}; \quad v(0) \simeq 1 - \frac{4\rho c}{D c_l} \quad (2.13)$$

Snell's law (2.5) predicts that there are two critical angles of incidence, θ_1 and θ_2 , for which the sines of the refraction angles of longitudinal and transverse waves in the solid are equal to unity:

$$\theta_1 = \arcsin \frac{c}{c_l} \quad \text{and} \quad \theta_2 = \arcsin \frac{c}{c_t} \quad (2.14)$$

When $\theta < \theta_1$, longitudinal waves are mainly excited in the solid (the transverse sound contribution amounts here to a few percent), whereas when $\theta_1 < \theta < \theta_2$, only transverse sound is excited. When $\theta \geq \theta_2$, the total impedance of the solid

$$Z_s = Z_l \cos^2 2\theta_t + Z_t \sin^2 2\theta_t \quad (2.15)$$

is a pure imaginary quantity. Therefore the modulus of the amplitude ratio $\left| \frac{A_r}{A} \right| = 1$, whence the reflection coefficient $v = 1$, and

the transmission coefficient $w(\theta) = 1 - v(\theta) \equiv 0$. Thus, in the absence of attenuation, the total internal reflection takes place in the post-critical region ($\theta \geq \theta_2$), viz. acoustic energy does not pass into solid.

2.2.2. The Khalatnikov Theory of Liquid Helium-Solid Heat Transfer. Kapitza Resistance [2.2]

Let us consider a heat flux from liquid helium to the solid. The phonons from helium incident at the angle θ to an infinite liquid helium-solid interface follow the laws of classical acoustics. For this reason the probabilities that a phonon having the frequency ω will be either reflected or transmitted are equal, respectively, to either the reflection coefficients, $v(\omega, \theta)$, or transmission coefficients $w(\omega, \theta)$, of the energy of a plane acoustic wave.

A phonon from helium incident on a wall transfers an energy equal to $\hbar\omega \cdot w(\omega, \theta)$ to the solid. The number of phonons which are incident on a unit area per unit time is $n(\hbar\omega/k_B T) c \cos \theta$, where $n(\hbar\omega/k_B T) = [e^{\hbar\omega/k_B T} - 1]^{-1}$ is Planck's distribution function, and k_B is Boltzmann's constant.

The total power flux which is transferred to the solid is

$$W(T) = \int n(\hbar\omega/k_B T) c \cos \theta \hbar\omega w(\omega, \theta) \frac{d\mathbf{k}}{(2\pi)^3}$$

$$W(T) = \frac{\hbar}{(2\pi c)^2} \int_0^\infty n(\hbar\omega/k_B T) \omega^3 d\omega \int_0^{\pi/2} w(\omega, \theta) \cos \theta \sin \theta d\theta \quad (2.16)$$

If we assume that w does not vary or weakly varies with frequency in the vicinity of the predominating frequency, $\omega = 3k_B T/\hbar$, then when integrating with respect to a frequency, we shall have

$$W(T) = \frac{\pi^2 k_B^4 T^4}{60 \hbar^3 c^2} \int_0^{\pi/2} w(\theta) \cos \theta \sin \theta d\theta \quad (2.17)$$

When the temperature difference between helium and solid is equal to ΔT , the resultant power flux through the interface will be

$$\Delta W(T) = \frac{\pi^2 k_B^4 T^3 \Delta T}{15 \hbar^3 c^2} \int_0^{\pi/2} w(\theta) \cos \theta \sin \theta d\theta \quad (2.18)$$

By introducing Khalatnikov's notation,

$$F = \frac{1}{2} \frac{D}{\rho} \left(\frac{c_t}{c} \right)^3 \int_0^{\pi/2} w(\theta) \cos \theta \sin \theta d\theta \quad (2.19)$$

we obtain the original Khalatnikov formulae for the heat flux ΔW , and the Kapitza resistance, R_K :

$$\Delta W(T) = \frac{\rho c}{Dc_t} \frac{T^3 \Delta T}{c_t^2} \frac{2\pi^2 k_B^4}{15\hbar^3} F \quad (2.20)$$

$$R_K = \frac{Dc_t}{\rho c} \frac{c_t^2}{T^3} \frac{15\hbar^3}{2\pi^2 k_B^4} \frac{1}{F} \quad (2.21)$$

In order to calculate the function F , Khalatnikov subdivided the range of integration in (2.19) into three domains: from $\theta = 0$ to $\theta = \theta_1 = \arcsin \frac{c}{c_t}$, then from $\theta = \theta_1$ to $\theta = \theta_2 = \arcsin \frac{c}{c_t}$, and from $\theta = \theta_2$ to $\theta = \pi/2$.

The first two integrals determine the contribution of longitudinal and transverse waves that are excited in the solid by the phonons. This part of F function is normally denoted by F_1 and is easily calculated by means of (2.6), (2.11) from the acoustic theory.

The third integral denoted by F_2 is appropriate for angles of incidence that are within the total internal reflection region, where surface Rayleigh waves can be induced in the solid by incident phonons. The F_2 value is determined by the contribution of Rayleigh waves to the energy flux which is transferred to the solid and normal to the interface.

When there is no attenuation, at $\theta > \theta_2$, w is a pure imaginary quantity. In this case the Rayleigh waves energy transfer is only along the solid surface, and the energy flux normal to the interface vanishes ($F_2 = 0$). The F_2 value is nonzero only when the attenuation is present in the solid. Khalatnikov calculated F_2 at the limit of a strong coupling between Rayleigh wave and solid excitations, when Rayleigh wave energy is totally absorbed by the solid. The F_1 and F_2 calculation will be detailed in Sec. 2.2.4. Here we shall only note that the calculation performed in [2.7] using the Khalatnikov formulae demonstrates that, for the solids having Poisson's ratios from 0.2 to 0.45 [2.8], the value of F_1 is about 0.6 and F_2 varies from 1.4 to 0.8. Thus, for the majority of solids, $F = F_1 + F_2 = 2.0-1.4$, viz. the Rayleigh wave yields the same contribution to the heat flux as bulk waves do. Therefore, Khalatnikov's works show that accounting for the Rayleigh wave does not significantly improve the agreement between theory and experiment.

2.2.3. The Andreev Theory of Resonance Absorption of Sound by a Metal Surface

Khalatnikov's works do not discuss concrete mechanisms for surface wave energy absorption by the solid phase. Later on Little [2.9] and Andreev [2.10, 11] noted that the interaction be-

tween phonons and conduction electrons may be the basis for such a mechanism in metals.

In order to account for the acoustic energy absorbed by conduction electrons, Andreev introduced an additional term, Y , into the classical formulae (2.6)-(2.8). This term stands for the impedance of the transmission of sound across an interface which is accompanied by the excitation of a Rayleigh wave, and has a real part in the vicinity of the Rayleigh angle of incidence, θ_R . The latter is called the third critical angle of incidence, it falls within the region of total internal reflection angles near θ_2 , and is determined by the relationship

$$\sin \theta_R = \frac{c}{c_R} = \frac{c}{\xi c_t} \quad (2.22)$$

where c_R is the velocity of Rayleigh waves on a free surface of metal whereas $\xi < 1$ [2.8] (see also Sec. 2.2.5).

Taking into account the impedance Y , formulae (2.6)-(2.8) in the vicinity of the angle θ_R acquire the following form:

$$\frac{A_r}{A} = \frac{Z_s + Y - Z}{Z_s + Y + Z} \quad (2.23)$$

$$\frac{A_l}{A} = \frac{\rho}{D} \frac{2Z_l \cos 2\theta_t}{Z_s + Y + Z} \quad (2.24)$$

$$\frac{A_t}{A} = - \frac{\rho}{D} \frac{2Z_t \sin 2\theta_t}{Z_s + Y + Z} \quad (2.25)$$

$$Y = G \frac{p_0^4}{(\pi \hbar)^3} \quad (2.26)$$

from which at the angles of incidence close to θ_R , we have

$$w(\theta) = \frac{4B}{(B+1)^2 + (\theta - \theta_R)^2 [HDc_t^2/(\rho c)^2]^2} \quad (2.27)$$

Here p_0 is the electron momentum at the Fermi surface, $B = Y/\rho c$, while G and H are the functions of elastic constants of helium and metal.

As can be seen from (2.27), accounting for the sound absorbed by conduction electrons leads to a strong variation in the angular dependence of the acoustic transmission coefficient in the vicinity of the Rayleigh angle of incidence, θ_R . When the angle of incidence is θ_R , the wave vector projection of an incident wave onto the interface plane is equal in absolute value to the wave vector for a Rayleigh wave having the same frequency. The Rayleigh wave is excited in the resonance mode on the metal surface by the energy of incident sound wave. At $l_e \gg \lambda$, where l_e is the electron free path and λ is the sound wavelength in metal, and at an angle of incidence equal to θ_R acoustic energy will be almost completely absorbed.

The transmission coefficient $w(\theta)$ will demonstrate a sharp peak whose height is about unit and width is about $\rho c^2/Dc_l^2$.

Thus, by starting with the electron mechanism for phonon absorption in metals, Andreev was the first to predict the existence of an anomalously high transmission coefficient of sound from liquid helium into metal at the Rayleigh angle of incidence.

However, as was shown by Andreev himself, thereby heat transfer tends to be equal to the magnitude calculated by Khalatnikov only at the limit of a strong coupling of phonons with conduction electrons and it does not exceed this magnitude.

2.2.4. The Generalized Acoustic Theory

Merkulova [2.12] was the first to account for absorption of sound by the bulk of the solid, when calculating the amplitudes and phases of the reflection coefficient of a plane sound wave incident on the liquid-solid (water-soil) interface. As a result, the acoustic theory was generalized to include an absorbing solid medium. It was called the generalized acoustic theory. Shortly after, an absorption of sound in both media was accounted for by Mott [2.13].

In the vicinity of the Rayleigh angle of incidence, θ_R , a pronounced minimum in the reflection coefficient whose depth and width depend on the absorption coefficient of sound in the solid is reported to exist [2.12]. The phase of the reflected wave is abruptly changed, when passing through Rayleigh angle. These calculations were then confirmed in experiment [2.14].

In 1972, theoretical works by Khalatnikov and Adamenko [2.15], Peterson and Anderson [2.16], Haug and Weiss [2.17] were simultaneously published. In these studies the generalized acoustic theory was applied to describe the phenomenon of thermal phonons passing from the liquid helium into the solid. The basic mechanism for the attenuation of sound in dielectrics is said to be the attenuation on dislocations, whereas in metals it is composed of two constituents, viz. the attenuation on electrons and on dislocations.

In papers [2.16, 17] an angular dependence of the transmission coefficient of phonons passing from liquid helium to the solid, with a due regard for the bulk attenuation of sound in the solid was computer calculated. The attenuation in the liquid was taken to be zero.

The attenuation of sound in the solid was accounted for by introducing complex wave numbers:

$$k_{l,t} = \frac{\omega}{c_{l,t}} = k_{l,t}^{(0)}(1 + ip_{l,t}) \quad (2.28)$$

or complex velocities

$$c_{l,t} = c_{l,t}^{(0)}(1 + ip_{l,t})^{-1} \quad (2.29)$$

where $k_{l,t}^{(0)}$ and $c_{l,t}^{(0)}$ are real numbers and $p_{l,t}$ are the dimensionless attenuation parameters for energy of longitudinal and transverse waves and $0 < p_{l,t} < 1$. The attenuation parameters, $p_{l,t}$, can be expressed in terms of the absorption coefficients for acoustic energy which are

$$\gamma_{l,t} = \frac{1}{x} \ln \frac{J_0}{J},$$

$$J = J_0 e^{-\gamma_{l,t} x}$$

Since the imaginary part of the wave number is the attenuation coefficient of the wave amplitude, $k_{l,t}^{(0)} p_{l,t} = \frac{\gamma_{l,t}}{2}$ and

$$p_{l,t} = \frac{\gamma_{l,t} c_{l,t}^{(0)}}{2\omega} = \frac{1}{4\pi} \frac{\lambda_{l,t}}{l_{l,t}}, \quad (2.30)$$

where $\gamma_{l,t}$ is the energy absorption coefficient (in nepers per unit length), $\lambda_{l,t}$ is the sound wavelength, $l_{l,t}$ is the characteristic energy attenuation length (the distance required for intensity to be reduced by e times). In addition, boundary conditions require the generalizing of Snell's law to include complex velocities and wave numbers.

With due regard for attenuation, the amplitude reflection coefficient for the plane acoustic wave at a liquid-solid interface is

$$\left| \frac{A_r}{A} \right| = \left| \frac{\beta - 1}{\beta + 1} \right| \quad (2.31)$$

where

$$\beta = \frac{Z_l \cos^2 2\theta_t + Z_t \sin^2 2\theta_t}{Z} = \frac{Z_s}{Z} \quad (2.32)$$

is a complex number in the general case. The phase of a reflected wave is changed according to the following law:

$$\varphi = \arctan \frac{\operatorname{Im} \left(\frac{A_r}{A} \right)}{\operatorname{Re} \left(\frac{A_r}{A} \right)} = \arctan \frac{\operatorname{Im} \left(\frac{\beta - 1}{\beta + 1} \right)}{\operatorname{Re} \left(\frac{\beta - 1}{\beta + 1} \right)} \quad (2.33)$$

For the acoustic energy transmission coefficient we have

$$w(\theta) = 1 - \left| \frac{A_r}{A} \right|^2 = 1 - \left| \frac{\beta - 1}{\beta + 1} \right|^2 \quad (2.34)$$

After algebraic and trigonometric transformations we shall obtain

$$w(\theta) = \frac{4 \operatorname{Re} \beta}{|\beta + 1|^2} \quad (2.35)$$

where

$$\beta = \frac{D}{\rho} \cos \theta \left\{ \frac{\frac{c_1}{c} \left[1 - 2 \left(\frac{c_t}{c} \sin \theta \right)^2 \right]^2}{\sqrt{1 - \left(\frac{c_1}{c} \sin \theta \right)^2}} \right. \\ \left. + 4 \left(\frac{c_t}{c} \right)^3 \sin^2 \theta \sqrt{1 - \left(\frac{c_t}{c} \sin \theta \right)^2} \right\} \quad (2.36)$$

Figure 2.2 gives an angular dependence of the real part of the amplitude reflection coefficient, $\frac{A_r}{A}$, and of the reflected wave phase, φ , whereas Fig. 2.21 (Sec. 2.3) describes the angular dependence of the acoustic energy transmission coefficient, $\alpha(\theta) = w(\theta) \times \cos \theta$, for the ^4He -tungsten interface calculated by means of formulae (2.31)-(2.36) for several values of the attenuation parameter, p .

The diagrams show that accounting for sound absorption in a solid significantly changes the nature of the curves $v(\theta)$ and $w(\theta)$ in the region of total internal reflection angles. A narrow high peak in the transmission coefficient and a corresponding fall in the reflection coefficient appear at the angle of incidence, θ_R . One can easily see that in the vicinity of the Rayleigh angle the behavior of $w(\theta)$ resulted from the generalized acoustic theory is similar to that calculated by Andreev. This is to be expected because there is only one physical reason for this phenomenon, i.e. the absorption in a solid of the energy of the Rayleigh waves which are resonantly excited by means of a sound wave incident at the angle θ_R .

Using the formulae for the generalized acoustic theory we can easily calculate the heat flux from the interface, $\Delta W(T)$, and the Kapitza resistance, R_K , when w is frequency independent. Let us put the function F (2.19) in which transmission coefficient, $w(\theta)$, is determined by (2.35) and (2.36) into Khalatnikov's formulae (2.20) and (2.21). Then

$$R_K = \frac{15\hbar^3 c^2}{\pi^2 k_B^4 T^3} \left[\int_0^{\pi/2} w(\theta) \cos \theta \sin \theta d\theta \right]^{-1} \quad (2.37)$$

As in the basic Khalatnikov theory R_K will be proportional to T^{-3} .

If w depends substantially on frequency, then $W(T)$ should be calculated from (2.16). The resultant $R_K^{-1}(T)$ dependence will differ from the cubic one, since the predominating frequency depends linearly on temperature.

An increase in the heat flux according to the generalized Khalatnikov theory is mainly caused by the energy absorption of waves in solid that decreases exponentially normal to the interface. The waves are excited at large angles of sound incidence, and penetrate to a depth about $0.01-0.1\lambda$.

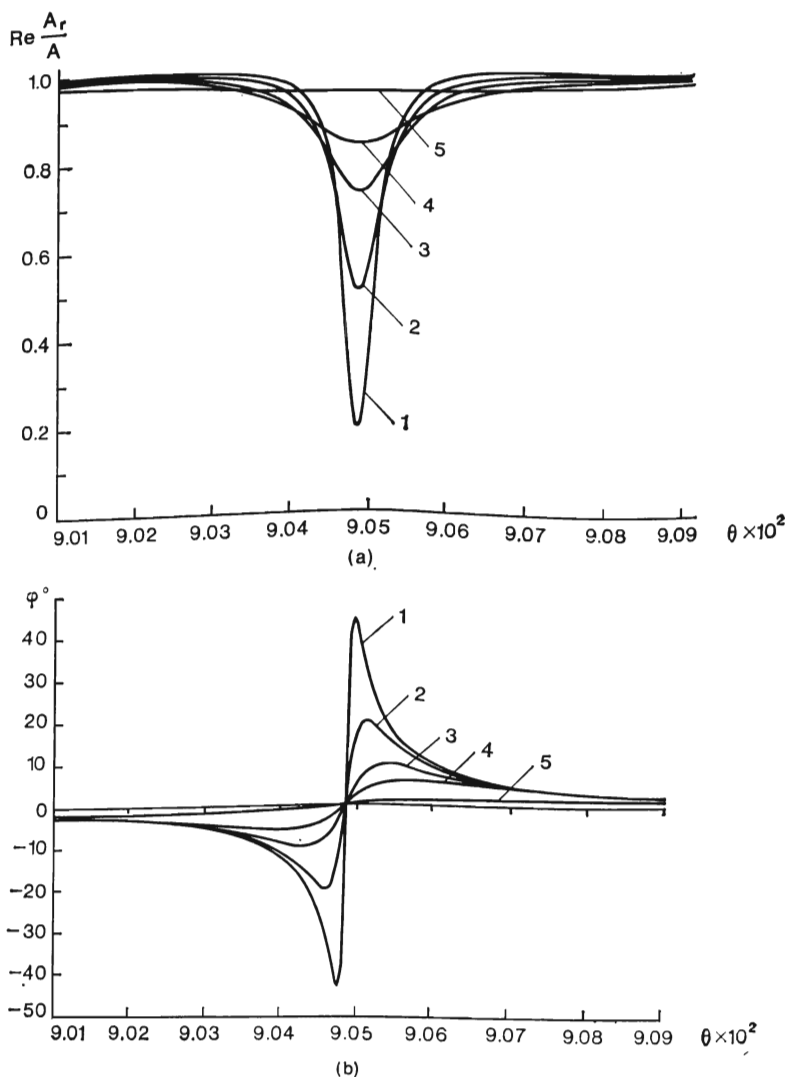


Fig. 2.2. Calculated dependence of the real part (a) and the phase (b) of the amplitude reflection coefficient in a plane acoustic wave incident from the liquid ${}^4\text{He}$ on the tungsten surface as a function of the angle of incidence (in the vicinity of the Rayleigh angle) for several attenuation parameters of sound in tungsten, p : 1— 1.5×10^{-4} , 2— 3×10^{-4} , 4— 1×10^{-3} , 5— 3×10^{-2} .

The total transmitted energy is greatly increased (up to two orders of magnitude) as a result of phonon absorption in the near-surface layer because the range of post-critical angles significantly exceeds Snell's cone.

2.2.5. Rayleigh Surface Waves

Unlike the bulk longitudinal and transverse waves that induce oscillations in the entire crystal lattice, a Rayleigh wave consists of two inhomogeneous waves: longitudinal and transverse

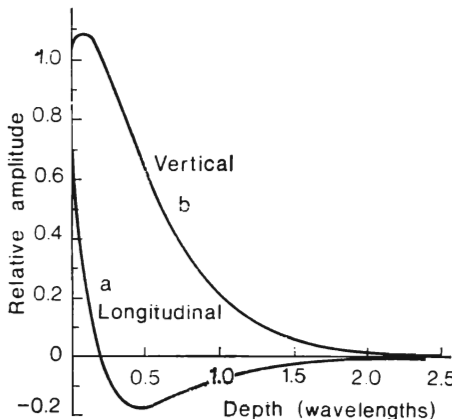


Fig. 2.3. Relative amplitudes a and b of particle motion in the Rayleigh wave as a function of the depth in an isotropic solid [2.18, 2.21].

waves. They propagate across the free surface of a solid with identical velocities c_R and attenuate along the normal to the surface at a depth of about a wavelength.

Suppose an isotropic solid occupies the half-space $z < 0$, while another half-space ($z > 0$) is a vacuum, and a Rayleigh harmonic plane wave propagates along the x -axis. Particles in the Rayleigh wave move in an ellipse whose major axes are parallel and perpendicular to the interface ($z = 0$):

$$\begin{aligned} u_x &= a \cos(k_R x - \omega t) \\ u_z &= b \sin(k_R x - \omega t) \end{aligned} \quad (2.38)$$

Here k_R is the wave number defined by the relation $k_R = \frac{\omega}{c_R}$.

Figure 2.3 plots the relative amplitudes a and b of particle motion in the Rayleigh wave versus the depth expressed in wavelengths, for an isotropic semi-infinite solid [2.18].

The figure shows that the trajectories of particles in the surface layer vary with depth. On the surface the amplitude ratio is 1.52 (1.51 for tungsten). At a distance of 0.2λ from the surface the longitudinal component passes through zero and, as a result, the direction of particle motion in ellipses changes.

Both components vanish at the depth of $2.0-2.5 \lambda$ which means that the Rayleigh wave energy is concentrated within a narrow surface layer $\sim 2\lambda$ thick. The energy can be transferred deep into the body of the solid only when a strong coupling between Rayleigh wave and phonons or electrons exists.

The Rayleigh wave velocity c_R in an isotropic solid is defined by the Rayleigh equation [2.8]:

$$\left[2 - \left(\frac{c_R}{c_t} \right)^2 \right]^2 = 4 \left[1 - \left(\frac{c_R}{c_l} \right)^2 \right]^{1/2} \left[1 - \left(\frac{c_R}{c_t} \right)^2 \right]^{1/2} \quad (2.39)$$

where c_l and c_t are the velocities of bulk longitudinal and transverse waves in a solid. The equation was derived assuming no stresses at the half-space boundary ($z = 0$). The phase velocity of the Rayleigh wave in (2.39) can be approximated by the relation [2.21]:

$$\frac{c_R}{c_t} = \xi \approx \frac{0.72 - (c_t/c_l)^2}{0.75 - (c_t/c_l)^2} \quad (2.40)$$

The ratio, $c_R/c_t = \xi$, is a constant characteristic for a given substance that depends entirely on the Poisson's ratio σ [2.8]. For different substances ξ varies from 0.874 to 0.955. Therefore, phase velocity of the Rayleigh wave is approximately 10% less than that of bulk transverse waves.

Since the Rayleigh wave consists of longitudinal and transverse components, its attenuation along an infinite plane smooth surface of a solid body is determined by absorption coefficients of the corresponding longitudinal and transversal waves within the surface layer $\sim 2\lambda$ thick.

As shown in [2.18, 19] the Rayleigh wave attenuation parameter p_R is a linear combination of the attenuation parameters for longitudinal and transversal waves (at small p 's):

$$p_R = A p_l + (1 - A) p_t \quad (2.41)$$

where

$$A = \frac{16(1 - \xi_0^2)}{\xi_0^2 \eta_0^2 (3\xi_0^4 - 16\xi_0^2 + 24 - 16/\eta_0^2)} \quad (2.42)$$

$$\xi_0 = \left| \frac{c_R}{c_t} \right|, \quad \eta_0 = \left| \frac{c_l}{c_t} \right|$$

The value of A depends only on the Poisson's ratio σ for a given substance and it is plotted in Fig. 2.4. As seen in the figure the Rayleigh

wave attenuation parameter is primarily determined by the attenuation parameter of transverse waves p_t . For tungsten ($\sigma = 0.28$):

$$A = 0.12, \quad p_R = 0.12 \quad p_t + 0.88 \quad p_t$$

At the solid-liquid interface Rayleigh waves undergo an additional attenuation due to the radiation of energy into the liquid. The radiation losses are proportional to the ratio $\rho c / D c_t$. On the liquid

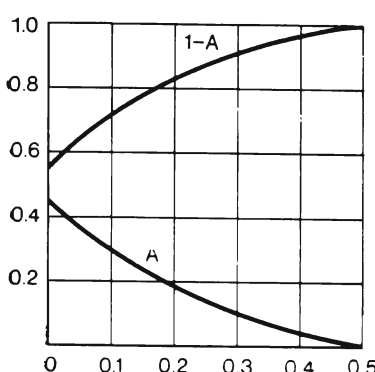


Fig. 2.4. Dependence of the coefficients A and $1-A$, which describe the interaction between the attenuation of Rayleigh and bulk waves in the solid, on Poisson's ratio σ [2.18].

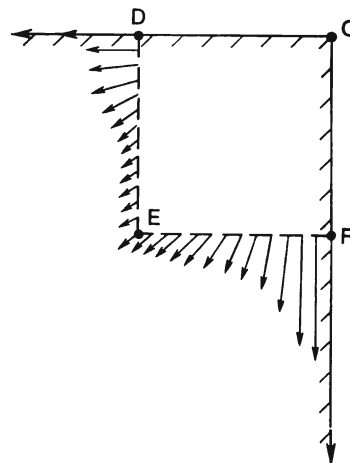


Fig. 2.5. Vector pattern of the total energy flux from a right angle for Rayleigh waves which are reflected, transmitted around the angle, and dissipated into bulk waves at the distance of $1.9 \lambda_R$ [2.21]. The incident wave propagates along the direction DO.

helium-tungsten interface the ratio is about 10^{-3} , hence an energy attenuation of the Rayleigh waves by e times occurs at the length, $l \sim 1000 \lambda_R$ (in the case of $f = 30$ MHz, $l = 10$ cm).

Transmission of Rayleigh waves is substantially influenced by surface defects (cracks, inhomogeneities, irregularities) [2.18, 2.20-22] and, when the geometry is restricted, by the angles with radii $r \leq \lambda_R$ [2.18, 20].

On the defects and angles a Rayleigh wave is attenuated due to dissipating into bulk longitudinal and transverse waves. The dissipation occurs because the condition of no stress at the interface is violated at these points for a combination of incident, reflected, and transmitted waves. As a result, the angles

and defects accumulate energy that will be transformed into bulk longitudinal and transverse waves.

Farnell's analysis [2.21] for a right angle shows that 41% of the energy of Rayleigh waves is transmitted around the angle, 13% is reflected, and 46% is dissipated into bulk waves. In Fig. 2.5 [2.21] vectors indicate the distribution of energy fluxes at the distance of $1.9 \lambda_R$ from the right angle for the Rayleigh waves reflected, transmitted and dissipated into bulk waves.

Brekhovskikh [2.20] followed by Urazakov and Fal'kovskii [2.21, 22] considered the attenuation of Rayleigh waves on periodic surface irregularities assuming the latter to be small and flattened. They have shown that with the spatial period of the irregularities, $\Lambda \leq 2\lambda_R$, the Rayleigh wave attenuation coefficient has a sharp maximum due to dissipating this wave into bulk ones.

The above properties of surface waves indicate that for an infinite, smooth boundary without irregularities the ultrasonic Rayleigh wave attenuation is governed by the coefficients of bulk absorption, most transverse, of sound in a solid. When sample dimensions are restricted and surface defects are comparable to a wavelength, the attenuation of a Rayleigh wave increases due to dissipating into bulk waves at angles and defects. Thereby the energy of Rayleigh waves can be fully transformed into that of bulk waves.

2.2.6. First Experiments on Reflection and Transmission Coefficients of Thermal Phonons Passing Across a Liquid Helium-Solid Interface

Weber, Sandmann, Dietsche, and Kinder [2.23] investigated the reflection of monochromatic phonons penetrating a solid from either vacuum or helium at $T \simeq 1\text{K}$. The phonons of a frequency 290GHz were injected into a LiF crystal by means of a superconducting tunnel junction. The coefficient of reflection from pure, fresh cleaved (in liquid helium at 1 K) surfaces was drastically increased (almost up to 100%) as compared to that for a noncleaved crystal surface. This revealed an important role played by surface state in heat transfer.

Mills and co-authors [2.24-26] studied an angular distribution of the emission and absorption of thermal phonons of an energy 1-3 K by the cleaved surface $\{100\}$ of a NaF crystal immersed in liquid helium.

Pulse technique was used for the measurements. Emitter and detector had angular dimensions of 8° and 3° respectively. Double averaging over the emitter and detector angles made it impossible to see the detailed structure of the angular distribution w for the NaF crystal. The authors [2.24, 25], however, discovered a central maximum of phonon emission and absorption within a narrow cone

of angles close to the critical angles (Fig. 2.6). In the initial observations [2.24] the cone was 2-3° wider than the calculated critical angle which could result from the dimensions of the emitter and detector employed as well as from absorption of Rayleigh waves. In the subsequent measurements of other cleaved facets of the NaF crystals [2.26] the central peak width corresponded to the calculated critical angle during negligibly small attenuating in a solid, which practically meant the lack of the Rayleigh maximum. Hence, the nature of

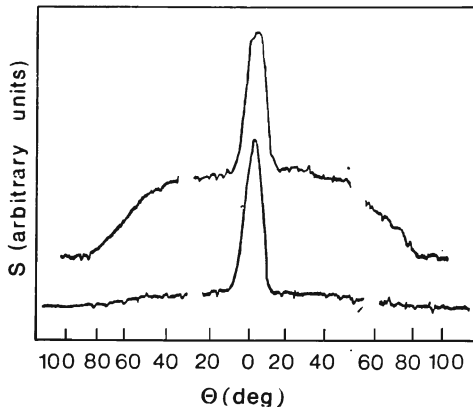


Fig. 2.6. Angular distribution of emission by the cleaved surface {100} of a NaF crystal into the liquid ${}^4\text{He}$ (upper curve) and absorption of thermal phonons from ${}^4\text{He}$ (lower curve) by the same surface, obtained for two heater temperatures 1.4 and 1.6 K, respectively, under a pressure of $p_{\text{He}} = 24$ atm [2.25].

the phenomenon was satisfactorily described by the generalized acoustic theory. For some NaF crystals the shape of central peaks for normalized curves at different T 's corresponded to the value of the attenuation parameter $p \simeq 0.03$, and for others, to $p \simeq 10^{-5}$, which evidenced different dislocation concentrations in the surface layer.

The extended wings outside the cone (Fig. 2.6), in authors' opinion, are caused by desorption of helium atoms from the crystal surface which is induced by high-energy phonons from the solid. As seen from Fig. 2.6, the desorption mechanism works only for the phonons emitted by a solid.

Note that to avoid the beam scattering by thermal phonons Mills and co-authors carried out these measurements in the collisionless region of liquid helium at a temperature of ~ 0.1 K and at a pressure of $P \geq 20$ atm. At lower pressures the phonon helium spectrum decays which results in a noticeable broadening of the thermal phonon beam in the course of its propagation in the liquid phase due to a spontane-

ous decay of its high-frequency phonons. Gurevich, Leichtman, and Lomakin [2.27, 28] demonstrated that beam broadening is associated with a finite time of transverse relaxation τ_{\perp} in three-phonon processes.

Broadening of directed phonon beams at $T < 0.6$ K imposes severe restrictions on investigation techniques for the angular dependence of the phonon reflection and transmission coefficients across a He-II-solid interface. Commonly, the measurements with high-energy phonons are performed at $P > 20$ atm and $T \leq 0.1$ K, where the phonons are stable and there is no scattering by thermal phonons. Acoustic (sound) phonons with low energy $\frac{E}{k_B} \sim 10^{-4}$ – 10^{-3} K (or 10–100 MHz) require only temperature restrictions ($T \leq 0.1$ K), since such phonons are stable at any pressure.

2.3. EXPERIMENTAL INVESTIGATIONS OF SOUND TRANSMISSION FROM LIQUID ^4He INTO A METAL

2.3.1. Experimental Procedure

The experiment involved measurement of the transmission coefficient of the acoustic energy of a plane monochromatic wave crossing liquid ^4He -metal interface versus its angle of incidence.

The measurements were carried out on samples of gold and tungsten at temperatures from 60 mK to 0.4 K under pressure of saturated helium vapour.

Consider the main relations between the measured quantities and the transmission coefficient of the acoustic energy $w(\omega, \theta) = \frac{J_2}{J_0}$.

Suppose a plane sound wave (or a flux of coherent low-frequency phonons) of energy J_0 and frequency ω is incident at the angle θ from liquid helium on a ^4He -metal interface. The reflected wave energy J_1 will be both scattered by the walls of measuring chamber and absorbed by the liquid. To maintain a constant temperature T in liquid, we shall remove this energy through the walls. The acoustic energy J_2 which is transmitted into the solid is composed of energies of all types of oscillations of the solid, and with sound absorption possible in the latter it will be transformed into a thermal energy. In view of the large difference between the acoustic impedances of liquid helium and a solid body, the reflection coefficient is close to unity, therefore, we can ignore the acoustic waves which emerge from the solid and are transmitted back into liquid for the second time. Thus, with a high degree of precision the transmission coefficient is equal to the fraction of the incident energy absorbed by the solid. Since the time for relaxation of acoustic into thermal

phonons in a metal at $T \simeq 0.1$ K ($\tau \leq 10^{-5}$ s), [2.29] is much less than the time needed to establish a thermal equilibrium between the liquid and solid ($\tau \sim 10^{-2}$) the temperature of the solid should rise by amount ΔT corresponding to the Kapitza jump.

In stationary conditions, when sound is continuously incident on an interface, the energy flux of acoustic phonons from a liquid to a solid is compensated by the return flux of thermal phonons from the solid to liquid,

$$\begin{aligned} \dot{Q}_{\text{ac. ph.}} &= \dot{Q}_{\text{therm. ph.}}, \\ \text{liq} \rightarrow s & \quad s \rightarrow \text{liq} \\ N\sigma_0 w \cos \theta &= \frac{\Delta T s}{R_K} \end{aligned} \quad (2.43)$$

so that

$$\Delta T = N\sigma_0 w \cos \theta \frac{R_K}{s} \quad (2.44)$$

Here N is the density of the acoustic energy flux on the surface of the solid body, $\sigma_0 \cos \theta$ is the sample area on which the sound is incident and which is taken to be normal to the acoustic flux, s is the total area of the sample, and R_K is the Kapitza resistance.

If the dependence $\Delta T(\theta)$ is measured at a constant liquid temperature T for various ω , it is possible to find experimentally the quantity

$$w(\omega, \theta) = \frac{\Delta T s}{N\sigma_0 \cos \theta R_K} \quad (2.45)$$

or

$$\alpha(\omega, \theta) = w \cos \theta = \frac{\Delta T s}{N\sigma_0 R_K} \quad (2.46)$$

It should be readily apparent that only the relative value of $\alpha(\omega, \theta)$ is found in experiment. To obtain the absolute value requires either the normalization of α through equating the experimental value to the theoretical one for zero angle, or the measurement (using some other technique) the incident and absorbed fractions of energy.

Let us estimate the order of magnitude of the quantities from (2.44) for the normal incidence of sound ($\theta = 0$) and the sufficiently low temperature of liquid helium ($T \simeq 0.1$ K). Proceeding from the requirements of linearity of the effect ($\Delta T \ll T$) and reliability of measuring ΔT the value of ΔT is taken equal to 1 mK.

Let us use the acoustic formula for the transmission coefficient at normal incidence (2.12) and the Khalatnikov formula for the Kapitza resistance (2.21). Then, for gold we shall have $w(0) = 2.1 \times 10^{-3}$, $R_K = \frac{180}{T^3}$ cm²K/W. Substituting these and the experimental values $\sigma_0 \sim 1$ cm² and $s \simeq 4$ cm² into (2.44) yields

$$N\sigma_0 = 10 \mu W$$

Taking into account the fact that quartz emits in both directions and its efficiency in helium is less than unity (20-50%), the overheat of a gold sample by 1 mK in stationary conditions (at $T = 0.1$ K) by means of incident sound requires cooling capacity of 40-100 μW . With an increase in temperature, the Kapitza resistance is reduced and sound absorption in liquid helium grows significantly, therefore the refrigerating capacity should quickly increase with T . Even at $T \simeq 0.4$ K and with the maximum refrigerating capacity of a dilution cryostat, the value of ΔT partially approaches the threshold sensitivity level.

Along with the high refrigerating capacity, measurements of overheating of the metal by sound require a high stability of temperature in the measuring chamber. At $T \simeq 0.1$ K the heat capacity of metal is significantly lower than that of liquid 4 He and the relaxation times are very small. Therefore the metal sample is in a thermal equilibrium with liquid and reproduces the smallest temperature fluctuations in the latter.

Note also that observing narrow Rayleigh maxima imposes heavy demands on both the emitter quality along with its fastening (the emission should be uniform and flattened in space), and the quality of a sample and its surface.

2.3.2. Apparatus

A piezoelectric quartz transducer emitting a plane monochromatic acoustic wave was placed in the chamber filled with liquid helium (see Fig. 2.10). A sample of the investigated metal M was mounted 1 cm above the quartz transducer. The angle of incidence, θ , was varied by rotating the sample, and was measured by a capacitance probe C. Two identical semiconductor thermometers made it possible to measure the absolute temperatures of the liquid and the metal, as well as their difference. The first thermometer, T_1 , was immersed into the liquid and the second, T_2 , was bonded to sample. The thermometer T_1 and the heater H placed in the liquid helium bath were used to stabilize the temperature of the liquid.

2.3.2.1. General Setup

The measurements were performed in a 3 He- 4 He dilution-refrigerator with 3 He circulating at a rate of 10^{-5} to 2×10^{-4} mole/s depending on the power dissipated inside measuring chamber. Figure 2.7 shows a sectional view of the bottom part of the cryostat. It had one capillary tube German silver and five sintered copper heat exchangers. In the absence of a load a temperature of 10-15 mK was achieved in the mixing chamber in the circulation mode. A measuring chamber of ~ 50 cm 3 volume and the mixing chamber were made

from the same block of annealed oxygen-free copper. Condensation of ^4He took place in the measuring chamber along a German silver capillary 0.2 mm in diameter and 1.5 m long. To eliminate a heat supply along the ^4He film, the capillary had a good thermal contact between the evaporation chamber and heat exchangers.

The temperature of the liquid in the measuring chamber was measured by semiconductor resistance thermometers. The constancy of the calibration of the semiconductor thermometers was checked with a ^3He condensation thermometer in the form of a coaxial cylinder cavity inside the chamber wall with a capillary to condense ^3He .

The sample was rotated by two bellows which were soldered vacuum-tightly into flanges of the vacuum vessel and measuring chamber, as well as interconnected by a textolite rod.

2.3.2.2. The Measuring Chamber

The chamber (Fig. 2.8) was an inverted can 4 cm in diameter and 5 cm high. The can bottom was also the bottom of the

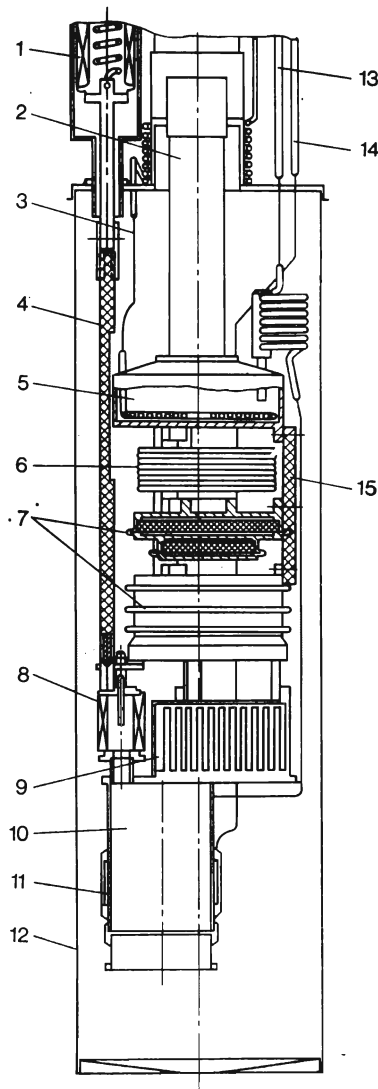


Fig. 2.7. Sectional view of the bottom part of the dilution refrigerator: 1—bellows on vacuum vessel flange, 2— ^3He pumping out tube, 3—the capillary to supply ^3He into the still, 4—textolite rod, 5—still, 6—tube heat exchanger, 7—sintered heat exchangers, 8—bellows on measuring chamber flange, 9—mixing chamber, 10—measuring chamber, 11— ^3He condensation thermometer, 12—vacuum vessel, 13—the line to condense ^4He into measuring chamber, 14—the capillary to fill-in ^3He condensation thermometer, 15—textolite holder for heat exchangers.

mixing chamber. The light metal framework 1 (Fig. 2.8) which consisted of two parallel disks 2 and 11 linked by thin vertical rods was inserted into the chamber from beneath. The upper disk carried

the sample, which could be moved, and the lower disk carried the emitter, which had a fixed position. The lower disk also formed the bottom part of the inverted small can 12. After alignment, the lower edge of the can 12 was soldered vacuum-tight to the measuring chamber.

The sample 16 was clamped in a double metal frame 8 suspended by four flat springs 7 to support 3 attached to the upper disk 2. The sample together with the frame were rotated by a rod 4 and a return spring 6, which set an initial angle of $\theta \approx 20^\circ$. The springs 7 provided rotation in one plane. An array of adjustable parallel plates 5 forming a variable capacitor was mounted on the upper part of the frame 8. Fixed plates were fastened on the disk 2. The change in the capacitance was proportional to the angle θ . The angle $\theta = 0$ corresponded to the maximum capacitance.

The rod 4 made from a nickel-chromium wire 0.3 mm in diameter was brought out into the cryostat vacuum vessel via the bellows on the cover of the measuring chamber. Once setting the initial angle θ , the wire was hermetically sealed in the bellows. The rod was moved by a second bellow soldered to the upper cover of the vacuum jacket

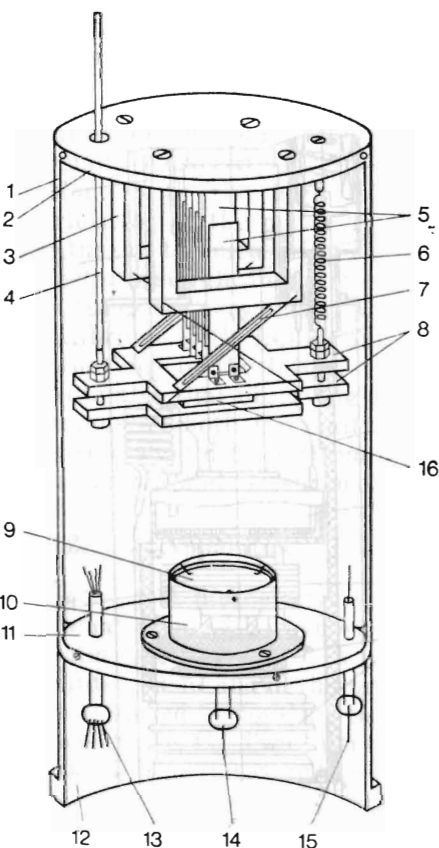


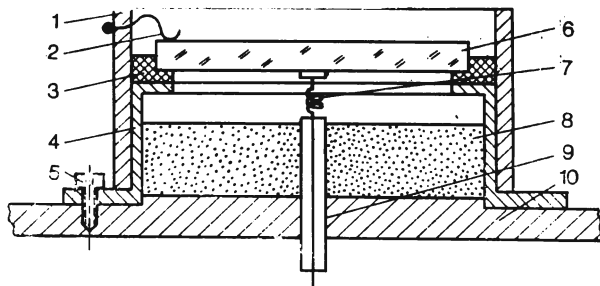
Fig. 2.8. Measuring chamber: 1—metal framework, 2, 11—parallel disks, 3—supports, 4—rod, 5—plates of variable capacitor, 6—return spring, 7—four flat springs, 8—double metal frame, 9—quartz transducer, 10—quartz transducer holder, 12—inverted can, 13, 14, 15—platinum-glass joints, 16—sample.

(Fig. 2.7). Condensation of helium in the upper bellow and continuous variation of its pressure made it possible to vary the angle θ from -20° to $+20^\circ$ at a constant rate that could be altered within a wide range.

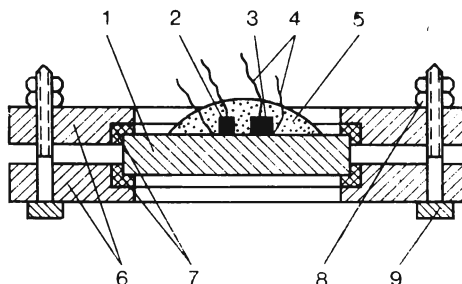
The quartz transducer 9 in a special holder 10 was mounted on the lower disk 11 so that the centers of the sample and quartz were on the same vertical line. Electrical leads made from a superconducting wire (tinplated constantan) passed into the measuring chamber through the platinum-glass joints 13-15.

2.3.2.3. Emitter

The circular (15 mm in diameter) and rectangular ($10 \times 11 \text{ mm}^2$) X-cut quartz plates were used to emit acoustic waves



(a)



(b)

Fig. 2.9. Sound source and sample. (a) Piezoelectric quartz transducer: 1—bronze cylinder, 2—three contact springs, 3—paper spacer, 4—stage, 5—screw, 6—piezoelectric quartz plate, 7—contact spring, 8—sound absorber, 9—insulator, 10—support disk. (b) Sample holder: 1—sample, 2, 3—thermometers, 4—electrical leads, 5—epoxy resin, 6—double frame, 7—textolite spacers, 8—nuts, 9—screw.

at 10, 20, and 30 MHz. The homogeneity of acoustic radiation was of a special concern. To ensure this, the characteristics of the quartz transducers were investigated by electronic and optical techniques.

The quartz plates having the best frequency characteristics both at room and helium temperatures were selected. At room temperature, the radial distribution of the intensity of the acoustic beam and its angular divergence in water and toluene were investigated by dark field technique. The travelling and standing waves that resulted from the addition of a direct wave and that reflected from the surface at a small angle were photographed for this purpose.

When the acoustic radiation is homogeneous, the image of the travelling waves (viewed as dome-shaped because of the attenuation in liquid) remains unchanged during quartz rotation. The interference pattern for standing waves is a system of parallel fringes. Deviation from parallelism indicates that the acoustic beam is diverged. At the fundamental frequency of 10 MHz, the best quartz plates ensured that at room temperature the divergence of the beam in water and toluene fitted the diffraction limit value, $\lambda/d = 36'$, within accuracy limits.

The quartz characteristics were found to be influenced strongly by the way the quartz was clamped. When the mechanical contact between the quartz plate and the holder is minimal and the plate emitted sound freely in the liquid, the efficiency is maximal (50%), thereby the frequency response in liquid helium is insignificantly distorted. Fig. 2.9a shows the quartz emitter and its mounting. The quartz plate 6 with thin-film gold electric contacts deposited on both sides, lies freely on a polished circular stainless steel table 4 with a central hole copying the plate's shape yet having slightly smaller dimensions. The plate is isolated from the table by a ring-shaped paper spacer 3. The upper and lower electrical contacts were established by light phosphor-bronze springs 2 and 7 whose wire diameter was 70 μm . The upper springs were soldered into a thin-walled bronze cylinder 1 that was slipped over the table.

The quartz plate emitted in both directions. The down part of the acoustic radiation was absorbed by the sintered copper filter 8.

2.3.2.4. Samples

The measurements were performed with two samples: a polycrystalline gold piece and a tungsten single crystal having the ratio of the electrical resistances at room and helium temperatures of $r_{300}/r_{4.2} = 36\,000$ for gold, and 64 000 for tungsten. The gold sample was a parallelepiped $13 \times 10 \times 1.9$ mm in size and was shaped by rolling followed by flattening in a press between polished quartz plates. The tungsten single crystal 1 in Fig. 2.9b was a circular disk 8.6 mm in diameter and 1.5 mm thick. The normal to the face electro-polished disk surface made angles of 23 and 30° with the axes [100] and [101], respectively. The surface quality of the samples was checked with a Linnik interferometer and it was

found that the surface irregularities and deviations from a planar surface did not exceed $0.5 \mu\text{m}$ for gold and $0.3 \mu\text{m}$ for tungsten.

Carbon and germanium thermometers were soldered on the gold, with one contact to the narrow strips ($d \simeq 0.2 \text{ mm}$) separated from the edge of the sample by spark machining. Similar thermometers 2 and 3 were bonded to the rear surface of the tungsten single crystal by an electrically conductive adhesive. Direct contact of these thermometers with liquid helium was eliminated by coating them with epoxy resin mixed with quartz powder 5. The samples were insulated from the contact with the frame 6 by means of the bakelite spacer 7.

2.3.2.5. Pickups

The semiconductor resistance thermometers which were in good thermal contact with the sample served as indicators of the energy absorbed in the sample.

Since the contact thermal resistance between two solids is much less than that between liquid helium and a solid body, the thermometers and the samples were in thermal equilibrium with one another.

Carbon and germanium thermometers with identical characteristics were used, whose resistances at $T < 1 \text{ K}$ were nominally between 10^3 and $10^6 \Omega$ and whose sensitivity ranged from 10^{-4} to $10^{-7} \text{ K}/\Omega$. The temperature dependence of the electrical conductivity was either exponential or sometimes in the form of a power law.

The carbon thermometers [2.30] were shaped like disks (3 mm in diameter and 1 mm thick) whose end surfaces carried electrolytic copper contacts. The germanium thermometers [2.31] were made from originally pure single-crystal germanium doped by neutron irradiation. They were shaped like $1 \times 1 \times 1 \text{ mm}$ cubes with alloyed indium contacts.

In order to measure the temperature in the liquid, the thermometers were used which were made from the same material and taken from the same batch as the thermometer attached to the sample. Both thermometers, T_1 and T_2 , were calibrated against magnetic susceptibility of cerium-magnesium nitrate and ^3He vapor pressure. The thermometer on the sample was also calibrated against the thermometer in liquid after every experimental record of $\Delta T(\theta)$.

Thermometer resistance was measured by ac bridges (Fig. 2.10) at frequency of 237 Hz , and with voltages of $6-60 \mu\text{V}$ across the thermometers corresponding to dissipation of $10^{-14}-10^{-12} \text{ W}$. The absolute temperatures of the liquid and the sample were measured accurate to 10^{-3} K and the difference between them was found to within 10^{-5} K . The rise of the temperature of the thermometers due to the flow of the measuring current did not exceed $5 \times 10^{-7} \text{ K}$.

2.3.2.6. Measurement of Angles

A capacitor with $C = 10-20 \text{ pF}$ together with an inductance coil with $L = 450 \mu\text{H}$ (the number of turns, $n_1 = 400$) formed an oscillatory circuit resonant at 1.3-1.7 MHz. In order to stabilize the inductance value, the coil was placed inside the cryostat vacuum jacket and had a thermal contact with the mixing chamber.

A secondary winding ($n_2 = 2-3$ turns) wound on the induction coil was connected via a coaxial cable to a noninverting input of a broad-

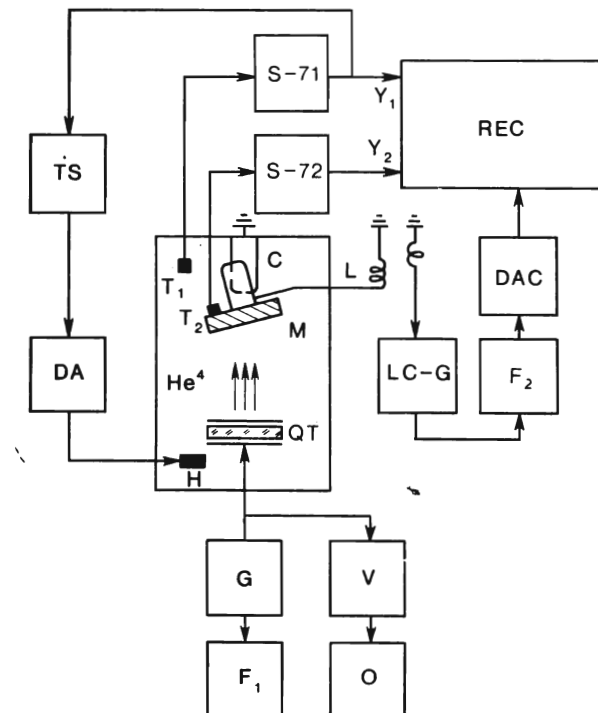


Fig. 2.10. Circuit diagram of the apparatus: G—an oscillator supplying the quartz transducer QT, F_1 —frequency meter, V —voltmeter, O —oscilloscope, TS—temperature stabilizer, DA—digital ammeter, S-71 and S-72—ac bridges, L—inductor, LC-G—oscillator for the angle-of-rotation tensor, F_2 —frequency meter for LC-generator, DAC—digital-analog converter, REC— X - Y two-pen recorder.

band amplifier with positive feedback. The amplifier was mounted on the cryostat cover and together with the resonance circuit made up an LC-oscillator.

At the resonance frequency the secondary winding is equivalent to an oscillatory circuit having the inductance of L/n^2 and capacity

Cn^2 , where $n = n_1/n_2$. Since the equivalent capacity Cn^2 is large, the instability in the capacitance of the connecting cable influenced the oscillator parameters only slightly.

The LC-oscillator frequency was measured with a frequency meter accurate to 1 Hz. This provided a sensitivity in the determination of the rotation angle measurements of the order of 1".

2.3.2.7. Temperature Stabilization of ^4He Bath

The first experiments already demonstrated that the liquid helium temperature in a measuring chamber did not remain constant. When rotating the sample, a monotonic increase in liquid helium temperature by 10^{-4} - 10^{-2} K in addition to a temperature drift was observed depending on the rate of frame motion. Along with it, there were also random temperature fluctuations of the same order of magnitude caused by various reasons. The major one being shocks and vibrations of the springs in the rotation system, as well as vibrations of the solution cryostat itself.

The first observations of the gold sample had shown that the acoustically induced increase in the temperature of the sample did not exceed 1 mK, and it was quite evident that the temperature of the liquid in the measuring chamber needed to be stabilized. For this purpose, a system was introduced to stabilize the temperature against the signal amplitude and its two derivatives [2.32].

2.3.3. Experiment

By pumping helium vapor from the external bath the system was cooled to ~ 1.3 K, when ^4He was condensed into the measuring chamber. Then, the condensation line was shut off by the valve in the cover for the duration of the experiment and the continuous action solution cryostat was turned on.

When the temperature was less than 0.1 K, the quartz transducer (Fig. 2.10) was subjected to an ac voltage from the quartz oscillator G. The ^4He temperature was slightly increased. When the oscillator was tuned to the resonance frequency of the quartz transducer, the voltage amplitude across the transducer was kept fixed by the voltmeter V. Frequency and waveform of the oscillator voltage were checked by the frequency meter F_1 and the oscilloscope O.

The temperature stabilizer TS then was switched on. The required temperature, T_0 , was set by adjusting a current through the heater H in the liquid ^4He bath. The digital ammeter DA followed the stabilizer operation. While the quartz transducer continuously emitted sound the angle θ was slowly varied and the resistances of the thermometers T_1 and T_2 which were measured by the ac bridges S-71 and S-72 were recorded simultaneously with an XY two-pen recorder as a

function of angle of incidence of the sound. In order to do this, the recorder's X -coordinate was supplied by a voltage proportional to the angle θ from the output of a digital-analog converter DAC. The latter was, in turn, connected to the frequency meter F_2 that measured the LC-oscillator frequency. The inputs Y_1 and Y_2 of the recorder were the voltages supplied by the outputs of the bridges.

2.3.4. Results of Measurements at $T > 0.2$ K

2.3.4.1. Gold

The technique was tested and the first measurements were performed on a gold sample. The measurements were carried out without temperature stabilization in the first version of the

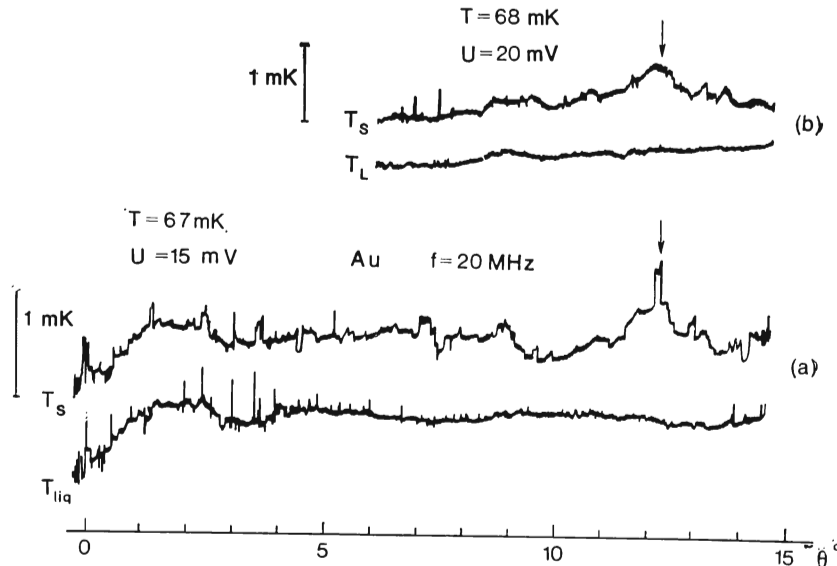


Fig. 2.11. Records of the temperature of the gold sample T_s and of the temperature of liquid ^4He T_{liq} , versus the angle of incidence of sound at different bath temperatures: a) $T = 67$ mK and b) $T = 68$ mK (without bath temperature stabilization). The frequency of sound $f = 20$ MHz, U is the voltage across the quartz transducer. The arrows are located over Rayleigh peaks.

system where the angle could be varied from 0 to 20° only in one direction away from the normal. The quartz emitter ensured that the frequency was 20 MHz. Two identical carbon thermometers were chosen as T_1 and T_2 .

In the absence of sound, when the sample was rotated at a constant velocity, both thermometers indicated the same monotonic temperature rise. It depended on the rotational velocity of the sample and initial temperature drift.

With an acoustic wave incident on the sample, the angular dependence curve of the sample temperature exhibited a peak $\Delta T \simeq 0.5$ mK (Fig. 2.11) at $\theta \sim 12.5^\circ$. The peak was not detected by the thermometer immersed in liquid. After multiple passages through this angle it was established that the peak corresponded to a maximum absorption of sound at this angle of incidence, since the peak was recorded in different experiments and at different temperatures.

An analysis of the curves presented in Fig. 2.11 shows that even at very slow rotation of the sample the temperature of the liquid is constant only within 10^{-4} - 10^{-3} K. At angles ranging from 0 to 6° the sample's temperature follows the temperature of the liquid and only at large angles starts to deviate, achieving a maximum at 12.5° , and then falling again.

Thus, the experiments with gold demonstrated that when the angle is close to the critical one ($\theta_2 = 12^\circ 12'$) the incident sound overheats a sample in a way that can be attributed to absorption of Rayleigh waves.

2.3.4.2. Tungsten

A tungsten single crystal was chosen because of its high purity as well as for the isotropy in the velocity of sound which is practically observed.

Sound was excited at frequencies of 10 and 30 MHz (fundamental and third harmonics, with the exact values 9.61 and 28.83 MHz). Two identical germanium thermometers were used to measure temperature.

The angle of incidence of the acoustic wave was varied continuously from -20° to $+20^\circ$. As in the first version of the system, rotation of the frame that held the sample resulted in a monotonic liquid heating.

Turning on the stabilizer suppressed the temperature drift and fluctuations down to 1.5×10^{-5} K. When the stabilizer could not suppress these fluctuations totally, the residual fluctuations were detected simultaneously by the two thermometers, one in the liquid and the other at the solid. Therefore, the irregularities on the signal curve could be eliminated by comparing the two records, viz. those of the sample and the liquid temperatures.

Figure 2.12 shows a typical record of $T_1(\theta)$ and $T_s(\theta)$ separately for the negative (a) and positive (b) angles θ , where the stabilized temperature of the liquid is $T = 0.282$ K, the sound frequency is 10 MHz, and the effective voltage across quartz transducer is equal

to 260 mV. The recording was directed from $-\theta$ to zero (a) and later on, from zero to $+\theta$ (b). Because of nonparallelism between the frame and sample planes, the θ zero drift from the origin appeared to be by $+1.5^\circ$. As it can be seen from the record, the temperature of

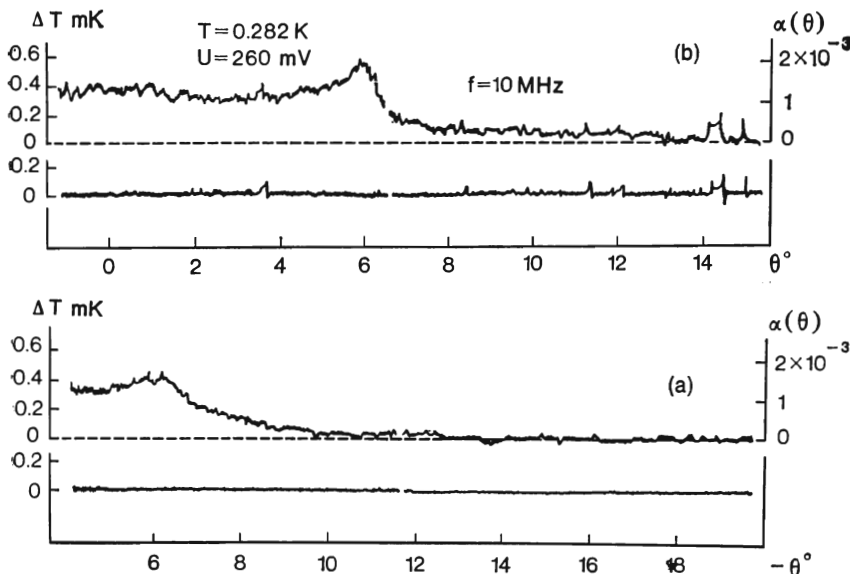


Fig. 2.12. Typical records of the temperature rise of the sample of tungsten due to the incidence of sound (upper curves a and b) and of the temperature of liquid ${}^4\text{He}$ (lower curves a and b) separately for the negative (a) and positive (b) angles θ . The stabilized liquid helium temperature $T = 0.282$ K, voltage across quartz transducer $U = 260$ mV. The frequency of sound $f = 10$ MHz. The scale on the right stands for the transmission coefficient, $\alpha(\theta) = w(\theta) \cos \theta$.

the sample increased by $\Delta T \simeq 0.5$ mK above the temperature of the liquid helium only within the range of angles of incidence $\delta\theta = \pm 6^\circ$. For $\theta = \pm 6^\circ$ the temperature rise is maximal, while outside this angular range it drops strongly, and then vanishes at $\theta \geq 13^\circ$.

Later on, the recorded interval was limited by the angular range, where the acoustically induced temperature rise of the sample had nonzero level. All experimental records presented below are given after matching the curves a and b (Fig. 2.12) with a due regard for zero drift. The acoustically induced temperature rise of the sample was calibrated against the liquid helium thermometer. Toward this end, after finishing a record and switching off the ultrasonic emitter, two stabilized temperatures in liquid helium were consecutively established such that the sample thermometer readings

corresponded to the temperatures before and after switching on the ultrasonic emitter.

Figures 2.13-15 display typical records of the acoustically induced rise of the temperature of the sample versus the angle of incidence

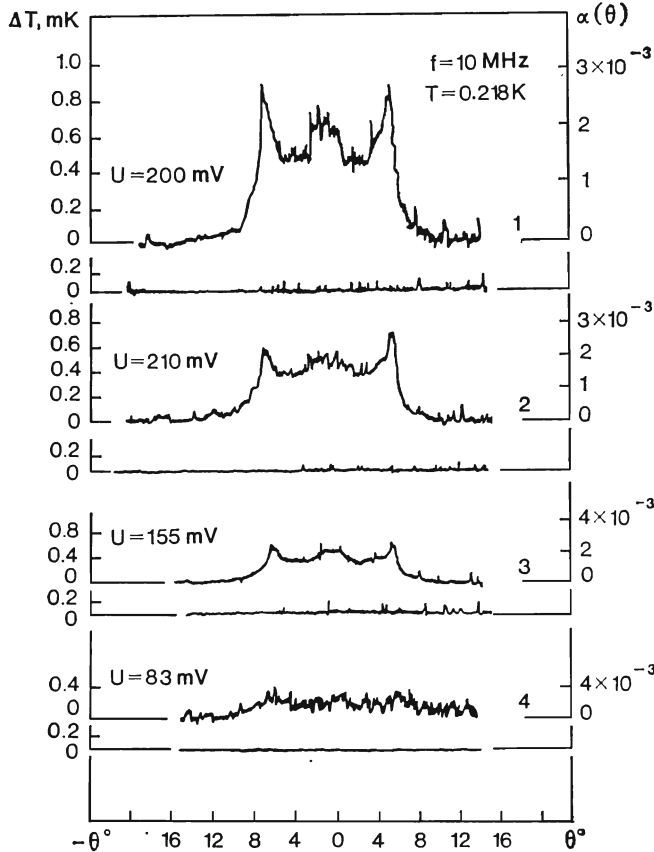


Fig. 2.13. Records of the temperature rise of the sample of tungsten due to the incidence of sound (upper curves) and of the temperature of liquid ${}^4\text{He}$ (lower curves) versus the angle of incidence of sound. The bath temperature $T = 0.218 \text{ K}$, the frequency of sound $f = 10 \text{ MHz}$, U is the voltage across quartz transducer. The scale on the right stands for the transmission coefficient. The time needed to obtain one record was $\sim 30 \text{ min}$.

of sound of frequencies 10 and 30 MHz at temperatures 0.2-0.4 K for different acoustic radiation powers which are proportional to the square of the effective voltage U^2 applied to the quartz transducer. The most characteristic curves for 30 MHz are depicted in Fig. 2.16.

In the plots the temperature rise of the sample ΔT in mK above the ${}^4\text{He}$ temperature is drawn to the left of the ordinate axis. To the right, the transmission coefficient of sound, $\alpha(\theta) = w(\theta) \cos \theta$ is drawn (the multiplier $\cos \theta$ takes into account the angular variation in the energy flux incident on the sample; at the angle of 6° the difference between α and w is less than 0.5%, whereas at the angle

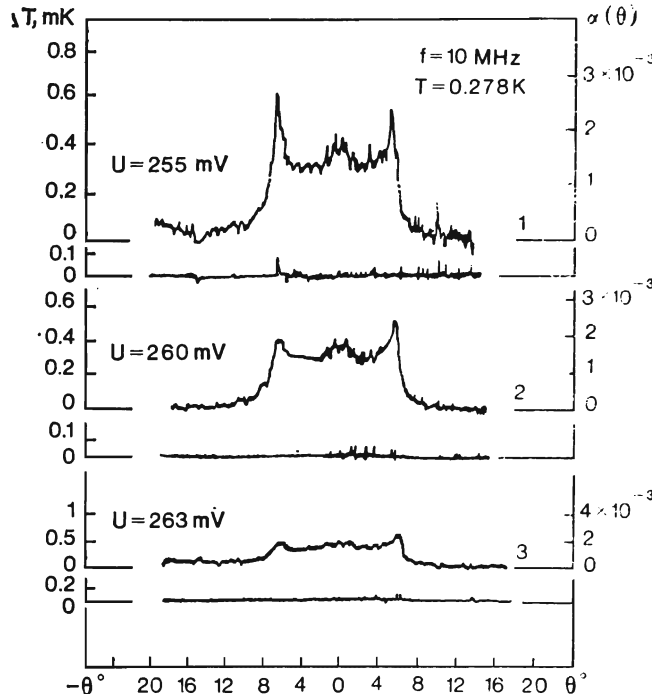


Fig. 2.14. Records of the temperature rise of the sample of tungsten due to the incidence of sound (upper curves) and of the temperature of liquid ${}^4\text{He}$ (lower curves) versus the angle of incidence of sound at the bath temperature $T = 0.278\text{ K}$ and the frequency of sound $f = 10\text{ MHz}$. U is the voltage across quartz transducer. The scale on the right stands for the transmission coefficient. The time needed to obtain one record was $\sim 30\text{ min}$.

of 15° , it is $\sim 3\%$). The value of $\alpha(\theta)$ was calculated from ΔT values after being normalized to zero angle. The value of $\alpha(0) = w(0)$, according to the acoustic formula (2.12), was taken to be

$$\alpha(0) = \frac{4\rho c D c_1}{(\rho c + D c_1)^2} \simeq \frac{4\rho c}{D c_1} = 1.4 \times 10^{-3} \quad (2.47)$$

The records were taken on different days of the continuous fortnight experiment without heating the sample. After the sample was

heated to liquid nitrogen temperature (accompanied by the evaporation of ${}^4\text{He}$ from the measuring chamber) and the ${}^4\text{He}$ was condensed again, the picture was somewhat changed, viz. the sample temperature rise at normal sound incidence was less and Rayleigh

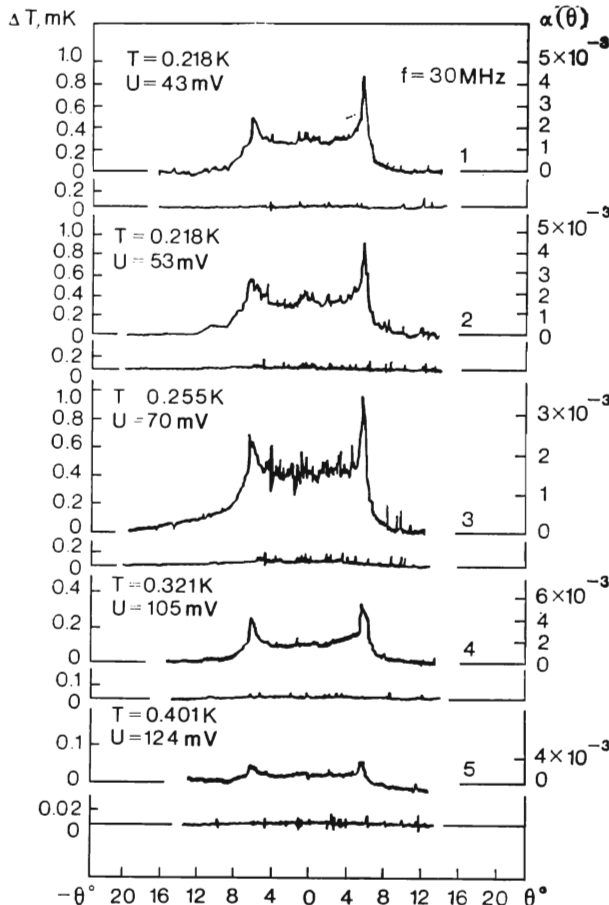


Fig. 2.15. Records of the temperature rise of the sample of tungsten due to the incidence of sound (upper curves) and of the temperature of liquid ${}^4\text{He}$ (lower curves) versus the angle of incidence of sound at the different bath temperatures and at the frequency of the sound $f = 30$ MHz. U is the voltage across quartz transducer. The scale on the right stands for the transmission coefficient. The time needed to obtain one record was $30 \sim \text{min}$.

peaks decreased. This could be a result of the sample surface being contaminated by condensed gases.

The records of the temperature rise of a tungsten single crystal by ultrasonic irradiation enabled the effective Kapitza resistance for the given sample to be estimated:

$$R_K = \frac{\Delta T s_0}{\dot{Q}} \quad (2.48)$$

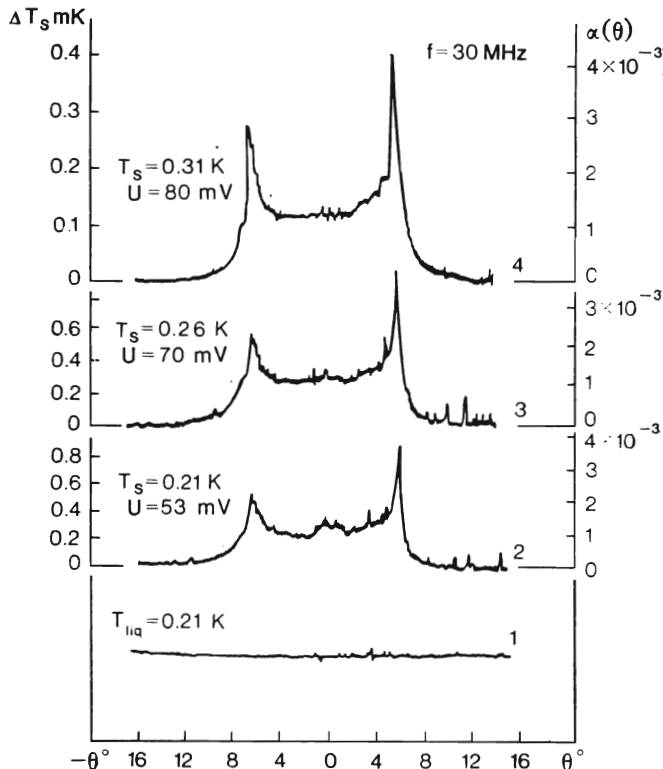


Fig. 2.16. Records of the temperature rise of the sample of tungsten due to the incidence of sound at the frequency $f = 30$ MHz and at three temperatures: $T = 0.21$ K (curve 2), $T = 0.26$ K (curve 3), and $T = 0.31$ K (curve 4) versus the angle of incidence of sound. U is the voltage across quartz transducer. The scale on the right stands for the transmission coefficient. Curve 1 is the record of the liquid ${}^4\text{He}$ temperature, $T_{\text{liq}} = 0.21$ K.

Here ΔT is the temperature rise of the sample, s_0 is the total sample surface area, \dot{Q} is the power absorbed by the sample, viz.

$$\dot{Q} = \dot{Q}_1 w(\theta) \quad (2.49)$$

where \dot{Q}_1 is the power of an acoustic wave incident on the sample surface and $w(\theta)$ is the transmission coefficient of the acoustic energy crossing the interface. For tungsten at normal incidence, according to (2.47), $w(0) = 1.4 \times 10^{-3}$.

The power \dot{Q}_1 was determined in the following way. The total power dissipated by the quartz transducer, \dot{Q}_0 , was calculated in terms of a quantity that should be subtracted from the power H

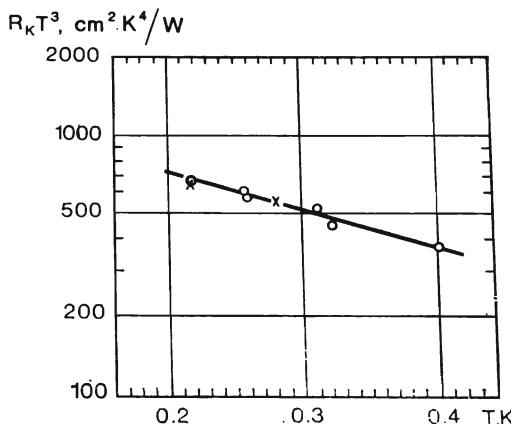


Fig. 2.17. $R_K T^3$ (for ${}^4\text{He}$ -tungsten) from the measurements of the transmission coefficient of sound across a liquid helium-metal interface: \circ —30 MHz, \times —10 MHz.

of the heater for the helium bath such that the bath temperature remained unchanged when the transducer was switched on.

The efficiency of the quartz transducer in liquid helium was found by measuring the temperature dependence of its Q -factor within the temperature range 1.5-4.2 K.

If the quartz transducer efficiency is $\sim \frac{1}{2}$, while it emits in both directions, then the acoustic power incident on the sample surface is equal to

$$\dot{Q}_1 = \frac{1}{4} \frac{\sigma_0}{s_{\text{qu}}} e^{-0.23\gamma_1 L} \dot{Q}_0 \quad (2.50)$$

Here s_{qu} is the emission surface of the quartz plate, σ_0 is the surface area on which sound is incident, L is the distance between the quartz plate and the sample (0.95 cm), γ_1 is the absorption coefficient of the acoustic energy in helium (dB/cm) [2.33].

When calculating R_K the following experimental values were used:

$$\dot{Q}_0 = 3.08 \times 10^{-9} (U)^2 \text{ W (at 10 MHz)}$$

$$\dot{Q}_0 = 2.93 \times 10^{-8} (U)^2 \text{ W (at 30 MHz)}$$

$$s_{\text{qu}} = 1.77 \text{ cm}^2, \quad \sigma_0 = 0.5 \text{ cm}^2, \quad s_0 = 1.57 \text{ cm}^2$$

U was measured in mV.

The results of evaluating R_K (${}^4\text{He-W}$) are illustrated in Fig. 2.17, where $R_K T^3$ is somewhat decreased with the temperature rise, this being characteristic for pure samples within the above temperature range [2.34]. The mean value at $T \simeq 0.2\text{ K}$, $R_K T^3 = 650 \text{ cm}^2 \text{ K}^4/\text{W}$, corresponds to the effective attenuation parameter for thermal phonons in tungsten calculated from (2.37), $p = 5 \times 10^{-2}$. The value of $R_K T^3$ is close to that found by Folinsbee and Anderson [2.35] for the tungsten samples polished, electropolished, and annealed in hydrogen.

2.3.5 Results of Measurements at $T < 0.2 \text{ K}$

In order to achieve a lower temperature in the solution cryostat, the tube heat exchanger was substituted by a more efficient

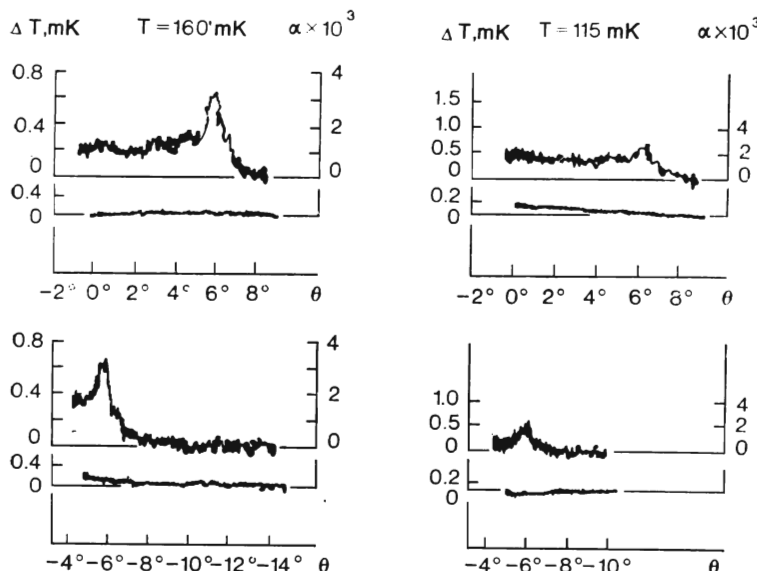


Fig. 2.18. Records of the temperature rise of the sample of tungsten due to the incidence of sound (upper curves) and of the temperature of liquid ${}^4\text{He}$ (lower curves) versus the angle of incidence of sound with the frequency $f = 30 \text{ MHz}$ at two bath temperature: 160 and 115 mK. The scale on the right stands for the transmission coefficient.

one, whose surface was more developed. In addition, the heat supply to the measuring chamber was reduced by limiting power which was dissipated in the angular pickup.

The typical results of measuring $\Delta T(\theta)$ within 60-160 mK for tungsten at frequency of 30 MHz are given in Figs. 2.18-20.

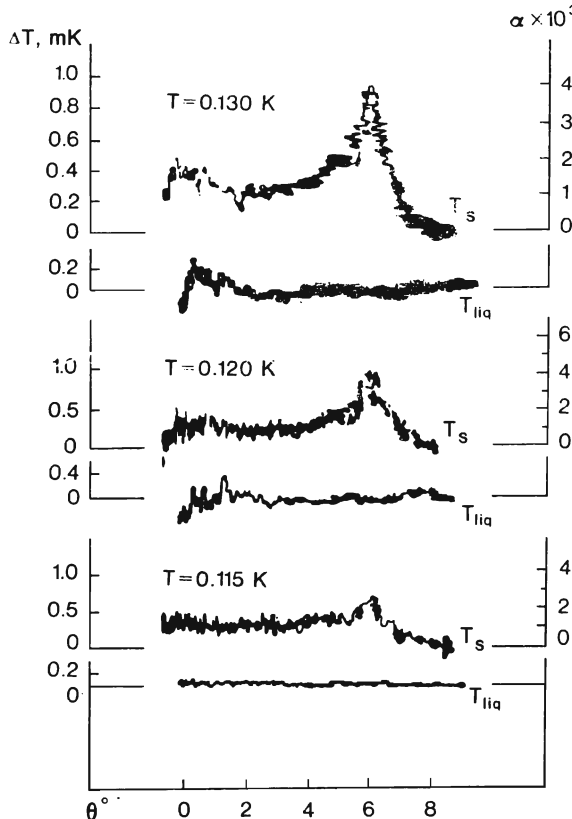


Fig. 2.19. Records of the temperature rise of the sample of tungsten due to the incidence of sound T_s and of the temperature of liquid ${}^4\text{He}$, T_{liq} versus the angle of incidence of sound (positive one) with the frequency $f = 30$ MHz at three temperatures: 115, 120, and 130 mK. The scale on the right stands for the transmission coefficient $\alpha \times 10^3$.

Fig. 2.18 shows synchronous records of the temperature rise both of the sample and liquid helium bath due to the incidence of sound plotted as a function of θ for two values of the bath temperature. The records are given for the positive and negative θ angles, when the liquid helium temperature being stabilized (within 3×10^{-6}

10^{-4} K). The scale on the right applies to the transmission coefficient of sound $\alpha(\theta)$, which is normalized at $\theta = 0$.

The same kind of records are given at fixed temperatures in Figs. 2.19 and 2.20 when the angles of incidence are positive. A rise in temperature of the solid near $\theta = 0$ in Fig. 2.20 is due to a heating of liquid helium induced by a motion of the frame. This effect was

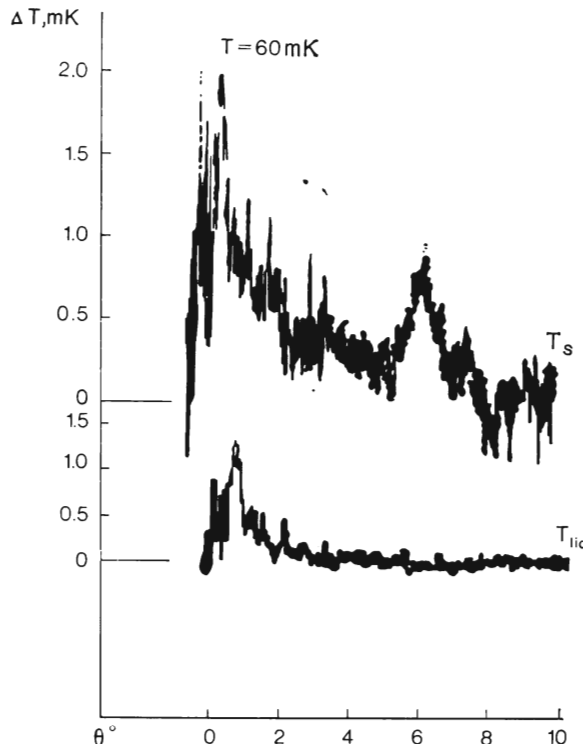


Fig. 2.20. Records of the temperature rise of the sample of tungsten due to the incidence of sound T_s and of the temperature of liquid ${}^4\text{He}$ T_{liq} versus the angle of incidence of sound (positive one) with the frequency $f = 30$ MHz at $T = 60$ mK.

not compensated by the stabilizer at the lowest temperature. As earlier, the records demonstrate the temperature rise of the sample which is induced by sound only in the immediate vicinity of the angle of normal incidence. At $\theta = \pm 6^\circ$ one clearly sees the maxima of the temperature rise of the solid above the temperature of the liquid helium bath. What is typical is that the Rayleigh peaks for $\theta = +6^\circ$ and -6° have the same height and the widths at midheight up are also the same ($\sim 30'$).

2.3.6. Discussion of Experimental Curves. Evaluation of Errors

In the present work a detailed investigation was made of the transmission of sound across the liquid helium-tungsten interface. The experiments with gold were performed in order to test technique and indicate qualitatively the generality of the phenomena at hand.

It follows from the experimental curves (Figs. 2.13-16 and 2.18-20) that acoustic phonons pass from liquid helium into a solid only in a narrow range of angles near normal incidence. At $\theta \geq 2\theta_R$ ultrasonically induced increase in the temperature of tungsten is absent and hence in this range phonons are totally reflected by the interface.

At $\theta = \pm 6^\circ$ there are sharp maxima of the temperature rise which are more pronounced at the sound frequency 30 MHz. The maxima correspond to the Rayleigh angle of incidence θ_R (the value of this angle $\theta_R = 5.2^\circ$ which is calculated from (2.22) and (2.39) agrees with the experimental angle within the limits of the measurement error). The peaks observed at $\theta \simeq 6^\circ$ are similar to the anomalies which appear in the experiments with gold at the angle of about 12.5° . Since the maxima are symmetric relative to the normal for both studied frequencies at both temperatures and lie within the range of angles of total internal reflection ($\theta_R > \theta_2 \simeq 4.8^\circ$), their appearance could be related to an increase in the energy transmission caused by the absorption of the Rayleigh surface waves resonantly excited by the incident acoustic wave. Figure 2.13 shows that the effect is linear, viz. the temperature rise of sample ΔT is proportional to the power of the incident acoustic wave U^2 .

Let us note two features of the experimental $\alpha(\theta)$ curves. The first is that at the frequency 30 MHz and $T > 0.2$ K the Rayleigh peaks at $-\theta_R$ and $+\theta_R$ differ in height, whereas at $T < 0.2$ K and for the curves at the frequency of 10 MHz they are usually equal. This might be connected with an inhomogeneous distribution of the intensity across the acoustic beam [2.28], with the inhomogeneity increasing on increase in the attenuation of sound in helium. If the acoustic beam axis does not coincide with the symmetry center and the rotation axis of the sample, then the total energy of the acoustic wave incident on the sample will be different at $-\theta_R$ and $+\theta_R$, and this fact may be responsible for the different heights of the resonance peaks. The stronger is the attenuation the greater the difference is, viz. it rises both with frequency and temperature. Within the collisionless region of liquid helium ($T < 0.2$ K), where the attenuation of sound on thermal phonons is practically absent, the heights of the Rayleigh peaks at positive and negative angles are equal.

The second feature is the presence of small maxima at $\theta = 0$ which arise only at low temperatures ($T \leq 0.2$ K) and are stronger at 10 MHz. This is due, perhaps, to the amplification of the energy of sound incident on the interface at $\theta = 0$ because of its repeated reflection between the quartz transducer and the sample. The effect increases when the attenuation in the liquid reduces, i.e. when the temperature and frequency are lowered.

The experimental curves in Figs. 2.13-16 and 2.18-20 were reproducible in the course of experiments.

Let us estimate the errors of the experimental data.

In recording the $\Delta T(\theta)$ curves, the voltage across the quartz plate was constant to within 2%. The relative error in the determination of ΔT and, therefore, α was mainly dependent on the accuracy in maintaining the bath temperature ($1.5 \cdot 10^{-5} - 10^{-4}$ K). Within the range of 0.2-0.4 K, this error varied from 2 to 10% for the Rayleigh angles and from 5 to 20% for the subcritical angles. The absolute temperatures of the liquid and the sample were measured to within 10^{-3} K. The reproducibility of Rayleigh maxima positions for all curves was accurate to one minute of arc. The absolute value of an angle was calculated to within 10% from geometric considerations.

2.3.7. Calculations Using the Generalized Acoustic Theory

2.3.7.1. Tungsten

The transmission coefficient of the acoustic energy from the liquid to the solid is determined by densities, sound velocities in both media, and parameters of the attenuation in the solid according to Eqs. (2.29), (2.35), and (2.36), respectively.

Figure 2.21 demonstrates the curves of $\alpha(\theta) = w(\theta) \cos \theta$ which are computer-calculated by applying the above formulas to a liquid ^4He -tungsten interface at some fixed values of $p = p_1 = p_t$. The following numerical parameters were used in these calculations: $\rho = 0.145 \text{ g/cm}^3$; $D = 19.4 \text{ g/cm}^3$; $c = 2.4 \times 10^4 \text{ cm/s}$; $c_1 = 5.11 \times 10^5 \text{ cm/s}$; $c_t = 2.88 \times 10^5 \text{ cm/s}$.

It is clear from the plots that there are three critical angles of incidence: $\theta_1 = 0.047$, $\theta_2 = 0.088$, and $\theta_R = 0.09049$, at which the curve $\alpha(\theta)$ has singularities. The angles θ_1 , θ_2 , and θ_R are determined from (2.14) and (2.22). In the absence of attenuation in the solid ($p = 0$) there is no Rayleigh peak [Fig. 2.21 (a)]. Certainly, in this case Rayleigh waves can be induced on the metal surface, but they transmit their energy only to the liquid [2.36, 2.18].

In the presence of the absorption in the solid ($p > 0$), the curve $\alpha(\theta)$ has a Rayleigh peak whose height and width both depend on p . This is due to the fact that the attenuation coefficient of a

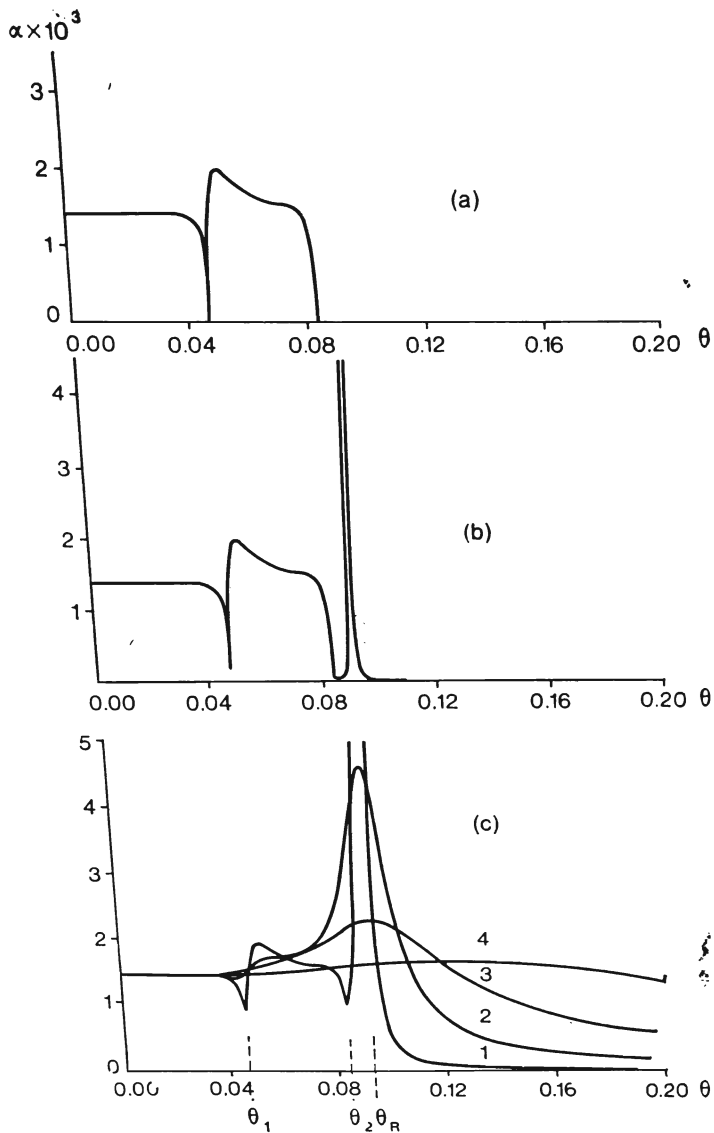


Fig. 2.21. Calculated dependence of the energy transmission coefficient of a plane monochromatic acoustic wave on the angle of incidence θ on the ${}^4\text{He}$ -tungsten interface at different attenuation parameters of sound in tungsten, p : (a) $p = 0$, (b) $p = 3 \times 10^{-4}$, (c) $p = 10^{-2}$ (curve 1), $p = 10^{-1}$ (curve 2), $p = 0.3$ (curve 3), $p = 1$ (curve 4).

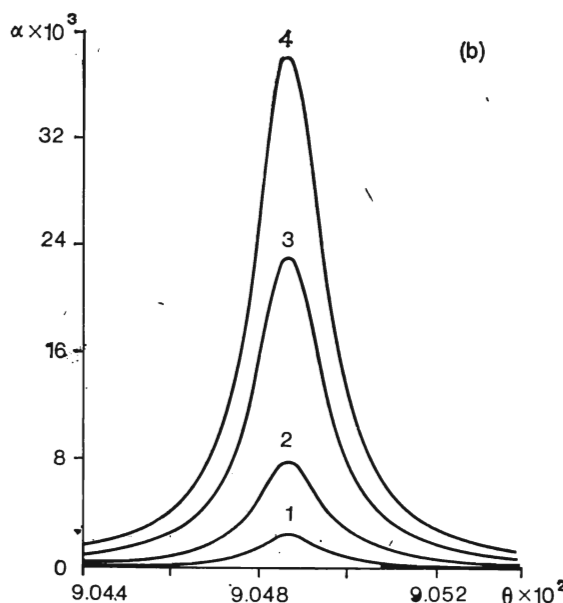
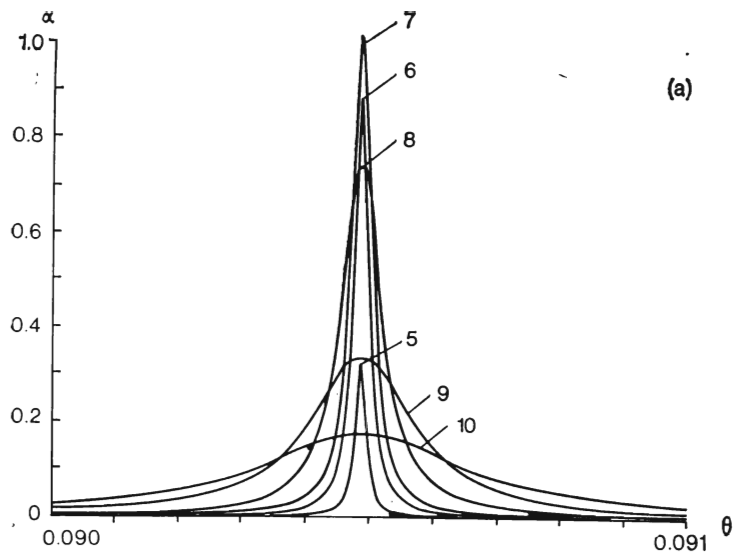


Fig. 2.22. Calculated dependence of the energy transmission coefficient of a plane monochromatic acoustic wave on the angle of incidence on the ${}^4\text{He}$ -tungsten interface in the vicinity of Rayleigh peak for different attenuation parameters: 1— $6 \cdot 10^{-8}$, 2— 2×10^{-7} , 3— 6×10^{-7} , 4— 1×10^{-6} , 5— 1×10^{-5} , 6— 5×10^{-5} , 7— 1×10^{-4} , 8— 3×10^{-4} , 9— 1×10^{-3} , 10— 1.9×10^{-3} .

Rayleigh wave travelling in a surface layer $\sim \lambda$ thick is controlled by the attenuation coefficients of bulk waves, mainly, the attenuation of the transverse wave (Fig. 2.4) [2.18, 19].

Figure 21 (b) evidences the dependence $\alpha(\theta)$ at $p = p_1 = p_t = 3 \times 10^{-4}$ (this value of p corresponds to the absorption coefficients of ultrasound for tungsten at 30 MHz amounting to $\gamma_1 = 1$ dB/cm and $\gamma_t = 1.7$ dB/cm which were obtained by extrapolating the results of measurements reported in Refs. [2.37, 38]).

The Rayleigh peak in Fig. 2.21 (b) has the height $\alpha_R = \alpha(\theta_R) = 0.74$ and the width at midheight $\delta = 7.55 \times 10^{-6}$ rad = 15". The minimal values of α at the angles θ_1 and θ_2 are no longer equal to zero.

Fig. 2.21 (c) shows the $\alpha(\theta)$ curves for high values of p .

It is seen from Fig. 2.21 that in the presence of absorption of sound in a solid, the character of the curves changes significantly for the angles $\theta > \theta_2$, whereas at $\theta < \theta_2$ the change in α is not so large.

The curves in Fig. 2.22 illustrate the process of the Rayleigh peaks appearance, starting from negligible but finite attenuations $p \neq 0$. The figure shows that these peaks are typical of resonance curves whose parameters (width and height) are controlled by attenuation. At small values of p the curves are symmetric. The total transmission at the Rayleigh angle [$\alpha(\theta_R) = 1, w(\theta_R) = 1$] for the liquid ^4He -tungsten system takes place at $p = 10^{-4}$ (curve 7). At the lower values of p the amplitude and the area under the Rayleigh peak both rapidly decrease, but at $p > 10^{-4}$ the amplitude decreases whereas the area increases. For very large values of p the $\alpha(\theta)$ curves are no longer of the resonance type.

The height α_R and width δ of the Rayleigh peak are plotted in Fig. 2.23 as a function of p . What is typical is that at very low values of p ($< 10^{-5}$) α_R rises linearly with p , whereas the peak width is approximately constant and equal to $\delta_0 = 1.8 \times 10^{-5} = 4"$.

The calculated integral of the transmitted energy of a plane wave,

$$J = \int_0^{\pi/2} \alpha(\theta) d\theta \quad (2.51)$$

is presented in Fig. 2.24 versus p . Here the level noted by dashed line on the ordinate corresponds to the energy transferred into a solid only in the form of transverse and longitudinal waves incident at a subcritical angle ($p = 0$). An increase in the attenuation produces a rise in the total energy integral and the inflection point of the curve (a maximum of the derivative) corresponds to $p = 10^{-4}$, when the transmission coefficient α at the Rayleigh angle is equal to unity.

Figure 2.24 shows that if we eliminate the regions of very large and very small values of p , we find that the contribution of the surface

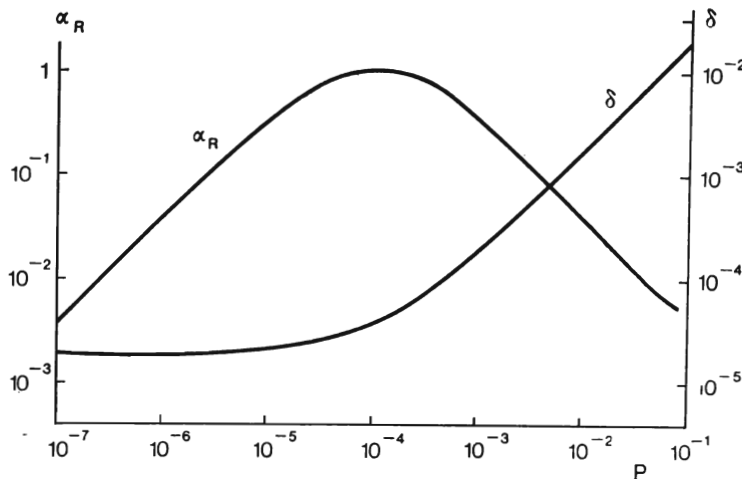


Fig. 2.23. Calculated dependences of the height α_R and width δ of the Rayleigh peak in tungsten on the attenuation parameter p .

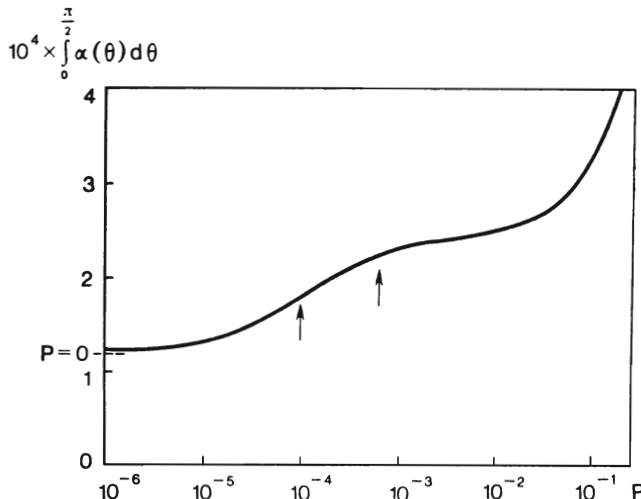


Fig. 2.24. Calculated dependence of the energy integral J of the transmitted acoustic energy from ${}^4\text{He}$ into tungsten on the attenuation parameter p . Arrows indicate the limits of the integral variations for the experimental curves $\alpha(\theta)$ and p 's corresponding to these limits.

waves into the energy integral is approximately equal to that of the bulk waves. A marked increase in the integral is observed when p approaches unity. However, when the attenuation is so strong, the process is no longer of the wave type. The sound incident from the liquid excites only the perturbations which were transmitted.

At very weak attenuation ($p < 10^{-5}$), the contribution of the Rayleigh waves is small amounting to only a few percent of the contribution of the bulk waves.

2.3.8. Comparison of Experimental Data with the Generalized Acoustic Theory

2.3.8.1. Tungsten

When comparing experimental and calculated curves for tungsten (Figs. 2.21, 22), the following difficulty was encountered. It was impossible to fit the height and width of the calculated curves to the Rayleigh peaks.

The value of p suitable for the width of the peaks was $(3.6-4.0) \times 10^{-2}$, whereas the height of the calculated peaks was then $(10-12) \times 10^{-3}$, viz. 2.5 times higher than the experimental one.

The value of p which agrees with the height of the peaks was $(9-10) \times 10^{-2}$, but then the width of the calculated peaks appeared to be twice as large as the experimental ones.

Yet the main reason why we could not use calculations to fit the experimental data is that for all these values of p the theoretical peaks possess extensive "tails" which contribute 11-12% and 28-30% to the transmitted energy integral outside the angle 0.2. In experiment, all curves made zero contribution outside the angle 0.15, thus indicating a smaller value of p .

It should be, however, noted that the theoretical curves were calculated for an infinite interface and an ideal plane wave. The first condition requires that the size of the sample L should not be less than the characteristic length l . This condition $L \sim l$, was approximately met in our experiment for the frequency $f = 30$ MHz only. The second condition cannot be satisfied in principle because of the real divergence of the sound beam. The quartz plate used in the present experiments had the sound beam divergence in water and toluene close to the diffraction limit, λ/d . The expected value of the diffraction beam broadening in helium at 10 and 30 MHz should be 6' and 2', respectively.

However, one sees from the experimental curves (Table 2.1) that the minimum Rayleigh peak width at $T \simeq 0.2$ K and $f = 30$ MHz was $\delta = 25-30'$, which was an order of magnitude larger than the diffraction limit. The possible reason for this discrepancy could be, first, the broadening of the acoustic beam due to imperfections of the emitter that cannot be detected when measuring in water and toluene and, second, roughness of the surface of the sample. A simple calculation shows that, with a smooth wave-like surface of the sample (it is conceivable that such a surface is formed by electro-polishing) with a period of ~ 330 μm and a height of ~ 0.3 μm ,

the range of angles of incidence and, consequently, the Rayleigh peak will spread to $25'$. The calculations by Brekhovskikh [2.20] and Urazakov and Fal'kovskii [2.22] demonstrate that such a wave-like surface will practically not change the transmission coefficient of Rayleigh waves into bulk ones.

Table 2.1. Basic Parameters of Experimental Curves (${}^4\text{He}$ -Tungsten)

f MHz	T , K	U , mV	$\alpha_R \times 10^3$	$\delta \times 10^3$, rad	$J \times 10^4$	$p \times 10^4$
10	0.218	200	2.67	—	1.87	1.25
10	0.28	200	2.41	—	1.8	1.0
30	0.21	43	4.5	7.2	2.05	2.4
30	0.218	53	4.36	8.6	2.02	2.2
30	0.218	53	4.2	9.2	2.02	2.2
30	0.258	70	4.7	9.2	2.1	3.0
30	0.311	80	4.5	10.5	2.25	6.6
30	0.321	105	4.37	11.8	2.22	5.8
30	0.401	124	2.8	11.8	2.06	2.5

Note: here f is the frequency of the incident acoustic wave, T is the helium bath temperature, α_R is the energy transmission coefficient at the Rayleigh angle of incidence, U is the effective voltage across the quartz transducer, δ is the width of the Rayleigh peak at mid- 0.2

height, $J = \int_0^\pi \alpha(\theta) d\theta$ is the integral of the experimental curve

taken over the angle of incidence, p is the attenuation parameter calculated by comparing the experimental value of the integral with the theoretical one.

The angular distribution of the incident wave intensity and the broadening of the range of the angles of incidence will result in smoothing out of all the singularities of the experimental curves $\alpha(\theta)$ and in broadening of the Rayleigh peak by an angle $\Delta\theta \gg \delta$. An observed additional broadening (up to $40'$) with temperature may be caused by an increase in the attenuation of sound in helium [2.28].

If the waviness does not alter the acoustic transmission coefficient (the period of the surface irregularities is $>\lambda$), then both the area under the Rayleigh peak and that under the whole experimental curve $\alpha(\theta)$ will be the same as in the ideal case. Thus, by using the invariability of the energy integral, one can compare the experimental results with the theory and evaluate the attenuation parameter p (and γ), for the sample considered.

To accomplish this, the experimental curves were normalized as shown in Fig. 2.25. Then the integrals

$$J(\theta) = \int_0^\theta \alpha(\theta) d\theta \quad (2.52)$$

of the experimental and theoretical curves $\alpha(\theta)$ were compared, thereby for each integral of the experimental curve (the experimental integral) such a p value was chosen that gave the best agreement of

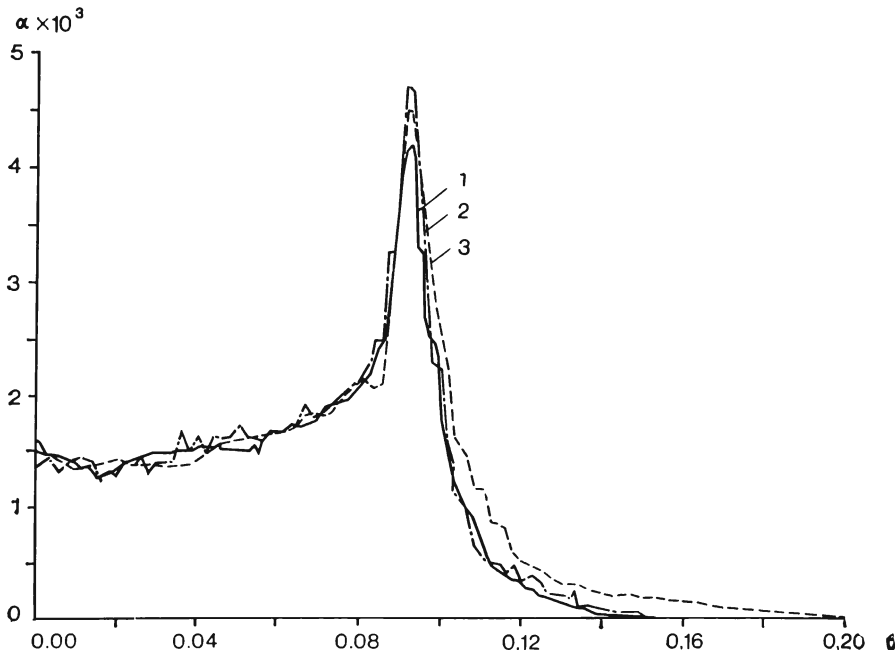


Fig. 2.25. The normalized experimental curves $\alpha(\theta)$ for the frequency of sound $f = 30$ MHz, and three temperatures: $T = 0.21$ K (curve 1), $T = 0.258$ K (curve 2), $T = 0.311$ K (curve 3).

the calculated with the experimental integral. The typical angular dependences of the integral of the energy transmitted into a sample at different temperatures and acoustic frequencies are presented in Figs. 2.26 and 2.27.

Note that the attenuation parameter $p = (2-6) \times 10^{-4}$ which is found for tungsten in this manner at $f = 30$ MHz and $T > 0.2$ K (see Table 2.1) satisfactorily agrees with the experimentally measured parameter of the bulk absorption of sound $p = 3 \times 10^{-4}$ [2.37, 38]. Thereby the experimental integral of the total energy is about twice

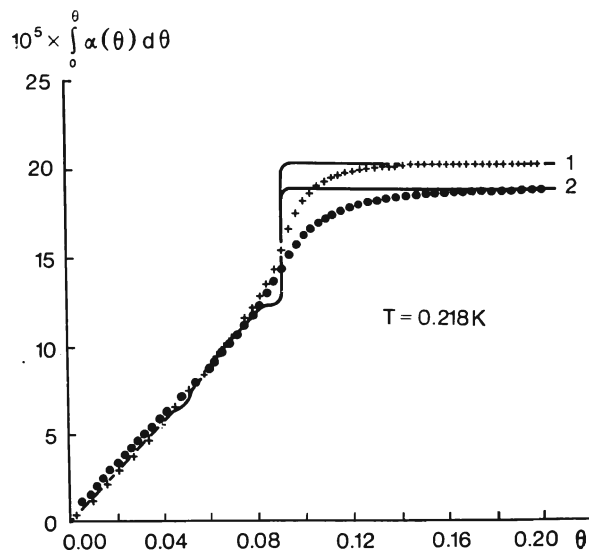


Fig. 2.26. The transmitted acoustic energy integral versus the angle θ for the experimental (dots) and theoretical (solid curves) dependences $\alpha(\theta)$: $f = 30$ MHz (curve 1), $f = 10$ MHz (curve 2), $T = 0.218$ K.

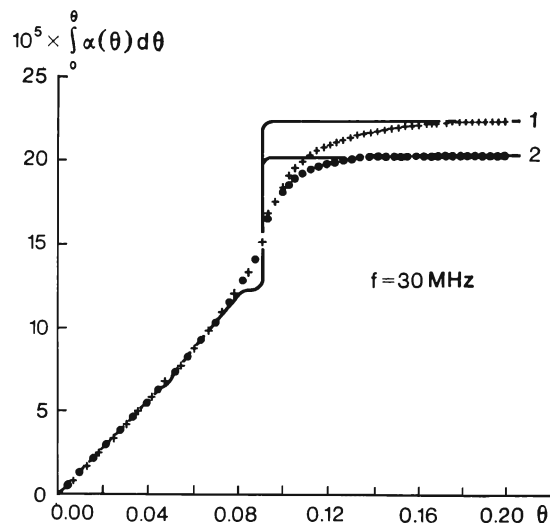


Fig. 2.27. The transmitted acoustic energy integral versus the angle θ for the experimental (dots) and theoretical (solid curves) dependences $\alpha(\theta)$: $T = 0.311$ K (curve 1), $T = 0.218$ K (curve 2), $f = 30$ MHz.

the energy integral for the critical angle θ_2 , that is the contribution of the surface and bulk waves is approximately the same.

For the acoustic frequency 10 MHz the attenuation parameter found by the same method from experimental data is equal to $p = (1.0-1.25) \times 10^{-4}$.

It should be noted that, although the accuracy of the energy integral determination from the experimental $\alpha(\theta)$ curves is 5-10%, a comparison of the experimental integral with a calculated one yields only an estimate of the parameter p which is subject to an error of the same order of magnitude as the value itself (50-100%), since, as has been indicated above, the experimental conditions are rather inconsistent with the solution of the problem stated (the bounded sample, the rough surface, the attenuation of sound in helium). The data corresponding to the temperature below 0.2 K for $f = 30$ MHz provide nearly the same value of $p = (2-3) \times 10^{-4}$, but because of the lower accuracy in evaluating the energy integral, these data are not included in Table 2.1.

Comparison of the p values for 10 MHz ($p = 1.25 \times 10^{-4}$) and for 30 MHz ($p = 2.2 \times 10^{-4}$, see Table 2.1) makes it possible to conclude that the frequencies used for a given sample correspond to a transition region between the quadratic (p is proportional to the frequency) and linear (p is frequency independent) dependence of the ultrasonic absorption coefficient γ on the frequency (for pure metals the linear frequency dependence of γ is observed at $f \geq 100$ MHz). This conclusion agrees with the value of the mean free path of the electrons in tungsten, $l_e \sim 0.1-0.3$ mm, which is estimated from the measurements of conductivity and cyclotron resonance frequency [2.39].

Thus, for an unbounded tungsten single crystal having a flat surface, the dependence of the transmission coefficient of sound across the interface on the angle of incidence of an ideal plane wave should have the form exposed in Fig. 2.21 (b) ($f = 30$ MHz). For $f = 10$ MHz, the dependence will be similar, but here $\alpha \simeq 1$, $\delta = 3.7 \times 10^{-5} = 8''$. The case in Fig. 2.21 (a) can be practically observed at very low frequencies $f \ll 10$ MHz.

The $\alpha(\theta)$ curves [1, 2 in Fig. 2.21 (c)] can clearly be expected at high frequencies (thermal phonons) and in the presence of defects in the surface layer. In another case [3, 4 in Fig. 2.21 (c)], the sample should have a sound-absorbing layer on the surface and the layer thickness should be comparable with the wavelength which is possible in the case of thermal phonons at $T > 1$ K.

It is seen from Table 2.1 that at $f = 30$ MHz the peak width δ , the energy integral, and consequently the attenuation parameter p , have a tendency to increase with temperature. According to the generalized acoustic theory, this fact could indicate an increase in the attenuation in the solid if the attenuation in the liquid were to

remain negligibly weak. However, the acoustic attenuation in ${}^4\text{He}$ rises with temperature as T^4 [2.33], and at 30 MHz becomes comparable with the attenuation in the solid at $T \geq 0.4$ K. In this case the above theoretical calculations are incomplete and should be improved, when the attenuation in the liquid can no longer be neglected.

2.3.8.2. Gold

The angular dependence of energy transmission coefficient for a plane sound wave incident on the surface of gold from liquid ${}^4\text{He}$ has been calculated in a manner similar to that described above. The parameters for gold were taken as follows: $D = 19.49 \text{ g/cm}^3$, $c_1 = 3.36 \times 10^3 \text{ m/s}$, $c_t = 1.24 \times 10^3 \text{ m/s}$ ($\eta = 2.71$).

To evaluate the expected absorption coefficient, one can use the absorption coefficients of longitudinal acoustic waves measured by Mac Farlane and Rayne in a gold single crystal [2.40]. For very high frequencies (330 MHz), the attenuation parameter averaged over all directions is $p_1 = 4.5 \times 10^{-4}$. Let us evaluate the quantity p_t . According to the theory of free electrons [2.38], for low frequencies $p_t = 0.75p_1$ for very high frequencies and $p_t = 0.81\eta p_1 = 2.2p_1$. Since the ultrasonic frequency (20 MHz) in experiments with gold is an intermediate one, then assuming p_1 (20 MHz) \approx $(1/2)p_1(\infty)$ and $p_t = 1.5p_1$ we shall obtain p_t (20 MHz) $\approx 3.5 \times 10^{-4}$.

The computer-calculated dependence $\alpha(\theta)$ for a liquid ${}^4\text{He}$ -gold interface with $p \approx p_t$ above is shown in Fig. 2.28. The shape of the $\alpha(\theta)$ curve somewhat differs from that for tungsten (see Fig. 2.21). In addition to the minima in α at the angles $\theta_1 = 0.071$ and $\theta_2 = 0.193$ as well as the Rayleigh peak at $\theta_R = 0.2045$, the $\alpha(\theta)$ curve exhibits a rather sizable "bump" at $\theta = 0.108 \approx 6.2^\circ$. The "bump" about 2.4 times exceeds the value of $\alpha(0) = 2.1 \times 10^{-3}$ while the analogous "bump" for tungsten exceeds $\alpha(0)$ only slightly. For the above value of $p = 3.5 \times 10^{-4}$, the height of the Rayleigh peak is $\alpha_R = 0.9$ and the width at midheight is $\delta = 2.1 \times 10^{-4}$.

The integral contribution of the Rayleigh peak amounts to $\sim 50\%$ of that of the bulk waves. In order to estimate the possibility of experimental observation, suppose that the real width of the Rayleigh peak for gold is identical with that for tungsten (viz. $25' = 7.3 \times 10^{-3}$ rad). In this case one can expect the Rayleigh peak height measured in experiments with a gold sample to be

$$\alpha_R = \frac{0.9 \times 2.1 \times 10^{-4}}{7.3 \times 10^{-3}} = 2.59 \times 10^{-2}$$

The experimental width of the Rayleigh peak for gold could be even larger than $25'$. The first reason is that the irregularities on the gold sample surface are much more pronounced than those on the

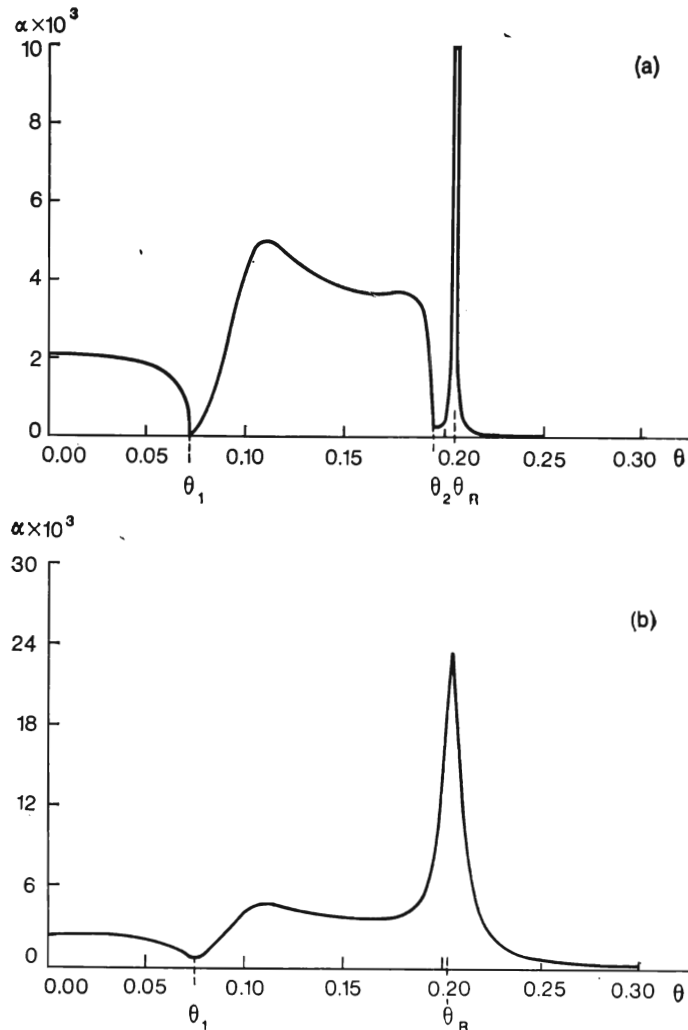


Fig. 2.28. Calculated dependence of the energy transmission coefficient of a plane monochromatic acoustic wave on the angle of incidence on the ${}^4\text{He}$ -gold interface at two attenuation parameters of sound p : (a) $p = 3.5 \times 10^{-4}$, $\alpha_R = 0.9$, $\delta = 2.1 \times 10^{-4}$, (b) $p = 3 \times 10^{-2}$.

tungsten sample. The second reason is that quartz transducer characteristics were probably worse because they were not specially checked in experiments with gold.

Therefore experimental peaks can happen to be lower than the above estimates and only slightly exceed the "bump" at $\theta = 6.2^\circ$.

2.3.9. Comparison with the Andreev Theory

Let us compare Andreev's results for the acoustic transmission coefficient with calculations in the framework of the generalized acoustic theory. To do this, consider the expression for $w(\theta)$ (2.27) in the vicinity of the Rayleigh angle θ_R at the small attenuation parameter $p \ll 1$. We expand $w(\theta)$ in powers of p and $\theta - \theta_R$ and neglect the terms of the second order:

$$w(\theta) = \frac{4pE}{(pE+1)^2 + (\theta - \theta_R)^2 M^2} \quad (2.53)$$

where E and M are functions of the elastic constants and of the helium-to-metal density ratio (without regard for the attenuation).

One can easily see that the formulae (2.27) and (2.53) have a similar form and that they describe a resonance curve, when $B = pE$ and $H \frac{Dc_t^2}{pc^2} = M$. In the region of small absorption ($pE \ll 1$, and $B \ll 1$), both formulae yield the same width of the Rayleigh peak, $\delta = 1.8 \times 10^{-5}$ (independent of the attenuation). At the same time in both cases the peak height α_R is proportional to the absorption of sound [p in (2.53) and p_0^4 in (2.27)].

This suggests that Andreev's theory predicts the same resonance of the energy transmission in the vicinity of the Rayleigh angle as the generalized acoustic theory does.

An estimate for tungsten gives $B \sim 10^{-2}$ (if we take $p_0 \approx \frac{2h}{a}$, where a is the lattice constant), hence $\alpha_R \simeq 4 \times 10^{-2}$ and $\delta = 1.84 \times 10^{-5}$. These parameters of the Rayleigh peak corresponding to $p \sim 10^{-6}$ are two orders of magnitude less than the experimental value.

However, as has been noted in [2.38], the measured ultrasonic absorption in tungsten (and molybdenum) was two orders of magnitude higher than the value calculated by the theory of free electrons. In the number of works (see, e.g. [2.41]) it has been said that the Fermi surface for transition group metals disagree considerably with one predicted by the model of free electrons and the tight-binding approximations is much preferable to describe the ultrasonic absorption in these metals.

This approximation was used in [2.37] to calculate the acoustic absorption in tungsten by electrons and holes with a due regard for the deformation potential. The absorption coefficients calculated by this method agree satisfactorily with the results of the present work.

One can hope that for the metals described in the framework of the free electron model, such as copper, gold, indium, etc. the Andreev's formula (2.26) will ensure the better quantitative agreement

with the experimental data. However, it should be noted that it is a simplest case of phonon transmission from helium into an isotropic single crystal which was investigated in the Andreev's theory as well as in the present experiments. The $w(\theta)$ dependence will be more complicated for anisotropic crystals (see, e.g. [2.21, 2.42]).

2.4. CONCLUSION

Thus, the investigation of the transmission of 10-30 MHz acoustic waves incident from liquid ^4He on the surface of tungsten and gold at temperatures from 60 mK to 0.4 K has demonstrated that the acoustic phenomena at an interface are of the character which is common to both metals.

The detailed study of the $^4\text{He}-\text{W}$ system has revealed that the sound waves incident from liquid helium on a tungsten surface were transmitted into the sample with the absorption coefficient $\sim 10^{-3}$ (in energy) only in a limited range of angles of incidence (in the vicinity of normal incidence) which exceeded slightly the critical Rayleigh angle.

The angular dependence of the energy transmission coefficient shows a well-pronounced maximum at the supercritical Rayleigh angle of incidence θ_R ($\sim 6^\circ$ for tungsten) followed by a rapid decrease down to zero. The maximum is caused by the absorption by metal of the surface Rayleigh wave excited resonantly by the incident acoustic wave.

The contribution of the surface Rayleigh waves into the total integral of the transmitted energy is approximately equal to the contribution of the bulk sound waves in the range of subcritical angles.

The experimental width of the Rayleigh peak in the collisionless region of liquid helium ($T < 0.2$ K) is independent of temperature, while at $T > 0.2$ K the width is found to increase with temperature. The width value of maxima (30-40') exceeds the diffraction one λ/d by an order of magnitude, that can be explained by roughness of the sample surface and imperfectness of the emitter.

The comparison between the experimental data and theory has shown that the observed pattern of the acoustic energy transmission across an interface can be adequately described by the generalized acoustic theory which takes into account the attenuation of bulk elastic waves in a solid. In the vicinity of the Rayleigh critical angle, the generalized acoustic theory and that advanced by Andreev are equivalent in their description of the resonance amplification of the transmission of sound.

The absorption of the Rayleigh waves energy is controlled by the absorption coefficient of bulk acoustic waves in metal. The absorption coefficients of tungsten which were found in this work agree quantita-

tively with the published experimental data and with the theoretical values calculated on the basis of the electron absorption mechanism. The Kapitza resistance for ^4He -W at $T \sim 0.2$ K found from the overheating of a tungsten sample by sound, $R_K T^3 \simeq 650 \text{ cm}^2 \text{K}^4 / \text{W}$ is three times lower than the theoretical value. The Kapitza resistance decreases with temperature. These results are in a good agreement with the data of other authors.

The author would like to thank P.L. Kapitza and A.F. Andreev for their interest in this investigation and discussions, V.N. Krutikhin, V.I. Voronin, and G.E. Karstens for their assistance in preparing the experiment and A.V. Dubrovin for discussing the results obtained and for computer calculations.

References

- 2.1. P. L. Kapitza, *Zh. Eksper. Teor. Fiz.* **11**, No. 1, 1 (1941).
- 2.2. I. M. Khalatnikov, *The theory of superfluidity*, Nauka, Moscow, 1971 (in Russian); *Introduction to the theory of superfluidity*, Benjamin, New York, 1965.
- 2.3. K. N. Zinov'eva, *JETP Lett.* **28**, 269 (1978).
- 2.4. K. N. Zinov'eva, *Sov. Phys. JETP* **52**, 1007 (1980).
- 2.5. K. N. Zinov'eva, V. I. Sitnikova, *Sov. Phys. JETP* **57**, 332 (1983).
- 2.6. L. M. Brekhovskikh, *Waves in layered media*, Academic Press, New York, 1960.
- 2.7. L. J. Challis, J. D. Cheeke, *Proc. Roy. Soc., London, Ser. A* **304**, 479 (1968).
- 2.8. L. D. Landau, E. M. Lifshitz, *Theory of Elasticity*, Pergamon Press, Oxford, 1966.
- 2.9. W. A. Little, *Phys. Rev.* **123**, 435 (1961).
- 2.10. A. F. Andreev, *Sov. Phys. JETP* **16**, 257, 1084 (1963).
- 2.11. A. F. Andreev, *Ph. D. thesis*, The Institute of Physics Problems of the USSR Academy of Sciences, Moscow, 1964.
- 2.12. V. M. Merkulova, *Sov. Phys. Acoust.* **15**, 404 (1970).
- 2.13. G. Mott, *J. Acoust. Soc. Amer.* **50**, 819 (1971).
- 2.14. F. L. Becker, R. L. Richardson, in: *Research Techniques in Nondestructive Testing*, Ed. R. S. Sharp, Academic Press, New York, 1970, vol. 1, p. 91.
- 2.15. I. M. Khalatnikov, I. N. Adamenko, *Sov. Phys. JETP* **36**, 391 (1973).
- 2.16. R. E. Peterson, A. C. Anderson, *J. Low Temp. Phys.* **11**, 623 (1972).
- 2.17. H. Haug, K. Weiss, *Phys. Lett.* **40A**, 19 (1972).
- 2.18. I. A. Victorov, *Rayleigh and Lamb Waves*, Plenum Press, New York, 1967.
- 2.19. F. Press, I. Healy, *J. Appl. Phys.* **28**, 1323 (1957).
- 2.20. L. M. Brekhovskikh, *Sov. Phys. Acoust.* **5**, 288 (1959).
- 2.21. G. W. Farnell, in: *Acoustic Surface Waves*, Ed. A. A. Oliner, Springer-Verlag, Berlin, 1978.
- 2.22. E. I. Urazakov, L. A. Fal'kovskii, *Sov. Phys. JETP* **50**, 592 (1979); *Sov. Phys. JETP* **52**, 132 (1980).
- 2.23. Y. Weber, W. Sandmann, W. Dietsche, and H. Kinder, *Phys. Rev. Lett.* **40**, 1469 (1978).
- 2.24. N. G. Mills, A. F. G. Wyatt, and R. A. Sherlock, *J. Phys. C* **8**, 289, 300 (1975).
- 2.25. A. F. G. Wyatt, G. J. Page, and R. A. Sherlock, *Phys. Rev. Lett.* **36**, 1184 (1976).
- 2.26. A. F. G. Wyatt, G. J. Page, *J. Phys. C* **11**, 4927 (1978).

- 2.27. V. L. Gurevich, B. D. Laikhtman, *Sov. Phys. JETP* 42, 628 (1975).
- 2.28. B. D. Laikhtman, A. V. Lomakin, *JETP Lett.* 23, 572 (1976).
- 2.29. R. Truell, C. Elbaum, and B. Check, *Ultrasonic Methods in Solid State Physics*, Academic Press, New York, 1969.
- 2.30. K. N. Zinov'eva, G. E. Karstens, *Cryogenics*, November, 622 (1974).
- 2.31. K. N. Zinov'eva, V. V. Veinberg, F. N. Vorobkalo, L. I. Zarubin, and S. T. Boldarev, *Instrum. and Experim. Technique* 25, 1277 (1983).
- 2.32. V. I. Voronin, *Instrum. and Exper. Techn.* 23, 1533 (1981).
- 2.33. B. M. Abraham, Y. Eckstein, J. B. Ketterson, M. Kuchnir, and J. Vig-nos, *Phys. Rev.* 181, 347 (1969).
- 2.34. A. C. Anderson, J. I. Connolly, and J. C. Wheatley, *Phys. Rev.* 135, A910 (1964).
- 2.35. J. T. Foliinsbee, A. C. Anderson, *J. Low Temp. Phys.* 17, 409 (1974).
- 2.36. A. Schoch, *Ergeb Exakten Naturwiss.* 23, 127 (1950).
- 2.37. K. B. Vlasov, A. B. Rinkevich, and F. Sh. Nasyr'ov, *Fiz. Met. Metalloved.* 47, 524 (1979).
- 2.38. C. K. Jones, J. A. Rayne, *Phys. Lett.* 13, 282 (1964).
- 2.39. R. Herrmann, V. S. Edelmann, *Sov. Phys. JETP* 26, 901 (1968).
- 2.40. R. F. MacFarlane, J. A. Rayne, *Phys. Rev.* 162, 532 (1967).
- 2.41. D. P. Almond, J. A. Rayne, *J. Low Temp. Phys.* 23, 7 (1976).
- 2.42. V. R. Volasco, F. Garsia Moliner, *J. Phys. C* 13, 2237 (1980).

3

Investigations of ^3He Superfluid Phases by Pulsed NMR Technique

Yu. M. Bun'kov, Cand. Sc. (Phys. and Math.)

3.1. INTRODUCTION

At present only two substances are known to remain liquids at temperatures down to absolute zero. These are the helium isotopes ^3He and ^4He . At sufficiently low temperatures both liquids pass into a quantum coherent state, in which they feature the phenomenon of superfluidity. ^4He superfluidity was discovered experimentally in 1937 by Kapitza [3.1] at the Institute of Physics Problems (IPP) of the USSR Academy of Sciences. Under atmospheric pressure the critical temperature for the ^4He transition into the superfluid state is 2.17 K.

Helium-3 differs substantially from helium-4 in that it has a half-integer spin, and as a result forms a Fermiliquid, i.e. it cannot become superfluid due to the Pauli exclusion principle. However, like conduction electrons in metals, the helium-3 atoms can form pairs that obey Bose statistics. That helium-3 could turn to superfluid state was predicted by Pitayevskii, also at the IPP [3.2]. He demonstrated that the quasiparticles in helium-3 should attract each other to form Cooper pairs with nonzero moment. However, in order to detect helium-3 superfluidity experimentally further advances in cryogenic engineering and cryophysics were necessary.

A major contribution was made by Pomeranchuk when he predicted that helium-3 in a compression chamber would cool if its transition to the solid state takes place. Helium-3 differs from most other substances in that at temperatures below 0.3 K the liquid-solid transition is accompanied by heat absorption rather than heat release. This is due to the entropy balance between the liquid and solid phases. In 1965, Anufriev, again at the IPP [3.3], was the first to demonstrate experimentally that the Pomeranchuk effect could be used to cool helium-3. The method was then employed by Osheroff, Richardson, and Lee to detect helium-3's transition to the superfluid state at a temperature of about 2.6 mK.

Thus, a great deal of experience has been accumulated and a tradition established in low temperature helium research at the IPP. Experimental investigations of helium-3's superfluid phases began at the IPP in summer 1982, when a copper nuclear demagnetization unit, designed and constructed by the group of physicists headed by A.S. Borovik-Romanov, was put into operation. The unit made it possible to work at temperatures down to 0.4 mK and to maintain

helium-3 continuously in the superfluid state for as long as 12 days. The first part of this article describes the equipment in what way it differs from others elsewhere.

The superfluidity of helium-3 has been extensively investigated in many laboratories. It turned out that the technique which yielded the most information about the structure and properties of helium-3 was NMR. It was using NMR that the two superfluid helium-3 phases, i.e. ${}^3\text{He-A}$ and ${}^3\text{He-B}$, were identified confirming the theoretical predictions of Anderson, Brinkman and Morell, and Balian-Werthamer [3.10-11]. Some extremely complicated dynamic and texture effects and ion mobility have also been studied. Acoustic and hydrodynamic methods have also been employed. These investigations are covered in a number of reviews, of which the most complete is that written by Lee and Richardson [3.4] in 1976.

Until recently the relaxation processes in superfluid helium-3A were not clearly understood. In 1975 Leggett and Takagi [3.12] using data from continuous NMR established the theory of magnetic relaxation in superfluid helium-3 phases. This theory, called the "intrinsic" relaxation theory, accounts for the transitions of ${}^3\text{He}$ atoms between the normal and superfluid states and adequately describes the shape of the continuous NMR line. Experiments with pulsed NMR performed in the same year by Corruccini and Osheroff [3.19], and other experimental evidence have demonstrated that relaxation of magnetization after it has been rotated through 90° is one to two orders of magnitude faster than might be expected from the theory of Leggett and Takagi. In 1979 Fomin showed theoretically that uniform precession in helium-3A is unstable and should decay into spin waves. A spatial nonuniformity results turning on "the fast diffusion" relaxation. The second part of this article considers the experimental detection of instability in helium-3A homogeneous precession and analyzes its effect on the relaxation.

In addition to its interesting magnetic properties, helium-3's superfluid phases possess the properties of liquid crystals, the most complex of which are the texture features, viz. those governed by the spatial orientation of the ordering parameter. Thus, the ordering parameter in superfluid helium-3 is given by the matrix $R(\mathbf{n}, \theta)$, which describes the rotation of the spin coordinates, at an angle $\theta = 104^\circ$ to the orbital about the \mathbf{n} axis. Thus, the NMR frequency depends on the orientation of the \mathbf{n} vector. In free helium, the \mathbf{n} vector is parallel to the external field \mathbf{H} . Under pulsed NMR excitation, the vector \mathbf{n} precesses with the Larmor frequency around \mathbf{H} in phase with the magnetization \mathbf{S} . If helium-3B is placed in a set of plane parallel plates, the \mathbf{n} vector will be deflected from the direction of \mathbf{H} . Thereby, the NMR frequency is substantially shifted as was demonstrated in experiments on continuous NMR. We carried out our experiments on pulsed NMR in helium-3B parallel plane

geometry. It turned out that given a sufficiently powerful radio-frequency pulse, it could "break" the n vector away from the position determined by the parallel plane geometry and could transform the texture into a state corresponding to free helium-3B. The third part of the present article deals with an investigation of this effect and the processes of texture reverse relaxation to the nonperturbed state.

3.2. THE EQUIPMENT FOR PRODUCING ULTRALOW TEMPERATURES

3.2.1. Operating Conditions

There are today a few dozen nuclear demagnetization refrigerators able to operate at temperatures around 1 mK. However, the variety of scientific tasks and the great number of cryogenic engineering problems have resulted in practically all of them being different. In this Section we consider the first Soviet nuclear demagnetization refrigerator which produced superfluid helium-3 in summer 1982. The preliminary cooling of the nuclear demagnetization stage is done by a ^3He - ^4He dilution refrigerator designed at the IPP. Since the dilution refrigerator must run nonstop for many days to ensure operation of the nuclear demagnetization refrigerator, it must be reliable. In some experiments the dilution refrigerator operated for as long as three months without a break. Thus this factor placed no restriction on the duration of the experiments.

Much thought has also been given to isolating the refrigerator from vibration- and high-frequency and ultrahigh-frequency electromagnetic fields. To isolate the equipment from electromagnetic radiation, the room in which it was installed was completely shielded by a copper screen 0.2 to 0.5 mm thick. The power and service lines all had HF filters or dielectric shunts.

Adequate vibration isolation presented more difficulties. The refrigerator was housed in the building of a large institute in the centre of a big city, so vibration is always present. To solve this problem we used a technique that so far as we know has not before been applied to similar setups. The cryostat was mounted on a heavy pendulum, which consists of a 800-kg concrete base suspended by ropes with the distance between the suspension point and the center of mass being 6 m (Fig. 3.1). The refrigerator was mounted on the base, which rests on the floor. When operating at ultralow temperatures, mobile bellows in the upper part of the suspension gear are pumped up and the base rises above the floor. In order to dampen vibration, the three bellows are connected via a small-diameter tube to a 40-l ballast vessel. The pump lines are designed as long bellows hose so that vibration cannot be transferred along

them. Two rotary bellow units were used to decouple the main (160 mm in diameter) pumping line of the dilution cryostat. One is shown in Fig. 3.1. To prevent the bellows being stretched when not blown up guy wires are used to compensate for the pressure. The addition of a booster pump the tube also improves the vibration isolation of the setup. All this resulted in vibrations with frequencies higher than 1 Hz being effectively damped. If the suspension base touches the floor, the helium-3 superfluid phase can only be maintained for 1 day, whereas when suspended the superfluid helium state can be worked with for 12 days after a single demagnetization process.

3.2.2. The Dilution Refrigerator

A conventional ^3He - ^4He dilution refrigerator was used to pre-cool the nuclear stage of the nuclear demagnetization cryostat. The principles of operation of dilution refrigerators are outlined by Lounasmaa [3.5]. Here we discuss features of our design [3.6].

The layout of the circulation system in the dilution refrigerator is shown in Fig. 3.2. Helium-3 is pumped out of the refrigerator (1) by a booster pump (2) which has a capacity of 900 l/s, by a pump (3) which has a capacity of 45 l/s and pumps (4, 5) which have a 5 l/s capacity. These pumps provide a helium circulation rate of 2×10^{-3} mole/s with input pressure of 2×10^{-2} torr and an output one of 100 torr. The ^3He then enters a purification system composed of self-contained nitrogen (7) and helium (8) traps. The trapping system prevents the refrigerator's ^3He return lines from blocking. The liquid nitrogen trap is essentially a large diameter tube (30 mm) filled

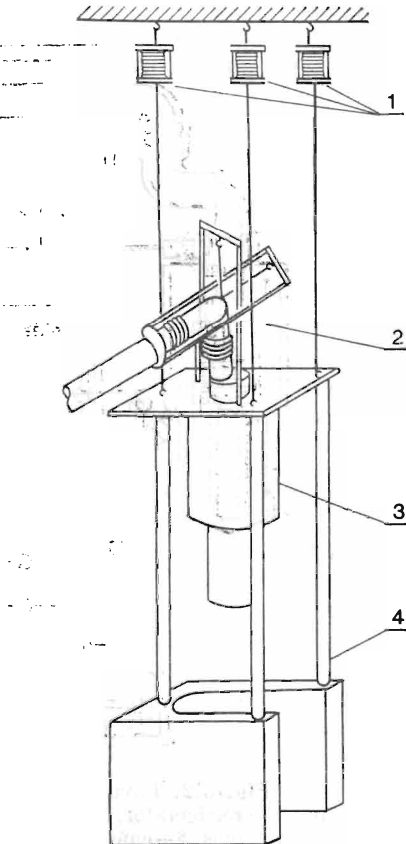


Fig. 3.1. Refrigerator vibration isolation: 1—bellows of the refrigerator lifting system and shock absorbers, 2—angular damper for the bellows, 3—the Dewar vessel with the demagnetization refrigerator mounted inside, 4—the 800-kg base.

with an adsorbent. In this tube the gaseous ^3He descends to the region of liquid nitrogen temperatures. In the helium trap, placed inside a standard transport helium Dewar vessel, the ^3He flows down a tube (10 mm in diameter) around an array of copper plates (~ 50 pieces) and then returns along the central tube so cooling the

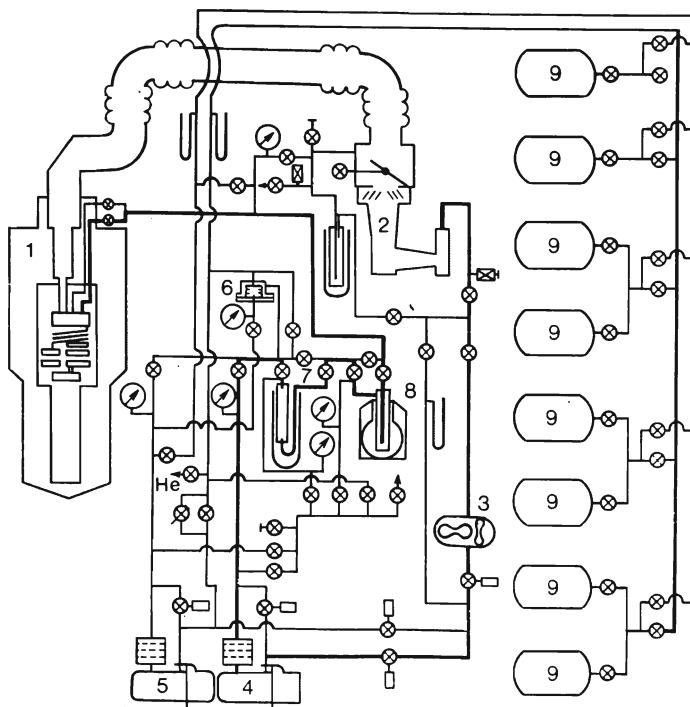


Fig. 3.2. Layout of distribution lines in the ^3He -in- ^4He dilution refrigerator: 1—refrigerator, 2—booster pump, 3—Roots pump, 4 and 5—roughing-down pumps, 6—emergency throttle, 7—liquid nitrogen trap, 8—liquid helium trap, 9—tank for storing mixture.

incoming ^3He . The helium trap effectively adsorbs air and the other gases from the helium, thus making it possible to operate even under emergency conditions, for example when the whole assembly has a leak of about 10^{-2} torr l/s.

To improve the reliability of the refrigerator, the ^3He return line and impedances are duplicated. When one of the return lines is blocked, the ^3He can be diverted to the other line. In addition, it is convenient to use both return lines simultaneously while the helium is condensing in the refrigerator.

Figure 3.2 also shows the emergency valve (6) for discharging the ^3He into tanks (9) to store the mixture should the ^3He circulation system get blocked. Two fore-pumps improved the reliability of the circulation system, since a failure of any of the four pumps only slows down the circulation rate whilst the unit can be replaced or repaired. Besides, the second fore-pump makes it possible to use the mixture in the tanks independently whilst the ^3He is being circulated.

The low temperature refrigerator stage is shown in Fig. 3.3. It is placed in a helium Dewar vessel which has a nitrogen shield. The ^3He flow from the return lines goes into a helium bath through a sintered heat exchanger (1) about 0.3 m^2 in area. The heat exchanger is a flat tablet 2 mm thick sintered from copper grains 10-40 μm in diameter. A similar heat exchanger (2) is located in the ^4He pot (3) and serves to remove the latent heat of condensation from the ^3He . The replacement of the coiled tubular heat exchanger, which we started off using, by a sintered one resulted in a drop in the condensation pressure of the ^3He from ~ 760 torr to 50-100 torr under the same conditions and the refrigerator began to operate more stably.

The ^3He then flows through an impedance of 10^{11} cm^{-3} , a coiled heat exchanger in a still (4), another $5 \times 10^9\text{ cm}^{-3}$ impedance, a coiled double-spiral heat exchanger (5), similar to the one described in [3.7], and finally enters the step heat exchangers (6). These are manufactured from flat copper disks, on both sides of which copper grains 10-40 μm in diameter are sintered-on (see inset in Fig. 3.3). The disks are assembled in stacks of the required dimensions. All the disks, except the one separating the concentrated and diluted ^3He fluxes, are drilled and threaded with close fitting tubes. The tubes are silver-brazed onto a cover inside a vacuum furnace and the disks are then welded around the circumference. This sort of heat exchanger offers little resistance to the ^3He flux, ensures adequate thermal contact over the heat exchanger body, and can be manufactured with various areas by changing the number of disks in the stacks. In our refrigerator, the heat exchangers had areas (on each side) of 1.5, 1.5, 3.0, and 6.0 m^2 , which correspond respectively to 1, 1, 3 and 7 disks. After passing through the refrigerator the ^3He goes into the mixing chamber (7), where by dilution in ^4He it absorbs heat. In solution with the ^4He , the ^3He diffuses through heat exchangers into the still (4) and is pumped out. A suppressor similar to that described in [3.7] is placed inside the chamber, with a heater tightly wound around the suppressor's evaporator.

The operation of the dilution refrigerator was checked by testing the mixing chamber with the sensor of a platinum NMR thermometer. Also, a heater was inserted into the chamber. Some power \dot{Q} was dissipated in the heater and the equilibrium helium temperature

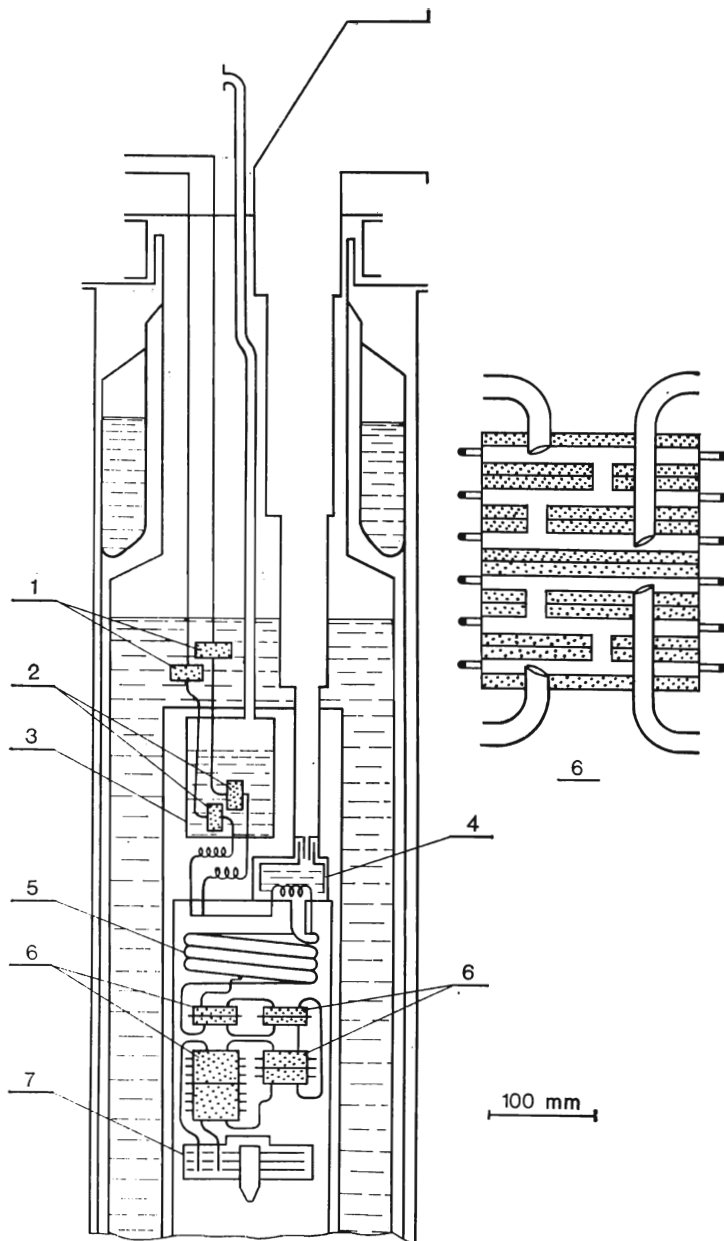


Fig. 3.3. The dilution refrigerator: 1 and 2—sintered heat exchangers for cooling and condensing incoming ^3He , 3— ^4He pot, 4—still, 5—coiled heat exchanger, 6—stepwise heat exchangers, 7—mixing chamber. Inset illustrates sectional view of the stepwise heat exchanger.

in the mixing chamber was registered at a given circulation rate, $\dot{\eta}$. The temperature dependences of the cooling capacity of the dilution refrigerator at a constant circulation rate are shown in Fig. 3.4. At the relatively high temperatures, the cooling capacity is proportional to the square of the temperature of the mixing chamber.

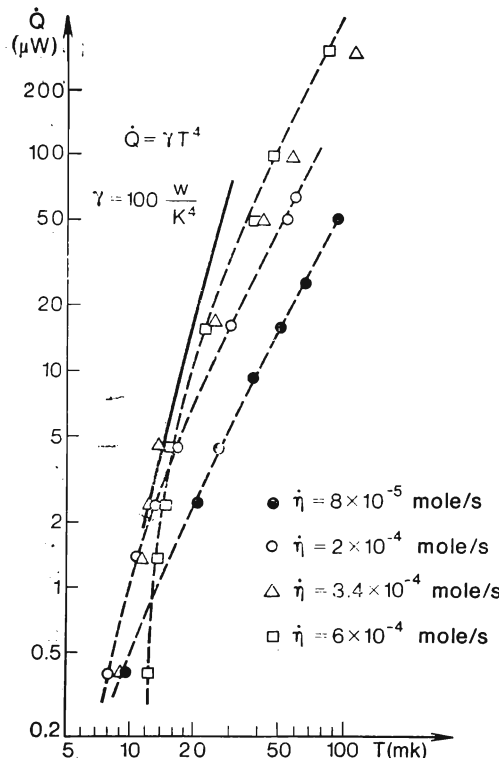


Fig. 3.4. Cooling capacity of the dilution refrigerator versus temperature inside mixing chamber for different ^3He circulation rates.

Further, when the temperature falls, for a given ^3He circulation rate the heat exchangers cease to handle the heat transfer between the supply and return helium-3 fluxes, this leading to a rapid drop in cooling capacity. On the other hand, at the same temperature, but for a lower circulation rate, the heat exchangers still cope with the heat flux and, as a result, the cooling capacity somewhat increases. Thus, for each temperature value in the working temperature range of the dilution refrigerator, there is an optimum helium circulation rate, that corresponds to the maximum cooling capacity. As was noted in [3.8], at the optimum circulation rate, the cooling capacity

of the dilution refrigerator depends on the forth power of temperature. In the temperature range from 8 to 30 mK the refrigerator has a cooling capacity of $100 \times T^4$ W. It was shown in [3.7] that the dilution chamber temperature can be written in the form:

$$T_{MC}^2 = 6.4 R_K \frac{\dot{\eta}}{\sigma} + 1.22 \times 10^{-2} \frac{\dot{Q}}{\dot{\eta}} \quad (3.1)$$

where the first term describes the heat recuperation in the heat exchangers, the second one is the heat absorption during the ^3He -in- ^4He dilution, R_K is the Kapitza resistance in $\frac{\text{m}^2\text{K}^4}{\text{W}}$, σ is the area of the heat exchangers, \dot{Q} is the heat supplied to the dilution chamber.

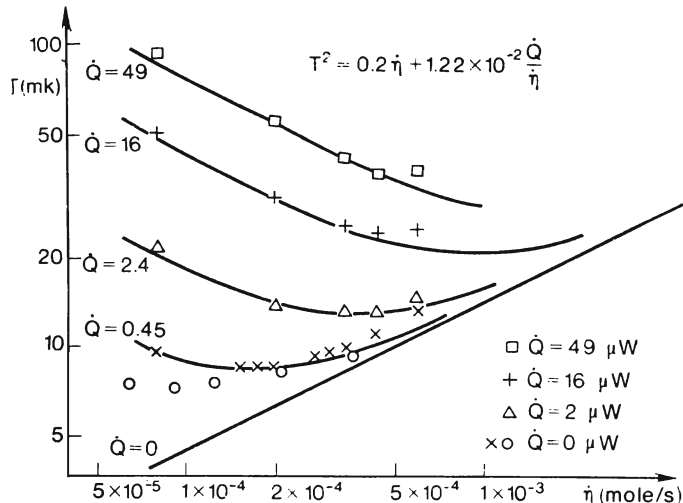


Fig. 3.5. Mixing chamber temperature versus ^3He circulation rate for different heat supplied to the mixing chamber. The theoretical curves are calculated from Eq. (3.1).

ber. This formula was derived for the case of a continuous heat exchanger with an optimum surface distribution. However, it is also valid for refrigerators having an array of stepwise heat exchangers. True, the effective area of a given configuration of stepwise heat exchangers is smaller than the real area. For our refrigerator, the value of $6.4 \frac{R_K}{\sigma}$ is 0.2. This is clearly seen from the curves of Fig. 3.5, which shows the dependence of the dilution refrigerator temperature on the ^3He circulation rate given a fixed heat release inside the dilution chamber. For theoretical curves, the value of \dot{Q} is increased by 0.4 mW to take into account a heat supply to the

chamber. With $R_K \simeq 0.05 \frac{\text{m}^2\text{K}^4}{\text{W}}$, the heat exchangers have an effective area of 1.5 m^2 , viz. the efficiency of the stepwise heat exchangers is 15%. However, it is substantially simpler to manufacture a stepwise heat exchanger even if its area has to be an order of magnitude larger than that a continuous heat exchanger would have.

The limiting temperatures obtained by the dilution refrigerator are 7.5 mK in the circulatory mode and 3.9 mK in the single-supply mode.

3.2.3. The Nuclear Demagnetization Refrigerator

In describing the nuclear demagnetization refrigerator we shall follow the same pattern as in the case of the dilution refrigerator. We refer the reader to the excellent review by Andres and Lounasmaa [3.9] to get an idea of the operation principles. We shall only deal with the features of the design and with refrigerator's characteristics. Figure 3.6 shows the layout of the nuclear demagnetization cryostat. The refrigera-

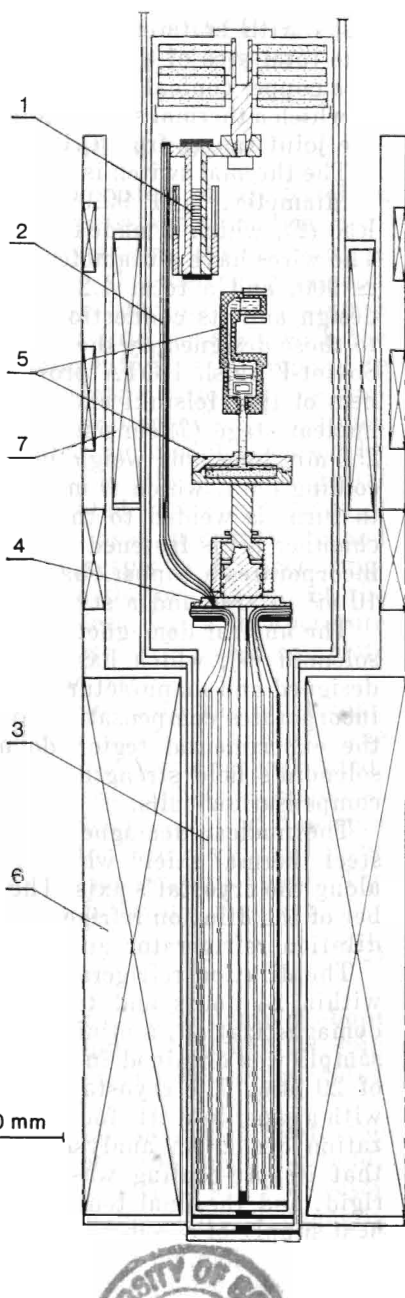


Fig. 3.6. Nuclear demagnetization refrigerator: 1—thermal switch, 2—heat lead, 3—nuclear demagnetization stage, 4—cup of the nuclear demagnetization stage, 5—experimental chamber filled with ${}^3\text{He}$, 6—superconducting solenoid, 7—field probe coil.

tor incorporates a dilution chamber that contains three copper disks with sintered layers of silver powder with 1000 Å grains. The total area of these layers is 300 m². The disks have been welded to a copper conical joint, 10 mm diameter and with a 10° apex angle, to which a thermal switch is fastened (1). The electrical resistance of the joint ranges from 0.1 to 0.3 μΩ at 4.2 K.

The thermal switch is made from 30 lead wires 10 mm long, 0.5 mm in diameter, and 99.99% pure. The switch is welded to the heat lead (2), which is made from a bundle of glass insulated copper wires. The wires have a diameter of 0.5 mm, a resistance ratio $R_{300}/R_{4.2} \simeq \simeq 900$, and a total 4.2 K resistance of 0.6 μΩ. The nuclear stage design and its connection to the experimental chamber are similar to those designed by the author for the rotating cryostat of the Joint Soviet-Finnish ROTA project. This makes the experimental chambers of the Helsinki and Moscow installations interchangeable. The nuclear stage (3) consists of 2136 copper wires 0.5 mm in diameter, 250 mm long, and weighing 840 g. Each set of 8 wires is welded to a cooling duct, which is made from the same sort of wire, and which, in turn, is welded to the nuclear stage's base member (4). An ³He chamber (5) is fastened to the base by a conical joint. The chamber incorporates a copper chamber with a sintered silver heat exchanger 10 m² in area and a stycast experimental chamber.

The nuclear demagnetization stage is put inside a superconducting solenoid (6), which has a critical field strength of 8.9 T and was designed and manufactured at the Kurchatov Institute. The solenoid incorporates compensating coils so that the field strength value over the experimental region do not vary by more than 0.03% of the solenoid's field strength. A field probe coil (7) is inserted into the compensation coils.

The nuclear demagnetization cryostat is screened by a stainless-steel thermal shield which is electroplated with copper and breaks along the cryostat's axis. The shield is fastened to the mixing chamber of the dilution refrigerator. A similar thermal shield protects the dilution refrigerator and is fastened to the still.

The dilution refrigerator cools the nuclear stage down to 20 mK within 24 hours and to 16 mK within 100 hours. Following the demagnetization, a minimum temperature of 0.6 mK for a helium-3 sample was obtained in the experimental chamber under a pressure of 29 atm. The cryostat makes it possible to perform experiments with a superfluid ³He for as long as 4-12 days after a single demagnetization cycle. An analysis of the refrigerator's operation indicated that its pre-cooling was limited by the thermal switch being too rigid, and the final temperature of ³He is limited both by a direct heat supply of about 1-2 nW to the chamber and by the heat transfer inside the chamber being too small. If these defects were eliminated, the cryostat would be able to cool the ³He down to about 0.1 mK.

3.3. INSTABILITY OF HOMOGENEOUS PRECESSION IN ${}^3\text{He-A}$ AND ITS EFFECT ON RELAXATION PROCESSES

3.3.1. Basic Properties of the ${}^3\text{He}$ Superfluid Phases

The coherent quantum state in a system of ${}^3\text{He}$ fermions is due to both the formation of ${}^3\text{He}$ atomic pairs and their Bose condensation. Accordingly, a macroscopic quantum system can be described in terms of a quantum-mechanical ordering parameter that is analogous to a single-particle wave function. In helium-3 which, as has been established, to be paired into the state with the orbital moment, $\mathcal{L} = 1$, and the spin moment, $\mathfrak{S} = 1$, a complete description of the system necessitates the introduction of the projections of the orbital and spin moments onto specified directions. The properties of ${}^3\text{He-A}$ are consistent with the model proposed by Anderson, Brinkman, and Morel [3.10], in which the spin and orbital terms of the ordering parameter are separated. The projections of the spin and orbital moments onto certain axes in coordinate and spin spaces, \mathbf{d} and \mathbf{l} , are $\mathfrak{S}_d = 0$ and $\mathcal{L}_l = 1$, respectively. Accordingly, specifying the \mathbf{d} and \mathbf{l} axes determines the orientation of the ordering parameter. By supplementing these by a temperature dependent gap in the excitation spectrum, we arrive at a complete description of the superfluid ${}^3\text{He-A}$ ground state.

The experimental properties of ${}^3\text{He-B}$ agree with the more complicated model of Balian and Werthamer [3.11], in which the spin and orbital terms of the ordering parameter are not separated. However, for every pair of atoms on the Fermi sphere, situated at the points \mathbf{K} and $-\mathbf{K}$, there is an axis $\mathbf{d}(\mathbf{K})$ such that the spin projections vanish. The direction of the vector $\mathbf{d}(\mathbf{K})$ is given by the relative positions of the paired atoms in momentum space. The quantities $\mathbf{d}(\mathbf{K})$ and \mathbf{K} are related in the following manner:

$$\mathbf{d}(\mathbf{K}) = \hat{R}(\theta, \mathbf{n}) \mathbf{K} \quad (3.2)$$

where $\hat{R}(\theta, \mathbf{n})$ is the matrix of rotation through an angle θ about the \mathbf{n} axis. The scalar θ and the vector \mathbf{n} completely define the spin part of the ordering parameter. Hence, they can be used for describing the ordering parameter of superfluid ${}^3\text{He-B}$.

For a nonexcited state in a rather strong magnetic field, the magnetization in ${}^3\text{He-A}$, \mathbf{S} , is directed along the magnetic field, whereas the vector \mathbf{d} is perpendicular to it. In ${}^3\text{He-B}$, \mathbf{S} and the vector \mathbf{n} are parallel to \mathbf{H} , but the energy retaining \mathbf{n} along \mathbf{H} (the magnetic anisotropy energy of the B-phase) is very low.

The equations of motion for the vectors characterizing the ordering

parameter in helium-3's superfluid phases were derived by Leggett [3.12]. Without going into the details of the derivation, we shall only clarify their physical meaning.

Spontaneous magnetization does not occur in superfluid ${}^3\text{He}$ (except for a special state in the vortex cores of rotating ${}^3\text{He-B}$ [3.13]), therefore the magnetic part of the free energy has the form:

$$F_H = \frac{\gamma^2 S^2}{2\chi} - \gamma \mathbf{H} \mathbf{S} \quad (3.3)$$

where χ is the susceptibility and γ is the ${}^3\text{He}$ gyromagnetic ratio. It can be easily shown that any deviation of ${}^3\text{He}$ magnetization from the equilibrium entails a precession of the vector \mathbf{d} . Let us consider the properties of the ordering parameter in the frame of reference rotating in phase with the \mathbf{d} vector. Let the rotation frequency be ω . In this frame, the free energy F_H must be augmented by the terms $\omega \mathbf{S}$. Thence, from the energy minimum condition with respect to \mathbf{S} we have

$$\omega = \frac{\gamma^2 S}{\chi} - \gamma \mathbf{H} \quad (3.4)$$

which corresponds to the precession of the \mathbf{d} vector in the laboratory frame with the frequency

$$\dot{\mathbf{d}} = \omega \times \mathbf{d} = \left(\frac{\gamma^2 S}{\chi} - \gamma \mathbf{H} \right) \times \mathbf{d} \quad (3.5)$$

This is one of the spin dynamics equations derived by Leggett for the ${}^3\text{He}$ superfluid phases. The second equation describes the variation of \mathbf{S} in time. In this equation an important role is played by the spin-orbital interaction caused by the interaction between the magnetic dipole moments of the ${}^3\text{He}$ nuclei. For ${}^3\text{He-A}$, the free energy of the dipole-dipole interaction has the form:

$$F_{DA} = -\frac{\chi \Omega_A^2}{2\gamma^2} (\mathbf{I} \mathbf{d})^2 \quad (3.6)$$

where Ω_A is a parameter with the dimension of frequency and whose physical meaning we shall consider below. Accordingly, for a strong magnetic field, where \mathbf{H} is the major orientating factor, we have $\mathbf{H} \perp \mathbf{d}$ and $\mathbf{d} \parallel \mathbf{I}$.

For the B phase, the free energy of the dipole-dipole interaction has the form:

$$F_{DB} = \frac{2}{15} \frac{\chi \Omega_B^2}{\gamma^2} \left(\frac{1}{2} + 2 \cos \theta \right)^2 \quad (3.7)$$

where Ω_B is a parameter with the dimension of frequency. The free energy has a minimum at the angle $\theta = \theta_0 = \arccos(-1/4)$. Accord-

ingly, the magnetic and dipole energies govern the equation of motion for \mathbf{S} in ${}^3\text{He}$:

$$\dot{\mathbf{S}} = \gamma [\mathbf{S} \times \mathbf{H}] + \mathbf{R}_D \quad (3.8)$$

where \mathbf{R}_D is the dipole-dipole moment, and can be written for ${}^3\text{He-A}$ in the simple form,

$$\mathbf{R}_D = \frac{\chi \Omega_A^2}{\gamma^2} [\mathbf{d} \times \mathbf{l}] (\mathbf{d} \mathbf{l}) \quad (3.9)$$

Accordingly, the system of equations (3.5)-(3.8) is complete for ${}^3\text{He}$ spin dynamics without dissipation. The solutions of this system in strong fields are two oscillation modes called the longitudinal and transverse modes according to the polarization of the \mathbf{S} vectors in them. In the limit of small oscillations, the longitudinal mode is associated with the oscillations of $|\mathbf{S}|$ and with oscillations of \mathbf{d} within a plane perpendicular to \mathbf{S} and with frequency Ω_A (Ω_B). This is why these frequencies were used in eqs. (3.6) and (3.7) as parameters of the dipole-dipole interaction. The longitudinal resonance frequencies which depend on both temperature and pressure are extremely suitable parameters for specifying the spin dynamics of the A and B phases of ${}^3\text{He}$.

The transverse mode constitutes the precession of the magnetization \mathbf{S} around the magnetic field and, simultaneously, the motion of the \mathbf{d} vector at the same frequency along a figure-of-eight trajectory (in ${}^3\text{He-A}$). In ${}^3\text{He-B}$, the \mathbf{n} vector precesses around \mathbf{H} (for free ${}^3\text{He}$). The precession frequency of the transverse mode is a superposition of the longitudinal oscillation frequency and that of the Larmor precession. The value of the additional term with Larmor precession frequency depends on the concrete situation. In particular, in a strong magnetic field in free ${}^3\text{He}$ (not bounded by closed vessel walls) with a space-uniform ordering parameter and in the absence of both superfluid currents and a strong electric field, the longitudinal mode frequency in ${}^3\text{He-A}$ is

$$\omega_L^2 = \gamma^2 H^2 + \Omega_A^2 \left(\frac{1}{4} + \frac{3}{4} \cos \beta \right)^2 \quad (3.10)$$

where β is the angle of deviation of \mathbf{S} relative to \mathbf{H} (tilting angle). For ${}^3\text{He-B}$ under these conditions, the precession frequency equals the Larmor frequency, when $\beta < 104^\circ$. The dynamic properties of ${}^3\text{He-B}$ will be considered in greater detail in Sec. 3.4, whereas now we shall turn to describing the "intrinsic" relaxation process proposed by Leggett and Takagi [3.14], within whose framework the relaxations in superfluid ${}^3\text{He}$ are generally treated.

3.3.2. "Intrinsic" Relaxation Mechanism in Superfluid ^3He

All the above ^3He properties were dealt with in the "nondissipative" approximation. One of the basic processes resulting in relaxation of the magnetization after its excitation are "collisions" between quasiparticles of the superfluid ^3He . The characteristic time of these collisions, τ , is a major parameter equalizing both the magnetic and orbital parts of the ordering parameter. Qualitatively, the "intrinsic" relaxation mechanism is reduced to the following process. Under equilibrium conditions and at a given temperature, a certain fraction of the ^3He atoms are in the superfluid state, the remaining being in the normal state. It should be remembered that ^3He atoms spend some time in the superfluid state and the rest of the time is spent in the normal state, where the time τ specifies the transition frequency of the atoms between the states. The ratio of superfluid fraction magnetic moment against the total ^3He magnetic moment will be denoted via the parameter λ :

$$\lambda = \frac{S_s}{S}; \quad 1 - \lambda = \frac{S_n}{S} \quad (3.11)$$

The spin dynamics equations for \mathbf{S}_s and \mathbf{S}_n will be different. The dipole-dipole moment \mathbf{R}_D does not directly influence \mathbf{S}_n . Accordingly,

$$\begin{aligned} \dot{\mathbf{S}}_s &= \gamma [\mathbf{S}_s \times \mathbf{H}] + \mathbf{R}_D \\ \dot{\mathbf{S}}_n &= \gamma [\mathbf{S}_n \times \mathbf{H}] \end{aligned} \quad (3.12)$$

However, the equations for \mathbf{S}_s and \mathbf{S}_n are not separated, since both yield an effective magnetic field that is incorporated into the equation of motion for \mathbf{d} vector,

$$\dot{\mathbf{d}} = \gamma \left[\mathbf{d} \times \left(\mathbf{H} - \frac{\gamma \mathbf{S}_s}{\chi_s} - \frac{\gamma \mathbf{S}_n}{\chi_n} \right) \right] \quad (3.13)$$

where χ_s and χ_n are the susceptibilities of ^3He superfluid and normal components, respectively.

When the magnetization of the superfluid or normal component is not the equilibrium one, then collisions between quasiparticles must take the magnetization back to equilibrium. The process can conveniently be specified by the vector $\boldsymbol{\eta} = \mathbf{S}_s - \lambda \mathbf{S} \equiv (1 - \lambda) \times \mathbf{S}_s - \lambda \mathbf{S}_n$, which describes the deviations of \mathbf{S}_s and \mathbf{S}_n , respectively, from equilibrium. In the frame of reference in which the equilibrium magnetization is at rest, the process of restoring \mathbf{S}_s and \mathbf{S}_n to the

equilibrium value can be described by the equations

$$\begin{aligned} (\dot{\mathbf{S}}_s + \dot{\mathbf{S}}_n)_{(\dot{\mathbf{S}}=0)} &= 0 \\ \dot{\eta}_{(\dot{\mathbf{S}}=0)} &= -\frac{1}{\tau} \eta \end{aligned} \quad (3.14)$$

Accordingly, from equations (3.12)-(3.15) in the laboratory frame we have the equations of the dynamics of a spin system with the "intrinsic" dissipation mechanism:

$$\begin{aligned} \dot{\mathbf{S}} &= \gamma [\mathbf{S} \times \mathbf{H}] + \mathbf{R}_D \\ \dot{\mathbf{d}} &= \gamma \left[\mathbf{d} \times \left(\mathbf{H} - \frac{\gamma}{\chi} \mathbf{S} - \frac{\gamma}{\chi_s} \eta \right) \right] \\ \dot{\eta} &= \gamma \left[\eta \times \left(\mathbf{H} - \frac{z_0 \gamma}{4 \chi_{n0}} \mathbf{S} \right) \right] - (1 - \lambda) \mathbf{R}_D - \frac{\eta}{\tau} \end{aligned} \quad (3.15)$$

where z_0 is the Fermi liquid correction describing the deviation of the ${}^3\text{He}$ normal component susceptibility, χ_n , from the ideal Fermi gas susceptibility, χ_{n0} ,

$$\chi_n = \chi_{n0} \left(1 + \frac{z_0}{4} \right)^{-1} \quad (3.16)$$

In the limit of relatively low precession frequencies ($\omega\tau \ll 1$) and small tilting angles, the system of equations (3.15) has the solution

$$\exp(-i\omega t - t/T) \quad (3.17)$$

For the longitudinal mode in the A-phase we have

$$\omega = \Omega_A; \quad \frac{1}{T_{\parallel}} = \frac{1-\lambda}{2\lambda} \Omega_A^2 \tau \left(1 + \frac{z_0}{4} \right)^{-1} \quad (3.18)$$

Accordingly, for the transverse mode we have

$$\omega^2 = \Omega_A^2 + \gamma^2 H^2; \quad \frac{1}{T_{\perp}} = \frac{1}{T_{\parallel}} \frac{\Omega_A^2}{\Omega_A^2 + \gamma^2 H^2} \quad (3.19)$$

For the B-phase, formula (3.18) is also valid, if we make the substitution $\Omega_A \rightarrow \Omega_B$. For magnetization tilting angles $\beta < 104^\circ$ the transverse mode has no frequency shift, and as a consequence the above relaxation mechanism fails.

The large β 's that are easily realized during experiments with pulsed resonance are very interesting. The expression for the relaxation in this case was derived using the adiabatic approximation by Fomin [3.15], and for the A-phase it has a form

$$\frac{du}{dt} = 2\kappa \left(\frac{\Omega_A}{4} \right)^6 (1-u)(35u^3 + 55u^2 + 25u + 13) \quad (3.20)$$

where $u = \cos \beta$ and κ is the phenomenological parameter. For the tilting angles $\beta \geq 20^\circ$, the relaxation is approximately linear.

In the limit of small β 's, expression (3.20) has the following asymptotic

$$(1 - u) = (1 - u_0) \exp [-\kappa \Omega_A^4 (t - t_0)] \quad (3.21)$$

Whence, by correlating this with (3.19) and taking into account that the variation in the transverse magnetization components is linear in β , whereas that of longitudinal components is proportional to β^2 (in the limit of small angles), we have

$$\kappa = \frac{1-\lambda}{\lambda} \tau \gamma^{-2} H^{-2} \left(1 + \frac{z_0}{4}\right)^{-1} \quad (3.22)$$

As was demonstrated in [3.16], as $T \rightarrow T_c$ the quantity τ from the Leggett-Takagi equation corresponds to τ_0 , viz. the time elapsed between collisions of quasiparticles in the normal ${}^3\text{He}$ phase. Since $\tau_0 \sim T^{-2}$, the value of τ obtained at different pressures should be proportional to T_c^{-2} . Therefore, following [3.17], in order to compare the results gained for different pressures, we have to specify the dissipative process of "intrinsic" relaxation by the parameter τT_c^2 .

The experimental research on relaxation processes in the spin system of ${}^3\text{He}$ superfluid phases originated from studies of the line broadening of steady-state NMR [3.18]. The results corroborated the validity of eqs. (3.18) and (3.19). The parameter τT_c^2 was found in these experiments to be $0.36 \mu\text{s (mK)}^2$.

Later experiments were performed on pulsed NMR [3.19, 20]. The restoration of longitudinal magnetization after a powerful RF pulse was studied in these experiments. To do this, the second RF pulse was fed into the system a certain delay time after the first pulse, and then the induction signal's amplitude was matched against the value of the longitudinal magnetization at the instant the second pulse is fed in. The first pulse forces the magnetization to deviate through 90° . According to (3.20), the relaxation of the longitudinal magnetization after this pulse must be almost linear except for small angles and must cover about $8T_\perp$. Thus, at a temperature of $T = 0.96T_c$, given the conditions contained in [3.19], the time it takes for full recovery of the magnetization (FRT) in a field of 463 Oe, i.e. T_{FRT} , should be $\sim 750 \text{ ms}$, whereas given the conditions in [3.20], in a field of 284 Oe it should be $\sim 500 \text{ ms}$. However, the experimental time for the complete restoration of magnetization appeared to be an order of magnitude shorter, i.e. 30 and 20 ms, respectively. A search thus began for another, faster mechanism that could lead to a relaxation in ${}^3\text{He-A}$ at large deviation angles β of the spin system.

To this end, we undertook studies of the damping of the induction signal inside superfluid ${}^3\text{He-A}$, in as homogeneous an external field as possible. According to (3.10), the precession frequency in ${}^3\text{He-A}$ should depend on the angle the magnetization vector has deviated,

i.e. β . Thus, following a change in the precession frequency during an induction signal we hoped to study the relaxation process occurring in a uniform magnetic field.

3.3.3. A Study of the ^3He -A Free Induction Signal

In order to study free induction, a new chamber was manufactured (Fig. 3.7). The experimental vessel was a cylinder 0.5 mm in diameter and 13 mm long connected through a narrow

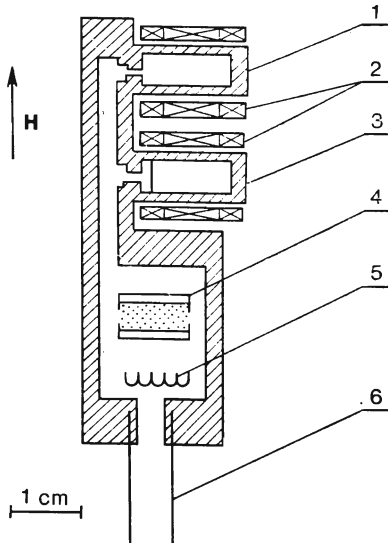


Fig. 3.7. Experimental chamber: 1—the chamber for studying ^3He in open geometry, 2—subdivided RF coils, 3—the chamber containing lavsan plates parallel to external field's direction, 4—NMR thermometer sensor, 5—heater, 6—the duct leading to the sintered heat exchanger in the nuclear demagnetization cryostat.

duct with the remaining volume of the ^3He container. The second experimental vessel was a parallelepiped $5 \times 5 \times 12$ mm in size and filled with lavsan (mylar) plates 0.01 mm thick spaced 0.3 mm apart. The plates were oriented along an external magnetic field. Since the ^3He -A precession frequency is a function of spin deviation angles, much thought was given to homogeneity in the driving RF field. To ensure this, the RF coil is subdivided into three sections whose numbers of turns were calculated and then corrected, after having measured the RF field's homogeneity. The resulting homogeneity was checked experimentally by means of an induction signal excited in a tiny pickup loop placed at different points on the RF

coil. The RF field's profile along the axis of experimental chamber is shown in Fig. 3.8. The figure also depicts the helium distribution in the chamber within the working range of RF field. The homogeneity of the external magnetic field is controlled by an induction signal in ${}^3\text{He}$'s normal phase. Helmholtz coils have been used to correct the linear gradients. In addition, a small permanent magnet placed outside the cryostat enabled us to decrease slightly the second

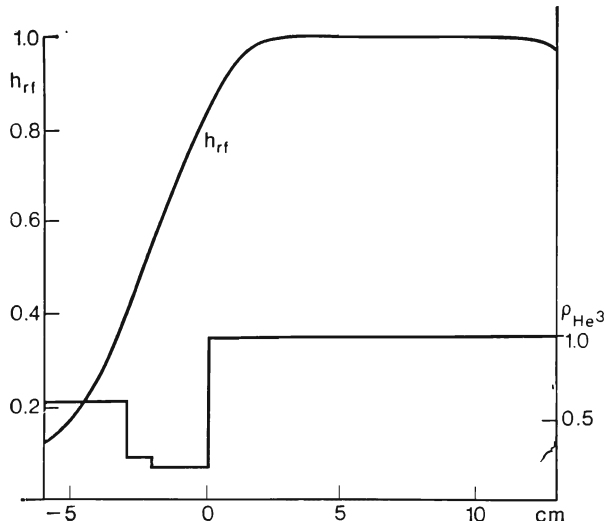


Fig. 3.8. RF field's amplitude distribution along the axis of the experimental chamber and the ${}^3\text{He}$ distribution inside the chamber without plates.

spatial derivatives of the magnetic field. The ${}^3\text{He}$ pressure in the experimental chamber was 2.1×10^4 torr. Our experiments were performed in a magnetic field which corresponded, in the limit of small β 's, to the ${}^3\text{He}$ -A precession frequencies of 250 and 500 kHz.

The setup's electronic equipment included a powerful RF pulse generator, a broad-band pre-amplifier, a resonance amplifier, and the Datalab-905 fast memory unit. The exciting RF pulse with a length of 4 periods at 250 kHz or 8 periods at 500 kHz, was applied across the RF coil. The spin induction signal was picked up by the same coil, amplified by the RF amplifier and stored at 1024 points. In order to make processing the data on the induction signal frequency and amplitude more convenient, a time delay between signal storage instants was made

$$\tau_n = \frac{4n+1}{4\omega}$$

where ω is the RF pulse frequency. Thus, at $n = 0$ the induction signal was written to 4 points per period. If the signal had to be observed for 250 periods, the spacing between the points was made in such a way that signals in adjacent points were changed in phase by $\sim\pi/2$. Next, the signal record was transferred to a computer and simultaneously observed on monitor. The external magnetic field was chosen so that after magnetization vector deviated through a small angle ($\sim 7^\circ$) the induction signal phase in the record points remains constant, viz. the induction signal frequency agrees with that of the

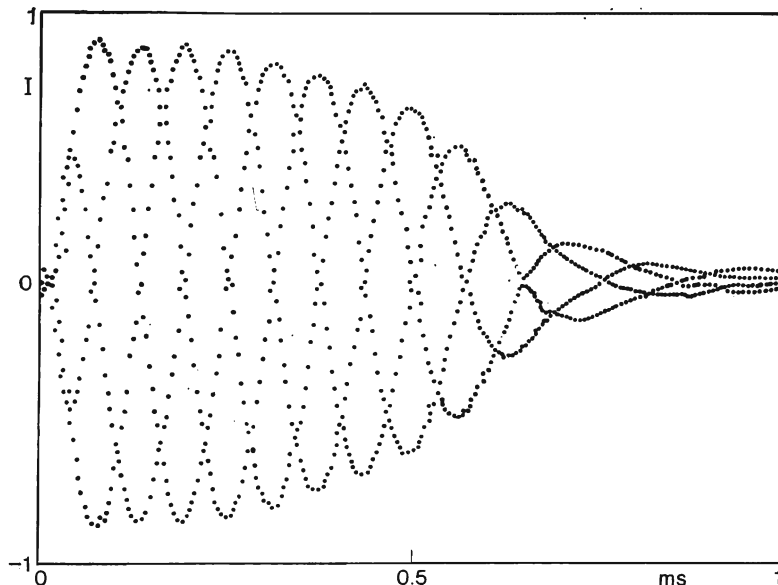


Fig. 3.9. The induction signal in ${}^3\text{He-A}$ following a change in the direction of the magnetization vector by $\beta = 81^\circ$. The signals were recorded when $\tau = (4 \times 250 \times 10^3)^{-1}$ s.

RF pulses. Since in the limit of small angles for ${}^3\text{He-A}$ we have $\omega_{\perp}^2 = \gamma^2 H^2 + \Omega_A^2$, Ω_A is determined using the value of resonance magnetic field, and from the known dependence $\Omega_A(T)$ we get the temperature. Figure 3.9 depicts a typical induction signal record for $\beta = 81^\circ$ ($\omega = 250$ kHz, $\Omega_A = 55$ kHz).

The recorded signal phase is clearly seen to be time-dependent, this indicating that the induction frequency differs from 250 kHz. We can also see that the rate at which the phase changes is time-dependent, too. The computer has approximated every 16 recorded points by a sinusoid of the appropriate frequency, phase, and amplitude, thus reconstructing the parameters of the primary induction signal and bringing out them graphically.

The ${}^3\text{He}$ β due to the RF pulse was dependent on the induction signal amplitude in the normal phase. The change in β caused by a frequency shift in A-phase amounts to no more than 2° at minimum Ω_A and $\beta \sim 100^\circ$, according to the computer calculations of the magnetization vector's motion caused by the RF fields [3.21].

As seen from Fig. 3.9, when the magnetization vector deviates through $\beta = 81^\circ$, the induction signal decays for ~ 0.8 ms. Such fast signal decay cannot be explained by an inhomogeneity in the

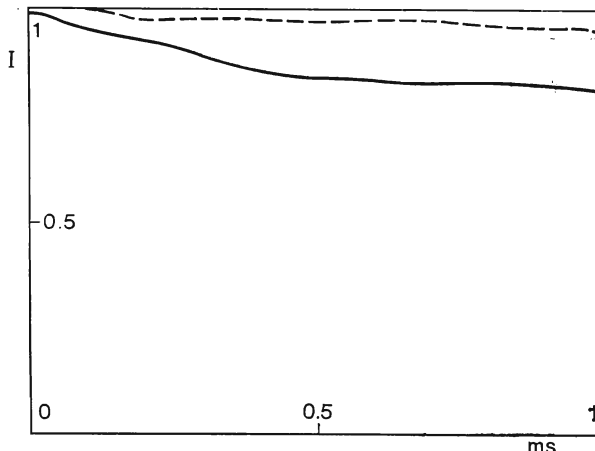


Fig. 3.10. Free induction signal's decay for normal ${}^3\text{He}$ phase at 250 kHz indicating the external magnetic field's homogeneity (dashed line) and the ${}^3\text{He}$ -A induction signal's decay calculated for the conditions in Fig. 3.9 and caused by RF field inhomogeneities (solid line).

external field, an RF field inhomogeneity, or an "intrinsic" relaxation. Fig. 3.10 presents the induction signal decay for the same field in the ${}^3\text{He}$ normal phase. This decay characterizes the external field inhomogeneity. The induction signal phasing-out in ${}^3\text{He}$ -A due to an RF field inhomogeneity has been computed for the given β 's and temperatures according to the RF field and ${}^3\text{He}$ distributions in the chamber (Fig. 3.8) and is also presented in Fig. 3.10. As can be seen, both of these "extrinsic" phasing-outs comprise a small fraction of the induction signal damping. In order to determine more exactly the inherent decay of the ${}^3\text{He}$ induction signal, the phasing-out contributions due to the inhomogeneities in the external and RF fields were excluded from the signal.

We have investigated the induction signal decay as it depends both on temperature and on the tilting angle β . Figure 3.11 contains the time dependencies of the induction signal's intensity at different β 's for a temperature $T = 0.93T_c$ and a frequency 250 kHz.

The experimental data are indicated by dots. The solid curve traces the induction signal decay for a spatially homogeneous relaxation process, as calculated from the Leggett-Takagi theory for $\omega = 250$ kHz and $\Omega_A = 55$ kHz.

The β value was calculated from (3.20) as a function of time, and the value of $S_{\perp}(t) = S_0 \sin[\beta(t)]$ was plotted. The constant value of τT_c^2 which specifies the "intrinsic" relaxation rate was chosen to be 0.29 μs (mK) 2 ; this somewhat differs from that obtained in the experiments on steady-state NMR [3.18], yet is in a good agreement with acoustic experiments [3.17] and our data (see below). The initial points of the experimental relationships obtained for the β 's are plotted according to the theoretical function $\beta(t)$.

It can be seen from Fig. 3.11 that for $\beta \leq 30^\circ$ ${}^3\text{He-A}$ magnetization relaxes in good agreement with the Leggett-Takagi theory. At larger β 's processes emerge that lead to a significantly more rapid change in transverse magnetization.

By means of the frequency dependence of the induction signal it is possible to test the process of longitudinal magnetization restoration. The solid curve in Fig. 3.12 shows the calculated time variation of the ${}^3\text{He-A}$ homogeneous resonance frequency caused by the "intrinsic" relaxation mechanism. According to (3.9), the induction signal frequency is influenced by $\beta(t)$ thus

$$\omega^2(t) = \omega^2 - \Omega_A^2 \frac{9}{16} [\cos \beta(t) - 1]^2 \quad (3.23)$$

The dots and crosses stand for the experimental time relationships of the induction signal frequency at different initial β 's. The initial experimental points for frequency are also fitted to the frequency values for the given β 's. It is clearly seen that for $\beta \leq 50^\circ$ the behavior of the induction signal frequency is consistent with the Leggett-Takagi theory of relaxation. For the larger β 's the restoration of the induction signal frequency occurs much more rapidly.

If the ${}^3\text{He-A}$ is assumed to remain homogeneous during relaxation, formula (3.10) will enable us to find the time variation of the longitudinal magnetization $\dot{S}_{||}(t)$ from the value of the induction signal frequency, whereas $S_{\perp}(t)$ can be found from the value of the induction signal's decay time. The total sample magnetization $[S_{||}^2(t) + S_{\perp}^2(t)]/2$ should be constant. However, for $\beta > 30^\circ$ the total magnetization appears to fall in much the same manner as $S_{\perp}(t)$ does, whence one can conclude that the spatial homogeneity of the precession in ${}^3\text{He-A}$ is strongly violated.

Alternatively, for $\beta \leq 30^\circ$, the ${}^3\text{He-A}$ precesses homogeneously and both the induction signal decay and the signal frequency variation are governed by the intrinsic relaxation mechanism. For $\beta \leq 20^\circ$ the induction signal decay is exponential with a time constant T_{\perp} , which is consistent with (3.19)-(3.21). Figure 3.13 shows the ex-

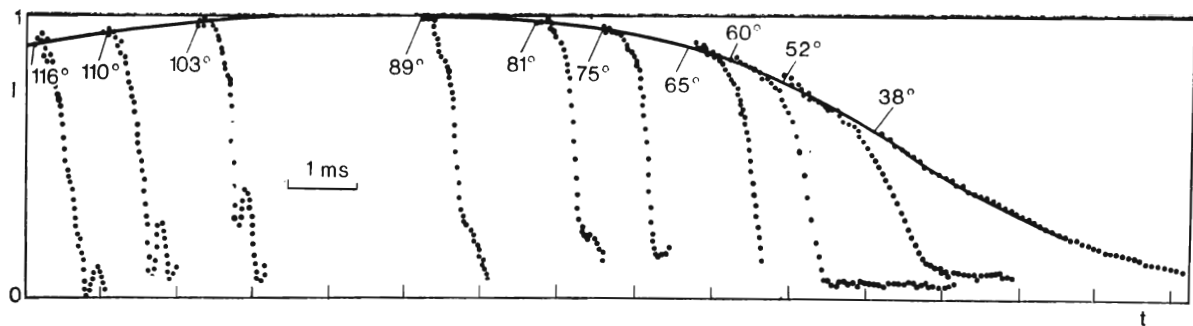


Fig. 3.11. $^3\text{He}-\text{A}$ [induction signal's decay for different β angles (dots). The solid curve is the induction signal's decay as calculated from the Leggett-Takagi theory under homogeneous relaxation conditions. The origin of the experimental dependences is fitted by the tilting angle β to the theoretical curve ($\omega = 250$ kHz, $\Omega_A = 55$ kHz).

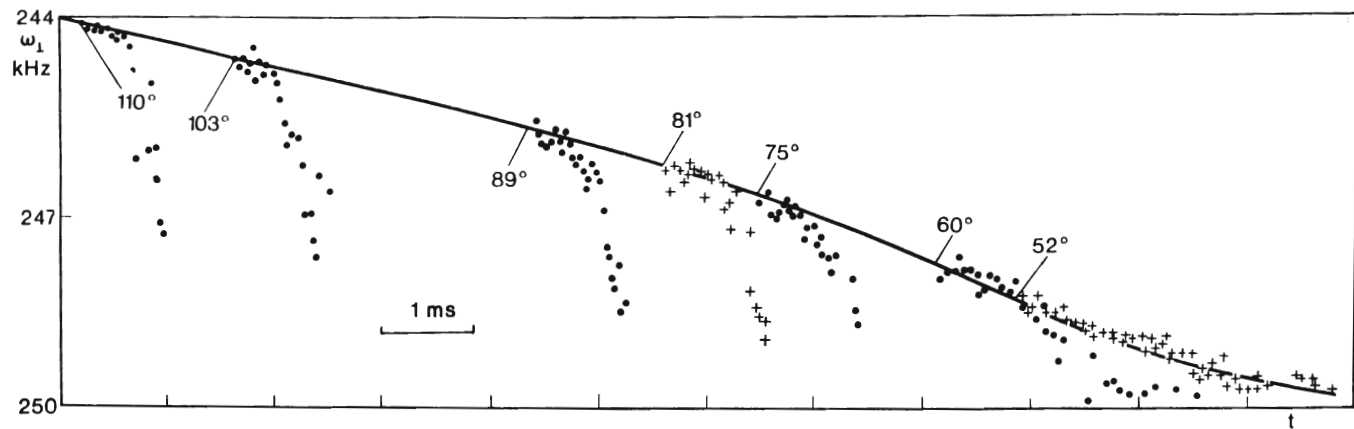


Fig. 3.12. Time variation of the induction signal's frequency for different β 's (dots and crosses). The solid line is the time dependence of the induction signal's frequency as calculated from the Leggett-Takagi theory under homogeneous relaxation conditions. The origin of the experimental dependences is fitted by the tilting angle β to the theoretical curve ($\omega = 250$ kHz, $\Omega_A = 55$ kHz).

perimental values of the induction signal's damping factor versus the frequency Ω_A which is determined by the temperature for NMR frequencies of 250 and 500 kHz. The figure also depicts the theoretical relationship

$$\frac{1}{T_{\perp}} = \frac{1-\lambda}{2\lambda} \frac{\Omega_A^4}{\Omega_A^2 + \gamma^2 H^2} \tau \left(1 + \frac{1}{4} z_0 \right)^{-1}$$

where $\tau = 4.6 \times 10^{-8}$ s, which corresponds to $\tau T_c^2 = 0.29 \mu\text{s}$ (mK) 2 .

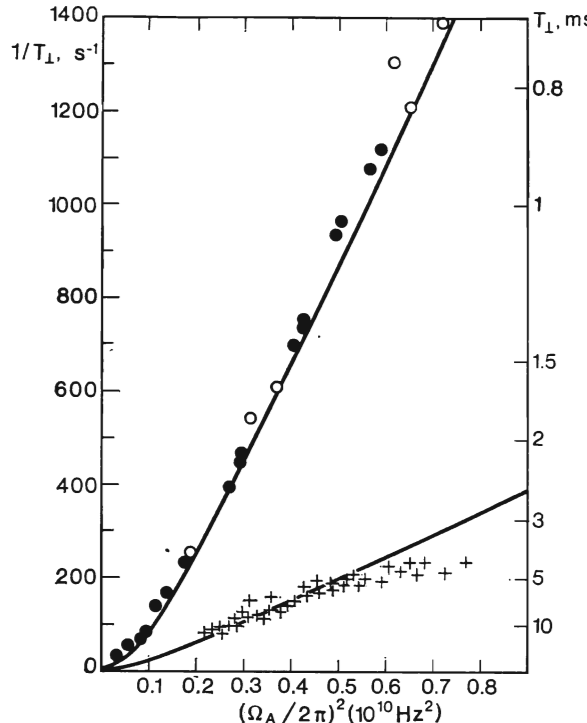


Fig. 3.13. Damping of the induction signal for $\beta \leq 30^\circ$ versus the longitudinal oscillation frequency, Ω_A , at the NMR frequencies of 250 kHz (●, ○) and 500 kHz (+) inside the chamber with $^3\text{He-A}$ open geometry (○, +), and inside the chamber with parallel plates (○). Solid line is the dependence as calculated from the Leggett-Takagi theory with the constant $\tau T_c^2 = 0.29 \mu\text{s}$ (mK) 2 .

The dependence of $\frac{1-\lambda}{\lambda} \left(1 + \frac{1}{4} z_0 \right)^{-1}$ on Ω_A (see Fig. 3.13) was obtained by recalculating the curve published in [3.17].

It follows from the experimental data, relaxation in a chamber containing a set of plates parallel to external field occurs at the same

rate as in an empty chamber. Moreover, note the systematic deviation of the experimental points from the theoretical curve at low temperatures and for 500 kHz.

The abrupt acceleration in the induction signal's decay at the large β 's can be explained by the theory of instability of $^3\text{He-A}$ homogeneous precession.

3.3.4. Instability of Homogeneous Precession in $^3\text{He-A}$

In 1979 the instability of homogeneous precession in $^3\text{He-A}$ was demonstrated theoretically by Fomin [3.22]. He showed that the homogeneous precession decays into spin waves of large am-

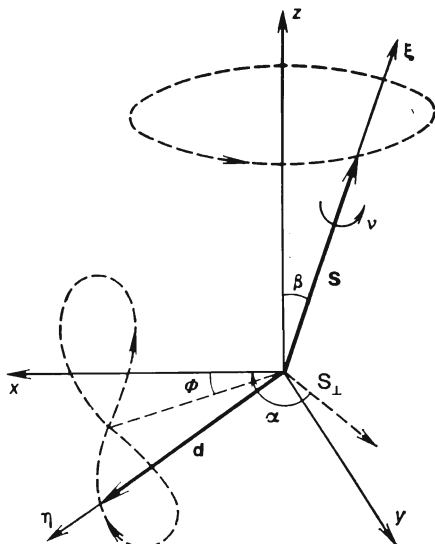


Fig. 3.14. The rest (x, y, z) and body (ξ, η, ζ) coordinate systems and the trajectories of the \mathbf{S} and \mathbf{d} vectors in a transverse oscillation mode. α , β , and v are Euler angles, $\Phi = \alpha - v$.

plitude [3.23] which can conveniently be considered in the frame of reference related to ^3He average magnetization [3.24].

For strong magnetic fields, such that $\left(\frac{\Omega_A}{\gamma H}\right)^2 \ll 1$, the vectors \mathbf{S} and \mathbf{d} are closely related. (In any case in order to excite them to move relatively to each other an energy of the order of Zeeman's energy is needed.) When \mathbf{S} deviates from the magnetic field direction, the magnetization vector precesses around \mathbf{H} , and is involved in slower motions caused by dipole-dipole interactions. Following Leggett and Takagi [3.14], we shall introduce a frame of reference (ξ, η, ζ) close-

ly connected with the vectors \mathbf{S} and \mathbf{d} and shall specify its orientation through the Euler angles α , β , and ν , which are respectively the angle of rotation around the axis $\mathbf{z} \parallel \mathbf{H}$, the inclination of the ξ axis from the \mathbf{z} -axis and the angle of rotation around the axis ξ (see Fig. 3.14).

In this frame of reference, Leggett's equations of motion have the much simpler form:

$$\begin{aligned}\dot{S} &= -\gamma H \frac{\partial F_D}{\partial \gamma} & \dot{\nu} &= \gamma H \left(S + \frac{\partial F_D}{\partial S} \right) \\ \dot{S}_z &= -\gamma H \frac{\partial F_D}{\partial \alpha} & \dot{\alpha} &= \gamma H \left(-1 + \frac{\partial F_D}{\partial S_z} \right)\end{aligned}\quad (3.24)$$

Here S is the magnetization along the ξ axis normalized over the equilibrium magnetization, and F_D is the free energy of dipole-dipole interaction.

Since we are interested in the case of precession of almost all the magnetization around \mathbf{H} , we shall assume that $S \simeq 1$. In this way we can compose a slow variable from the two fast variables γ and α , i.e. $\Phi = \alpha + \gamma$, and average the dipole-dipole energy over a fast variable, $\langle E_D(\alpha, \Phi, S_z, S) \rangle = V(\Phi, P/S)$. As a result, we obtain

$$\begin{aligned}\dot{S} &= -\gamma H \frac{\partial V}{\partial \Phi} & \dot{\Phi} &= \gamma H \left(S - 1 + \frac{\partial V}{\partial S} \right) \\ \dot{P} &= 0 & \dot{\alpha} &= \gamma H \left(-1 + \frac{\partial V}{\partial P} \right)\end{aligned}\quad (3.25)$$

where $P = S_z - S$ is the adiabatic invariant of motion.

It can be seen that the precession \mathbf{S} occurs at the frequency

$$\omega_{\perp} = \gamma H \left(-1 + \frac{\partial V}{\partial P} \right) \quad (3.26)$$

(given the approximation $\Omega_A^2 \ll \gamma^2 H^2$). On the other hand, when not at equilibrium, \mathbf{S} and Φ execute small oscillations at a frequency

$$\omega_{\parallel}^2 = \frac{\partial^2 V}{\partial \Phi^2} \gamma^2 H^2 \quad (3.27)$$

For ${}^3\text{He-A}$, the averaged dipole-dipole potential has the form

$$V_A = -\frac{\Omega_A^2}{8\gamma^2 H^2} \left[\left(1 + \frac{P}{S} \right)^2 + \frac{1}{2} \cos 2\Phi \left(2 + \frac{P}{S} \right)^2 \right] \quad (3.28)$$

At $S = 1$ and $\Phi = 0$, π the homogeneous precession frequency will be

$$\dot{\omega}_{\perp} = -\gamma H - \frac{1}{8} \frac{\Omega_A^2}{\gamma H} (4 + 3P) = -\gamma H - \frac{1}{8} \frac{\Omega_A^2}{\gamma H} (1 + 3 \cos \beta),$$

since $P = S - S_z \approx \cos \beta - 1$.

Figure 3.14 shows the precession of the \mathbf{S} and \mathbf{d} vectors, and indicates the positions of the angles α , β , v , Φ , as well as the fixed (x, y, z) and precessing (ξ, η, ζ) frames of reference.

The spatially homogeneous precession appears to be unstable in ${}^3\text{He-A}$. In fact, by virtue of the equations of motions, the quantity P is an adiabatic invariant and can be considered as a thermodynamic variable. Let us substitute the ${}^3\text{He}$ volume into two parts and exchange the quantity δP between them. This exchange is energetically unfavorable if the second differential of the free energy with respect to P is positive. Under the conditions of our problem, this requirement will reduce to

$$\frac{\partial^2 V}{\partial P^2} > 0 \quad (3.30)$$

This is equivalent [3.24] to the condition

$$\frac{d\omega_{\perp}(P)}{dP} > 0 \quad (3.31)$$

For ${}^3\text{He-A}$, we have $\frac{d\omega_{\perp}(P)}{dP} = -\frac{3}{8} \frac{\Omega_A^2}{\gamma H} < 0$, and this means that the homogeneous precession is unstable. Thus, it is energetically favorable to increase P in one part of the volume, and this will be equivalent to an increase in the deviation angle β , and simultaneously to decrease P (and β) in the other part of the volume so that, on the average, the available adiabatic invariant P will be conserved. The spatial structure of the developing instability is extremely complicated. A growth in the instability should be resisted by ${}^3\text{He}$ gradient energy, viz. the elastic energy of the ordering parameter. Besides, spin diffusion should result in an effective ${}^3\text{He}$ relaxation to the $\mathbf{S} \parallel \mathbf{H}$ state as soon as a spatial inhomogeneity begins to develop. In the limit of small perturbations to the homogeneous precession, this problem was solved in [3.22, 3.23, 3.25]. The ${}^3\text{He-A}$ precession at the frequency $\omega_{\perp}(\cos \beta)$ and $S = S_0 = \text{const}$; $\beta = \beta_0 = \text{const}$; $\alpha = \alpha_0(t) = \omega_{\perp}t + \text{const}$; $\Phi_0 = 0$ was investigated with respect to its stability to perturbations in the S , β , α , Φ quantities, which depend on a spatial variable \mathbf{r} , the perturbations being respectively $\cos \beta = \cos \beta_0 + \varepsilon(\mathbf{r})$; $\alpha = \alpha_0 + v(\mathbf{r})$; $S = S_0 + \sigma(\mathbf{r})$; and $\Phi = \Phi_0 + \Psi(\mathbf{r})$. With a due regard for the gradient energy and spin diffusion, the solution of the linearized equations of motion for the Fourier components of the perturbations has the form of spin waves:

$$\varepsilon = \varepsilon_0 \exp(-i\omega t - i\mathbf{K}\mathbf{r})$$

$$v = v_0 \exp(-i\omega t - i\mathbf{K}\mathbf{r})$$

$$\Psi = \Psi_0 \exp(-i\omega t - i\mathbf{K}\mathbf{r})$$

$$\omega = \left[\frac{C_h}{4\gamma^2 H^2} \left(-\frac{3}{4} \Omega_A^2 \sin^2 \beta + C_h \right) \times \right. \\ \left. \times \frac{\Omega_A^2 (3 - \cos \beta) (1 + \cos \beta) + 4C_h}{\Omega_A^2 (1 + \cos \beta)^2 + 4C_h} \right]^{1/2} - iD_h \quad (3.32)$$

where $C_h = C_{\alpha\beta}^2 K_\alpha K_\beta$; $D_h = D_{\xi\eta} K_\xi K_\eta$; and $C_{\alpha\beta}^2$ is the tensor of the squared velocities of the spin waves and $D_{\xi\eta}$ is the tensor of spin diffusion coefficients.

In the limit of a ${}^3\text{He}-\text{A}$ spin system at rest,

$$\cos \beta = 1, \quad \omega = \frac{C_h}{2\gamma H} - iD_h \quad (3.33)$$

and for the perturbations ε, v, Ψ we have solutions in the form of travelling spin waves damping due to spin diffusion.

For a spin system inclined to \mathbf{H} through the angle β , the oscillation frequency of the spatial inhomogeneities with the \mathbf{K} value satis-

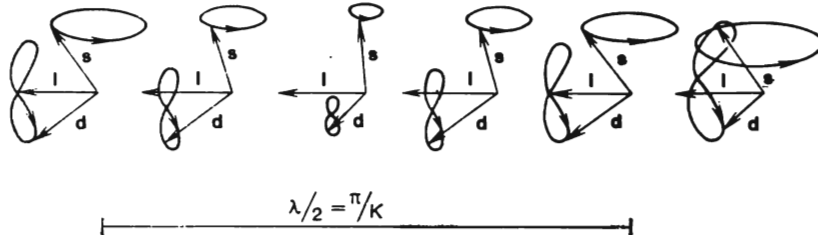


Fig. 3.15. The spatial distributions of the precession phase and amplitude, and the angle Φ for the case of a growing spatial inhomogeneity with the wave vector \mathbf{K} .

fying the condition $C_{\alpha\beta}^2 K_\alpha K_\beta < \frac{3}{4} \Omega_A^2 \sin^2 \beta$ appears to be strictly imaginary and the solution of the equations of motion for the perturbations takes the form:

$$\begin{aligned} \varepsilon &= \varepsilon_0 \exp(\Gamma_h t - i\mathbf{K}\mathbf{r}) \\ v &= v_0 \exp(\Gamma_h t - i\mathbf{K}\mathbf{r}) \\ \Psi &= \Psi_0 \exp(\Gamma_h t - i\mathbf{K}\mathbf{r}) \end{aligned} \quad (3.34)$$

where Γ_h is the modulus ω , see (3.32). Thus, a spatial inhomogeneity with a rising increment Γ_h develops against a homogeneous precession background. The ε, v, Ψ values are found to be of the same order of magnitude, whereas σ is substantially smaller. This mode can be represented qualitatively as in Fig. 3.15.

To estimate the effect of developing inhomogeneities on the experimentally observed amplitude and frequency of the free induction signal, both a suitable recalculation and an integration over all

the \mathbf{K} 's must be performed. It should be borne in mind that in the general case the initial perturbations ε_0 , v_0 , and Ψ_0 also depend on \mathbf{K} and the problem becomes very involved.

Assuming that amplitudes of the initial perturbations are independent of \mathbf{K} (e.g. thermal fluctuations), and by using the fact that Γ_k has a maximum (Γ_{\max}) with respect to \mathbf{K} , it was shown in [3.25] that the experimentally observed values of the transverse magnetization and precession frequencies depend on time, i.e.

$$\langle S_{\perp} \rangle = S_{\perp 0} \left[1 - \frac{A_s}{\sqrt{2\Gamma_{\max} t}} \exp(2\Gamma_{\max} t) \right] \quad (3.35)$$

$$\left\langle \frac{d\alpha}{dt} + 1 + \frac{3}{8} \frac{\Omega_A^2}{\gamma H} (1 + \cos \beta) \right\rangle = \frac{A_{\delta}}{\sqrt{2\Gamma_{\max} t}} \exp(2\Gamma_{\max} t) \quad (3.36)$$

where A_s and A_{δ} are the constants corresponding to the initial perturbations in the system. Assume for simplicity that $C_{\alpha\beta}^2$ is proportional to $D_{\alpha\beta}$, we find that Γ_{\max} can be written as

$$\Gamma_{\max} = \frac{3}{16} \left(\frac{\Omega_A^2}{\gamma H} \sin^2 \beta \right) K_m \quad (3.37)$$

where K_m is the maximum-in- z value of the function

$$K(z) = 2 \left[z(z-1) \frac{2+3zu+u}{2+3zu-u} - \Lambda z \right] \quad (3.38)$$

where

$$\Lambda = \frac{2\omega D_k}{C_{\alpha\beta}^2}, \quad u = 1 - \cos \beta, \quad z = \frac{4}{3} C_k \frac{1}{\Omega_A^2 \sin \beta} \quad (3.39)$$

The build up of the inhomogeneities has naturally to be somewhat restricted. However, even if this process is stopped, the resultant inhomogeneity will effectively lead to a very fast longitudinal relaxation. In fact it follows from (3.25) that

$$\frac{dS_z}{dt} = -\gamma H \frac{\partial V}{\partial \Phi} = \frac{1}{8} \frac{\Omega_A^2}{\gamma H} (1 + \cos \beta)^2 \sin 2\Phi \quad (3.40)$$

In the homogeneous case, $\sin 2\Phi = 0$ and the magnetization volume runoff is absent. Given an instability, $\sin 2\Phi$ is to be nonzero, which fact should be followed by a longitudinal relaxation with a time constant of

$$\tau_{\text{min}} \simeq \frac{8\gamma H}{\Omega_A^2} \quad (3.41)$$

Simultaneously, the time constant of the "intrinsic" relaxation for a 90° deviation (full recovery time) is

$$\tau_{\text{PT}} \simeq \frac{\gamma^2 H^2}{\Omega_0 \Omega_A^2} \quad (3.42)$$

where $\Omega_0 \simeq 250$ Hz. Thus, even a small deviation from the equilibrium value leads to a substantial speed up of relaxation.

3.3.5. Experimental Studies of an Instability in the Homogeneous Precession in ${}^3\text{He-A}$

As was demonstrated in [3.20], the shape of the induction signal's decay is described by a dependence like

$$I_{\perp} = I_0 [1 - A \exp(t/T_{\Phi})]; \quad (3.43)$$

for $\beta > 50^\circ$, this being consistent with formula (3.35). A more detailed analysis of the experimental curves showed that a better agree-

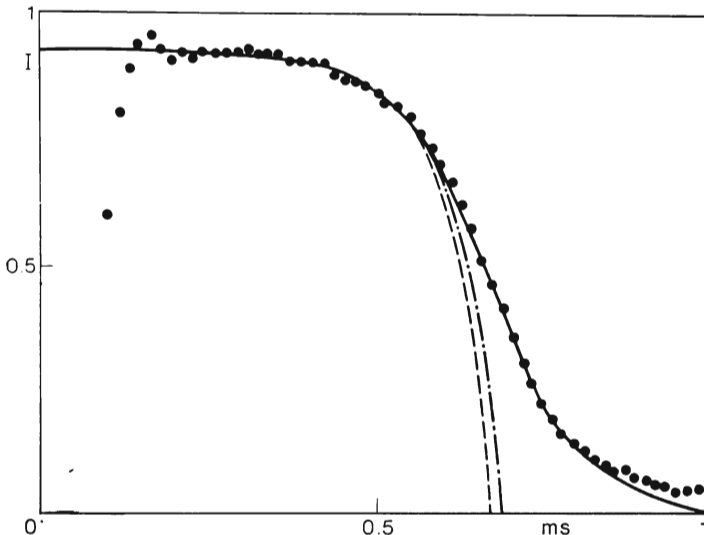


Fig. 3.16. ${}^3\text{He-A}$ induction signal's decay at $\beta = 81^\circ$, $\omega = 250$ kHz, $\Omega_A = 55$ kHz. The functions given are: $I_0 [1 - 10^{-4} \exp(t/T_{\Phi})]$ (dashed curve),

$$I_0 \left[1 - \frac{2 \times 10^{-3} \exp(t/T_{\Phi})}{\sqrt{t/T_{\Phi}}} \right] \text{ (dash-dotted curve),}$$

$$I_0 / [1 + 10^{-4} \exp(t/T_{\Phi})] \text{ (solid curve). For all functions, } T_{\Phi} = 75 \text{ } \mu\text{s.}$$

ment with the experiment is provided by an empirical function of the form:

$$I_{\perp} = I_0 \frac{1}{1 + A \exp(t/T_{\Phi})} \quad (3.44)$$

The latter does not differ from (3.43) in the region of t , where $A \exp(t/T_{\Phi}) \ll 1$, viz. within the domain for which the theory of homogeneous precession instability is valid. On the other hand, the function in (3.44) mirrors the fact that an instability's development has to be restricted. In Fig. 3.16 dependences similar to (3.43),

(3.44), and (3.35) are compared with an experimental curve for the induction signal's decay, given $\beta = 81^\circ$, $\omega = 250$ kHz, and $\Omega_A = 55$ kHz. For all three curves, $T_\Phi = 1/2\Gamma_{\max} = 75\mu\text{s}$.

The behavior of the instability build up increment $1/T_\Phi$ versus the angle β , the external magnetic field, and the temperature was investigated in [3.21]. Figure 3.17 shows the dependence of the build

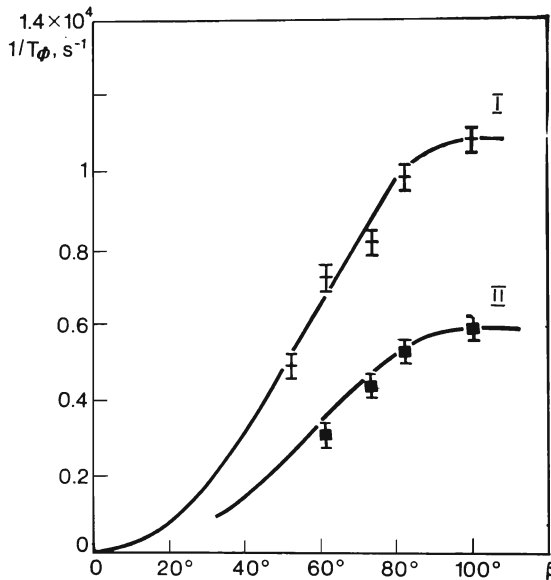


Fig. 3.17. Increment of instability growth $1/T_\Phi$ versus β at $\omega = 500$ kHz for temperatures $T = 0.82 \cdot T_c$ (I) and $T = 0.9 \cdot T_c$ (II). Solid curve is proportional to the theoretical function (4.37).

up increment, $1/T_\Phi$, on β at $T = 0.82 T_c$, and $T = 0.9 T_c$ ($\Omega_A = 79$ kHz and 60 kHz). The experimental points are in a good agreement with the curves given by (3.37) up to a constant.

The way the instability build up increment depends on temperature (Ω_A) and external field strength also agrees with (3.37) to a factor of 2. Thus, all functions of this type are consistent with the theory of instability proposed by Fomin. The quantitative discrepancy between the results might be caused by the fact that under the experimental conditions the chamber size is only about 50 times larger than one wavelength, for which the instability develops most rapidly. On the other hand, when $2\pi/K$ of order of the size of the chamber, the initial perturbations resulting in instability is much larger than the thermal perturbations because of boundary effects. As a result, the value of the initial perturbations depends on K . It is quite possible that inhomogeneities with smaller K 's manage to develop faster

than those with the optimum K because their initial perturbations are significantly stronger.

Finally, the induction signal's amplitude and its frequency as functions of time were carefully compared. The frequency proved to vary in the same way as does amplitude, although it requires a slightly smaller initial perturbation. Figure 3.18 compares the two for $\beta = 81^\circ$. The quantity A in the time dependence of frequency is half

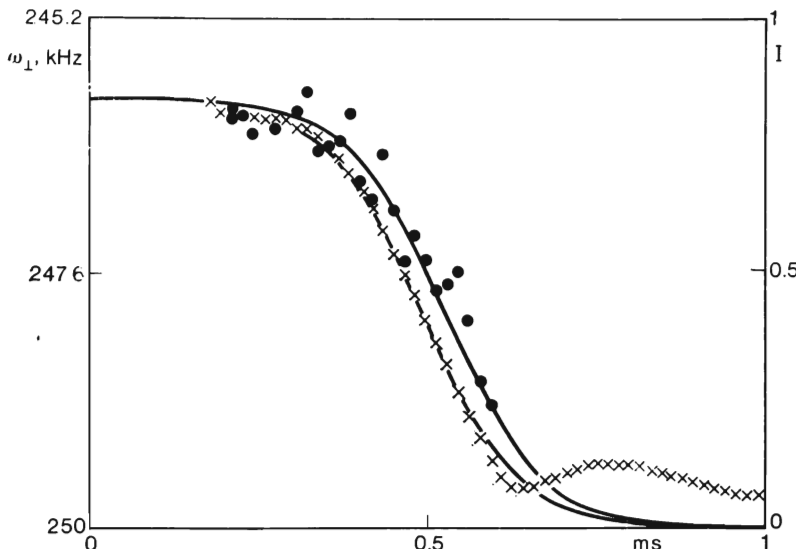


Fig. 3.18. The induction signal's decay (×) and the variation in the induction signal's frequency (●) over time. The solid curves are calculated from the functions: (lower) $I_0/[1 + 10^{-4} \exp(t/T_\Phi)]$ and (upper) $250 - 4.5 [1 + 5 \times 10^{-5} \exp(t/T_\Phi)]^{-1}$.

that in the time dependence of amplitude and this is qualitatively consistent with Fomin's theory [see (3.35) and (3.36)]. In fact, the phasing out of homogeneous precession results in the formation of a texture and, simultaneously, in a diffusive relaxation of magnetization. Either of these effects must reduce the frequency shift relative to the equilibrium value. Alternatively, the change in frequency shift must lag behind the phasing out because of a decrease in the total magnetization.

The good agreement between the experimental results given above and the theory shows that the homogeneous precession in $^3\text{He-A}$ is unstable and decays into large amplitude spin waves, as was predicted by Fomin. Accordingly, the longitudinal relaxation of the spatially inhomogeneous $^3\text{He-A}$ should speed up at the expense of spin diffusion. In this way the enigma of fast relaxation in $^3\text{He-A}$ has been unravelled.

3.4. A TEXTURE TRANSITION IN ^3He -B INDUCED BY A RADIO FREQUENCY FIELD

3.4.1. Threshold Effect in Pulsed ^3He -B NMR

The superfluid ^3He ordering parameter near the chamber walls is very distorted, at least, for distances of the order of a coherent wavelength. In other words, the properties of ^3He near the surface can substantially differ from those in the bulk. The influence of the distortion in the ordering parameter in the layer near the wall on the ^3He can be described by means of a surface energy that orientates the vectors of the ordering parameter.

For ^3He -B, this energy has the form [3.4]:

$$F = -f[\mathbf{N} \cdot \hat{R}(\theta, \mathbf{n}) \mathbf{H}]^2 - b \left[(\mathbf{N}\mathbf{n})^2 - \frac{5}{18} (\mathbf{N}\mathbf{n})^4 \right] \quad (3.45)$$

where \mathbf{N} is the normal to surface and $\hat{R}(\theta, \mathbf{n})$ is the matrix of rotation through an angle θ about the \mathbf{n} axis. In the region of fields greater than 50 Oe, the main contribution to the energy is made by the first term. When magnetic field lies on the surface plane, viz. $\mathbf{N} \perp \mathbf{H}$, the \mathbf{n} vector is rotated relative to the field direction through the angle $\beta = \text{arc cos}(1/\sqrt{5}) \simeq 63^\circ$, and relative to \mathbf{N} through $\sim 60^\circ$.

Alternatively, the magnetic anisotropy energy far from walls

$$F = a(\mathbf{n}\mathbf{H})^2 \quad (3.46)$$

will tend to orientate \mathbf{n} parallel to \mathbf{H} .

The change in the orientation of the \mathbf{n} vector away from a wall is governed both by this energy and by that inhibiting the formation of an ordering parameter gradient, viz. the bending of the ordering parameter. As a result a spatial distribution of the \mathbf{n} vector, viz. a "texture", becomes established. The \mathbf{n} vector direction changes over a distance called the magnetic length and equal for ^3He -B to

$$R_H \approx 10/H \text{ (cm)} \quad (3.47)$$

If the ^3He occupies a volume between parallel plates spaced a distance much smaller than R_H , then the \mathbf{n} distribution between the plates will be homogeneous and the direction of \mathbf{n} will only be governed by the surface energy given by (3.45). In particular, when $\mathbf{N} \perp \mathbf{H}$, the \mathbf{n} vector will be inclined by 63° from \mathbf{H} throughout the volume. This is why the transverse NMR frequency is also shifted with respect to that of the Larmor frequency and is equal to

$$\omega^2 = \frac{1}{2} (\gamma^2 H^2 + \Omega_B^2) + \left[\frac{1}{4} (\gamma^2 H^2 + \Omega_B^2)^2 - \gamma^2 H^2 \Omega_B^2 \cos^2 \beta \right]^{1/2} \quad (3.48)$$

where Ω_B is the longitudinal resonance frequency in ^3He -B.

Ahonen et al. [3.26, 27] used steady-state NMR on a chamber filled with ${}^3\text{He}$ and between parallel plates with the interplate spacing smaller than R_H , and external magnetic field directed parallel or inclined to their surfaces. The NMR frequency was proved to be shifted with respect to the Larmor one, in a good agreement with (3.48). This corresponds to a magnetization vector precession provided that its deviation from equilibrium is small.

The problem becomes drastically more complicated if we consider system's behavior for large β 's. Here the Zeeman magnetic energy may be much larger than the surface energy, viz. (3.45). The results of investigations of the induction signals in ${}^3\text{He}$ between parallel plates for different β 's are presented in [3.28].

This investigation was stimulated by the need to apply pulsed NMR techniques to the study of the \mathbf{n} vector texture in a rotating ${}^3\text{He}$ [3.29-30] and took place within the framework of the joint Soviet-Finnish project ROTA. When a rotation chamber full of ${}^3\text{He}$ -B is accelerated or slowed strong countercurrent flows of normal and superfluid components arise which also orientate the \mathbf{n} vector. However, this nonequilibrium situation lasts less than 1 minute. During this period an NMR spectrum within a broad range of fields is not registerable. In order to take a snap photograph of the frequency distribution in the chamber, we wanted to use the induction signal's Fourier transform after system had been excited by an RF pulse. However, it was first necessary to look into the behavior of \mathbf{n} vector texture under pulsed NMR.

The experiments were carried out in the lower experimental chamber shown in Fig. 3.7 at an NMR frequency of 500 kHz with a magnetic field of about 154 Oe. In this field $R_H \simeq 1$ mm, viz. it is possible to assume that the \mathbf{n} vector texture is homogeneous between the plates, and prior to a perturbation the \mathbf{n} vector is everywhere at an angle $\beta = 63^\circ$ to the magnetic field's direction. The RF circuit in the setup used was similar to the one described in Sec. 3.3, except that the RF field's amplitude in the coil was limited to 2 Oe. Thus the value of β induced by the RF pulse was changed by varying the exciting signal's pulse length.

The induction signal after the RF pulse was recorded by a Data-lab-905 digital memory unit, with both the induction signal's frequency and amplitude being measured. The induction signal turned out to have a threshold, the signal being undetected for shorter RF pulses. For RF pulses longer than 25 μs (this corresponding to a $\beta=50^\circ$ in normal ${}^3\text{He}$), a long induction signal was produced whose decay time was dependent mainly on the external field inhomogeneity and great exceeded the pick-up system's deadtime (~ 200 μs in our case). Increasing the RF pulse length led to an increase in the induction signal's intensity and then the signal began to oscillate (Fig. 3.19). The induction signal's frequency proved always

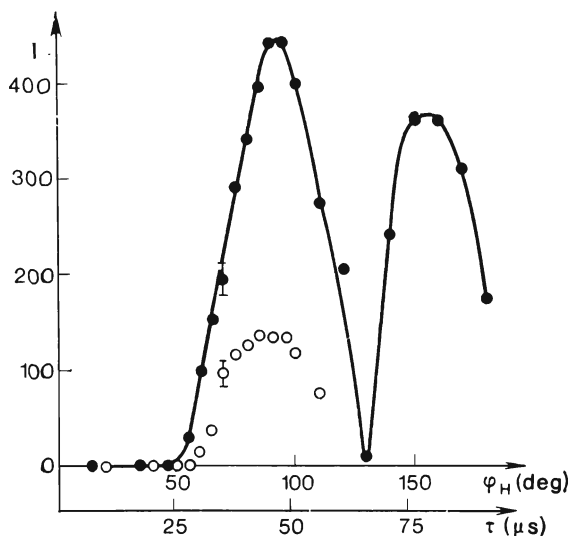


Fig. 3.19. Induction signal intensity versus RF pulse length for $T = 0.61 T_c$ (●) and $T = 0.49 T_c$ (○).

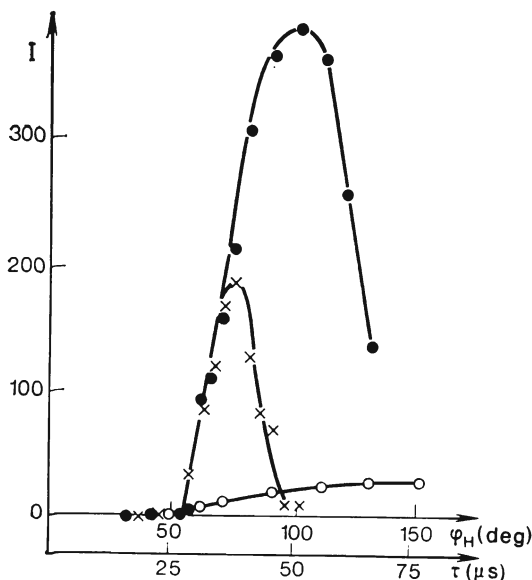


Fig. 3.20. Induction signal intensity versus RF pulse length at $T = 0.55 T_c$ and for RF field frequencies of 500 kHz (○), 540 kHz (×), and 550 kHz (●).

to be the Larmor frequency and changed in accordance with variations in the external field. The induction signal amplitude strongly depends on the pulsed RF field frequency. The RF frequency ω for which there is an optimum induction signal satisfies the condition

$$\omega_{\perp} > \omega > \gamma H,$$

where ω_{\perp} is the frequency of the steady-state NMR signal within the given geometry. Fig. 3.20 shows how the induction signal's intensity depended on the RF pulse length for RF field frequencies of 550 kHz which corresponds to the ω_{\perp} value at the given temperature, 500 kHz, which is the Larmor frequency, and 540 kHz, for which the induction signal is at a maximum at the given temperature. The RF field frequency corresponding to the induction signal's maximum varied between 550 and 530 kHz in a field of 154 Oe, when the temperature ranged from 0.5 T_c to 0.7 T_c . That the pulse threshold length is independent of the RF field frequency is important. Figure 3.19 demonstrates the dependence of the induction signal's intensity on RF signal's pulse length for the optimum RF frequency at the temperatures of 0.61 T_c and 0.49 T_c . This plot demonstrates that the threshold pulse length is independent of temperature.

3.4.2. A Texture Transition in $^3\text{He-B}$

Following Golo et al. [3.31], we shall analyze the ordering parameter's motion in $^3\text{He-B}$ under experimental conditions in the frame of reference composed of the coordinates θ , \mathbf{H} ($\mathbf{S} \perp \mathbf{H}$), and \mathbf{Hn} . The solid lines in Fig. 3.21 indicate the positions in this frame of the ordering parameter corresponding to the stable stationary solutions of the Leggett equations for $^3\text{He-B}$ [3.32-33]. In these positions the motion of magnetization vector is simple and periodic. However if the ordering parameter that results from, say, an RF field pulse, should fall outside the stationary solutions, it must return to them due to the fast relaxation. The lines ACB and $A'C'B'$ correspond to the oscillation mode described by Brinkman and Smith [3.34] which originate in ^3He given an open geometry, when the magnetization vector is deviated through the angle β up to 104° . The $^3\text{He-B}$ precession frequency for this mode is the Larmor frequency. The lines AOB and $A'O'B'$ correspond to the static position of the ordering parameter given parallel geometry. Accordingly, the precession frequency S near this position is described by (3.48). Finally, OO' and CC' correspond to the WP mode and to the magnetization vector's precession in the open ^3He volume for $\beta > 104^\circ$.

The motion of the ordering parameter induced by the RF field was analyzed by computer [3.31], since under experimental conditions the Ω_B/ω was too small for asymptotic methods to be applied. Numerical solutions of the Leggett-Takagi equations demonstrated that under an RF field the ordering parameter moves along the trajectory KL ($K'L'$) shown schematically in Fig. 3.21. When the

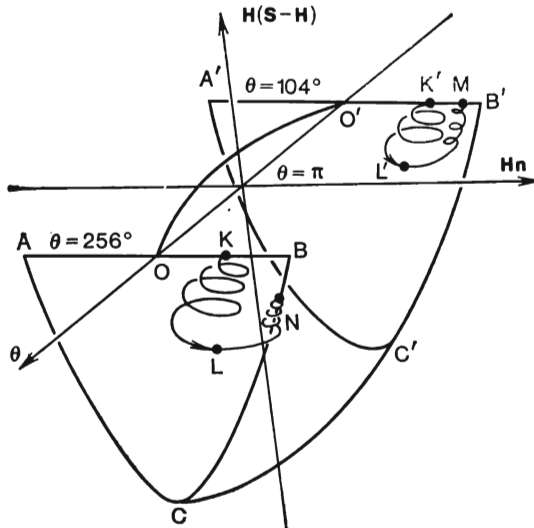


Fig. 3.21. Diagram showing stable branches of the stationary solutions of the Leggett-Takagi equations and the trajectories of a spin system.

RF field is switched off, the ordering parameter either returns quickly into the state corresponding to parallel geometry ($L'M$) or else exits to the Brinkman-Smith mode. According to these numerical calculations, the threshold pulse length at which the transition occurs from the relaxation into the static position to the relaxation into the Brinkman-Smith mode would be to 22 μ s under experimental conditions, and this is in a good agreement with the experimental results for the threshold length of induction signal's formation period.

Thus, about 200 μ s after an RF pulse longer than the threshold one, the ordering parameter turns out to be in the Brinkman-Smith mode. This means that the n and S vectors both precess with the same (Larmor) frequency, as they do in an open geometry. By contrast, with a shorter RF pulse, the ordering parameter relaxes into a state corresponding to a parallel plate geometry. In so doing, if the initial conditions for the ${}^3\text{He}$ in different chamber sections are dispersed, the ordering parameter will follow slightly different

trajectories. Since the precession frequency far from the Brinkman-Smith mode is strongly dependent on the position of the ordering parameter, the induction signals from different parts of the sample will be phased-out. Probably, this is why an induction signal is not observed when the ordering parameter moves along the $L'M$ trajectory.

3.4.3. Studies of the Brinkman-Smith Relaxation Mode with Parallel Plate Geometry

According to the Leggett-Takagi equations, the ordering parameter having relaxed into the point N in the Brinkman-Smith mode then relax no further. Quite naturally, in reality relaxation does occur, and this was investigated by us [3.35].

After a delay time with respect to the first RF pulse, a second RF pulse was applied. Figure 3.22 shows an oscillogram of the beats

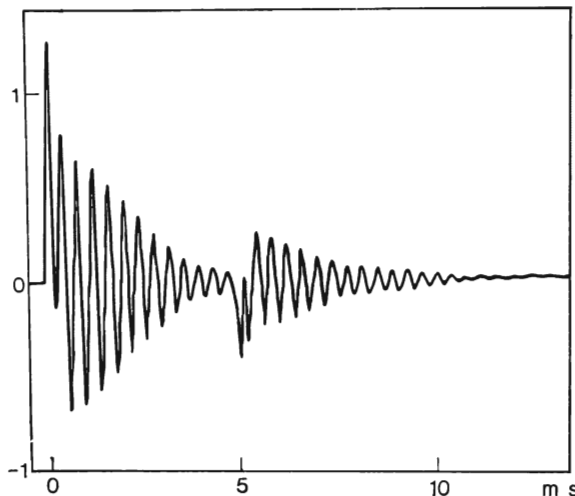


Fig. 3.22. The beat pattern between the induction signal at the Larmor frequency and the sampling frequency of the Datalab-905 memory unit after two exciting pulses 45 μs ($t = 0$) and 8 μs ($t = 5 \text{ ms}$) long.

between the induction signal and the sampling frequency of the Datalab-905 memory unit. When the first RF pulse was 45 μs long and the second 8 μs long, the delay time between the pulses amounted to 5 μs . Clearly there is an induction signal following the second, short RF pulse. Figure 3.23 shows the intensity of the induction signal versus the second pulse's length; delays between the first pulse (45 μs long) and second pulse were 10 ms, 20 ms, and 2 s.

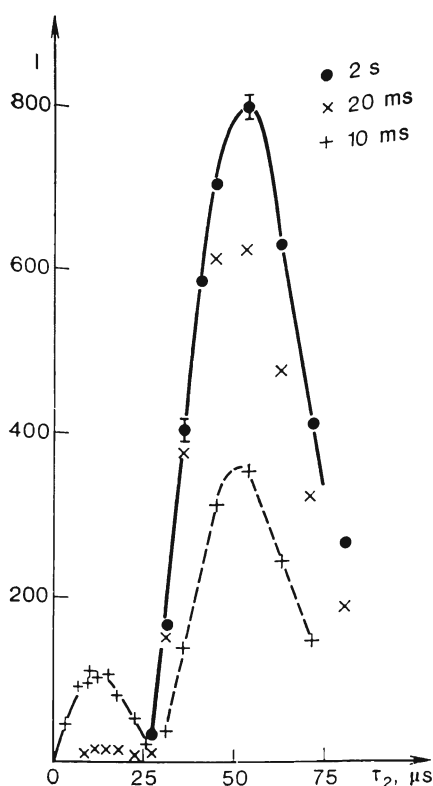


Fig. 3.23. The induction signal's intensity after the second pulse versus the length of the second pulse for the delay between pulses: 10 ms (+), 20 ms (×), and 2 s (●).

obtained by averaging over 5-10 experiments. It is clearly seen that under experimental conditions the induction signal's intensity depends exponentially on the delay time. Therefore, the exponential index is a function of the first pulse length. When the first pulse is 45 μ s long, viz. when the magnetization vector S and n vector deviate most strongly from the external magnetic field direction due to the RF field of the first pulse, the ^3He relaxation in the Brinkman-Smith mode proceeds relatively slowly. With first RF pulse lengths of 35 and 60 μ s, viz. when the ordering parameter falls within the region of small deviations of n and S from the H direction, the ^3He leaves the Brinkman-Smith mode much fast-

The formation of an induction signal with a short second RF pulse is logically due to a fraction of the ^3He being in the Brinkman-Smith mode at the moment the second pulse is applied. In fact, the ^3He 's ordering parameter is displaced along the Brinkman-Smith oscillation mode by the RF field. Therefore, threshold effects are absent for this ^3He fraction and in the limit of short RF pulses the induction signal represents a linear system's response to an RF pulse input. Consequently, if we accept the above hypothesis that an induction signal is formed within the range of short RF pulses, then by measuring the dependence of the induction signal's intensity on the delay time between pulses, it will be possible to estimate the ^3He relaxation in the Brinkman-Smith mode. The induction signal's intensity within a small duration of the second pulse depends on both the delay time and the first pulse length.

Figure 3.24 shows the induction signal's intensity after the second pulse (8 μ s long) versus the delay time between the pulses for first pulse length's of 35, 45, and 60 μ s. The experimental points were

er. We can conclude from this that the ${}^3\text{He}$ relaxation is inhomogeneous.

In fact, with a homogeneous relaxation of the ordering parameter, the amount of ${}^3\text{He}$ in the Brinkman-Smith mode were constant as long as the motion followed the curve NB , and then it would fall drastically. The experimentally smaller amount of ${}^3\text{He}$ in the Brinkman-Smith mode suggests that probably ${}^3\text{He}$ "droplets" form which have a static configuration, and that these droplets gradually grow in size, growing the faster, the smaller the Zeeman energy stored in ${}^3\text{He}$.

Thus, a powerful RF pulse transforms the ${}^3\text{He}$ -B texture in parallel plate geometry into a configuration corresponding to open geometry. Restoring the equilibrium texture proceeds inhomogeneously.

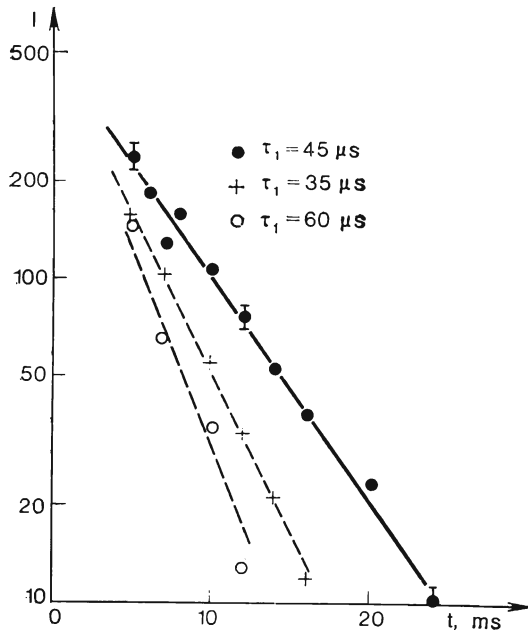


Fig. 3.24. The induction signal's intensity after a second pulse (8 μs long) versus the interpulse delay time for the following first pulse lengths: 35 μs (+), 45 μs (●), and 60 μs (○).

3.5. CONCLUSION

More than a decade has elapsed since the discovery of ${}^3\text{He}$ superfluidity, yet the properties of ${}^3\text{He}$ -A and ${}^3\text{He}$ -B are so complicated and yet so interesting that this problem will supply conun-

drums for many more years to come. The efforts of experimental physicists are also demanded by such problems as the magnetic ordering of solid ^3He and the superfluidity of ^3He in solution with ^4He as well as by the many other solid state problems. Consequently, the prospects for fundamental research in the domain of ultralow temperatures are very broad at present.

To summarize, I would like to express my profound gratitude to the participants in the joint experimental venture at the nuclear demagnetization installation of the IPP of the USSR Academy of Sciences and primarily to our supervisor A. S. Borovik-Romanov as well as to V. V. Dmitriev and Yu. M. Mukharskii. Our group engineer S. M. Elagin was a great help in the installation and servicing of the apparatus. The experiments were substantially speeded up by the theoretical works of I. A. Fomin, V. L. Golo, and A. A. Lehmann.

References

- 3.1. P. L. Kapitza, *Dokl. Akad. Nauk SSSR* 18, 211 (1938); *Nature* 141, 74 (1938).
- 3.2. L. P. Pitaevskii, *Sov. Phys. JETP* 37, 1267 (1960).
- 3.3. Yu. D. Anufriev, *JETP Lett.* 1, 155 (1965).
- 3.4. D. M. Lee, R. Richardson, in: *The Physics of Liquid and Solid Helium, Part II*. Ed. Bennemann and Ketterson, J. Wiley and Sons, New York, 1978.
- 3.5. O. V. Lounasmaa, *Experimental Principles and Methods below 1 K*, Academic Press, London—New York, 1974.
- 3.6. Yu. M. Bun'kov, V. V. Dmitriev, Yu. M. Mukharskii, and G. K. Tvalashvili, *XXII Sov. Conf. of Low Temp. Phys.* 3, 248, Kishinev, 1982 (in Russian).
- 3.7. G. Frossati, *J. de Phys.* C6, 1578 (1978).
- 3.8. T. O. Niinikoski in: *Proc. ICEC-6*, Grenoble, 1976, p. 102.
- 3.9. K. Andres, O. V. Lounasmaa in: *Progress in Low Temp. Phys.*, vol. VII, North Holland, 1982, p. 221.
- 3.10. P. W. Anderson, P. Morel, *Phys. Rev.* 123, 1911 (1961).
- 3.11. R. Balian, N. R. Werthamer, *Phys. Rev.* 131, 1553 (1963).
- 3.12. A. J. Leggett, *Rev. Mod. Phys.* 47, 331 (1975).
- 3.13. P. Hakonen, M. Krusius, M. Salomaa, I. Simola, Yu. M. Bun'kov, V. P. Mineev, G. E. Volovik, *Phys. Rev. Lett.* 51, 1362 (1983).
- 3.14. A. J. Leggett, S. Takagi, *Phys. Rev. Lett.* 34, 1924 (1975).
- 3.15. I. A. Fomin, *Sov. Phys. JETP* 50 (1), 144 (1979).
- 3.16. P. Bhattacharya, C. Y. Pethick, and H. Smith, *Phys. Rev. Lett.* 35, 473 (1975).
- 3.17. J. C. Wheatley, in: *Progress in Low Temp. Phys.*, vol. VIIA. Ed. D. F. Brewer, North Holland, 1978, p. 1.
- 3.18. W. G. Gully, C. M. Gould, R. C. Richardson, and D. M. Lee, *J. Low Temp. Phys.* 24, 563 (1976).
- 3.19. L. R. Corruccini, D. D. Osheroff, *Phys. Rev. B* 17, 126 (1978).
- 3.20. R. W. Gianetta, E. N. Smith, and D. M. Lee, *J. Low Temp. Phys.* 45, 295 (1981).
- 3.21. A. S. Borovik-Romanov, Yu. M. Bun'kov, V. V. Dmitriev, and Yu. M. Mukharskii, *JETP Lett.* 39, 469 (1984).
- 3.22. I. A. Fomin, *JETP Lett.* 30, 164 (1979).

- 3.23. I. A. Fomin, *Sov. Phys. JETP* **51** (6), 1203 (1980).
- 3.24. I. A. Fomin, *J. Low Temp. Phys.* **31**, 509 (1978).
- 3.25. I. A. Fomin, *JETP Lett.* **39**, 466 (1984).
- 3.26. A. I. Ahonen, M. Krusius, and M. A. Paalanen, *J. Low Temp. Phys.* **25**, 421 (1976).
- 3.27. A. I. Ahonen, T. A. Alvesalo, M. T. Haikola, M. Krusius, and M. A. Paalanen, *J. Phys. C* **8**, L269 (1975).
- 3.28. A. S. Borovik-Romanov, Yu. M. Bun'kov, V. V. Dmitriev, and Yu. M. Mukharskii, *JETP Lett.* **37**, 716 (1983).
- 3.29. Yu. M. Bun'kov, P. J. Hakonen, and M. Krusius, *Proc. Sanibel Symp. on Quantum Fluids and Solids, AIP Conf. Proc.*, No. 103, 1983, p. 194.
- 3.30. G. E. Volovik, A. D. Gongadze, G. E. Gurgenishvili, M. M. Salomaa, and G. A. Kharadze, *JETP Lett.* **36**, 489 (1982).
- 3.31. V. L. Golo, A. A. Lehmann, and I. A. Fomin, *JETP Lett.* **38**, 146 (1983).
- 3.32. I. A. Fomin, *Zh. Eksp. Teor. Fiz.* **84**, 2109 (1983).
- 3.33. V. L. Golo, A. A. Lehmann, *Zh. Eksp. Teor. Fiz.* **85**, 9 (1983).
- 3.34. W. F. Brinkman, H. Smith, *Phys. Lett.* **53A**, 43 (1975).
- 3.35. Yu. M. Bun'kov, V. V. Dmitriev, Yu. M. Mukharskii, *Phys. Lett.* **102A**, 194 (1984).

Table 4.1. Physical Properties of Beryllium

Lattice constants at 0 K	$c = 3.5814 \text{ \AA}$ $a = 2.2828 \text{ \AA}$
Elementary cell volume	$\Omega = 1.6162 \times 10^{-23} \text{ cm}^3$
Brillouin zone dimensions	$\Gamma A = 0.878 \times 10^8 \text{ cm}^{-1}$ $\Gamma K = 1.832 \times 10^8 \text{ cm}^{-1}$
Radius of free electron sphere	$k_F = 1.942 \times 10^8 \text{ cm}^{-1}$
Some parameters of Fermi surface:	
"coronet" neck diameter	$k_{zm} = 3.59 \times 10^8 \text{ cm}^{-1}$
frequency *) for $H \parallel [1\bar{2}10]$	$\gamma = 0.110 \text{ MGs}$
effective mass	$m_y = -0.0212 \text{ m}$
Extremum "cigar" cross sections for $H \parallel [0001]$	
frequencies	$\alpha^1 = 9.42 \text{ MGs}$ $\alpha^2 = 9.72 \text{ MGs}$
effective masses	$m_{\alpha^1} = 0.168 \text{ m}$ $m_{\alpha^2} = 0.170 \text{ m}$

*) The case in point is magnetic frequencies (1 MGs = 10^8 Gs).

pockets in the third zone (Fig. 4.1). The volumes of the hole and the two electron sheets are the same, viz. beryllium is a compensated metal.

The metallic beryllium has a relatively small number of carriers in the conduction zone and hence a low density of states at the Fermi level [4.11]. Its Debye temperature by contrast is very high and amounts to 1480°C [4.15]. As a result of the low density of states and of the high Debye temperature, quantum effects in beryllium are more pronounced than in most other metals, and besides they appear at higher temperatures. This feature makes beryllium a good substance for investigating the effects caused by CMB.

The MB in beryllium was discovered as a result of measurements of the magnetoresistance of single crystals in pulsed magnetic fields up to 150 kOe [4.16]*. An abrupt change in the field dependence of the resistance was observed for $H \parallel [0001]$ in 50 kOe. Further investigations in stationary magnetic fields made it possible to establish the coherent character of the MB in beryllium.

* There was a mistake in determination of the directions of the open trajectories induced by the MB in [4.16].

The first prominent manifestation of CMB in beryllium to be noticed was the observation of giant oscillations in the resistance of a binary sample as it depends on field strength for $H \parallel [0001]$

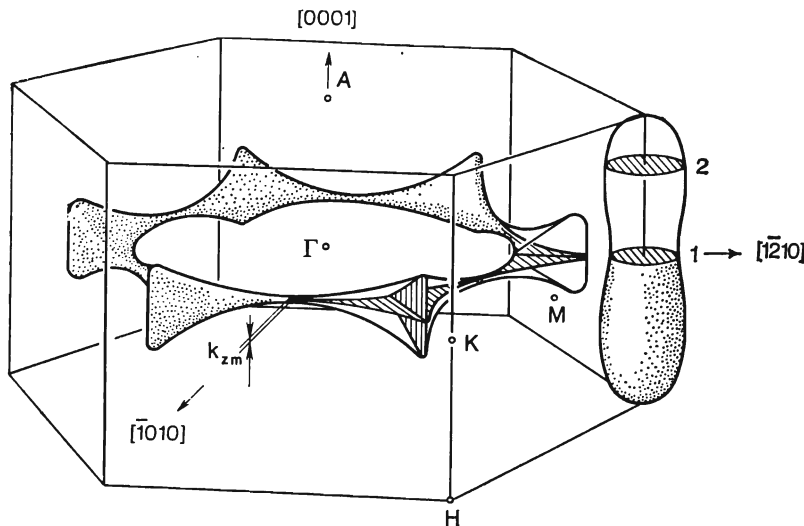


Fig. 4.1. The Fermi surface of beryllium. The numbers indicate the extremum "cigar" cross sections for $H \parallel [0001]$: 1—the central cross section, 2—a noncentral cross section.

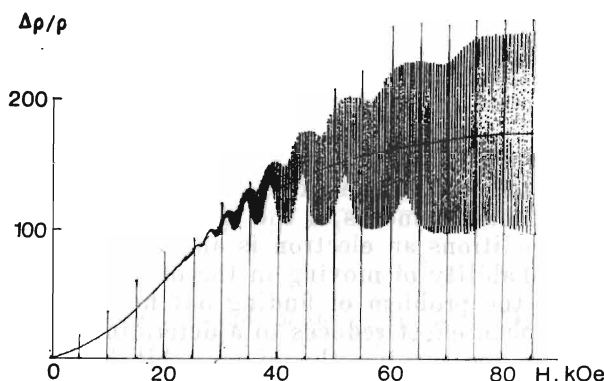


Fig. 4.2. The resistance of a binary $[10\bar{1}0]$ beryllium sample versus magnetic field strength for $H \parallel [0001]$ at 1.9 K.

[4.17]. This behaviour was observed at $T = 1.9$ K for a sample with the $[10\bar{1}0]$ orientation having the residual resistance ratio $RRR = 400$. It is depicted in Fig. 4.2. The quadratic rise of resist-

4

Experimental Investigations of Coherent Magnetic Breakdown

*N. E. Alekseevskii, Assoc. Mem. USSR Acad. Sc., and
V. I. Nizhankovskii, Cand. Sc. (Phys. and Math.)*

4.1. INTRODUCTION

As is known, thermodynamic and kinetic characteristics of electrons in a metal in magnetic field are determined by the topology of the Fermi surface (FS) of the metal. The FS's of most metals (excluding the alkaline and noble ones) consist of several sheets. It was at first assumed that both the sizes of individual FS sheets and the intersheet spacings are sufficiently large, amounting to $1/a$ (where a is the metal's lattice constant). The motion of electrons across a given FS sheet is then wholly independent of any electron movements across an adjacent sheet, whereas the thermodynamic and kinetic coefficients are determined by simply summing the contributions from individual sheets of FS.

Thus, if all FS sheets are closed and $n_e \neq n_h$ (n_e and n_h being the numbers of electrons and holes, respectively), then the metal's electrical resistance should be saturated with increasing a magnetic field. However if $n_e = n_h$, then there should be an unlimited growth in the magnetoresistance.

A quadratic growth of magnetoresistance should also be observed when the electron trajectories are open for a given direction of the magnetic field H and this naturally is only possible on open FS sheets.

These results were presented in 1956-1958 in theoretical papers by Lifshitz, Azbel', Kaganov, and Peschanskii [4.1, 2] and they were in a good agreement with experimental data [4.3, 4].

However, starting in 1961, changes in the behaviour of the kinetic and thermodynamic coefficients in the increasing magnetic field were discovered in a number of metals*.

These changes proved to be due to quantum tunnelling transitions of electrons between individual FS sheets in regions of K-space where the interzonal energy gaps $\Delta\epsilon$'s are small and the electron trajectories pertaining to adjacent FS sheets approach each other. This phenomenon was called "magnetic breakdown" (MB) [4.6]. The investigations of the last few years demonstrated that magnetic breakdown is a widespread phenomenon because of the smallness of the pseudopotential in many metals. It has now been detected in about half of all metals, and in many alloys and compounds.

* The first observation may actually have been made in 1955 [4.5].

The influence of MB on the dynamics of conduction electrons is governed by the dependence of MB probability on magnetic field, $W = \exp(-H_0/H)$, where H_0 is the breakdown field [4.7]:

$$H_0 = \frac{2m^*c}{e\hbar} \cdot \frac{(\Delta\varepsilon)^2}{\varepsilon_F}$$

The MB probability rises with magnetic field strength, and this rise leads to a change in connectivity of some of the electron trajectories. Hence open electron trajectories may be formed from closed ones and vice versa. A change in the relation between n_e and n_b (compensation ratio) is also possible. As a result, metal kinetic characteristics are changed in a radical way.

Under MB conditions, the kinetic phenomena in a metal are unusually sensitive to imperfections in the crystalline structure. If the electrons are scattered from impurities and dislocations more frequently than they undergo interzonal MB transitions, then an electron can be thought of as a classical particle realizing a randomly moving (in Brownian motion) along a net of paired MB orbits. This approach to describing the kinetic characteristics of a metal under MB conditions was called stochastic [4.8].

However if MB transitions are much more frequently than scattering from impurities and dislocations, then the resulting kinetic characteristics of metals are governed by the quantum interference between the wave functions of the electrons undergoing multiple scattering from MB centers. The kinetic phenomena in metals in this, a coherent magnetic breakdown (CMB), become substantially more complex and interesting. The theory of CMB was developed by Slutskin [4.9].

We wish now to review some of the experimental data produced when studying MB in beryllium, aluminium, niobium, and the dioxide RuO_2 . This choice of materials to be investigated was not accidental. On one hand, they represent the large classes of substances, which differ both in type (simple and transition metals, and compounds) and structure (hexagonal, tetragonal, cubic and face and body centered), in which MB has been observed. On the other hand, the phase-coherent features of MB are most clearcut in these objects.

4.2. BERYLLIUM

Beryllium is crystallized into a hexagonal, close-packed structure with $c/a = 1.57$ which is somewhat less than the ideal (see Table 4.1). The beryllium FS was determined as a result of both zone structure calculations [4.10-12] and measurements of the de Haas-van Alphen effect [4.13, 14]. It consists of a coronet-like hole sheet in the second zone and two identical cigar-like electron

ance in low fields which is characteristic of the compensated metals with a closed FS, is replaced at $H = 30$ kOe by a trend to saturation followed by resistance oscillations with a relative amplitude of approximately unity.

This unusual behaviour can be explained in the following way [4.18]. The hole "coronet" is separated from the electron "cigars" by a small interzonal gap and when the magnetic field is high enough electrons can tunnel across the gap with the result that the central layer electrons become able to move round the two-dimensional net of the coupled MB orbits. The thickness of this decompensating layer is limited by the diameter of the "coronet" necks (Fig. 4.1). As the result of the phase coherency conservation the magnetic breakdown effective probability W_{eff} will oscillate as magnetic field is changed, the frequency F of the oscillations being determined by the conventional quantization rule of orbit around the "cigar". Consequently, the magnetoresistance saturation is caused by the MB decompensation, whereas the oscillations in it are due to the oscillations in W_{eff} .

MB is a purely quantum phenomenon and because the electron wave function is usually governed by two parameters, viz. the amplitude and phase, two problems emerge. The first is to find out how the amplitude of the electron wave function varies during MB. This reduces to the determination of the breakdown field strength H_0 . This does not impose any stringent requirement on the quality of the samples to be studied.

By contrast, in order to solve the second problem, viz. the elucidation of the phase-coherent effects, the extremely perfect crystals are needed because any scattering changes the phase of the electron wave function. The observation of the phase-coherent effects of MB in beryllium proved to be feasible due to its unique physical properties.

The breakdown field in beryllium was determined from the field dependence of the amplitude of the de Haas-van Alphen effect [4.19] and from measurements of the Hall effect [4.20].

Under MB conditions an electron is able to move in new orbits, whereas the probability of moving in the old ones is duly reduced. Because of this the problem of finding out how MB influences the de Haas-van Alphen effect reduces to a determination of the probability amplitude for turning the given orbit by electrons [4.21]. Since an electron must "abstain" from MB thrice per revolution, as it turns the central cross section of a "cigar", the extra multiplier in the de Haas-van Alphen amplitude will be $(1 - W)^{3/2}$.

In order to find out H_0 [4.19] the de Haas-van Alphen effect in beryllium was measured in pulsed magnetic fields up to 150 kOe by a nonresonance technique with two samples having the RRR's of 130 and 1400. The signals from the three extremum cross sections

of the "cigars", viz. the central one, which is influenced by MB, and two identical cross sections located below and above the central one, which are not influenced by MB were fixed simultaneously. The results are shown in Fig. 4.3 in traditional coordinates. In low

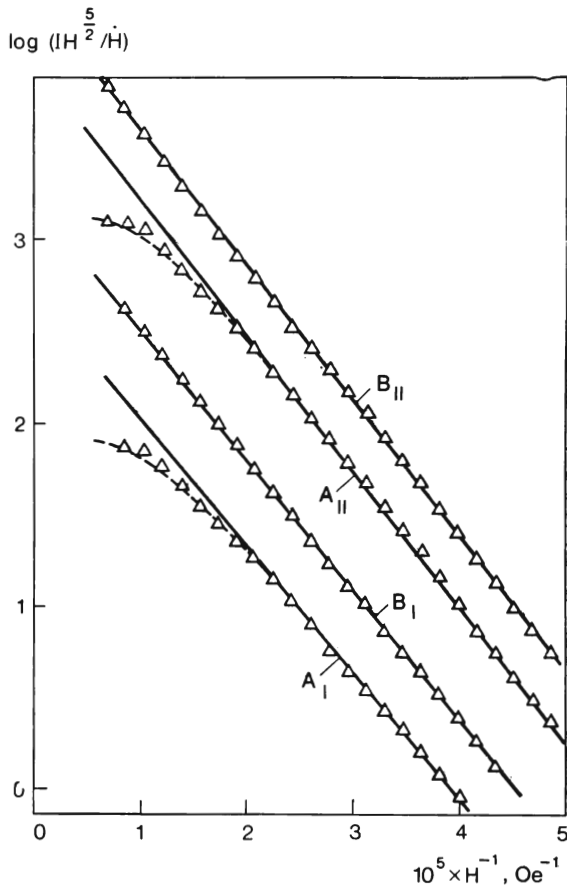


Fig. 4.3. The amplitude of the de Haas-van Alphen effect in beryllium versus the reciprocal of the magnetic field strength for $H \parallel [0001]$. A —the signal from "cigar" central cross section; B —the signal from noncentral cross sections. The indices I and II pertain to the samples with $RRR = 130$ and 1400, respectively. Dashed lines describe the theoretical dependences for $H_0 = 130$ kOe.

fields the slopes of all the dependences are about the same, but as the field increases the de Haas-van Alphen effect amplitude from the central cross section begins to grow more slowly. This is due

to the leakage of electrons from central orbit caused by MB. The breakdown field in beryllium $H_0 = 130$ kOe was determined by fitting the experimental data.

A study of MB influence on the diagonal and nondiagonal elements of beryllium magnetoresistance tensor was performed in [4.20]. In mounting the sample special attention was concentrated on obtaining a uniform distribution of the current over the sample cross section, and so each current lead was consisted of several wires

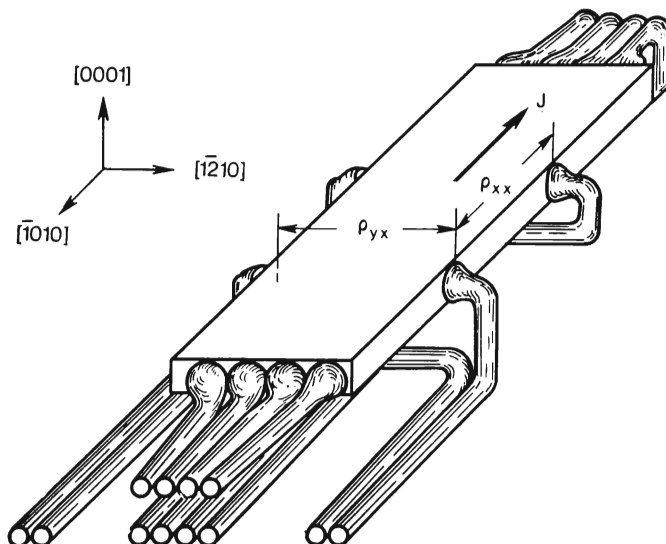


Fig. 4.4. Mounting of the sample with dimensions $0.3 \times 0.8 \times 5.0$ mm for the measurement of the Hall effect in beryllium. Current and potential leads from copper wire are welded on by means of a pulsed laser.

which served to level off the resistances (Fig. 4.4). The elements of the conductivity tensor were calculated by inverting the resistance tensor. In Fig. 4.5 the dependences of the monotonic components σ_{xx} and σ_{yy} on magnetic field is presented. An abrupt change in σ_{xy} at $H = 30$ kOe is due to MB decompensation. The way the σ_{xy} varies due to MB has been theoretically calculated within the framework of a stochastic model (by neglecting phase coherency in large orbits) in [4.22]. Since, according to [4.23], the influence of the coherency effects on σ_{xy} should be small, the use of the stochastic approach to calculate the increment $\Delta\sigma_{xy}$ is quite admissible.

It proved to be more convenient when processing experimental

data to use MB decompensation* Δn rather than the increment $\Delta\sigma_{xy}$ by employing the well-known relationship $\Delta\sigma_{xy} = \Delta n e c / H$. As we noted above, the MB layer thickness in beryllium was limited

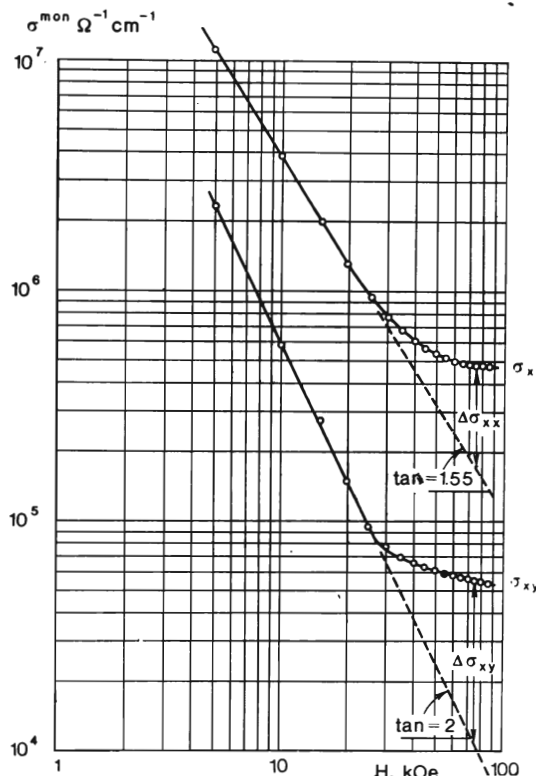


Fig. 4.5. The magnitude of elements of the conductivity tensor for beryllium versus the magnetic field. In low fields, $\sigma_{xx} \sim H^{-1.55}$, $\sigma_{xy} \sim H^{-2}$. The MB has a pronounced effect for $H \geq 25$ kOe.

by the diameter of the "coronet" necks k_{zm} , therefore as $W \rightarrow 1$ the decompensation will be $(\Delta n)_{W \rightarrow 1} = S k_{zm} / 4\pi^3$, where S is the Brillouin zone cross section area (a substitution of numerical values yields $(\Delta n)_{W \rightarrow 1} = 0.96 \times 10^{21} \text{ cm}^{-3}$). A comparison of the experi-

*
$$\Delta n = \frac{1}{4\pi^3} \int dk_z [S_e(k_z, \varepsilon_F) - S_h(k_z, \varepsilon_F)] = \frac{1}{4\pi^3} (V_e - V_h),$$
 where S_e and S_h are the cross section areas of FS electron and hole sheets, while V_e and V_h are, respectively, their volumes.

mental dependence of the normalized MB decompensation $\Delta n/(\Delta n)_{w \rightarrow 1}$ on magnetic field and the theoretical curves for different values of the breakdown field H_0 is illustrated in Fig. 4.6. This figure shows that the behaviour of $\Delta\sigma_{xy}$ is well described by the stochastic model, while $H_0 = (110 \pm 10)$ kOe.

The situation is different for the diagonal elements ρ_{xx} and σ_{xx} . If we estimate a feasible increment $\Delta\sigma_{xx}$ due to MB within the

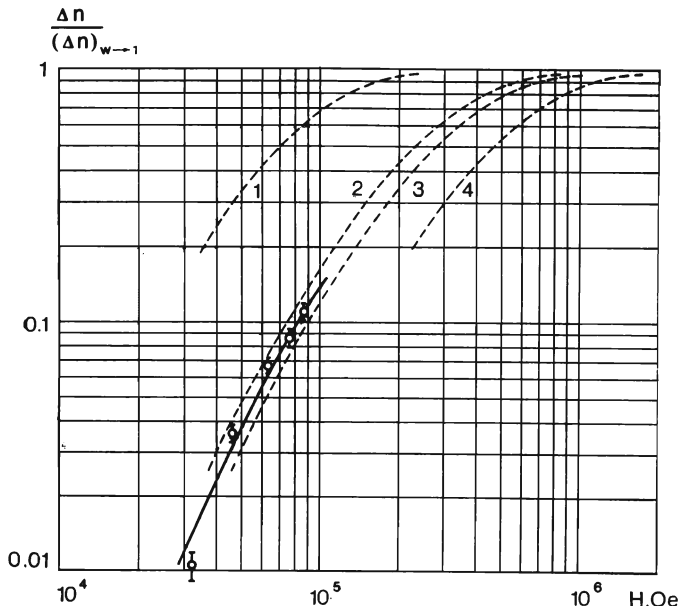


Fig. 4.6. The normalized MB decompensation for beryllium versus the magnetic field. Dashed lines are the theoretical curves for different values of the breakdown field H_0 : 1— $H_0 = 30$ kOe; 2— $H_0 = 100$ kOe; 3— $H_0 = 120$ kOe; 4— $H_0 = 200$ kOe.

framework of stochastic model [4.22], then for $H = 80$ kOe we obtain $\Delta\sigma_{xx}^{\text{stoch}} \simeq 5.5 \times 10^4 \Omega^{-1} \text{cm}^{-1}$, which is almost an order of magnitude smaller than the experimentally observed value of $\Delta\sigma_{xx} \simeq 3 \times 10^5 \Omega^{-1} \text{cm}^{-1}$ (Fig. 4.5). This is because the stochastic theory cannot take into account the quantum current states which are peculiar to the CMB theory [4.23] and whose contribution to the diagonal elements of the conductivity and resistivity tensors is decisive. For the same initial conditions the CMB theory provides a much more significant increment, $\Delta\sigma_{xx}^{\text{coh}} = 3.6 \times 10^5 \Omega^{-1} \text{cm}^{-1}$, which practically matches experiment. Note that neglecting the quantum current states brought the authors of [4.24] to an erroneous

conclusion. They found the breakdown field in beryllium by fitting monotonic part of ρ_{xx} to the dependence provided by stochastic theory, the result being $H_0 = 30$ kOe. Experimental data on MB decompensation disprove this result.

Thus, bringing in the notions of the CMB theory is necessary even to describe the behavior of the monotonic components of σ_{xx}

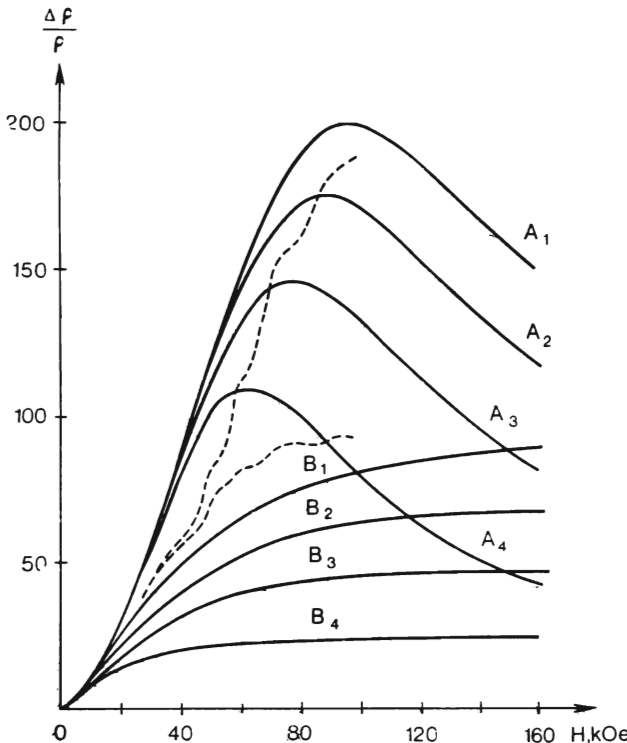


Fig. 4.7. Envelopes of the MB oscillations of beryllium resistivity. The letters A and B denote the theoretical envelopes of oscillations according to maxima and minima, respectively. For the A_1 and B_1 curves the ratio of the MB layer thickness to the diameter of the "coronet" neck, $\gamma = 1$, for A_2, B_2 curves $\gamma = 0.75$, for A_3, B_3 $\gamma = 0.5$, for A_4, B_4 $\gamma = 0.25$. Experimental data are illustrated by the dashed line.

and ρ_{xx} , especially when considering the oscillating components. Thus, in Fig. 4.7 we see a comparison between an envelope of the MB oscillations of beryllium resistivity and the theoretical curves provided by CMB theory [4.18]. The best agreement with experiment occurs for theoretical envelopes with index 1, which are constructed

assuming the MB layer thickness is equal to the diameter of the "coronet" necks k_{zm} (for other envelopes they are smaller).

An eye-catching phenomenon was detected when investigating the MB influence on Hall effect in beryllium [4.20]. It was proved that ρ_{yx} had an oscillating component whose amplitude is strongly dependent on the angle α between a hexagonal sample's axis and the magnetic field. The amplitude vanishes at $\alpha = 0^\circ$, reaches a maximum at $\alpha = 2^\circ$ and then falls off. Moreover, a phase shift

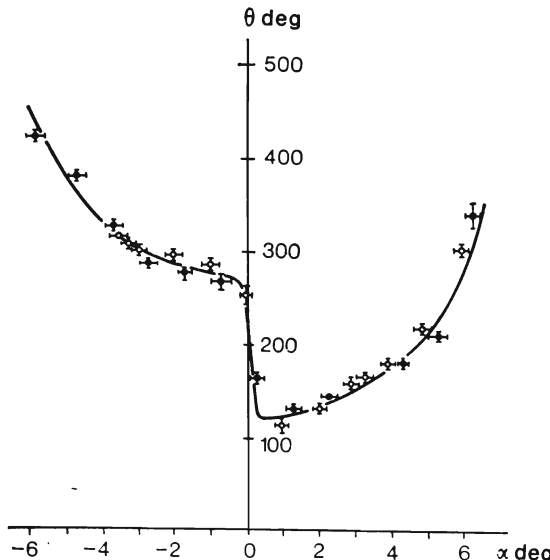


Fig. 4.8. Phase difference between the oscillations ρ_{yx} and ρ_{xx} versus the angle α between the hexagonal axis of the sample and the magnetic field direction. Mean value of the magnetic field $H = 85.6$ kOe. Light and black circles show the data obtained when commuting magnetic field direction.

between the ρ_{yx} and ρ_{xx} oscillations was observed and was found to be influenced by the angle α in a very complicated manner (see Fig. 4.8). The experimental data as a whole were successfully explained by the fact that a ρ_{yx} signal measured for $\alpha \neq 0$ was mainly due to a linear combination of the diagonal elements, ρ_{xx} and ρ_{yy} , of the resistivity tensor [4.25], which contain giant amplitude oscillating components. The monotonic increase in the phase difference between the ρ_{yx} and ρ_{xx} oscillations as α grew was ascribed to an increase in the phase difference between the ρ_{xx} and ρ_{yy} oscillations. Since the frequencies of the latter are governed by the same extremum cross sections of a "cigar", the emergence, as such,

of a phase difference contradicts classical notions and is an impressive manifestation of phase-coherent MB effects in beryllium.

Because of the significance of the phase difference between the ρ_{xx} and ρ_{yy} oscillations, it was necessary to determine this quantity directly [4.26]. To do this, an S-shaped sample (Fig. 4.9) was cut so that the ρ_{xx} and ρ_{yy} could be measured simultaneously. Signals proportional to ρ_{xx} and ρ_{yy} were fed into the X and Y inputs of

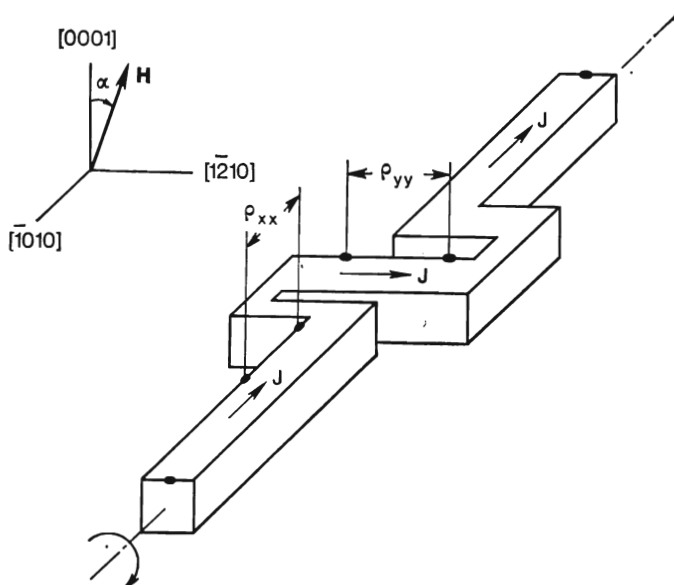


Fig. 4.9. Mounting of the sample for the simultaneous measurement of ρ_{xx} and ρ_{yy} .

a XY -recorder. When the magnetic field was changed by somewhat more than the oscillation period, the recorded diagram was a curve closely resembling an ellipse. From the parameters of the ellipses recorded for different angles α the values of the monotonic and oscillating signal components, ρ_{xx} and ρ_{yy} , and the phase difference between them can be determined. Some of the records are illustrated in Fig. 4.10. When the direction of the magnetic field was parallel to the hexagonal sample's axis, the ellipse degenerated into a straight line segment, which demonstrates that the phases of the ρ_{xx} and ρ_{yy} oscillations coincide. For $\alpha \neq 0$ a phase difference θ arises between the oscillations that increases monotonically with α (e.g. in Fig. 4.10c the ellipse is close to a circle and the phase difference is close to 90°).

These experiments give birth to the conclusion that whereas the MB oscillation period of beryllium's resistivity is governed by the extremum cross sections of the "cigars", their phase depends on the linkage-orbits over "coronets". In fact, at $\alpha = 0$ the circumferences of all the linkage-orbits are the same and the phases of the ρ_{xx} and ρ_{yy} oscillations coincide. For $\alpha \neq 0$ the circumferences of the linkage-orbits in the X and Y directions are different and a phase difference between oscillations is observed. The phase difference can

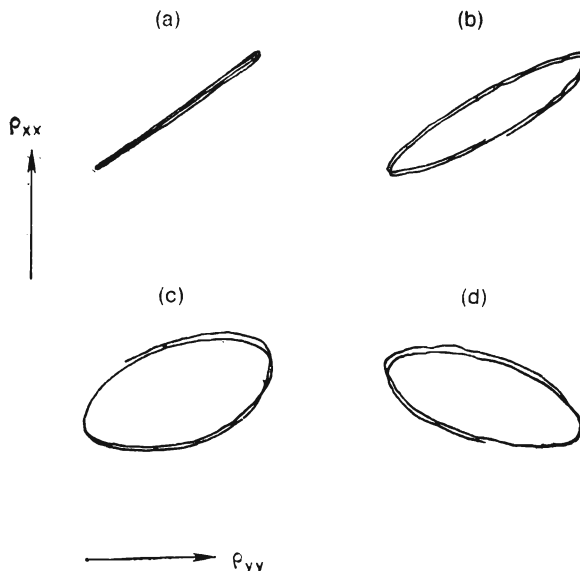


Fig. 4.10. Records of ρ_{xx} versus ρ_{yy} for different angles α between the hexagonal axis of an *S*-shaped sample and the magnetic field direction at $H = 55$ kOe: (a)— $\alpha = 0^\circ$, (b)— $\alpha = 0.7^\circ$, (c)— $\alpha = 1.75^\circ$, (d)— $\alpha = 2.1^\circ$.

only arise when electron wave function's phase does not change along the linkage-orbits in a random way, viz.. when the MB in the beryllium is coherent. Conclusive evidence for this was obtained from measurements in the nonuniform magnetic field produced within a small gap between the pole pieces made from polycrystalline dysprosium [4.26]. According to [4.23], due to the de Haas-van Alphen effect the nonuniform magnetic field produces a rapidly oscillating additional component of the magnetic field, which leads to chaotic variations in the electron wave function's phase, while for grad $H/H_0 \geq 10^{-1}$ cm^{-1} coherency must be violated. Experiments have demonstrated that in a nonuniform magnetic field the phase difference between the ρ_{xx} and ρ_{yy} oscillations disap-

pears whereas the oscillation amplitude is reduced to the value predicted by stochastic theory.*

This interpretation enables us to explain in a somewhat different manner the low-frequency component of the MB oscillations of beryllium's resistivity, which is especially pronounced when temperature decreases (Fig. 4.2).

It was suggested in [4.27] that the reason for the low-frequency component is the large value of the de Haas-van Alphen effect from noncentral extremum cross sections of a "cigar", this large value leading to the formation of diamagnetic domains for $dM/dB > > 1/4\pi$. In this case gaps appear in the dependence of the induction inside the sample on the external field and the resistivity oscillations entering the forbidden induction zones simply vanish. Since frequencies of the oscillations from the central and noncentral cross sections of the "cigar" differ by about 3%, the period of the low-frequency oscillations of magnetoresistance proves to be equal to 33 times the period of the high-frequency oscillations.

This explanation of the low-frequency component has a number of drawbacks. First, direct data [4.28] on magnetization oscillations obtained on a very pure beryllium sample having $RRR \simeq \simeq 2 \times 10^3$ demonstrate that in a field of $H = 20$ kOe susceptibility reaches the critical value of $1/4\pi$ at temperatures below 3 K. However, the low-frequency component is also clearly seen at $T = 4.2$ K, even for samples having $RRR \simeq 100$. Moreover, the low-frequency oscillation amplitude may be several fold larger than the high-frequency one (in the field of about 25 kOe in Fig. 4.2) which is practically independent of the sample shape. Second, it follows from model calculations of magnetoresistance oscillations in nonuniform magnetic fields [4.27] that the high-frequency amplitude should be peak between the peaks and troughs of the low-frequency component. This conclusion contradicts experiment, since the high-frequency's amplitude peaks are always in the troughs of the low-frequency component.

This discrepancy can be eliminated by taking into account the phase-coherency of the MB in beryllium and as a consequence the high sensitivity to magnetic field nonuniformity of the amplitude of resistivity oscillations due to MB. This high sensitivity is caused by the long circumference of the linkage-orbits over the "coronet", the conservation of phase coherency on which links being a necessary condition for the existence of CMB. Even a small irregularity in the induction arising well before the formation of the diamagnet-

* Magnetic field inhomogeneity was probably the main reason why oscillations in beryllium's resistivity could not be measured in a pulsed magnetic field [4.16].

ic domains can reduce the magnetoresistance oscillation amplitude down to what is predicted by stochastic theory. Therefore, the magnetoresistance will have a maximum amplitude where the susceptibility oscillation amplitude is at a minimum. This condition is satisfied in the troughs of the low-frequency component. In addition, since even the monotonic part of ρ_{xx} strongly depends on whether the breakdown is phase-coherent, the low-frequency oscillations observed at $H = 25$ kOe in the absence of the high-frequency ones can be treated as oscillations of the monotonic part of ρ_{xx} between its coherent and stochastic values.

Note that the existence of quantum current states ("quasiparticles" as termed by Pippard [4.29]) was rigorously proved in theory only for one-dimensional configurations. The case of two-dimensional nets (as in beryllium) involves considerable mathematical difficulties. The experimental data on the MB in beryllium is an indication of the applicability of quantum current states for two-dimensional nets too.

An unexpected manifestation of the two-dimensional character of CMB in beryllium was detected by precise measurements of MB oscillation phase of resistivity and thermopower in terms of the angle between a sample's hexagonal axis and the direction of the magnetic field [4.30]. In order to improve the measurement accuracy, the magnetic field was produced by a superconducting solenoid operating in the persistent current mode and measured using the NMR technique. To scan the field up to 1 kOe there an additional superconducting coil placed inside the main solenoid was used. In order to eliminate the influence of the magnetic field, frozen in the solenoid's windings, on the field uniformity, in each run the field distribution along the solenoid's axis was measured by NMR and the samples were placed in the region with the greatest uniformity. The initial position of a sample, $H \parallel [0001]$, was set using magnetoresistance extrema (a minimum during turning and a local maximum during inclination).

Each record contained from 2 to 12 oscillations depending on the value of the main solenoid field. The measured signal, the current through the field scanning coil, and the voltage from the output of the lock-in amplifier in the circuit for detecting the NMR resonance were measured using digital voltmeters and the results were recorded on punched tape for processing by computer. The processing yields the absolute magnetic field value, identifies the maxima and minima in the MB oscillations, produces a straight line corresponding to the monotonic fraction of the measured resistance signal or thermopower, and determines the coordinates of the points where the measured oscillations intercept the straight line. The magnetic field at these points, viz. the zeros of the oscillations, were used in the subsequent calculations of phase and frequency of

the MB oscillations. All the measurements were made at $T = 4.2$ K.

The variation in the phase of the MB oscillation as the sample was turned around its longitudinal axis was also investigated in [4.30]. To do this, there one of the oscillation zeros was selected and the way its position depended on the angle α between the hexagonal axis of the sample and the magnetic field direction was recorded.

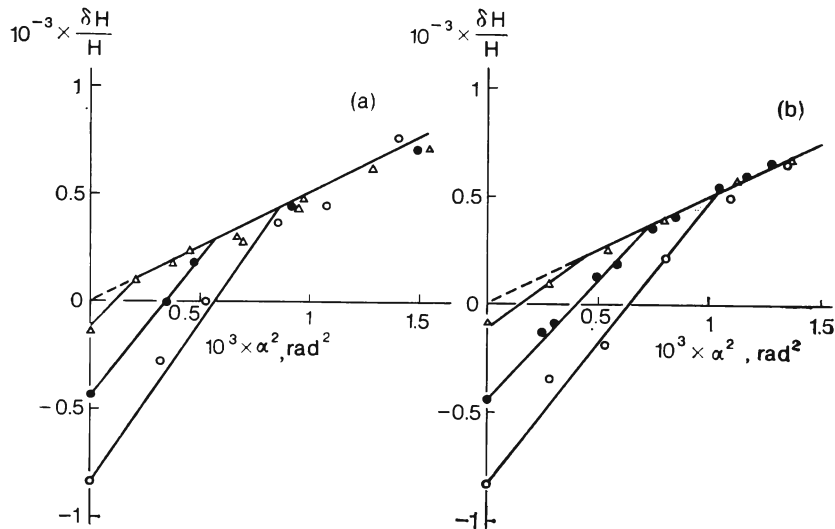


Fig. 4.11. Angular dependences of the relative shift of the MB oscillation phases for beryllium: (a)—sample $[10\bar{1}0]$, (b)— $[1\bar{2}\bar{1}0]$. $\Delta—H = 23.43$; $\bullet—35.25$; $\circ—52.56$ kOe.

This turning leads to a change in the area of the extremum cross section of the FS sheet responsible for the oscillations (the "cigars" in the case of beryllium), and this yields the change in position of the oscillations, $\delta H/H = \delta F/F$. For small turns,

$$\frac{\delta F}{F} = \frac{1}{\cos \alpha} - 1 \simeq 0.5\alpha^2 \quad (4.1)$$

that is the following must be fulfilled:

$$\delta H/H = \alpha^2/2 \quad (4.2)$$

The experimental $\delta H/H$ versus α^2 plots obtained with the samples $[10\bar{1}0]$ and $[1\bar{2}\bar{1}0]$ are presented in Fig. 4.11. The choice of the origin of the relative phase variation $\delta H/H$ is generally speaking arbitrary. The experimental $\delta H/H$ versus α^2 plots presented in Fig. 4.11 were

constructed so as to satisfy the relationship (4.2) for large α 's. The validity of (4.2) for $\alpha > 3^\circ$ follows from the results of direct measurements of $F(\alpha)$ [4.31].

It can be seen from Fig. 4.11 that relationship (4.2) is fulfilled for the sufficiently large angles between the direction of the magnetic field and the hexagonal axis. As magnetic field direction approaches the hexagonal axis, the results deviate from (4.2), the deviations being the larger the higher is the magnetic field. The angular range, within which the additional oscillation phase shift can be observed, is somewhat different for the $[10\bar{1}0]$ and $[1\bar{2}10]$ samples, while the shift values at $\mathbf{H} \parallel [0001]$ are the same. This means that $\rho_{xx} = \rho_{yy}$ due to symmetry.

The analysis in [4.30] demonstrated that the additional MB oscillation phase shift could be explained neither by an anomalous change in frequency, nor by the Schoenberg effect.

The two factors explaining this are the two-dimensionality of the MB trajectories at $\mathbf{H} \parallel [0001]$ and the phase coherency of the MB in beryllium. The two-dimensionality of the MB net under the CMB conditions results in it being more sensitive to variations in the phases of the electron wave function than in the one-dimensional case of a linear chain of coupled MB orbits. In the latter case the role of phase indicator is only played by small closed FS cross sections, whereas the variations in the phases of the electron wave functions along linkage-orbits between them do not appear in the final expressions for oscillations of kinetic coefficients. This takes place because the wave functions can only interfere on closed orbits. In the two-dimensional case there is a net of intersecting orbits and in addition to the interference of wave functions on small closed FS cross sections they interfere on the linkage-orbits. This is what leads to the sensitivity of kinetic coefficients to small variations in the phases of the wave functions. This variation emerges, for example, during an MB transition of carriers from one FS sheet to another. According to [4.32], the jump in the phase of the wave function during such a transition depends on the magnetic field's strength, and this may be associated with the observed field dependence of the MB oscillation phase shift. In principle, other reasons are possible resulting in small variations in the phase of the electron wave function.

As has been noted above, we do not yet have a rigorous theory for CMB in the two-dimensional case. There is only an estimate of the range of magnetic field directions for which the influence of two-dimensionality cannot be neglected. According to [4.33], this range amounts to $\alpha_0 \sim \kappa^{1/2}$, where $\kappa = e\hbar H/cp_0^2$ is a parameter of quasi-classicality, and p_0 the characteristic momentum. For beryllium this estimate at $H = 50$ kOe is $\alpha_0 \simeq 10^{-2}$ rad, which is in a reasonable agreement with the experimental data in Fig. 4.11.

Thus, the experimental data from [4.30] indicates the two-dimensional character of CMB in beryllium.

There are other experimental results which have no direct relationship to studies of the MB phenomenon itself, but give an idea of using other methods of investigation and possibilities to gain new information.

The uniqueness of beryllium as an object to investigate MB was reflected in the experimental results of [4.34], where it was shown that by increasing the temperature up to 78 K, the MB began to occur in lower fields than it does at 4.2 K. This phenomenon was called "thermal breakdown" and is related to the fact that owing to the high Debye temperature of beryllium the spread in the Fermi distribution, viz. the overlapping of electron wave functions within the MB regions, grows with temperature much faster than the increase in electron scattering by phonons. A theoretical analysis of this problem is given in [4.35].

Another paper [4.36] recorded observations of helicon resonances in a hexagonal plate in stationary and pulsed magnetic fields. Since the excitation of helicoidal waves is only possible when the numbers of electrons and holes are unequal [4.37], this method is especially suitable for studying MB decompensation in initially compensated metals.

In [4.38] the influence of hydrostatic pressure on the MB in beryllium was investigated. It was proved that the kink in the field dependence of the monotonic part of resistivity due to MB was shifted with pressure towards lower fields, viz. the breakdown field H_0 was decreased. Similar data can be used to get the differential characteristics of the pseudopotential.

Finally, in [4.39] the MB in beryllium was applied to practical ends, namely, the oscillations of beryllium's magnetoresistance were used in the design of a device for measuring magnetic field and its nonuniformity, which can operate in gradients up to 15 kOe/cm.

4.3. ALUMINIUM

Aluminium is a metal with the face-centered cubic lattice whose electron structure has now been investigated to high accuracies. The approximation of quasi-free electrons is quite satisfactorily in aluminium, while the slight difference between its FS and the free-electron one can be described by means of only two pseudopotential coefficients [4.40]. The match between aluminium's FS and experiment is illustrated in Fig. 4.12. The FS consists of a hole sheet in a second zone and three "fourfold rings" in the third one [4.41].

Since the aluminium FS sheets are closed and the metal itself is uncompensated, we would anticipate its magnetoresistance will be saturated with field growth. All the same, magnetoresistance of even polycrystalline samples of aluminium began to rise again with field [4.42]*. Later and as a result of detailed measurements on single crystals, this uncommon behavior was explained as due to magnetic breakdown leading to the formation of open trajectories

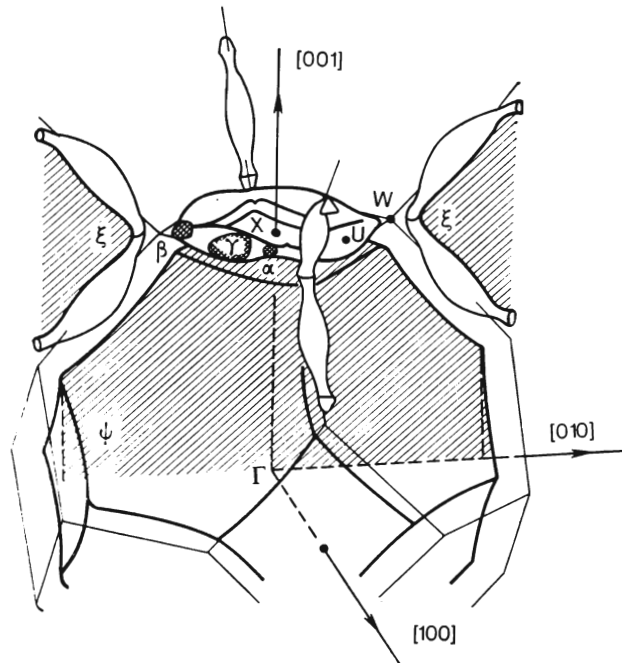


Fig. 4.12. The Fermi surface of aluminium. The α , β , and γ letters denote the extremum cross sections of the "fourfold ring" for $\mathbf{H} \parallel [100]$.

within a very narrow interval of magnetic field direction near the four-order axes [4.43]. Here the decisive argument proved to be the detection of large amplitude oscillations in the magnetoresistance (Fig. 4.13). The oscillation frequency suggested that the MB in aluminium takes place at the vertices of Brillouin zone W via the small cross sections of the "fourfold ring" (the β -orbits). The characteristic breakdown field in aluminium is $H_0 \simeq 40$ kOe. A stereographic projection of the open MB trajectories was constructed in [4.44]. This projection looks like a square with sides 1° long, from whose vertices emanate "whiskers" about 5° in length.

* The unexpectedness of this result forced its validity to be questioned even by Luthi and Olsen.

The oscillations in the magnetoresistance of aluminium indicated the presence of phase coherency for small β -orbits. Still, the question

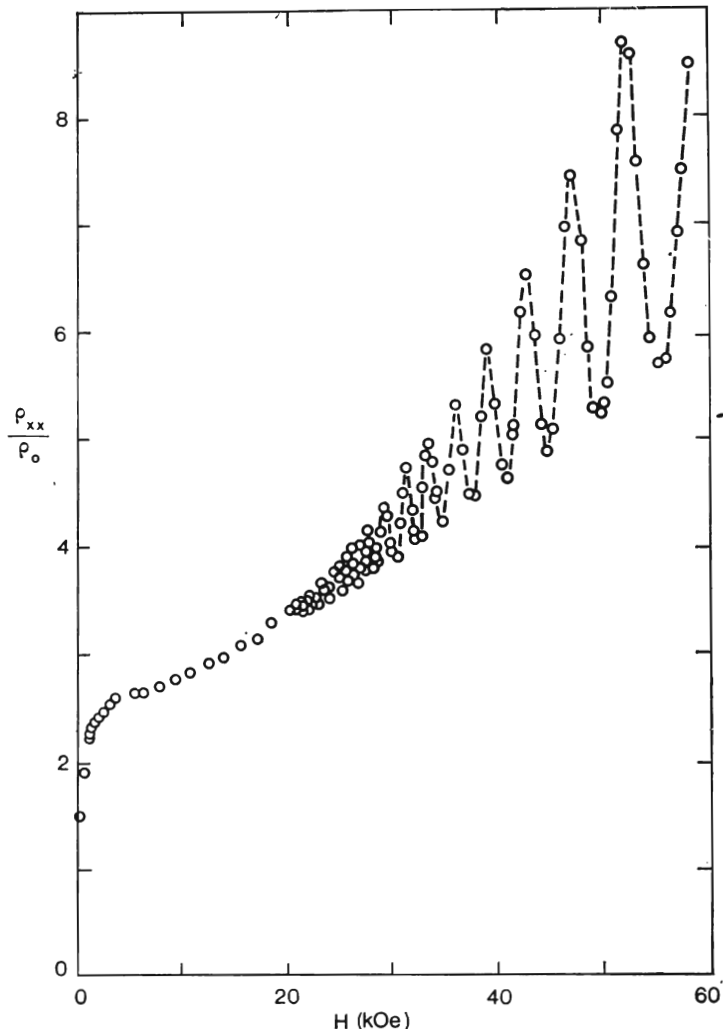


Fig. 4.13. The MB oscillations of the resistance in aluminium. The magnetic field direction is deviated from the [100] axis through the angle of 0.4° .

of whether the phase coherency is conserved for large parts of the trajectories passing over the FS hole sheet remained open for a long time. The first corroboration of MB coherency in aluminium came

as a result of a detailed investigation of the dependence of the monotonic part of magnetoresistance on vacancy concentration C_v [4.45]. The measurements were made on two aluminium samples with [100] orientations with a low density of dislocations about 10^5 cm^{-2} . The initially high resistance ratio $\text{RRR} = 2.5 \times 10^4$ was lowered down by an order of magnitude after introducing the vacancies

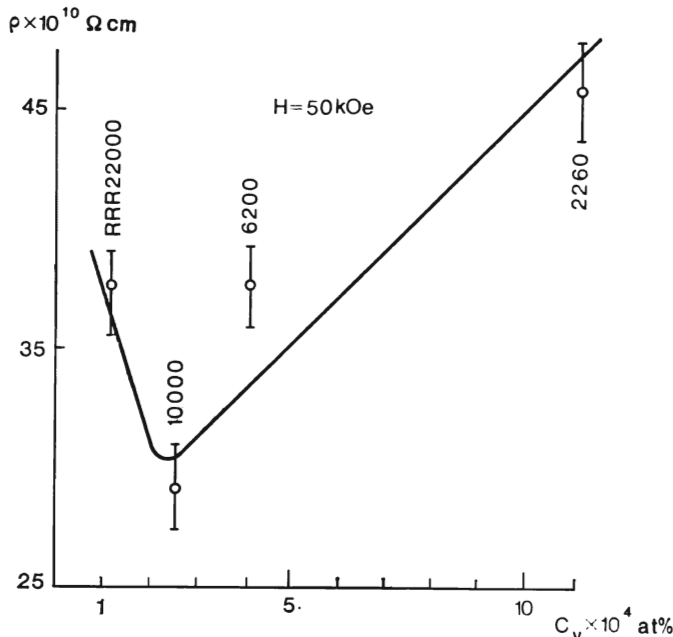


Fig. 4.14. The monotonic part of magnetoresistance of aluminium in the field of $H = 50$ kOe versus the vacancy concentration. The magnetic field direction is chosen at the boundary of a two-dimensional region of open MB trajectories.

produced by quenching from high temperatures. The monotonic part of aluminium's magnetoresistance in the field of 50 kOe is plotted in Fig. 4.14 versus the vacancy concentration. The feature here is the presence of a minimum at $C_v = 2 \times 10^{-4}$ atom %.

The minimum can be explained by the CMB model. The open MB trajectories yield a quadratic contribution to the magnetoresistance, $\rho \sim WH^2 \frac{\Delta p}{p_F}$, where Δp is the MB layer thickness. The scattering from vacancies violates the phase coherency, which brings about a fall in the MB contribution in inverse proportion to C_v . In addition we must take into account the presence of the conventional addend, which is proportional to C_v , so that at the

end we arrive at $\rho^{\text{coh}} \sim AC_v + \frac{B}{C_v} WH^2 \frac{\Delta p}{p_F}$. Clearly, given a fixed magnetic field, the C_v dependence of ρ^{coh} should pass through a minimum.

By assuming from the very beginning that phase coherency is violated for large orbits, viz. by using the framework of stochastic MB model, we obtain $\rho^{\text{stoch}} \sim A'C_v + B'WH' \frac{\Delta p}{p_F}$. In this case, the C_v dependence of ρ^{stoch} has no minimum and the magnetoresistance itself is much smaller than it is using the coherent model. Indeed, the calculation in [4.43] used the stochastic model and yielded a magnetoresistance an order of magnitude lower than the value measured on very pure aluminium samples [4.45].

Thus, investigations of the monotonic part of aluminium's magnetoresistance and performed on the samples with different contents of point defects resulted in the conclusion that phase coherency is present for every segment of the MB trajectories.

Another corroboration of the coherent character of the MB in aluminium was obtained in [4.44] when studying oscillatory effects. The authors were investigating the oscillations of the thermopower, its high sensitivity to MB had been pointed out in several papers, [4.46-48]. Widening the range of magnetic fields to 150 kOe and using the samples with $\text{RRR} = 2 \times 10^4$ enabled oscillations with new frequencies to be detected. The examples of the experimental field dependences of aluminium's thermopower are presented in Fig. 4.15. In addition to the β -orbit oscillations the record contains ϵ - and ν -oscillations too. The ϵ -oscillations intermediate in frequency are discernible from $H = 65$ kOe, while the ν -oscillations are

Table 4.2. Physical Properties of Aluminium

Lattice constant at 0 K	$a = 4.032 \text{ \AA}$
Elementary cell volume	$\Omega = 1.639 \times 10^{-23} \text{ cm}^3$
Brillouin zone dimensions	$\Gamma K = 1.653 \times 10^8 \text{ cm}^{-1}$ $\Gamma X = 1.558 \times 10^8 \text{ cm}^{-1}$ $\Gamma W = 1.742 \times 10^8 \text{ cm}^{-1}$ $k_F = 1.757 \times 10^8 \text{ cm}^{-1}$
Radius of free electron sphere	
Parameters of extremum cross sections of the "fourfold ring" for $H \parallel [100]$:	
frequencies	$\alpha = 0.282 \text{ MGs}$ $\beta = 0.468 \text{ MGs}$ $\gamma = 3.914 \text{ MGs}$
effective masses	$m_\alpha = 0.091 \text{ m}$ $m_\beta = 0.102 \text{ m}$ $m_\gamma = 0.180 \text{ m}$

only seen for $H > 120$ kOe. The effective masses of carriers responsible for the β - and ν -oscillations were evaluated from temperature dependences, viz. $m_\beta \simeq 0.1$ m , $m_\nu \simeq 0.45$ m . This could not be done for the ϵ -oscillations because a drop in temperature to 2.4 K was not accompanied by any noticeable change in their amplitude.

An analysis of the possible MB trajectories enabled the ν -oscilla-

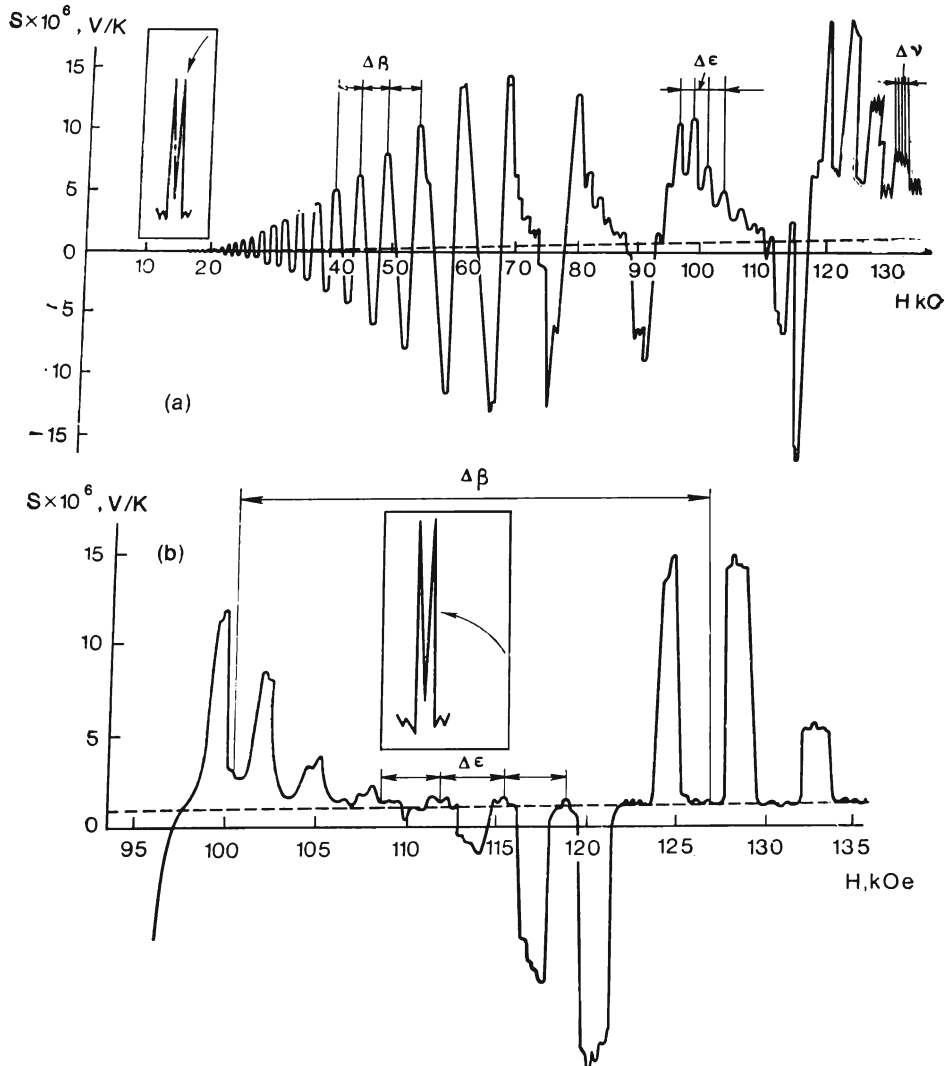


Fig. 4.15. MB oscillations of the thermopower in aluminium. The insets illustrate the sample positions at the instant of recording.

tions to be ascribed to an extreme orbit along one of the "fourfold ring" branches. This conclusion was also supported by a trustworthy value of effective mass (see Table 2).

The case of the ϵ -oscillations is more complicated. MB orbits with the required cross section could not be found and so it was assumed that the ϵ -oscillations were due to interference, this being why they are absent in the oscillations of thermodynamic quantities and have weak temperature dependences [4.49].

However, this conclusion must be treated with caution. The point is that the shape of these oscillations are markedly not sinusoidal, while their frequency is suspiciously close to that of the transverse extreme cross section of the "fourfold ring" branch (the γ -branch in the de Haas-van Alphen effect [4.50]). Moreover, these oscillations are observed in the range of fields, for which the β -oscillations are too nonsinusoidal. To explain the last point, the authors of [4.44] resorted to the Schoenberg effect [4.51] claiming that, under the conditions favourable for a strong de Haas-van Alphen effect, the internal field in a sample might be quite different from the applied magnetic field. This idea may prove useful in explaining the ϵ -oscillations, too. In fact, direct measurements [4.50] have shown that the main part of oscillatory magnetization comes from γ -orbits, so it is rather probable that in rising magnetic field the sample will laminate in diamagnetic domains with the frequency γ . The magnetization and thermopower signal are at maximum within the magnetic field intervals for which the diamagnetic domains are not established, whereas within the intervals for which the diamagnetic domains do exist, the induction in the sample is nonuniform and the thermopower signal falls (practically to zero—see Fig. 4.15b). That is segments of nonuniform magnetization are "cut" from the field dependence of thermopower. The domain structure period has to be of the order of the cyclotron radius r_H^γ of the electrons responsible for the period [4.52]. In this case $r_H^\beta \ll r_H^\gamma \ll r_H^\gamma$, and the emergence of a domain structure need not necessarily end in the violation of phase coherency for β -orbits, but it may completely liquidate the phase coherency for γ -orbits and the linkage-orbits across the hole sheet in the second zone of aluminium FS. Therefore, even though the period of the giant oscillations in both magnetoresistance and thermopower is governed by the β -section of the "fourfold ring" the absolute value of the oscillations depends considerably on whether the phase coherency is conserved for linkage orbits. If the phase coherency is not conserved, the oscillations practically vanish*.

* The destruction of phase coherency in nonuniform magnetic field was observed in experimental investigations of beryllium's resistance MB oscillations [4.26] (see pp. 186-187).

This interpretation leads to two conclusions. First, only CMB can be that sensitive to irregularities in the magnetic induction and this implies that the MB in aluminium is coherent, and second, there is a good argument in favor of a correlation between large thermopower signals and CMB.

4.4. NIOBIUM

The interest in the electron structure of VB transition metals with cubic body-centered lattice was provoked by their high transition temperatures to the superconducting state besides general physical reasons. In particular, niobium is the record holder in Periodic Table having a $T_c = 9.25$ K at normal pressure [4.53]. However, following the detection in it of the MB [4.54] which occurs through a spin-orbital gap, it becomes clear that it might be possible to obtain information about the spin-orbital interactions in transition metals, about the way the interaction depends on atomic number, and about the impact on crystalline lattice symmetry. The study of the MB in transition metals is thus of special significance. In addition, the coherent effects are often accompanied by oscillations of the kinetic coefficients, thus yielding additional important information on the topology of FS.

The Fermi surface of niobium (Fig. 4.16) has been investigated in a number of theoretical [4.55-58] and experimental [4.59-63] papers. It consists of a hole “octahedron” inside the second zone as well as hole ellipsoids and an open multiply connected surface (“jungle gym”) in the third one (Table 4.3). The “octahedron” is

Table 4.3. Physical Properties of Niobium

Lattice constant	$a = 3.295$ Å
Elementary cell volume	$\Omega = 1.789 \times 10^{-23}$ cm ³
Brillouin zone dimensions	$\Gamma H = 1.907 \times 10^8$ cm ⁻¹ $\Gamma N = 1.348 \times 10^8$ cm ⁻¹
Minimum neck diameter of the open multiply connected sheet of the	
Fermi surface in the third zone	$d = 0.21$ ΓH
Extremum cross section of the “octahedron” for $H \parallel [100]$:	
frequency	$\gamma = 104.6$ MGs
effective mass	$m_\gamma = -5.2$ m

rather tightly “embedded” in the multiple “jungle gym” and non-relativistic calculations yield contacts of the sheets of the FS

on the ΓP symmetry lines and on the necks of the “jungle gym” (Fig. 4.17). Spin-orbital interaction completely removes the degeneracy on the necks, however the point contacts between the FS sheets can remain intact along the ΓP line, which is a third order symmetry axis.

The impact of MB on niobium’s magnetoresistance was studied in [4.64]. The measurements were made with the extremely pure samples having RRR from 3×10^4 to 6×10^4 .

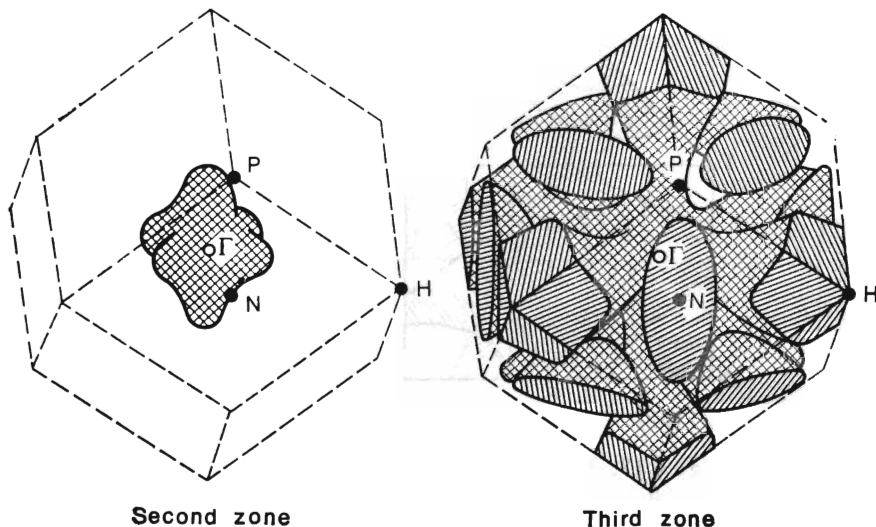


Fig. 4.16. The Fermi surface of niobium. The sheet inside the second zone is called “octahedron”, the third zone contains the ellipsoids centered at the points N and the open multiply connected surface named “jungle gym” (the latter’s “sleeves” cross Brillouin zone boundaries near the H vertex).

Niobium is an uncompensated metal with two-dimensional regions of open trajectories around the third and fourth order axes. Niobium’s resistance should depend quadratically on the magnetic field inside the regions except for the centers, where the open trajectories are transformed into a net of closed ones, and the magnetoresistance is saturated. However, the measurements have demonstrated that inside the two-dimensional region around the fourth-order axis there are isolated magnetic field directions (corresponding to “troughs” in the angular dependence of the magnetoresistance, see Fig. 4.18a) for which there are sizable deviations from the quadratic dependence (Fig. 4.18b). This was the signature of MB.

The breakdown field in niobium was determined from the way the magnetoresistance depends on the field in the “troughs”, the

field being at 7.5° to the axis [100]. A geometrical analysis of the spatial layout of MB trajectories for such a magnetic field orientation is given in Fig. 4.19. In this case only the type A and B trajectories are possible. One closed orbit A_2 is located along the "octahedron" and between the open trajectories A_1 and A_3 . Three closed orbits are located between the open trajectories B_1 and B_3 : two along the "octahedrons" and one (B_2) across jungle gym. Since the MB probability for B type trajectories is much smaller than for A

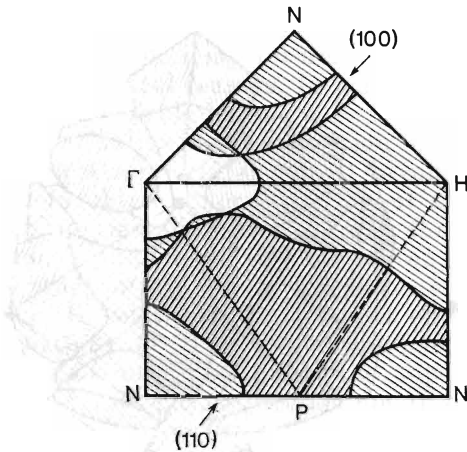


Fig. 4.17. The central (100) and (110) cross sections of niobium's FS. The "octahedron" (without hatching) is centered at the zone center (at the point Γ). The space between the "jungle gym" and ellipsoids is shaded by inclined lines. In the (110) cross section, the contacts between "octahedron" and "jungle gym" are located on the ΓD line and "jungle gym" necks, while those in the (100) cross sections are only on the "jungle gym" necks (which is opened along the ΓH line).

type ones, the contribution of the former can be neglected. The deviations of magnetoresistance from the quadratically rising curve are due to the MB, as a result of which an electron can pass from one open trajectory onto another having the opposite direction of motion of an electron. It follows from symmetry conditions that the probability of such a transition for the A_1 and A_3 trajectories is exactly equal to the probability of an electron moving along a closed orbit around the A_2 "octahedron". If we use the CMB model (keeping in mind the high quality of the available samples) and take into account that there are eight points of magnetic breakdown, then the probability that an "octahedron" will be traced

is defined [4.21] as $W = \prod_{i=1}^8 q_i = \prod_{i=1}^8 (1 - W_i)$, where W_i is the

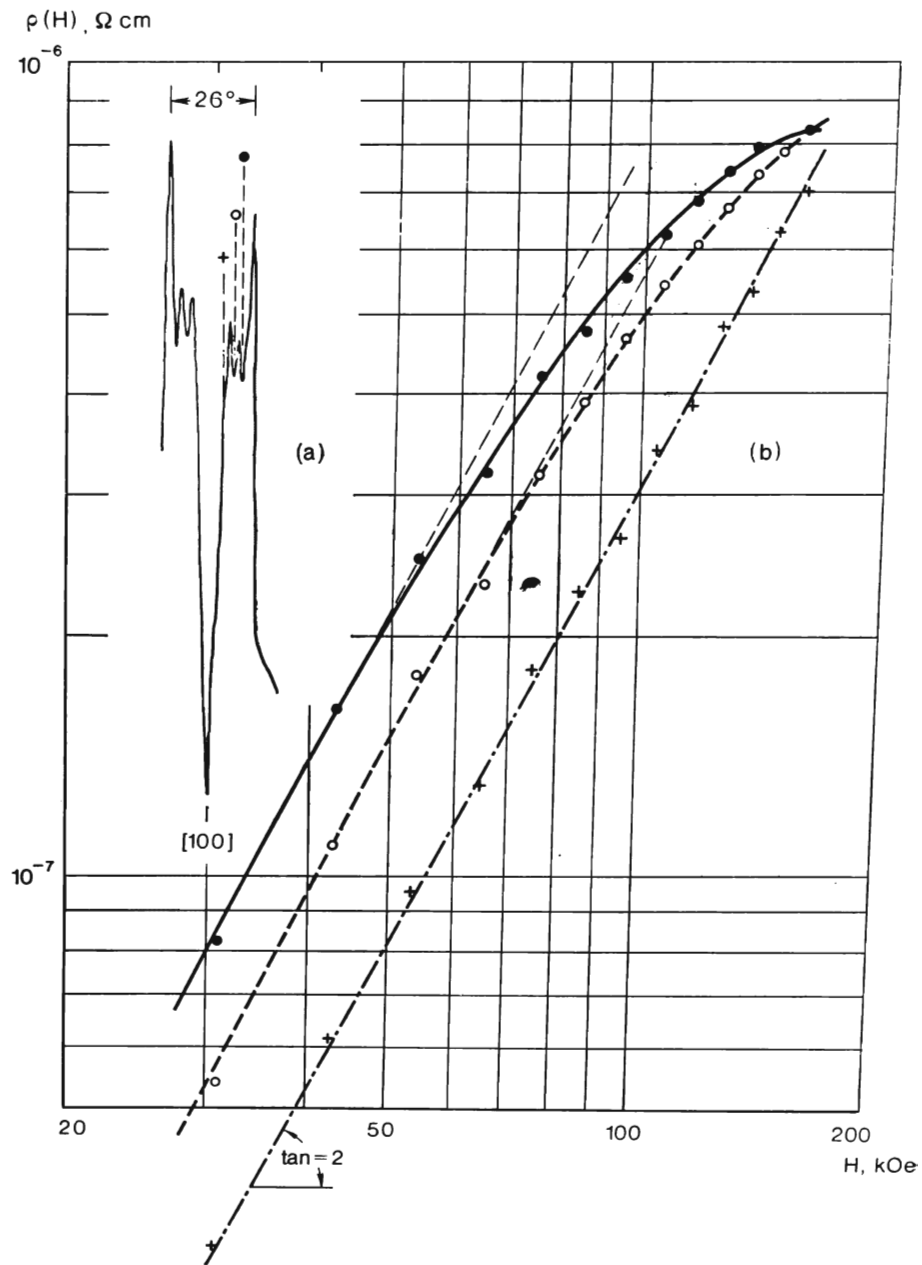


Fig. 4.18. Angular dependence of the magnetoresistance for niobium sample inside the two-dimensional region of open trajectories around a fourth order axis. The dependence is obtained in the field of 160 kOe at $T = 4.2$ K (a). The field dependences of the resistance at different points inside the two-dimensional region (b). When the angle α between the magnetic field direction and the [100] axis is $\alpha = 4^\circ$ (marked +), then $\rho \sim H^2$; for $\alpha = 7.5^\circ$ (marked ○) and 10° (marked ●) the deviations from the parabolic path are observed.

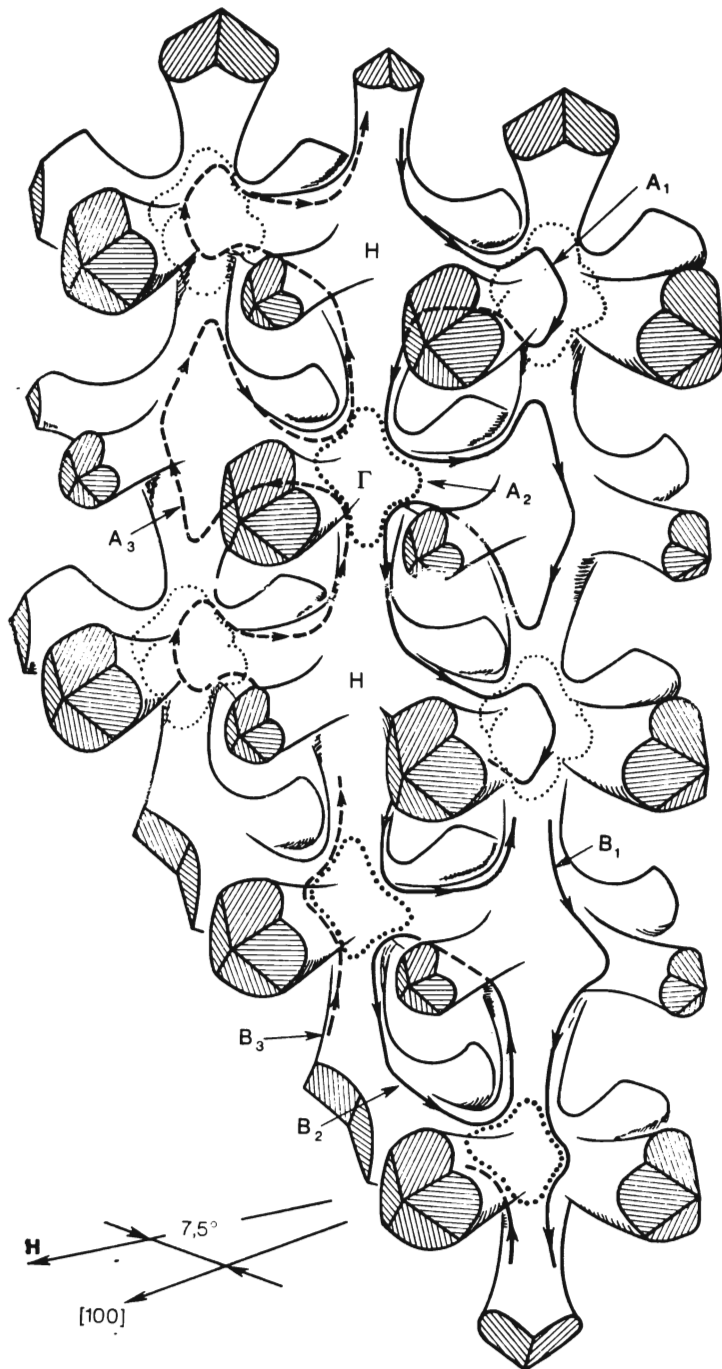


Fig. 4.19. Spatial position of the MB trajectories in niobium.

probability of magnetic breakdown at the i -th point, while the dependence of the resistance on the magnetic field will have the form $\rho \sim WH^2$. Without going into detail of the W_i calculation, and comparing the theoretical curves for different values of the breakdown field H_0 with the experimental data (Fig. 4.20), we find that $H_0 = (280 \pm 20)$ kOe. Thence the interzonal energy barrier

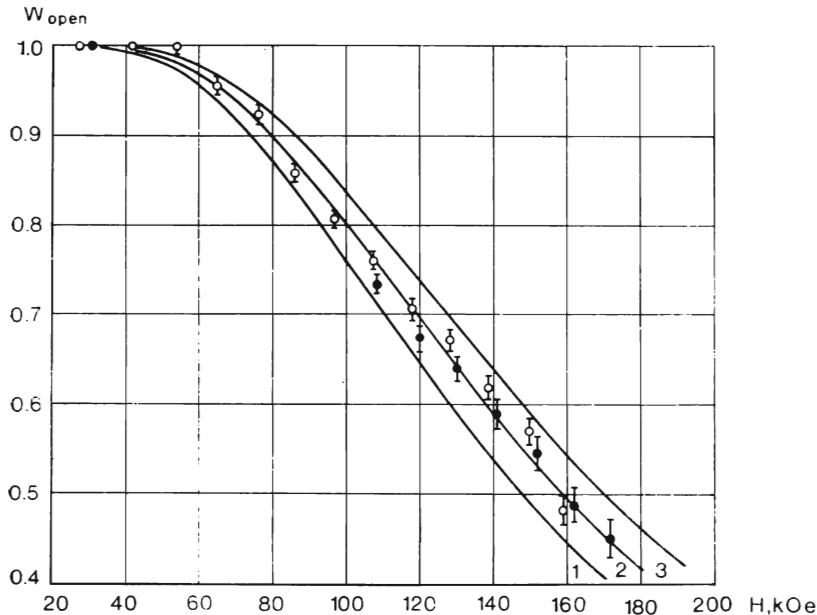


Fig. 4.20. The probability of electron's motion in an open trajectory along the "jungle gym" versus the magnetic field for $\alpha = 7.5^\circ$. Experimental points were obtained with the niobium [001] sample having $RRR = 6 \times 10^4$ at $T = 2.2$ (marked \bullet) and at 4.2 K (marked \circ). The theoretical curves 1, 2, 3 are calculated for the different values of the breakdown field strengths: 1—260; 2—280; 3—300 kOe.

in niobium can be estimated, i.e. $\Delta\epsilon = 0.09$ eV. It is interesting to note that this practically coincides with the energy of spin-orbital interactions that was obtained spectroscopically for Nb^{3+} ions [4.65].

The essential point is the assumption about the phase-coherent character of the MB in niobium. This assumption would be supported by a detection of giant oscillations in the kinetic coefficients. It is not realistic to expect to detect large amplitude magnetoresistance oscillations in the case of niobium. Its FS does not have a small diameter limiting the thickness of the MB layer so that the oscillation phase can be considered constant within the boundaries of the

layer as does beryllium's FS (its limiting dimension being the diameter of the "coronet" necks, k_{zm}). The thermopower is another matter. Above (e.g. with aluminium) it was shown that thermopower is abnormally strong under conditions of CMB. This gave rise to hopes that MB oscillations thermopower might be detectable in niobium.

Simultaneous measurements of thermopower and magnetoresistance were performed with a niobium sample cut along the fourth-order axis and having RRR 3×10^3 [4.66]. The angular dependence

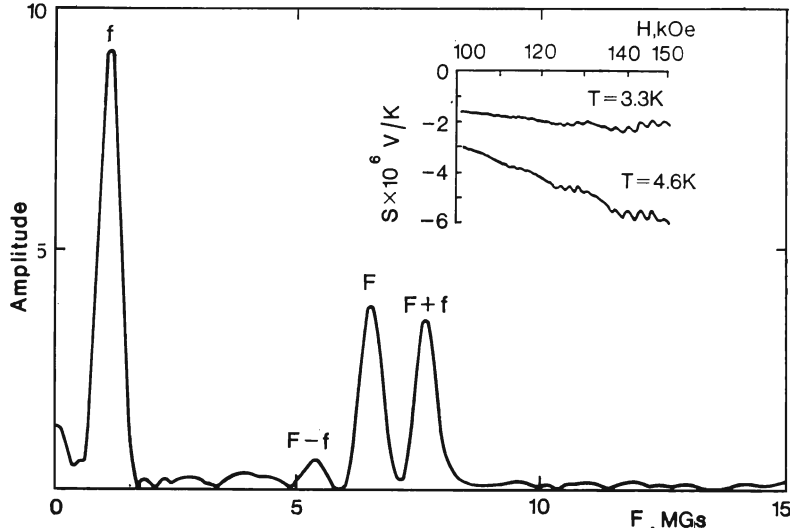


Fig. 4.21. The MB oscillations of the thermopower of niobium for $\mathbf{H} \parallel [110]$ and their Fourier transform.

of the thermopower as a whole matched the behaviour of the magnetoresistance except for $\mathbf{H} \parallel [110]$, where a narrow thermopower peak was observed. For this orientation of the magnetic field, the conical point contacts between the "octahedron" and "jungle gym" and lying on the symmetry line GP (Fig. 4.17) take on great significance. The strong thermopower signal is in this case undoubtedly related to the high MB probability W near the conical points (at a conical point itself $W = 1$).

The magnetic field dependences of thermopower include oscillations with a complicated spectrum (Fig. 4.21). These oscillations have a low frequency $f = 1.1$ MGs, a high frequency $F = 6.5$ MGs, as well as combined frequencies, $F + f$ and $F - f$. Similar dependences were obtained for the directions of the magnetic field close to [110], for which the frequencies we cited were found and moreover

their amplitudes in terms of the angle α from the [110] axis began to grow, achieving a maximum at $\alpha \simeq 3^\circ$, and then diminishing. These oscillations can be easily understood using the CMB model. The MB trajectories for $\mathbf{H} \parallel [110]$ are illustrated in Fig. 4.22a. This shows that the directions of electrons moving across the “jungle gym” and across the “octahedron” are the same, whereas they can pass from one FS sheet onto another at the necks of the “jungle gym” and in the regions of the conical point contacts. Similar, albeit

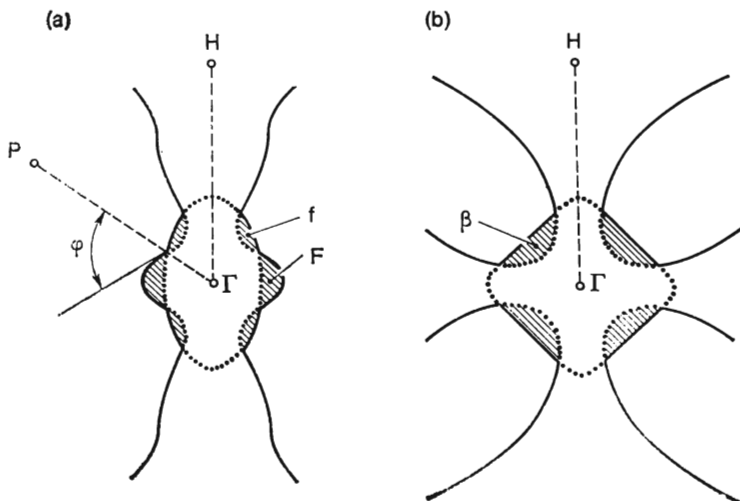


Fig. 4.22. The scheme of MB trajectories in niobium. Solid lines show the trajectories along "jungle gym", points—along "octahedron". The dashed cross sections give rise to the interference oscillations in thermopower: (a) — $\mathbf{H} \parallel [110]$, (b) — $\mathbf{H} \parallel [100]$.

simpler, situation was considered in [4.67] as applied to magnesium. It was proved that if the MB is phase-coherent, then coupled MB trajectories with the same direction form a sort of "quantum interferometer" whose "base" are the cross sections between the trajectories. The amplitude of the interference oscillations weakly depends on the temperature because the appropriate effective mass equals the difference between the effective masses of the quantum interferometer's two orbits and is small as a rule.

An elementary analysis demonstrates that a quantum interferometer a scheme of which is given in Fig. 4.22a can provide oscillations with the frequencies F , f , $F + f$, $F - f$, $2f$, $F + 2f$, $F - 2f$, the amplitudes of which depend on the relation between the MB probability on neck W_n and that in the region of the conical point contact W_c . If W_n and W_c are of the same order of magnitude, then

the amplitudes of all components will be about the same. However, only the first four frequencies were experimentally observed (Fig. 4.21). This is only possible if $W_n \ll W_c$, that is, if the contact on the ΓP line is really a point contact.

When $\mathbf{H} \parallel [100]$, the thermopower oscillations contain only one frequency, $\beta = 8.64$ MGs. The MB trajectories for this case are

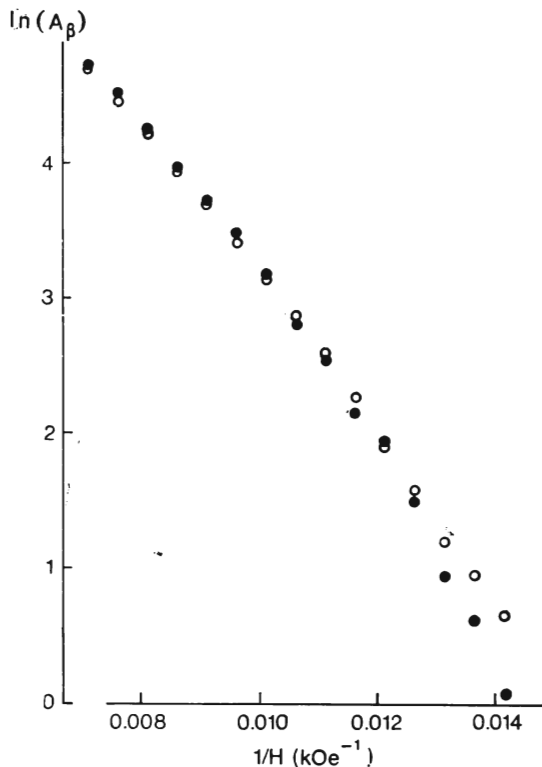


Fig. 4.23. The amplitude of the MB thermopower oscillations versus the reciprocal of the magnetic field for $\mathbf{H} \parallel [001]$ when studying the MB in niobium under uniaxial stretching of the sample: \circ —the free sample, \bullet —the stretched sample.

shown in Fig. 4.22b. The amplitude of the thermopower oscillations A_s depends on several factors, including the MB probability $W = \exp(-H_0/H)$ and the temperature and impurity broadenings of the Landau levels described by the effective mass m^* and Dingle's temperature T_D , respectively. At the limit of the low magnetic fields (compared to H_0) only the exponential multipliers in A_s

remain

$$A_s \sim \exp \left[-H_0/H - k \frac{m^*}{m} (T + T_D)/H \right] \quad (4.3)$$

where $k = 150$ kOe/deg.

The behaviour of the oscillation amplitude versus the reciprocal of the magnetic field for $\mathbf{H} \parallel [100]$ is given in Fig. 4.23. The effective mass of the β -oscillations can be found from the temperature dependence of the de Haas-van Alphen effect [4.63] and is equal to $m^* = 0.3 m$. Evaluating Dingle's temperature from RRR yields $T_D = 0.3$ K. By substituting these values into (4.3) and by using the experimental data in Fig. 4.23, we can obtain an additional estimate of the breakdown field in niobium, $H_0 = (280 \pm 300)$ kOe. This is in a full agreement with the results obtained from an analysis of the field dependence of the magnetoresistance.

The complete spectrum of the MB oscillations of niobium's thermopower is given in Fig. 4.24. To improve the sensitivity when recording this spectrum, a modulation of temperature gradient along the sample was used. The heater was powered by an 8 Hz ac current, and the signal from the sample potential leads was applied to the input of a selective lock-in amplifier tuned for 16 Hz. This significantly suppressed the noise and completely eliminated the drifts induced by parasitic emf's in the connecting wires.

The frequencies of the thermopower MB oscillations are governed by the cross sections between "jungle gym" and the "octahedron". It is quite probable that some spectral branches, e.g. F , are governed by a nonextremum cross section from the MB near a conical point. In fact, the observation of MB oscillations in niobium's thermopower was the first experimental corroboration of the existence of the "octahedron", as it had not been detected before in the measurements of the de Haas-van Alphen effect [4.61] or those of magnetothermal oscillations [4.62]. Analogous considerations applied to investigations of the MB in vanadium [4.68] enabled the authors to establish that the FS of vanadium and niobium FS's are similar thus to choose vanadium's FS model.

The most curious feature of CMB in niobium is the MB near the conical point. Thus, the breakdown field $H_0^* k_z$ away from the conical point is proportional to k_z^2 , i.e. $H_0^* = (\pi \hbar c/e \tan \varphi) k_z^2$, where the angle φ is indicated in Fig. 4.22a. Since the amplitude of the interference MB oscillations is a function of the product $W(1 - W)$ (one factor gives the amplitude of a wave passing down one branch of the "interferometer", the other of a wave going down the other), there always will be a k_z for which $W = 0.5$ and the oscillation amplitude is at a maximum. Thus, if the MB is due to the presence of a conical point contact between the FS sheets, then the MB oscillation's frequency will depend on the cross section slightly away

from the conical point (perhaps, on a nonextremum cross section).

Another feature of the conical point is that it exists because of the high symmetry of the ΓP line on which it is located. Therefore we should expect that even a very small deformation of the sample, lowering the symmetry of its crystal lattice, will be accompanied

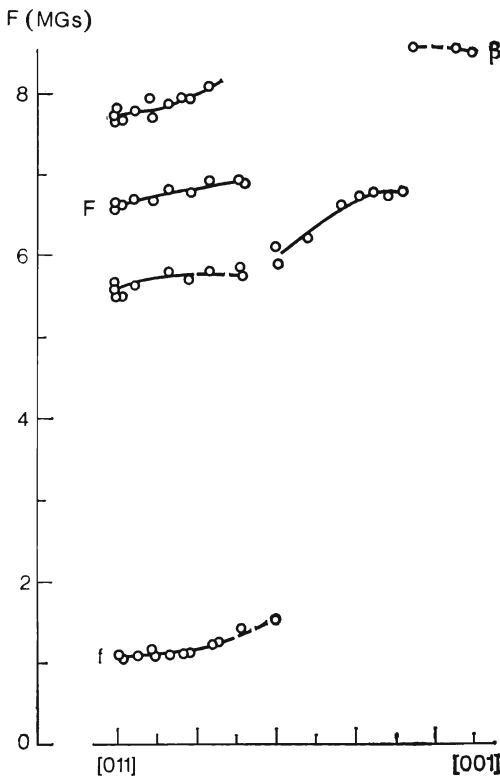


Fig. 4.24. The spectrum of magnetic breakdown thermopower oscillations in niobium.

by the disappearance of the conical point contacts. The effect of a uniaxially stretching a sample on the MB in niobium was investigated in [4.69].

In order to stretch the sample uniaxially the big difference between the thermal expansion coefficients of niobium and fused quartz was utilized. The setup is shown schematically in Fig. 4.25. The sample 1 was cut along the [100] direction by the electric-spark method from a single crystal of niobium with $RRR = 3 \times 10^3$ and then electropolished. The sample has the "arms" between which

the sectional spacer 3, 4, 5 was set made from fused quartz. The tabulated thermal expansion coefficients show that cooling to liquid helium temperatures should stretch the niobium sample by 1.6%. It will actually be stretched by less because of elastic deformations of the arms. In a number of measurements the sample

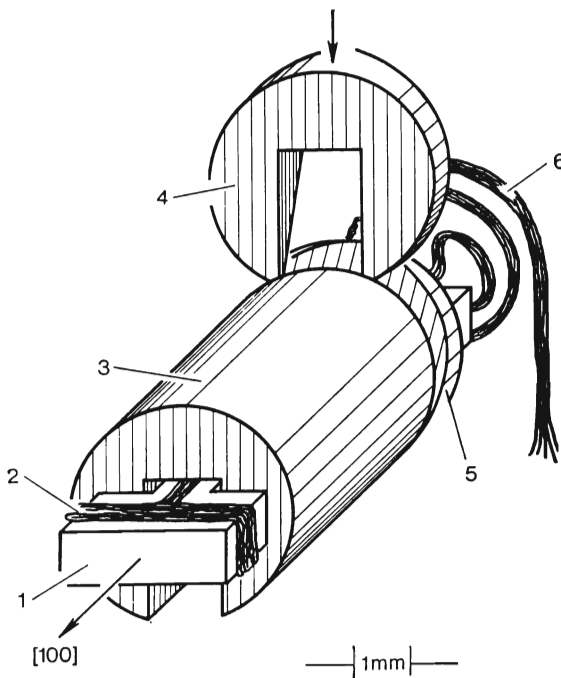


Fig. 4.25. Mounting of the niobium sample to study the uniaxial stretching effects: 1—the sample, 2—the heater, 3, 4, 5—the sectional spacer made from fused quartz, 6—twisted cable composed from current and potential leads.

was stretched to a third the maximum value. In order to do this, an air gap of about 0.07 mm was left between the quartz spacer and the arms when assembling at room temperature.

Eight experimental runs were performed, four runs with the sample stretched and four without stretching, the runs being alternated. The reproducibility of the results as a whole indicated the absence of residual deformation in the sample.

The influence of stretching on niobium's thermopower oscillations for $H \parallel [110]$ can be seen from Fig. 4.26. The examples here are (a) the thermopower recorded with a stretched sample and (b) with a free sample. Data gathered for this direction of a magnetic field

are given in Table 4.4, the frequency ν (MGs) and amplitude A (relative units) being given for each component of oscillation spectrum.

Table 4.4. The uniaxial stretching effect on the niobium thermopower oscillations at $H \parallel [011]$. The data were obtained for $90 \text{ kOe} \leq H < 150 \text{ kOe}$. Frequencies are measured in MGs while amplitudes in arbitrary units

$\Delta l, \text{ mm}$	f		F		$F + f$		$F - f$	
	freq.	ampl.	freq.	ampl.	freq.	ampl.	freq.	ampl.
$\Delta l = 0$	1.14	4.65	6.54	1.93	7.68	1.77	5.40	0.30
$\Delta l = 0.03$	1.11	4.40	6.54	1.82	7.65	1.81	5.46	0.22
$\Delta l = 0.1$	1.06	3.11	6.68	1.78	7.72	1.90	5.64	0.11

This Table shows up the unexpected result that in spite of the assumptions made, the F frequency oscillations which corresponds to the cross section between the conical point contacts (Fig. 4.22a),

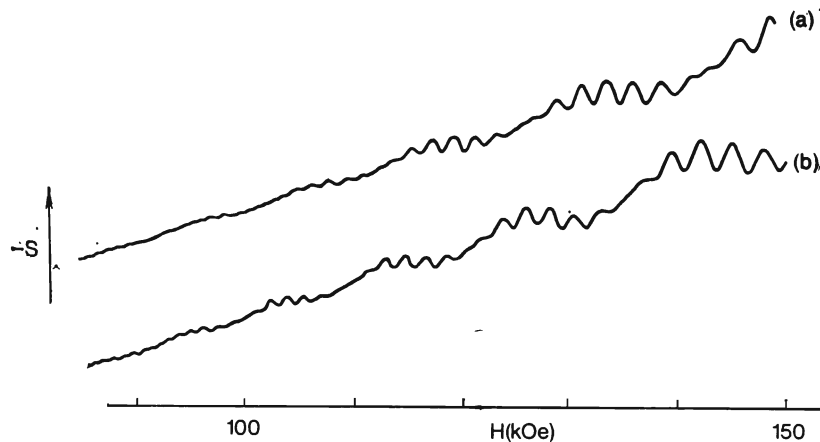


Fig. 4.26. The thermopower oscillations in niobium under uniaxial stretching the sample for $H \parallel [011]$: (a)—the stretched sample, (b)—the free sample.

do not change in amplitude when the sample is stretched. The amplitude of the low-frequency component f , which corresponds to the cross section between the "jungle gym" neck and conical point contact changes the most.

When interpreting these data, it should be borne in mind that the oscillations with the F frequency stem from the $W = 0.5$ cross section and consequently their amplitude is the maximum possible (see p. 207). Therefore, even if the sample is deformed so that the conical point contact disappears, but the resultant gap satisfies the condition of $W > 0.5$, then there will still be a cross section for which $W = 0.5$ and hence the amplitude of the oscillations of frequency F will remain unchanged.

The low frequency f oscillations depend on the cross section between the conical point contact and the "jungle gym" neck. In the first approximation, their amplitude is defined by the expression:

$$A_f \sim \sqrt{W_c (1 - W_c) W_n (1 - W_n)} \quad (4.4)$$

where W_c and W_n are the probabilities of the MB near a conical point and on the "jungle gym" neck, respectively. By assuming that the cross section is specified by the condition $W_c = 0.5$ (for which the oscillation's amplitude is the greatest), a decrease in the f oscillation's amplitude as the sample is stretched can be ascribed to a widening of the gap on neck, the change in the breakdown field being given by

$$(H_0)_1 - (H_0)_2 = \bar{H} \ln (A_2/A_1), \quad (4.5)$$

where \bar{H} is the averaged field.

Substitution the experimental data in (4.5) yields an increase in the breakdown field on the neck of about 100 kOe when the sample is stretched.

On the other hand, the amplitude of the β -oscillations is directly determined by the MB probability on necks of the "jungle gym" (Fig. 4.22b), and the measurements demonstrated that this was not changed by stretching the sample (Fig. 4.23).

These results may be reconciled by assuming the spin-orbital gap is changed anisotropically. The influence of the gap extension in the direction of the stretching force is thus compensated by the gap decrease perpendicular to the force so that the resultant amplitude of the β -oscillations is unchanged.

Of great physical interest is also a comparison of the experimental data on the MB in transition metals whose Fermi surfaces are almost the same. The point is that this sort of analysis is practically the only way to determine the influence of spin-orbital interaction's on the electron structures of transition metals.

At present we can compare qualitatively the results of experimental studies of the MB in the VB group metals, viz. vanadium, niobium, and tantalum which all have similar Fermi surfaces.

In vanadium MB thermopower oscillations were observed in the magnetic fields lower than needed to induce them in niobium, and

this is notwithstanding the fact that the quality of the investigated samples was markedly lower ($RRR = 1.5 \times 10^3$) [4.68]. On the other hand, no sign of MB could be observed for tantalum in the magnetic fields below 175 kOe [4.68].

Comparing these data suggests that interzonal energy gap caused by spin-orbital interaction widens as the atomic number rises. This conclusion is not unexpected, since it was found to be true some time ago for atoms and ions, for which the gap widens in proportion to Z^4 . It should be noted however that this preliminary data favor the conclusion that the interzonal energy gap in transition metals widens at a markedly slower rate than Z^4 .

4.5. RUTHENIUM DIOXIDE, RuO_2

Ruthenium dioxide RuO_2 is an oxide with the rutile (TiO_2) structure and possesses metallic conduction down to liquid helium temperatures [4.70]. The Fermi surfaces for this sort of oxides have been investigated thoroughly especially for RuO_2 , OsO_2 , and IrO_2 . The oxides have a tetragonal structure with a ratio of $c/a = 0.7$ (see Table 4.5) and two molecules in each elementary

Table 4.5. Physical Properties of RuO_2

Lattice constants	$a = 4.4919 \text{ \AA}$ $c = 3.1066 \text{ \AA}$
Brillouin zone dimensions	$\Gamma Z = 1.0113 \times 10^8 \text{ cm}^{-1}$ $\Gamma X = 0.6994 \times 10^8 \text{ cm}^{-1}$
Oscillation frequencies for $\mathbf{H} \parallel [100]$	$\gamma = 28.7 \text{ MGs}$ $\delta = 78.3 \text{ MGs}$
Specific electrical resistance at room temperature	$\rho_{300 \text{ K}} = 4 \times 10^{-5} \Omega \text{ cm}$

cell. Transition metal's atoms are arranged in body-centered tetragonal lattices with each metal atom surrounded by six oxygen atoms. Because of low symmetry of the crystalline lattice, the oxides FS's are strongly anisotropic. An attractive feature of RuO_2 is the small value of the spin-orbital interaction, and this makes us hope we may be able to detect MB and thus find a new and useful source of information about the FS topology.

The first calculations of ruthenium dioxide's electron structure were nonrelativistic [4.71] and the resulting cross sections of the FS by principal symmetry planes are shown in Fig. 4.27a. The electron sheet e_5 is almost an ellipsoid, the hole sheet h_4 contacts the latter at several points and "punches through" the facets (001) and (010)

of Brillouin zone. This means that they should be open both along the tetragonal [001] and binary [110] axes. Experimentally, no open trajectories were observed along the [110] direction [4.72], nor was the neck of the h_4 branch detected in this direction [4.73, 74]. Therefore the nonrelativistic zone structure was deformed to eliminate the openness [4.74]. The FS cross sections given by this semiempirical approach are shown in Fig. 4.27c. The model has a new element in the FS, viz. a hole ellipsoid h_3 at Z whose existence had no direct experimental corroboration.

The introduction into the zone calculations of a small (all in all 0.011 Ry) spin-orbital interaction eliminated the branches of the hole sheet h_4 along the [110] direction that contradicted experi-

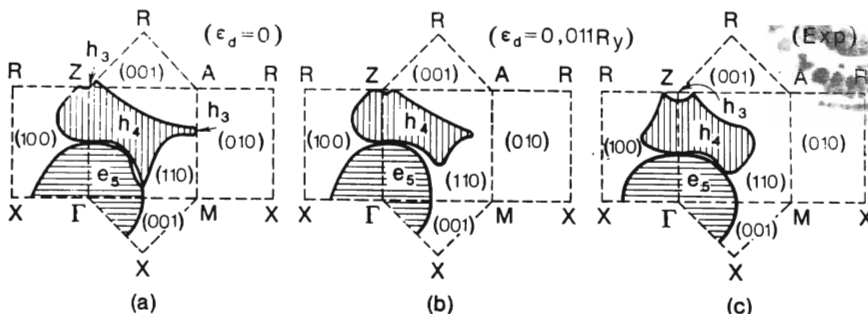


Fig. 4.27. The central cross sections of the FS in RuO_2 [4.54]: (a)—nonrelativistic calculation ($\epsilon_d = 0$), (b)—calculation with a due regard for spin-orbital interaction ($\epsilon_d = 0.011$ Ry), (c)—semiempirical model.

ment. Nevertheless the new FS element was not produced (Fig. 4.27b) [4.71]. Also, the spin-orbital interaction eliminated the contacts between the electron and hole sheets of the RuO_2 FS that were predicted by the nonrelativistic calculations. The spin-orbital gap between e_5 and h_4 along the ΓZ line remained however extremely small because of the accidental degeneracy of the zones slightly below ϵ_F . Thus open trajectories along the tetragonal [001] axis remained as before possible due to MB.

In the relativistic model, the electron sheet e_5 closely resembles an ellipsoid. The hole sheet h_4 is similar to the surface well-known as the “dog’s bone”, but with two exceptions. First, the h_4 sheet crosses the facet (001) of the Brillouin zone with a finite slope, as a result of which h_4 within the scheme of repeated zones has a constriction with sharp edges. The second feature of the h_4 hole sheet that can be clearly seen from a three-dimensional image of the FS relativistic model (Fig. 4.28) is the flatness of its “arms”. These features of the h_4 hole sheet can explain the data on the magnetothermal oscillations in RuO_2 [4.74], where neither the constriction of h_4 at $\mathbf{H} \parallel$

$\parallel [001]$, nor the central extremum cross section of h_4 at $\mathbf{H} \parallel [110]$ were detected. However, the final decision in favor of the FS relativistic model for RuO_2 was made after detecting magnetic breakdown and investigating the MB oscillations of resistance and thermopower.

Single crystals of RuO_2 were grown by a transport technique in an open system. The samples were cut out along the principal crystallographic directions $[001]$, $[010]$, and $[110]$ and had $\text{RRR} = 600-700$. The current and potential leads were glued on with

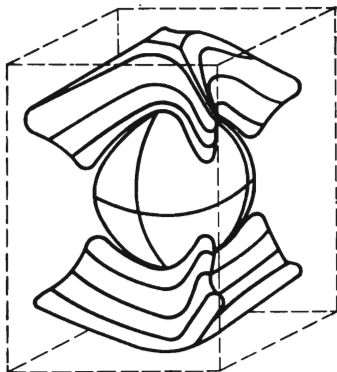


Fig. 4.28. Relativistic model of the FS for RuO_2 .

silver paste and the mounted sample was placed in an apparatus [4.75] in which it could be rotated by 360° and the rotation axis inclined by 14° . A magnetic field up to 150 kOe was generated using a superconducting solenoid. The oscillating signals were processed by the technique used to investigate the MB in niobium.

The results of the measured angular and field dependences of RuO_2 magnetoresistance are presented in Fig. 4.29. The angular functions are slowly changing, whereas the field dependences are close to quadratic. Sharp magnetoresistance minima in the directions perpendicular to the tetragonal $[001]$ axis were only observed for the binary $[110]$ and $[010]$ samples. A trend to saturation can be seen in the field dependences of resistance recorded at these minima (the lower curves in Fig. 4.29e, f). This behaviour of the magnetoresistance is in agreement with an earlier assumption [4.72] about the presence of open trajectories along the tetragonal $[001]$ axis. It must however be said that the trend to saturation emerges only at $\omega_c\tau > 5$, whereas the resistance increment $\Delta\rho/\rho$ in this case is abnormally large and amounts to 50, in spite of the quasiclassical theory, for which $\Delta\rho/\rho \sim 1$. These features can be explained by tracing the origin of the open trajectories due to a magnetic breakdown.

The magnetic breakdown is also responsible for the resistance and thermopower oscillations observed with the [010] sample for $\mathbf{H} \parallel \parallel [100]$. The magnetoresistance oscillations were of small amplitude, and like those of niobium, can be explained by the absence of a small diameter of the Fermi surface for RuO_2 that would limit the MB-layer thickness. The thermopower oscillations were much more pronounced and were not only observed for $\mathbf{H} \parallel [100]$ but also near the direc-

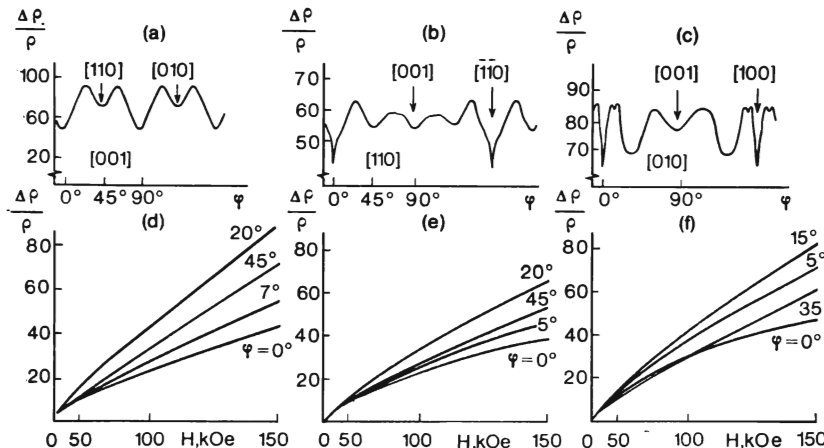


Fig. 4.29. The angular (a-c) and field (d-f) dependences of RuO_2 magnetoresistance: a, d—the sample is cut along tetragonal axis, b, e—the binary [110] sample, c, f—the binary [010] sample. The angular dependences are obtained in the transverse magnetic field of 150 kOe. The ordinates in Figs. d-f are squared magnetic field strengths, therefore the function $\Delta\rho/\rho \sim H^2$ is a straight line.

tion (Fig. 4.30). Spectral composition of the oscillations is rather complicated because it includes four frequencies, $f_1 = 28.8$ MGs, $f_2 = 79.2$ MGs, $f_3 = 108$ MGs and $f_4 = 136.8$ MGs (Fig. 4.31). The origins of each of these frequencies can be found from the relativistic model of the FS of RuO_2 . In this model (Fig. 4.32), the f_1 frequency corresponds to the cross section of the hole sheet h_4 , while f_2 corresponds to the cross section of the electron ellipsoid e_5 . Then the f_3 frequency corresponds to the “figure-of-eight” composed of the h_4 and e_5 cross sections and f_4 corresponds to the involved self-intersecting orbit composed of two cross sections of h_4 and one cross section of e_5 .

It is curious that for $\mathbf{H} \parallel [100]$ the highest possible frequency f_4 had almost the same amplitude as that of the lowest frequency f_1 , and given a small deviation in the magnetic field from the [100]

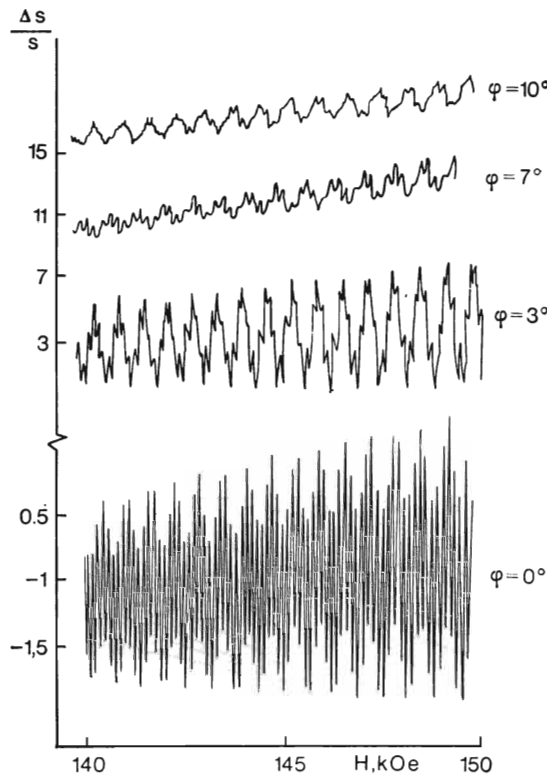


Fig. 4.30. The thermopower oscillations measured in the [010] sample of RuO_2 for different angles φ between the magnetic field direction and the [010] axis. The thermopower scale in absolute units is the same for all curves.

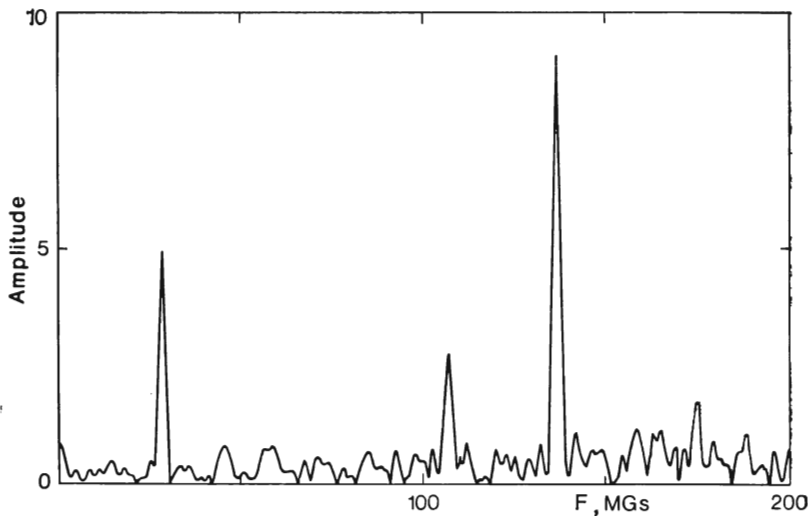


Fig. 4.31. Fourier transform of the thermopower oscillations in RuO_2 .

direction the f_4 amplitude exceeded the amplitudes of all the other frequencies.

In order to clarify this point, the temperature dependencies of the magnetoresistance oscillation amplitudes were studied. The

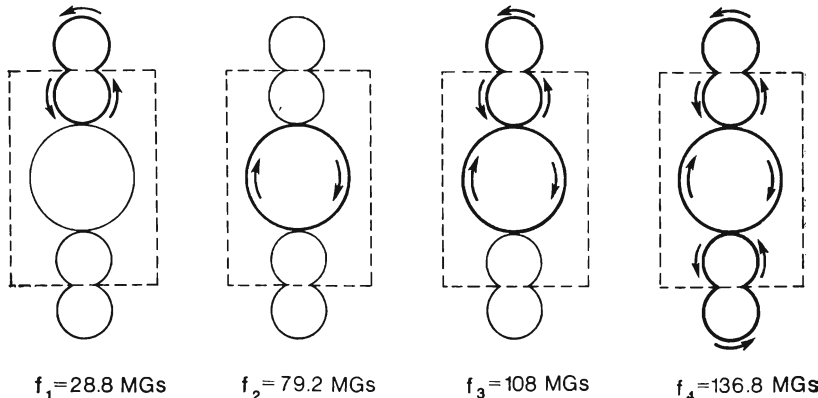


Fig. 4.32. The MB orbits in RuO_2 corresponding to the observed magnetoresistance and thermopower oscillations. The dashed line is the Brillouin zone boundary.

effective masses estimated therefrom proved to be $m_1^* = 0.5 m$ and $m_4^* = 0.3 m$ for the f_1 and f_4 frequencies, respectively. Hence, the effective mass of the largest MB orbit is smaller than that of the smallest one.

This effect, which could be called "mass compensation", has a simple explanation. The effective mass of a complex self-crossing trajectory can be found as the algebraic sum of the effective masses of its constituent orbits. Thus the large effective mass of an electron orbit around the e_5 ellipsoid proves to be compensated by the two effective masses of the

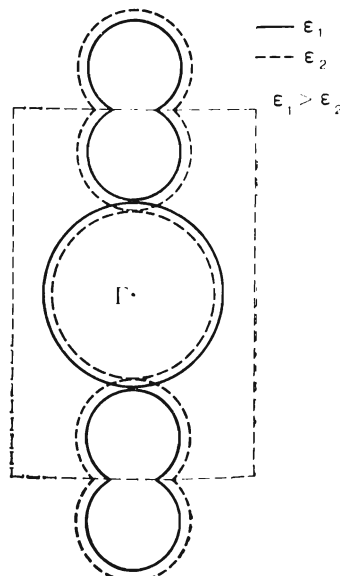


Fig. 4.33. The scheme to explain how the energy influences complex MB orbit.

hole orbits around h_4 . This conclusion can be confirmed by plotting the self-crossing trajectories for two energies (Fig. 4.33). When the energy changes, the electron and hole contours are deformed in opposite directions so that the total orbit area remains unchanged, and this in terms of the effective mass ($m^* \sim dS/d\epsilon$) does mean that $m^* \simeq 0$.

In this respect MB oscillations of RuO_2 are similar to the interference oscillations observed in magnesium [4.67] and niobium [4.61]. But there is still a substantial difference in that whereas the interference oscillations can incorporate both additive and differential harmonics, the oscillations from alternate electron and hole orbits can only consist of the sums of the initial frequencies.

It should be noted that the detection of magnetoresistance and thermopower oscillations from the giant orbits extending beyond the single Brillouin zone is evidence of the phase-coherent character of the MB in RuO_2 . On the other hand, these investigations were carried out using samples of relatively low quality. This enables us to be optimistic that we may find further manifestation of this interesting effect in other compounds, high-quality single crystals of which are not as simply fabricated.

4.6. CONCLUSION

The data given in this review demonstrate that the quantum features of the behavior of current carriers in metal, which are most pronounced during CMB, are quite often observable in experiment. Further progress in this branch of research we expect not only will yield new results for physics of metals, but will also assist in widespread utilization of the metal's plasma properties to solve a number of practical problems.

References

- 4.1. I. M. Lifshitz, M. Ya. Azbel', and M. I. Kaganov, *Sov. Phys. JETP* **4**, 41 (1957).
- 4.2. I. M. Lifshitz, V. G. Peschanskii, *Sov. Phys. JETP* **35**, 875 (1959).
- 4.3. N. E. Alekseevskii, Yu. P. Gaidukov, *Sov. Phys. JETP* **35**, 383 (1959).
- 4.4. N. E. Alekseevskii, *2 Internationales Symposium Reinststoffe in Wissenschaft und Technik*, 28 September—2 October, Dresden, GDR, 1965.
- 4.5. J. S. Dhillon, D. Schoenberg, *Philos. Trans. Roy. Soc. London Ser. A* **248** (1955).
- 4.6. M. H. Cohen, L. M. Falikov, *Phys. Rev. Lett.* **7**, 231 (1961).
- 4.7. E. J. Blount, *Phys. Rev.* **126**, 1636 (1962).
- 4.8. R. W. Stark, L. M. Falikov, *Progr. in Low Temp. Phys.* **5**, 235 (1967).
- 4.9. A. A. Slutskin, *Doctor's thesis*, Khar'kov (1981).
- 4.10. T. L. Loucks, P. H. Culter, *Phys. Rev.* **133A**, 819 (1964).
- 4.11. T. L. Loucks, *Phys. Rev.* **134A**, 1618 (1964).
- 4.12. J. H. Terrell, *Phys. Lett.* **8**, 149 (1964).
- 4.13. B. R. Watts, *Proc. Roy. Soc. London Ser. A* **282**, 521 (1964).

- 4.14. J. H. Tripp, P. M. Everett, W. L. Gordon, and R. W. Stark, *Phys. Rev.* **180**, 669 (1969).
- 4.15. G. Ahles, *Phys. Rev.* **145**, 419 (1966).
- 4.16. N. E. Alekseevskii, V. S. Egorov, *Sov. Phys. JETP* **18**, 268 (1964).
- 4.17. N. E. Alekseevskii, V. S. Egorov, and A. V. Dubrovin, *JETP Lett.* **6**, 249 (1967).
- 4.18. N. E. Alekseevskii, A. A. Slutskii, and V. S. Egorov, *J. Low Temp. Phys.* **5**, 377 (1971).
- 4.19. N. E. Alekseevskii, V. S. Egorov, *JETP Lett.* **8**, 185 (1968).
- 4.20. N. E. Alekseevskii, V. I. Nizhankovskii, *Sov. Phys. JETP* **38**, 533 (1974).
- 4.21. A. B. Pippard, *Proc. Roy. Soc. London Ser. A*, **270**, 1 (1962).
- 4.22. L. M. Falikov, A. B. Pippard, and P. R. Sievert, *Phys. Rev.* **151**, 498 (1966).
- 4.23. A. A. Slutskin, *Sov. Phys. JETP* **31**, 589 (1970).
- 4.24. D. J. Sellmyer, I. S. Goldstein, and B. L. Averbach, *Phys. Rev.* **B4**, 4628 (1971).
- 4.25. I. M. Lifshitz, M. Ya. Azbel', and M. I. Kaganov, *Sov. Phys. JETP* **4**, 41 (1957).
- 4.26. N. E. Alekseevskii, V. I. Nizhankovskii, *Fiz. Met. Metalloved.* **38**, 1105 (1974).
- 4.27. W. A. Reed, J. H. Condon, *Phys. Rev.* **B1**, 3504 (1970).
- 4.28. I. R. Testardi, J. H. Condon, *Phys. Rev.* **B1**, 3928 (1970).
- 4.29. A. Pippard, in: *The physics of metals*. Ed. J. Zeiman, Cambridge at the University Press, 1969.
- 4.30. N. E. Alekseevskii, V. I. Nizhankovskii, *Sov. Phys. JETP* **56**, 661 (1983).
- 4.31. V. S. Egorov, *JETP Lett.* **22**, 38 (1975).
- 4.32. A. A. Slutskin, *Sov. Phys. JETP* **26**, 474 (1968).
- 4.33. A. A. Slutskin, *Sov. Phys. JETP* **38**, 1057 (1974).
- 4.34. N. E. Alekseevskii, V. S. Egorov, *Sov. Phys. JETP* **19**, 815 (1964).
- 4.35. M. I. Kaganov, A. M. Kadigrobov, and A. A. Slutskin, *Sov. Phys. JETP* **26**, 670 (1968).
- 4.36. A. B. Tandit, *Diploma thesis*, The Institute of Physics Problems of the USSR Academy of Sciences, Moscow, 1978.
- 4.37. O. V. Konstantinov, V. I. Perel', *Sov. Phys. JETP* **11**, 117 (1960).
- 4.38. N. E. Alekseevskii, V. I. Nizhankovskii, *JETP Lett.* **17**, 250 (1973).
- 4.39. N. E. Alekseevskii, Cz. Bazan, M. Glinski, A. V. Dubrovin, and V. I. Nizhankovskii, *J. Phys. E* **12**, 648 (1979).
- 4.40. N. W. Ashcroft, *Philos. Mag.*, **8**, 2055 (1963).
- 4.41. E. P. Vol'skii, *Sov. Phys. JETP* **19**, 89 (1964).
- 4.42. B. Lüthi, J. L. Olsen, *Nuovo Cimento* **3**, 840 (1956).
- 4.43. R. J. Balkombe, R. A. Parker, *Phil. Mag.*, **21**, 533 (1970).
- 4.44. V. I. Gostishchev, M. Glinski, A. A. Drozd, and S. Ye. Dem'yanov, *Sov. Phys. JETP* **47**, 579 (1978).
- 4.45. V. N. Morgan, V. I. Khotkevich, *Dokl. Akad. Nauk Ukrain. SSR Ser. A* **8**, 751 (1976).
- 4.46. W. Kesternich, C. Papastaikoudis, *Phys. Status Solidi (B)* **64**, K41 (1974).
- 4.47. W. Kesternich, C. Papastaikoudis, *J. Low Temp. Phys.* **21**, 517 (1975).
- 4.48. V. S. Egorov, *Sov. Phys. JETP* **45**, 1161 (1977).
- 4.49. V. L. Ginzburg, A. A. Slutskin, *Sov. J. Low Temp. Phys.* **5**, 298 (1979).
- 4.50. P. T. Coleridge, P. M. Holtman, *J. Phys. F*, **7**, 1891 (1977).
- 4.51. D. Shoenberg, *Philos. Trans. Roy. Soc. London Ser. A* **255**, 85 (1962).
- 4.52. M. Ya. Azbel', *Sov. Phys. JETP* **26**, 1003 (1968).
- 4.53. N. E. Alekseevskii, V. I. Nizhankovskii, and K.-H. Bertel, *Fiz. Met. Metalloved.* **37**, 63 (1974).
- 4.54. N. E. Alekseevskii, K.-H. Bertel, and V. I. Nizhankovskii, *JETP Lett.* **19**, 72 (1974).
- 4.55. L. F. Mattheiss, *Phys. Rev.* **B1**, 373 (1970).

- 4.56. R. A. Deegan, W. D. Twose, *Phys. Rev.* **164**, 993 (1967).
- 4.57. J. R. Anderson, D. A. Papacostopoulos, J. W. McCaffrey, and J. E. Scirber, *Phys. Rev.* **B7**, 5115 (1973).
- 4.58. N. Elyashar, D. D. Koelling, *Phys. Rev.* **B15**, 3620 (1977).
- 4.59. N. E. Alekseevskii, K.-H. Bertel, A. V. Dubrovin, and G. E. Karstens, *JETP Lett.* **6**, 132 (1967).
- 4.60. E. Fawcett, W. A. Reed, R. R. Soden, *Phys. Rev.* **159**, 553 (1967).
- 4.61. G. B. Scott, M. Springford, *Proc. Roy. Soc. London Ser. A* **320**, 115 (1970).
- 4.62. M. H. Halloran, J. H. Condon, J. E. Graebner, J. E. Kunzler, and F.S.L. Hsu, *Phys. Rev.* **B1**, 336 (1970).
- 4.63. D. P. Karim, J. B. Ketterson, G. W. Grabtree, *J. Low Temp. Phys.* **30**, 389 (1978).
- 4.64. N. E. Alekseevskii, V. I. Nizhankovskii, K.-H. Bertel, *Fiz. Met. Metalloved.* **42**, 931 (1976).
- 4.65. W. Gordy, W. V. Smith, and R. F. Trambarulo, *Microwave Spectroscopy*, J. Wiley, New York, 1952.
- 4.66. N. E. Alekseevskii, K.-H. Bertel, V. I. Nizhankovskii, M. Glinski, and G. Fuks, *Sov. Phys. JETP* **46**, 366 (1977).
- 4.67. R. W. Stark, C. B. Friedberg, *Phys. Rev. Lett.* **26**, 556 (1971).
- 4.68. N. E. Alekseevskii, M. Glinski, V. I. Nizhankovskii, *J. Low Temp. Phys.* **34**, 53 (1979).
- 4.69. N. E. Alekseevskii, M. Glinski, V. I. Nizhankovskii, *Proc. Phys. of Transition Met. Conf.*, Leeds, England, 1980.
- 4.70. J. B. Goodenough, in: *Prog. Sol. State Chem.* Ed. by H. Reiss, vol. V, Pergamon Press, Oxford, 1971.
- 4.71. L. F. Mattheiss, *Phys. Rev.* **B13**, 2433 (1976).
- 4.72. S. M. Marcus, *Phys. Lett.* **A28**, 191 (1968).
- 4.73. S. M. Marcus, S. R. Butler, *Phys. Lett.* **A26**, 518 (1968).
- 4.74. J. E. Graebner, E. S. Greiner, and W. D. Ryden, *Phys. Rev.* **B13**, 2426 (1976).
- 4.75. Cz. Bazan, *Proc. Symp. Phys. Propert. Sol. in High Magn. Fields.* Ed. R. Troc, Wroclaw, Poland, 1978.

5 Weak Electron Localization and Magnetoresistance Oscillations of Cylindrical Normal Metal Films

*Yu. V. Sharvin, Assoc. Mem. USSR Acad. Sc., and
D. Yu. Sharvin*

5.1. INTRODUCTION

The idea for the experiment described below was suggested in 1981 by Altshuler, Aronov, and Spivak (AAS) [5.1] who predicted that the electrical resistance of a tube made from a normal metal should oscillate when the longitudinal magnetic field strength inside the tube changes. The period of these oscillations should correspond to the magnetic flux variation in the hollow by the value of the flux quantum, $\Phi_0 = hc/2e = 2 \times 10^{-7} \text{ Oe} \cdot \text{cm}^2$. Two points here are of special interest. First, the flux quantum, Φ_0 , which contains twice the electron charge in the denominator, has until now only appeared in the physics of superconductivity where the double charge is due to the pairing of the electrons responsible for the onset of superconductivity.

Second, it was claimed in [5.1] that this oscillatory interference effect does not require perfectly monocrystalline samples and can be distinctly observed in disordered conductors whose electron free path is by many orders of magnitude smaller than the sample diameter.

In fact, the observation of this phenomenon would be a direct proof of some basic concepts of physics of disordered conductors (more exactly, of the "weak localization" theory).

A rigorous treatment of theory of the problem can be found in a review by Altshuler, Aronov, Khmelnitskii, and Larkin [5.2], which was published in an earlier volume of this series. To introduce the experiment description we shall simply confine ourselves to quasiclassical estimates and the discussion of ready-made formulae without any pretence at rigour.

A great number of beautiful phenomena, e.g. the de Haas-van Alphen effect*, cyclotron resonance, the galvanomagnetic, and size effects clearly demonstrate the applicability of quasiclassical no-

* An analysis of the de Haas-van Alphen effect can be based on the Bohr-Sommerfeld quasiclassical condition for a change in the wave function phase during a closed motion, $\frac{1}{\hbar} \oint \left(\mathbf{p} + \frac{e}{c} \mathbf{A} \right) \cdot d\mathbf{r}_\perp = 2\pi n$, where the integral of the generalized electron quasimomentum, $\mathbf{p} + \frac{e}{c} \mathbf{A}$, in the magnetic field having the vector potential \mathbf{A} , is taken over an electron trajectory in a real space projected onto a plane perpendicular to the field.

tions about the motion of quasiparticles (electrons) inside a pure monocrystalline metal along definite trajectories between collisions with lattice inhomogeneities, and given that the free path and the admissible error in electrons' coordinates substantially surpass their wavelength, λ .

Let us discuss, to what extent these notions can be utilized to describe the transfer phenomena inside a metal with a sizable amount of lattice distortions.

If we restrict ourselves to a consideration of an isotropic metal and an elastic electron scattering by randomly positioned non-interacting centers, viz. impurities or atomic sized defects, then we obtain from classical arguments the usual relation for conductivity $\sigma = ne^2\tau_e/m = ne^2l_e/mv_F$, where the free path between elastic collisions l_e can be expressed in terms of the scattering cross-section for a single center s and the centers concentration N in a form $l_e = 1/Ns$. Consequently, the metal's resistivity ρ is here proportional to N at least for small impurity concentration.

This answer can be explained from the quantum viewpoint as follows. Assuming that an electron is scattered by each center in the form of a spherical wave, the intensity at any point is a result of the random phase interference. This is why the resultant intensity is the simple sum of the intensities of the arriving waves. At $l \gg \lambda$ this situation enables trajectory notions to be used and demonstrates that in the first approximation $\rho \sim N$ according to the quantum-mechanical model too.

However, it is evident that as N increases the additivity of scattering cross-sections is somewhat violated because of an increase in λ/l even for the simplest model of noninteracting, elastically scattering centers, and the corrections are to be found. The solution of this nontrivial problem proved to be unexpectedly simple and elegant and has led to the explanation and prediction of a number of interesting effects. Let us consider, e.g. the process of electron diffusion. Suppose that as a result of elastic collisions, an electron wave function has appeared with a given energy* that occupies a certain region around the point O (Fig. 5.1) and continues to be scattered via interactions with inhomogeneities. Despite the universal chaos all the electron waves which originate from a small (as compared to λ) vicinity of O and return there after a number of elastic scatterings interfere pairwise in a regular manner. A wave successively scattered by centers 1, 2, 3, ..., $N - 1$, N , arrives at the point O with the same phase as another wave that travels

* By considering the electrons as noninteracting, we deal only with one-electron wave function. However, when using classical terms we shall sometimes use the plural for electron, too. We shall as yet neglect the interaction between the electron spin and defects.

along an equidistant reverse path $O, N, N-1, \dots, 3, 2, 1, O$ (these we shall call conjugate waves) and their, equal in magnitude, amplitudes A add together so that the intensity $(2A)^2$ which arises is twice the intensity that arises from adding waves with a random phase difference, viz. $A^2 + A^2 = 2A^2$. Certainly, the intensity at point O is only doubled for the superposition of the waves that

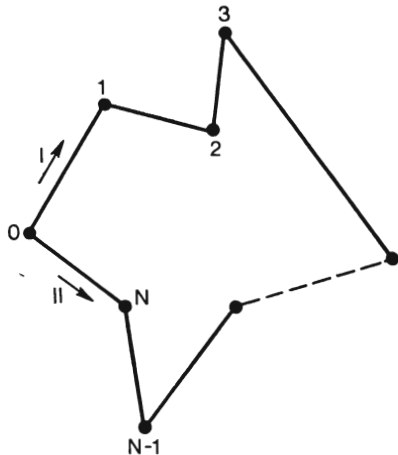


Fig. 5.1.

emerge from a vicinity of O smaller than λ . However, waves also arrive at O that have random phases from the whole region with nonzero wave function. We must also take into account that those conjugated waves which do not manage to return to O within a certain period of time τ_ϕ will not be coherent either due to inelastic interactions or for some other reason. As $\tau_\phi \rightarrow 0$, the interference correction should vanish completely.

Let us try to evaluate the interference corrections for conductivity or another kinetic coefficients, such as thermal conductivity or electron diffusion, in the form of small corrections to classical expressions. Since the relative corrections to these coefficients are the same, the correction being introduced to the value of free path, we shall, for convenience, consider diffusion.

If an electron is located at $t = 0$ at the origin $\mathbf{r} = 0$, then at time τ_ϕ it will have moved away from the origin a distance of the order of the diffusion length, $L_\phi = \sqrt{D\tau_\phi} = \sqrt{l_e l_\phi / 3}$, where $D = v_F l_e / 3$ is the diffusion coefficient. Since at helium temperatures l_ϕ can reach the value of about 1 cm, then even for small l_e of 10^{-6} cm we shall get macroscopic values of L_ϕ of 10 μm . If any of the dimen-

sions of the sample (e.g. film thickness) is not much larger than L_φ , then the sample's shape will, obviously, have to be allowed for.

First, consider the case of a three-dimensional conductor. In the classical case the density of probability for electron at t has the following form:

$$C(\mathbf{r}, t) = |(4\pi Dt)^{-3/2} \exp(-r^2/4Dt)| \quad (5.1)$$

Now let us calculate the number of conjugated trajectories. The electrons leave a region near $\mathbf{r} = 0$ of the λ size ($\lambda \ll l$) at Fermi velocity. In time dt the number that leave will be $C(0, t) v_F \lambda^2 dt$. At an instant $t_0 > t + \tau_e$ a fraction proportional to $C(0, t_0 - t)$ will return to the vicinity of $\mathbf{r} = 0$. If $t_0 - t < \tau_\varphi$, these trajectories will contribute to the interference correction term. The relative contribution of the trajectories to electron density at t_0 is

$$\frac{C(0, t)}{C(0, t_0)} C(0, t_0 - t) v_F \lambda^2 dt \quad (5.2)$$

Taking into account that for $t \gg \tau_\varphi$ and $(t_0 - t) \ll \tau_\varphi$, we can put $C(0, t) \approx C(0, t_0)$, then integrate from $t = t_0 - \tau_\varphi$ to $t = t_0 + \tau_e$, and get the following estimate for the relative decrease in diffusion coefficient or conductivity:

$$\frac{\delta D}{D} = \frac{\delta \sigma}{\sigma} \approx - \int_{\tau_e}^{\tau_\varphi} (Dt)^{-3/2} \lambda^2 v_F dt \approx - \frac{\lambda^2}{l_e^2} (1 - \sqrt{\tau_e/\tau_\varphi}) \quad (5.3)$$

Thus, in the three-dimensional case the correction is controlled by short reverse trajectories, while it does not rise infinitely as $\tau_\varphi \rightarrow \infty$.

If instead we have thin "quasi-two-dimensional" films $a \ll L_\varphi$ thick or wires $a_1 \ll L_\varphi$ in diameter, the dependence of the correction on τ_φ substantially increases. Thus at $t > a^2/D = \tau_1$ the volume which an electron is in increases not as $(Dt)^{3/2}$, but more slowly either as aDt in a film or as $a_1^2 \sqrt{Dt}$ in a wire.

For a quasi-two-dimensional film we have

$$\frac{\delta \sigma}{\sigma} \approx - \int_{\tau_1}^{\tau_\varphi} \frac{\lambda^2 v_F dt}{aDt} \approx - \frac{\lambda^2}{a l_e} \ln \frac{\tau_\varphi}{\tau_1} \quad (5.4)$$

or for two-dimensional conductivity

$$\delta \sigma_{\square} = a \delta \sigma \approx \frac{\lambda^2 \sigma}{l_e} \ln \frac{\tau_\varphi}{\tau_1} \approx - \frac{e^2}{\hbar} \ln \frac{\tau_\varphi}{\tau_1} \quad (5.5)$$

It is noticeable that in the two-dimensional case the dimensional coefficient in the expression for $\delta \sigma_{\square}$ contains only universal constants. Using the numerical factor obtained from exact calculations,

we get

$$\delta\sigma_{\square} = -\frac{e^2}{2\pi^2\hbar} \ln \frac{\tau_{\varphi}}{\tau_1} = -\frac{e^2}{\pi^2\hbar} \ln \frac{L_{\varphi}}{a} = -2.47 \times 10^{-5} \ln \frac{L_{\varphi}}{a} \Omega^{-1} \quad (5.6)$$

The most direct experimental check of the interference mechanism which forms the basis of this calculation would be the observation of a sample conductivity variation that would arise from an introduction of a phase shift between the interfering conjugated waves. This is the aim of the experiment proposed by Altshuler et al. [5.1].

If the sample is a thin-walled hollow cylinder whose perimeter is of the order of L_{φ} , then the coherent conjugated waves will have trajectories that envelope the cylinder cavity. The presence of such trajectories will obviously lead to a larger correction to σ_{\square} for cylinder walls than is given by formula (5.6). If a magnetic field with the flux Φ is produced inside the cylinder cavity, the magnetic vector potential \mathbf{A} will be nonzero within cylinder walls, although the field itself may be absent. A nonzero \mathbf{A} will result in the change in a phase shift φ along trajectories that is dependent on the direction of wave motion. The phase difference between the waves returning to the origin from each side (I and II) will be the same for all trajectories:

$$\begin{aligned} (\Delta\varphi)_I - (\Delta\varphi)_{II} &= \frac{1}{\hbar} \oint \left(\mathbf{p}_I + \frac{e}{c} \mathbf{A} \right) \cdot d\mathbf{r}_I - \frac{1}{\hbar} \oint \left(\mathbf{p}_{II} + \frac{e}{c} \mathbf{A} \right) \cdot d\mathbf{r}_{II} = \\ &= 2 \frac{e}{\hbar c} \oint \mathbf{A} \cdot d\mathbf{r}_I = \frac{2\pi\Phi}{\Phi_0} \end{aligned} \quad (5.7)$$

When the flux Φ is changed, the part of the correction to conductivity that is related to the enveloping trajectories will oscillate with period $\Phi_0 = hc/2e$.

The integrals from (5.7) are reminiscent of the Bohr-Sommerfeld quantization conditions for the wave function of a particle in a magnetic field, but here no conditions are imposed on the phase difference and thus on the energy of the electron states. The AAS effect is an analogue of Aharonov and Bohm effect [5.3]. In 1959 Aharonov and Bohm demonstrated that the interference pattern formed by two coherent electron beams in a vacuum must be displaced by an integer number of fringes when the magnetic flux enveloped by the beams changes by an integer number of quanta hc/e . In our case, the flux quantum is half this value since the electron goes round the flux region at least twice.

In the next Section we shall present the results of our searches for the AAS effect. A number of experiments to measure the resistance of hollow cylinders in longitudinal magnetic field have already been performed earlier with the samples made from superconducting metals [5.4-8]. This was done to study the phenomenon of mag-

netic field quantization in superconductors, and the first were the experiments by Parks and Little [5.4] in 1963. They observed resistance oscillations with a period of $hc/2e$ in flux. The important aspect of the oscillations was the phase: at $H = 0$ the sample's resistance was at a minimum while the simple theory covering the AAS effect indicates that at $H = 0$ the resistance should be at a maximum.

We shall start by describing the most recent experiments in which we detected the AAS effect in this simple form. In Sec. 5.3 we shall return to the chronological sequence of events and shall trace the AAS effect manifestations in more complicated cases including those of superconducting metals.

5.2. AN EXPERIMENT WITH LITHIUM FILM *

5.2.1. Experimental Technique

After some preliminary experiments, we chose lithium for preparing the sample, notwithstanding its high reactivity. On the basis of the published data on spin-orbital interactions [5.10] we could expect that given its low atomic number ($Z = 3$) the spin states of the electrons in lithium would not be affected significantly by elastic scattering by defects and sample surface. This makes lithium suitable for confirming the simplest variant of the theory.

The data in [5.10] and the influence of spin-orbital interactions on the AAS effect will be discussed in Sec. 5.3.

Another advantage of lithium is its relatively high vapour pressure thus favouring the formation of pure films. As a matter of fact, it is the nonvolatile impurity atoms having finite magnetic moments that are dangerous. When colliding with these atoms, random reorientation of the electron spin occurs, the coherency of conjugated waves is violated, and the value of L_φ is decreased even at low temperatures.

Lithium was condensed into a quartz filament about $1 \mu\text{m}$ in diameter and $b = 1 \text{ cm}$ in length. The filament's ends were glued with BF compound to platinum wires that served as the current leads, and the filament was placed along the axis of a helium Dewar in which the lithium was condensed by a tantalum evaporator moving around the filament. As this was happening the Dewar vessel was evacuated by a diffusion pump and a small quantity of pure helium was admitted through a small tube into the bottom of the vessel so that the pressure was maintained at 10^{-3} Torr. The Dewar vessel's walls and the shield in its upper part were cooled by liquid nitrogen. The film about 10^{-5} cm in thickness was then annealed at room

*

For the short communication version see [5.9].

temperature and atmospheric pressure of pure helium. Then liquid helium was fed in.

In our experiment the magnetic field strength cannot be changed inside the lithium cylinder hollow, while maintaining the field at zero within the walls. The sample was simply placed in a homogeneous magnetic field H with its axis parallel to the direction of the field. The sample's resistance R was measured as a function of H by a dc potentiometer with a sensitive photoamplifier and an XY-recorder. The recorder input was protected against short-period noises by an RC-filter with $RC \approx 2$ s. The measurements were performed mainly at night.

5.2.2. Experiments at 1.1 K

In Fig. 5.2 a record of $\Delta R (H)$ is presented for a sample having $R = 1985 \Omega$ at 4.2 K and $R_{300}/R_{4.2} = 2.8$ (solid line). This

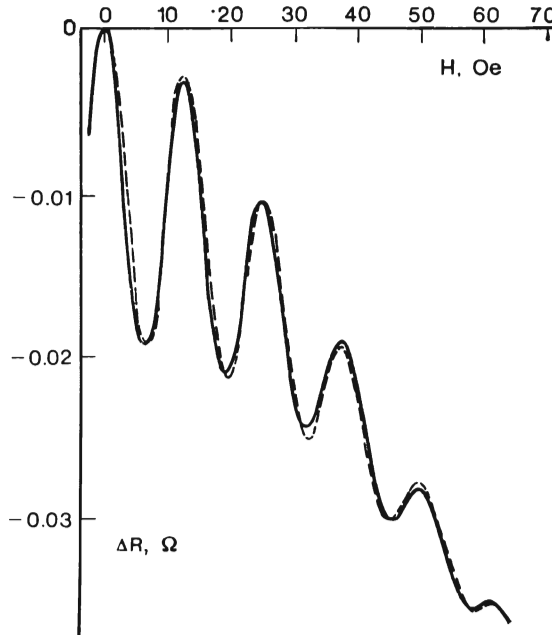


Fig. 5.2. $\Delta R (H)$ for a lithium sample with $R = 1985 \Omega$. The solid curve is the average of four experimental curves, the dotted line is a calculation using formula (5.9).

record was obtained by averaging four successive records taken with the increasing and decreasing H values to eliminate the persistent zero drift.

The helium bath temperature was 1.1 K. Due to Kapitza's thermal resistance at the sample-liquid helium interface the sample's temperature was higher than that of bath by about 0.2-0.4 K because of heating by the measuring current of 40 μ A.

The curve $\Delta R (H)$ in Fig. 5.2 has a pronounced period of 12.6 Oe, and the damping oscillations are superimposed onto the monotonic fall in the resistance. The diameter of the quartz filament was measured after the helium experiment had been finished. The lithium was carefully washed off and the filament diameter measured by scanning electron microscope; it proved to be $1.30 \pm 0.03 \mu$ m. This suggests that the field strength produced by a single flux quantum $hc/2e$ inside the cylinder's hole amounts to 15.6 Oe. This value, quite naturally, agrees only roughly with the period observed since we have not yet accounted for film thickness. For a more accurate calculation of the period the quantity πr^2 , where r is the average cylinder radius, must be used instead of the hole area. Because we did not measure the cylinder wall thickness a directly, we utilized another method to compare with the theory. We determined a from the monotonic fall in resistance, that is, from the negative longitudinal magnetoresistance of the film, which is the phenomenon considered by Altshuler and Aronov [5.11] and which we observed in our experiments.

The longitudinal field present in the film induces phase shifts for those conjugated trajectories which do not envelope the cylinder cavity but which trap some magnetic flux, equal in order of magnitude to $Ha\sqrt{Dt}$, where t is the time of travel along a trajectory (here it is assumed that $\sqrt{Dt} \gg a$). Since the areas of these contours are random in value, the corresponding random phase shifts will reduce the interference correction term in the same way as other coherency losses which we described by τ_ϕ . The corresponding time τ_H can be evaluated for the field H from the relationship $Ha\sqrt{Dt_H} \approx \Phi_0$. This is applicable when $\sqrt{Dt_H} \gg a$, that is when $H \ll \Phi_0/a^2$. Given the exact numerical coefficient, we have $\tau_H = \frac{3\Phi_0}{\pi^2 D a^2 H^2}$ [5.11]. The expression defining the resulting time of phase failure has the familiar form $\tau_\phi(H)^{-1} = \tau_\phi^{-1} + \tau_H^{-1}$. To derive the correction $\delta\sigma_\square$ in the longitudinal field H we need to substitute $\tau_\phi(H)$ for τ_ϕ in (5.6). It is handy to introduce a new diffusion length $L_\phi(H) = \sqrt{Dt_\phi(H)}$ expressible in terms of $L_\phi(0) = \sqrt{Dt_\phi}$, viz.

$$L_\phi(H) = L_\phi(0) \left[1 + \frac{\pi^2}{3} \left(\frac{a L_\phi(0) H}{\Phi_0} \right)^2 \right]^{-1/2} \quad (5.8)$$

It is then substituted into (5.6) in place of L_ϕ .

The reduction of oscillation amplitude with field strength is also caused by the presence of a field within the film body (this leading

in calculations to the superposition of oscillations having slightly different periods). Here the value of the amplitude will depend on $2\pi r/L_\Phi(H)$.

The resultant expression for the shape of the $\Delta R(H)$ curve is:

$$R(H) - R(0) = R^2 \frac{2\pi r}{b} \frac{e^2}{\pi^2 \hbar} Z [L_\Phi(H), L_\Phi(0)] \quad (5.9)$$

where

$$Z [L_\Phi(H), L_\Phi(0)] = \ln \frac{L_\Phi(H)}{L_\Phi(0)} + \\ + 2 \sum_{n=1}^{\infty} \left[K_0 \left(n \frac{2\pi r}{L_\Phi(H)} \right) \cos 2\pi n \frac{\pi r^2 H}{\Phi_0} - K_0 \left(n \frac{2\pi r}{L_\Phi(0)} \right) \right] \quad (5.10)$$

Here $K_0(x)$ is MacDonald's function [$K_0(x)$ dies away quickly at $x > 1$ tending to e^{-x}]. This expression written for noninteracting electrons with no spin-orbital interactions, was used to approximate the experimental data for the lithium sample*. In Fig. 5.2 the dashed curve shows results calculated from formula (5.9) with $r = 0.72 \mu\text{m}$, $L_\Phi(0) = 2.22 \mu\text{m}$, and $a = 0.127 \mu\text{m}$. Thus, the value $2r - a = 1.31 \mu\text{m}$ proved to be close to the above diameter of the quartz filament, i.e. $1.30 \pm 0.03 \mu\text{m}$.

Let us note that here the condition $a \ll L_\Phi(0)$ for a film to be quasi-two-dimensional is satisfactorily fulfilled. The fulfilment at the maximum field strength of $H = 65 \text{ Oe}$ of another condition $a \ll \sqrt{\Phi_0/H} = 5.6 \times 10^{-5} \text{ cm}$ is not so reliable, yet the good agreement between the monotonic components of the calculated and experimental curves for the whole range of fields demonstrates that the approximation is still satisfactory.

Another corroboration of the applicability of (5.9) is the agreement with experiment of the oscillation damping magnitude which is calculated for a determined from the monotonic component.

The experiments were repeated with the same sample after it had been reheated close to room temperature and stored at liquid nitrogen temperature for three days. As a result, the sample's resistance at 4.2 K rose from 1985 to 2560 Ω , probably because the sample had been partially oxidized. The curve parameters at 1.1 K were not changed significantly and a comparison with (5.9) leads to the

* In the first approximation, r was determined from the period of the oscillations, then $L_\Phi(0)$ was taken from the first oscillation amplitude having $L_\Phi(H) = L_\Phi(0)$, and then a was calculated from the value of the monotonous part of the curve. In the sigma expression only the term with $n = 1$ was used. The results are somewhat better than those in [5.9] due to the additional data. The calculations in [5.9] were performed also with formula (5.9) of this article. The corresponding expression (1) for ΔG in [5.9] contains an error, viz. an extra factor of two in denominator.

values of $r = 0.72 \mu\text{m}$, $L_\varphi(0) = 1.96 \mu\text{m}$ and $a = 0.116 \mu\text{m}$. Oscillations with a gradually falling amplitude were observed at higher temperatures too, up to 2.6 K.

Pronounced oscillations in the magnetoresistance of a 1 μm diameter cylinder made from lithium film where peak spacings corresponded to the change $hc/2e$ in the magnetic flux within the mean cross section of the hollow cylinder were also observed by Ladan and Maurer [5.12].

The interference mechanism of weak localization effects in disordered conductors was clearly demonstrated in the described experiments which can be compared with the simplified formula (5.9) reflecting the main features of the phenomenon.

However, it is interesting to see how the AAS effect is manifested in other metals and to compare experimental data with a more sophisticated theory.

It will thus be possible to evaluate the upper bound of the value of spin-orbital interaction in lithium and to derive quantitative data pertaining to the temperature dependence of τ_φ .

5.3. EXPERIMENTAL OBSERVATIONS OF THE LONGITUDINAL MAGNETORESISTANCE OSCILLATIONS OF CYLINDRICAL FILMS OF DIFFERENT METALS, AND THE AAS EFFECT

The first such experiments, as we noted before, were performed with superconducting samples (tin, lead, indium, aluminium, etc.) as their resistance has been measured in the region of the superconductive transition [5.4-7]. Strictly speaking, what had been observed were oscillations of the $H_c(T)$ curve for thin-walled tiny cylinders, produced as a result of quantizing the states of superconductive electrons. (The Bohr-Sommerfeld condition was imposed on the motion of paired electrons around the cylinder.) When the samples are of good quality the oscillations corresponded to complete transitions from one phase to another. The $R(H)$ curve is shown in Fig. 5.3 for an aluminium sample 1.33 μm in diameter at $T = 1.125 \text{ K}$, and is taken from Groff and Parks [5.6]. This curve clearly demonstrates that the phenomenon differs from the AAS effect.

Significant difficulties were encountered in interpreting the results from Shablo, Narbut, Tyurin, and Dmitrenko [5.8]. They undertook a search for resistance oscillations in film cylinders with very small diameters, $2 \times 10^{-5} \text{ cm}$, and made from aluminium with an admixture of oxygen in the temperature range $T > T_c$, with $T_c = 1.7 \text{ K}$. According to a theory by Kulik and Mal'chuzhenko [5.13-14] the oscillations should be related to the presence of superconducting fluctuations, and their amplitudes should be controlled by the factor

$\exp[-2\pi r/\xi(T)]$, where $\xi(T)$ is the coherency length of the superconducting fluctuations, the length falling as $T - T_c$ grows, and $2\pi r$ is the sample circumference. According to calculations, the oscillations should be observed near T_c and disappear around 2.5-

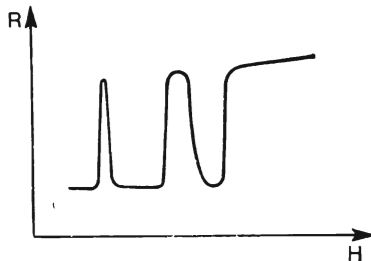


Fig. 5.3. An oscillatory transition between superconducting and normal states in a magnetic field for an aluminium film: $a = 2.5 \times 10^{-5}$ cm, $2r = 1.33$ μ m, $b = 0.07$ cm, $R_n \approx 9\Omega$, $T = 1.125$ K [5.6].

3.0 K. In experiments, however, they were distinctly traced up to 8 K (see Fig. 5.4): something which could not be explained at that time.

After Altshuler, Aronov and Spivak published their paper [5.1], it was noted [5.15] that the mechanism they had suggested enabled the results Shablo et al. had obtained to be explained. Now the

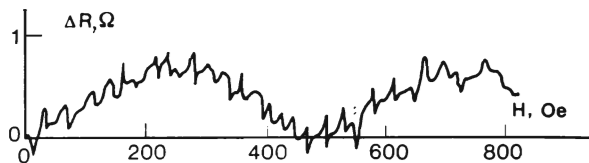


Fig. 5.4. $\Delta R(H)$ at $T = 6.0$ K for a cylindrical aluminium + oxygen film: $a \approx 1.1 \times 10^{-6}$ cm, $2r = 2.4 \times 10^{-5}$ cm, $R = 8000\Omega$, $T_c = 1.7$ K [5.8].

temperature dependence of the amplitude incorporates the quantity L_ϕ instead of the coherency length $\xi(T)$ and L_ϕ can be quite comparable with $2\pi r$ over the whole region, where the oscillations were observed.

When we were investigating cylindrical cadmium films (a superconductor with $T_c = 0.55$ K) for the AAS effect, we also observed at temperatures of 1.2-2.3 K the oscillations with a minimum at $H = 0$ (Fig. 5.5) and the positive longitudinal magnetoresistance (LMR) up to 4.2 K [5.15]. These experiments confirmed for samples with simpler composition the results obtained by Shablo et al. [5.8].

In order to eliminate the influence of superconductivity, where possible, we started the experiments with magnesium, which is a normal conductor down to the lowest probed temperatures (0.017 K [5.16]). The oscillations observed in this case are shown in Fig. 5.6 [5.15]. The arrows indicate the magnetic field strength values that correspond to the integer number of the flux quanta $hc/2e$, which pass through the hole in the MgI sample, the hole diameter being

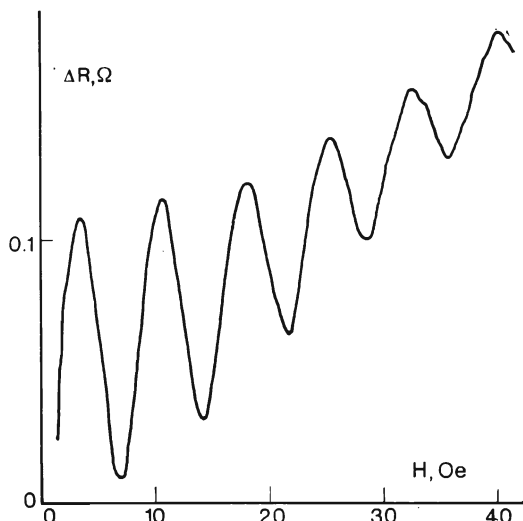


Fig. 5.5. $\Delta R (H)$ at $T = 1.2$ K for a cadmium sample (see Table 5.1).

measured by scanning electron microscope. It might be assumed that these curves are those of a normal metal, however in this case too, the oscillations had a minimum at $H = 0$ and LMR was positive.

Until now the opposite oscillation phase and a negative LMR have only been observed for lithium.

It is possible to interpret all these experimental data, if the influence of superconducting fluctuations (Larkin [5.17]) and of a change in the electron spin state during collisions on magnetoresistance of films (Hikami et al [5.18], Altshuler et al [5.19]) is taken into account in the AAS effect theory. The results [5.17–19] for the transversal magnetoresistance of plane films have been applied to the case of a hollow cylinder [5.9]. The resultant formula has the form of a difference between two terms containing Z-functions [see (5.10)]

having different arguments:

$$\frac{R(H) - R(0)}{R^2} \frac{b}{2\pi r} \frac{\pi^2 \hbar}{e^2} = - \left(\frac{1}{2} + \beta \right) Z [L_\varphi(H), L_\varphi(0)] + \\ + \frac{3}{2} Z [\tilde{L}_\varphi(H), \tilde{L}_\varphi(0)] \quad (5.11)$$

where

$$\frac{1}{\tilde{L}_\varphi(H)} = \frac{1}{D\tau_\varphi} + \frac{2}{D\tau_{so}} + \frac{\pi^2}{3} \left(\frac{aH}{\Phi_0} \right)^2 = \frac{1}{L_\varphi^2(H)} + \frac{2}{D\tau_{so}}.$$

Here τ_{so} is the spin flip time due to spin-orbital interaction, β is the positive correction term from [5.17] to take into account the

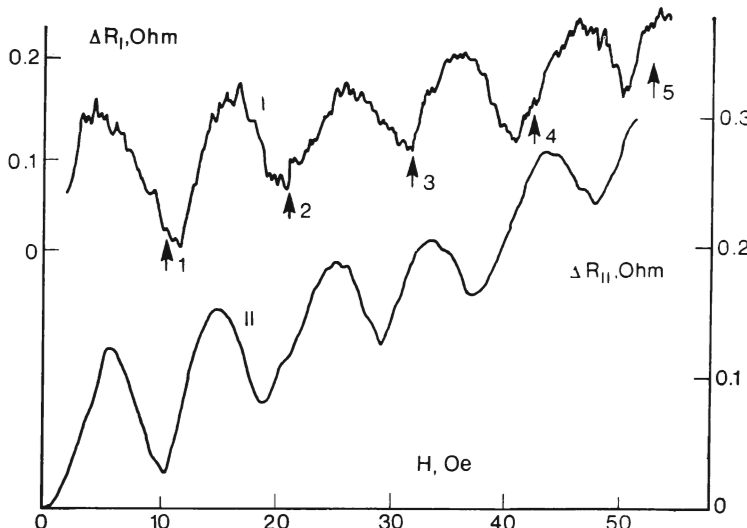


Fig. 5.6. $\Delta R(H)$ for MgI and MgII samples (see Table 5.1).

influence of superconducting fluctuations. When $T = 2T_c$, e.g. $\beta \simeq 2$, while near T_c we have $\beta = \pi^2/[4 \ln(T/T_c)]$, and at $T \gg T_c$, $\beta = \pi^2/[6 \ln(T/T_c)]^2$.

Notice that $\beta \neq 0$ even for nonsuperconductive metals and tends to zero as the temperature falls. For good metals $\beta \sim 10^{-2}$ in the helium range of temperatures.

The change in the electron spin state during collisions can be taken into account in (5.11) in two ways depending on the collision type.

Given interactions with paramagnetic impurities a loss of coherence can occur between conjugated waves due to a random change in the spin state of one of the beams. These events have an additive

contribution to the increase in the total reciprocal of the phase relaxation time, $1/\tau_\varphi$. When there is a large quantity of paramagnetic impurities, the localization correction term vanishes completely.

During collisions with nonmagnetic impurities, defects, or a sample surface, spin-orbital interactions can also change the electron spin state within a certain period of time τ_{so} . A magnetic field impulse effecting the spin arises in the electron's frame of reference as it travels through the electric field produced by a defect. It is essential for this case that an electron moving along the same trajectory in the opposite direction must have the same rotations of the spin state both in the opposite order and with the opposite signs. The coherency of conjugated waves for the given trajectory will thus be conserved. If $\tau_{so} \ll \tau_\varphi$, then after summing the intensities for the different return trajectories for all the possible rotations of the spin state the resultant intensity proves to be smaller than the simple sum of the intensities of all the waves and consequently the localization correction term changes in sign, viz. "antilocalization" occurs instead. The calculation for the limiting case of $\tau_{so}/\tau_\varphi \rightarrow 0$ in this comparatively clear form was performed by Bergmann [5.20]. When τ_{so} decreases the second term in (5.11) becomes small, the magnetoresistance changes in sign, and at $\tau_{so} \ll \tau_\varphi$ and $\beta \ll 1$ becomes half in absolute value the magnetoresistance that would be there in the absence of spin-orbital interactions for the same τ_φ .

The ratio of the cross section of the spin-orbital interaction to that of elastic scattering from an impurity with atomic number Z is, according to an estimate [5.21], equal to about $(\alpha Z)^4$, where $\alpha = 1/137$ is the fine structure constant.

A review of experimental data [5.10] shows that in the case of small pure samples with atomic number Z there is generally, to an order of magnitude, an analogous relationship, viz $\tau_b/\tau_{so} = (\alpha Z)^4$, where τ_b is the time between surface collisions.

We shall now discuss the results of our experiments with different substances.

5.3.1. Magnesium

Since $T_c < 0.017$ K for magnesium [5.16] and $\beta < 0.1$ at the temperature of our experiments, we neglected β in our estimates.

The positive LMR and the appropriate oscillation phase having a minimum at $H = 0$ in Fig. 5.6 should be caused by spin-orbital interaction. Notwithstanding the relatively small atomic number of magnesium ($Z = 12$), we shall have $\tau_\varphi/\tau_{so} \gg 1$ at low temperatures, because τ_φ rises whereas τ_{so} is not substantially dependent on temperature.

Processing the curves in Fig. 5.6 assuming $\tau_\phi/\tau_{s0} \gg 1$ yields results for the MgI and MgII samples similar to each other and presented in Table 1. When $\tau_\phi/\tau_{s0} < 10$, the agreement between the experimental and calculated data starts to deteriorate.

Table 5.1.

Sample	MgI	MgII	Cd
T_{bath}	1.1 K	1.1 K	1.2 K
Measuring current	10 μA	10 μA	10 μA
R	9.2 k Ω	12.3 k Ω	3.1 k Ω
Length	1 cm	1 cm	1 cm
Filament diameter from microscopic measurements	1.58 μm		
$2r$	1.62 μm	1.66 μm	1.92 μm
R_{\square}	4.7 Ω	6.4 Ω	1.9 Ω
τ_ϕ/τ_{s0}	> 10	> 10	$\approx 10^2$
a	9×10^{-6} cm	1.0×10^{-5} cm	1.2×10^{-5} cm
$L_\phi(0)$	2.2 μm	1.7 μm	2.9 μm

Notice that when Bergmann [5.22] investigated the magnetoresistance of plane cold-deposited magnesium films in fields normal to the film surface, he had $\tau_\phi/\tau_{s0} < 1$ at 4.6-20 K.

We used plane magnesium films produced by our technique (condensing at liquid nitrogen temperature in the presence of helium at a pressure of 10^{-3} Torr followed by annealing at room temperature), to measure normal magnetoresistance at liquid helium temperatures in order to trace the growth in the ratio τ_ϕ/τ_{s0} as the temperature falls.

The reduced two-dimensional magnetoconductivity

$$g = \frac{R_{\square}(H) - R_{\square}(0)}{R_{\square}^2} \frac{2\pi^2\hbar}{e^2}$$

is presented in Fig. 5.7 as a function of the reduced magnetic field $h = 4\pi L_\phi^2(0) H/\Phi_0$ for the film having the resistance per square $R_{\square} = 5.5$ Ohm together with theoretical curves for $g(h)$ at different values of τ_ϕ/τ_{s0} and plotted according to [5.18]. Film thickness was determined from LMR measurements and proved to be equal to 6.4×10^{-6} cm, whereas $L_\phi(0) = 1.26 \mu\text{m}$ at $T = 1.07$ K. While these film parameters are close to those of our cylindrical films, the

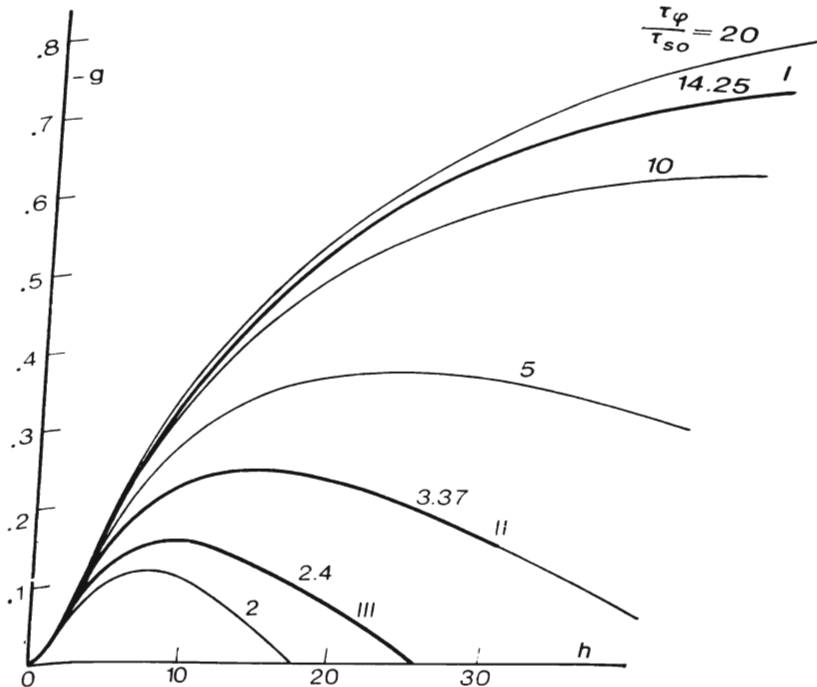


Fig. 5.7. $g(h)$ for a plane magnesium film, $a = 6.4 \times 10^{-6}$ cm, $R_{\square} = 5.5 \Omega$, in a transverse magnetic field. The heavy solid lines are experimental curves: I—1.07 K, II—3.46 K, III—4.2 K. The light solid lines are calculations according to [5.18] for different τ_{ϕ}/τ_{so} values.

ratio τ_{ϕ}/τ_{so} rose from 2.4 to 14.4 as the temperature fell. An increase in temperature by a few degrees from 4.2 K, evidently would take the sample from the "antilocalization" to localization mode.

5.3.2. Cadmium

Since $Z = 48$ for cadmium, the estimated ratio τ_{ϕ}/τ_{so} for our experiments should, according to [5.10], be of a large value about 10^2 . This enables us to neglect the second term in (5.11). Our results are presented in Table 5.1. For an experimental temperature of $T = 1.2$ K, the value of $\beta = 1.25 \pm 0.1$ corresponds, according to [5.17], to $T_c = 0.48 \pm 0.02$ K for our film. Since we did not measure T_c directly for our cadmium sample, we can only say that the agreement with the theory was qualitative. The experiments with cadmium are an example of the AAS effect in a superconductive metal, where the presence of superconducting fluctuations leads to a significant amplification of the effect (in our case, about threefold).

Here the features of the interference mechanism are conserved, viz. it is both the diffusion of normal electrons and the phase difference between the conjugated electron waves enveloping the sample hollow which control the oscillations, whose amplitude is governed by the value of $2\pi r/L_\varphi$.

5.3.3. Lithium

We can evaluate the upper bound on τ_φ/τ_{s0} for our sample using (5.11) and the data from the Fig. 5.2. The shapes of the curves near $\tau_\varphi/\tau_{s0} = 0$ proves that ΔR is rather insensitive to variations in τ_φ/τ_{s0} so that, despite the comparatively high quality of the experimental curves we achieved for lithium, we still get practically the same good agreement with experiment for large values of τ_φ/τ_{s0} (up to 0.2) as we got in Fig. 5.2 for which we assumed $\tau_\varphi/\tau_{s0} = 0$. The calculated film thickness is the same here and for Fig. 5.2 to an accuracy of 1%, though the value of $L_\varphi(0)$ noticeably increases from 2.2 μm for $\tau_\varphi/\tau_{s0} = 0$ up to $L_\varphi(0) = 3 \mu\text{m}$ for $\tau_\varphi/\tau_{s0} = 0.2$.

The published data concerning τ_{s0} for lithium have a sizable spread, and for samples produced by sputtering in neutral gas the values of τ_b/τ_{s0} amount to $10^{-5} \approx 10^2 (\alpha Z)^4$. From this viewpoint, a value of $\tau_\varphi/\tau_{s0} = 0.2$ at $T = 1.1 \text{ K}$ is quite feasible. At higher temperatures, however, this value should be reduced in proportion to τ_φ .

The AAS oscillations have been measured at temperatures up to 2.6 K and monotonic LMR observed up to 4.22 K. By finding the film thickness at 1.1 K from the LMR value, we can calculate both $L_\varphi(0)$ and l_φ .

Given a value of $\rho \cdot l = 1 \times 10^{-11} \Omega \cdot \text{cm}^2$ for lithium from the model of free electrons, we obtain a value for the elastic path $l_e = \rho l / (R_\square \cdot a) = 9 \times 10^{-7} \text{ cm}$ (from Fig. 5.2 data) and the values of $l_\varphi = 3L_\varphi^2/l_e$ and $\tau_\varphi = l_\varphi v_F$ ($v_F = 1.2 \times 10^8 \text{ cm/s}$ for free electrons). A summary of all the data for $l_\varphi(T)$ is presented in Fig. 5.8, where $1/\sqrt{l_\varphi}$ is plotted along the ordinate axis in the form of segments whose upper end corresponds to the calculation for $\tau_\varphi/\tau_{s0} = 0$ and whose lower one to the calculation for $\tau_\varphi/\tau_{s0} = 0.2$ at 1.1 K.

At $T > 2 \text{ K}$, where any temperature difference between the sample and the helium bath can be neglected, the points fall along a straight line corresponding to the expression $1/l_\varphi = CT^2$ where $C = 2.8 \pm 0.1$. This result is of course tentative being the characteristic of only a single sample. The value of the T^2 coefficient can substantially depend on the technique for making the film. For bulk lithium the temperature dependent fraction of resistance varies from 1.2 to 10 K as T^2 [5.23-24] due to electron-electron collisions. Yet this mechanism makes a tenfold smaller contribution to $1/\tau_\varphi$ than it does in our case.

The estimates of the additional small-angle electron-electron scattering that should occur in disordered films, and which is proportional to T [5.25] yield a contribution within our temperature range that is also tenfold smaller than the observed value.

Electron-phonon scattering in disordered conductors has been investigated in a number of theoretical works (see, e.g. [5.26-31]),

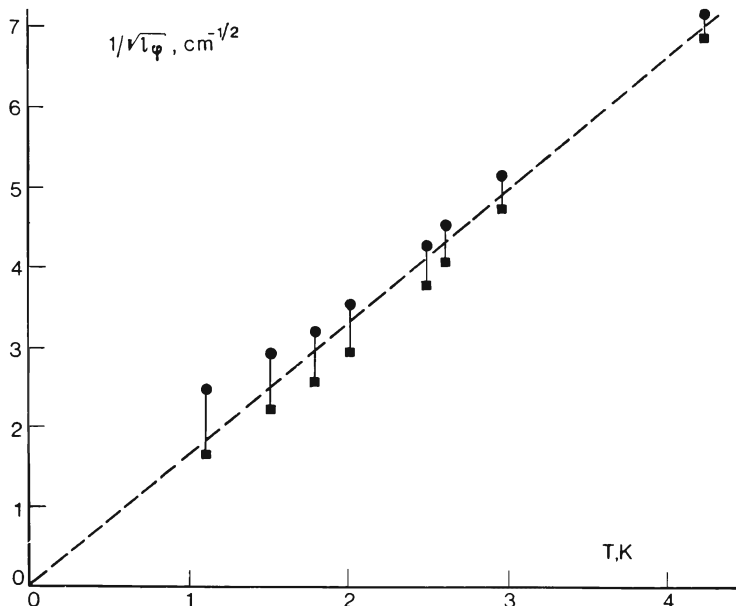


Fig. 5.8. $1/\sqrt{l_\varphi}$ versus T for a cylindrical lithium film. ● is a calculation at $\tau_\varphi/\tau_{s0} = 0$, ■ is a calculation at $\tau_\varphi/\tau_{s0} = 0.2$ for 1.1 K. The $T > 2.6$ K data were obtained from LMR measurements. Dashed line indicates the function $1/l_\varphi = 2.8 T^2$.

yet the problem does not at all seem to be finally resolved. Taylor [5.27] proposed the following relationship at low temperatures for the additional resistance $\Delta\rho$, caused by an inelastic scattering of electrons from impurities,

$$\Delta\rho/\rho_0 = \pi^2 \bar{p}^2 T^2 / 2M\theta^3 = AT^2 \quad (5.12)$$

where \bar{p}^2 is the mean square of the momentum transferred in a collision, M is the mass of ions of base material, ρ_0 is the residual resistance, and θ is the Debye temperature. Relations whose coefficients of T^2 are close by order of magnitude to each other were also obtained in the works [5.28-31]. Let us compare our results with the relatively simple expression (5.12) keeping in mind that

the region of the applicability of (5.12) is limited from the low temperature side by the temperatures for which the phonon wavelength is smaller than electron's path (see [5.30]), whereas in our temperature range they are of the same order.

Substituting into (5.12) M for lithium and $\theta = 344$ K and putting $\bar{p}^2 = 2p_F^2$ for the isotropic scattering according to the free electron model yields $A \approx 2 \times 10^{-6}$ K $^{-2}$, whereas for our film $l_e/l_\varphi = 2.5 \times 10^{-6} T^2$.

It has to be mentioned that (5.12) was earlier confirmed in an experiment at $0.18 \text{ K} \leqslant T \leqslant 1.3 \text{ K}$ for a set of bulk samples made from alloys of potassium and rubidium, and the proportionality between $\Delta\rho$ and ρ_0 verified [5.32]. The quadratic dependence of $1/\tau_\varphi$ on T was observed for films by Bergmann in the case of magnesium [5.22], and by Gershenzon et al. for silver and copper [5.33]. The coefficients in those cases are in agreement with (5.12) or analogous relations to an order of magnitude though τ_φ was not found to be proportional to τ_e in either study. Here further investigations will be of undoubtedly interest.

5.4. CONCLUSION

The main aim of our experimental search for the effect predicted by Altshuler, Aronov, and Spivak was to observe directly the interference of electron waves scattered from defects, this interference being responsible for the weak localization of electrons in disordered conductors.

We have demonstrated that these interference phenomena are distinct not only in a simple case (exemplified by lithium), but also in the presence of factors which complicate the picture (superconducting fluctuations, spin-orbital interaction of electrons). The new observations of the AAS effect see in [5.34-38].

References

- 5.1. B. L. Altshuler, A. G. Aronov, B. Z. Spivak, *JETP Lett.* **33**, 94 (1981)
- 5.2. B. L. Altshuler, A. G. Aronov, D. E. Khmelnitskii, A. I. Larkin, in: *Quantum Theory of Solids, Advances in Science and Technology in the USSR (ST), Physics Series*. Ed. I. M. Lifshitz, MIR Publishers, Moscow (1982), p. 130.
- 5.3. Y. Aharonov, D. Bohm, *Phys. Rev.* **115**, 485 (1959).
- 5.4. R. D. Parks, W. A. Little, *Phys. Rev.* **133**, 97 (1964).
- 5.5. L. Meyers, W. A. Little, *Phys. Rev. Lett.* **11**, 156 (1963).
- 5.6. R. P. Groff, R. D. Parks, *Phys. Rev.* **176**, 567 (1968).
- 5.7. L. Meyers, R. Meservey, *Phys. Rev.* **B4**, 824 (1971).
- 5.8. A. A. Shablo, T. P. Narbut, S. A. Tyurin, I. M. Dmitrenko, *JETP Lett.* **19**, 246 (1974).
- 5.9. B. L. Altshuler, A. G. Aronov, B. Z. Spivak, D. Yu. Sharvin, Yu. V. Sharvin, *JETP Lett.* **35**, 588 (1982).
- 5.10. R. Meservey, P. M. Tedrow, *Phys. Rev. Lett.* **41**, 805 (1978).

- 5.11. B. L. Altshuler, A. G. Aronov, *JETP Lett.* **33**, 499 (1981).
- 5.12. F. R. Ladan, J. Maurer, *Compt. Rend. Acad. Sc.* **297**, Serie II, 227 (1983).
- 5.13. I. O. Kulik, *Sov. Phys. JETP* **31**, 1172 (1970).
- 5.14. I. O. Kulik, K. V. Mal'chuzhenko, *Fizika Tverdogo Tela* **13**, 2945 (1971).
- 5.15. D. Yu. Sharvin, Yu. Sharvin, *JETP Lett.* **34**, 272 (1981).
- 5.16. R. L. Falge, Jr., N. M. Wolcott, R. A. Hein, I. E. Cox, J. W. Gibson, *Bull. Am. Phys. Soc.* **II** **13**, 730 (1968).
- 5.17. A. I. Larkin, *JETP Lett.* **31**, 219 (1980).
- 5.18. S. Hikami, A. I. Larkin, Y. Nagaoka, *Progr. Theor. Phys.* **63**, 707 (1980).
- 5.19. B. L. Altshuler, A. G. Aronov, A. I. Larkin, D. E. Khmelnitskii, *Sov. Phys. JETP* **81**, 768 (1981).
- 5.20. G. Bergmann, *Solid State Comm.* **42**, 815 (1982).
- 5.21. A. A. Abrikosov, L. P. Gor'kov, *Sov. Phys. JETP* **15**, 752 (1962).
- 5.22. G. Bergmann, *Phys. Rev. Lett.* **48**, 1046 (1982).
- 5.23. G. Krill, *Solid State Comm.* **9**, 1065 (1971).
- 5.24. M. M. Sinvani, A. J. Greenfield, M. Danino, M. Kaveh, N. Wiser, *J. Phys.* **F11**, L83 (1981).
- 5.25. B. L. Altshuler, A. G. Aronov, D. E. Khmelnitskii, *J. Phys.* **C15**, 7367 (1982).
- 5.26. S. Koshino, *Prog. Teor. Phys.* **24**, 1049 (1960).
- 5.27. P. L. Taylor, *Phys. Rev.* **135A**, 1333 (1964).
- 5.28. Y. Kagan, A. P. Zhernov, *Soviet Phys. JETP* **23**, 737 (1966).
- 5.29. H. Takayama, *Z. Phys.* **263**, 329 (1973).
- 5.30. V. N. Fleurov, P. C. Kondratenko, A. N. Kozlov, *J. Phys.* **F10**, 1953 (1980).
- 5.31. G. Bergmann, *Z. Phys.* **B48**, 5 (1982).
- 5.32. C. W. Lee, W. P. Pratt, Jr., J. A. Rowlands, P. A. Schroeder, *Phys. Rev. Lett.* **45**, 1708 (1980).
- 5.33. M. E. Gershenson, B. N. Gubankov, Yu. E. Zhuravlev, *Sov. Phys. JETP* **56**, 1362 (1982).
- 5.34. M. Gijs, C. Van Haesendonck, and Y. Bruynsraede, *Phys. Rev. Lett.* **52**, 2069 (1984).
- 5.35. B. Pannetier, J. Chaussy, R. Rammal, and P. Gandit, *Phys. Rev. Lett.* **53**, 718 (1984).
- 5.36. M. Gijs, C. Van Haesendonck, and Y. Bruynsraede, *Phys. Rev. B* **30**, 2964 (1984).
- 5.37. J. M. Gordon, *Phys. Rev. B* **30**, 6770 (1984).
- 5.38. B. Pannetier, J. Chaussy, R. Rammal, and P. Gandit, *Phys. Rev. B* **31**, 3209 (1985).

6

Brillouin-Mandelstam Scattering* In Magnetic Materials

*A.S. Borovik-Romanov, Mem. USSR Acad. Sc., and
N.M. Kreines, D. Sc. (Phys. and Math.)*

6.1. INTRODUCTION

Combination scattering of light was independently discovered in 1928 by Landsberg and Mandelstam** in quartz crystals [6.1] and by Raman and Krishnan [6.2] in liquids. It is an important method for investigating the spectra of elementary excitations in a substance [6.3]. The phonon spectra in crystals were then studied in great detail and a following terminology was developed***. The scattering from optical phonons is accompanied by relatively large frequency shifts of between 300 and 3000 cm^{-1} , and was named combination scattering of light (CSL) or the Raman effect. The light scattering from acoustic phonons is called Brillouin-Mandelstam scattering (BMS) or Brillouin scattering (BS). Mandelstam [6.5] and Brillouin [6.6] independently predicted the effect, and it was discovered experimentally by Gross [6.7].

The elementary excitations in magnetic materials are spin waves, or magnons. Single-sublattice ferromagnets possess only one branch of spin waves, frequently called the acoustic branch, though there is always a narrow gap whose energy is of the order of the sum of the anisotropy and Zeeman energies, ($0.1\text{-}1.0 \text{ cm}^{-1}$), and the frequency is quadratic in the wave vector. In multi-sublattice ferromagnets there is always one low frequency acoustic branch of the spin waves together with several other branches, generally called "optical" branches, whose energy is of the order of the exchange energy ($100\text{-}1000 \text{ cm}^{-1}$). The spectra of most antiferromagnets have substantial gaps with energies equal to the exchange energies ($100\text{-}1000 \text{ cm}^{-1}$), or equal to the geometric mean of the exchange and anisotropy energies ($1\text{-}100 \text{ cm}^{-1}$). However, some types of antiferromagnets (easy plane and cubic) have spectra with an additional "acoustic" branch. The gap in this branch is comparatively small ($< 1 \text{ cm}^{-1}$). It is quite natural to apply this classification of scattering types to magnons. That is, assign the term combination scattering to magnon branches with substantial gaps (more than 10 cm^{-1}), and the term BMS to the "acoustic" branches.

The first experiments to observe the scattering of light from magnons were set up by Fleury et al. [6.8-10]. They observed scattering

* Also Brillouin scattering, see below.

** Also transliterated Mandelstam.

*** The terminology is discussed by Ginsburg in [6.4].

from magnon branches with noticeable gaps ($3\text{-}5\text{ cm}^{-1}$) in the energy spectra for the antiferromagnetic fluorides of the transition elements. BMS from magnetic materials was first investigated by Sandercock and Wetling [6.11] in yttrium-iron garnet (YIG). These experiments were made feasible by the high contrast multi-pass Fabry-Perot interferometer Sandercock [6.12] had developed.

Light scattering can be also observed from the spin system of a paramagnet in a magnetic field. This was observed in semiconductors for free charge carriers [6.13] and in a paramagnetic crystal [6.14] for magnetic ions.

Magnon energies typically observed in BMS lie around 30 GHz ($\approx 1\text{ cm}^{-1}$). At these frequencies the spin system can be easily excited by microwaves at ferromagnetic and antiferromagnetic resonance (FMR and AFMR) or by the parametric pumping of the spin waves. The observation of spin waves by BMS after they have been pumped by microwave power broadens the study of the relaxation processes of spin waves. We were able to report the first observation of AFMR relaxation in CoCO_3 by BMS [6.15]. Kreines and Zhotikov* [6.16] then discovered light scattering from magnons and phonons created by parametric pumping. A combination of microwave pumping and optical spectroscopy appeared to be effective in another type of experiments, where satellites were observed in the spectrum of light passed through a crystal in which a resonance (FMR, AFMR, or EPR) was excited. This result can be regarded as BMS from coherently pumped excitations that have the wave vector $\mathbf{q} = 0$. It can be also treated as a modulation of light by FMR, EPR or AFMR. Hanlon and Dillon were the first to do such experiments using a ferromagnetic crystal, CrBr_3 [6.17].

Up to now, the number of experiments on BMS in magnetic materials has not been large, and they are reviewed in [6.18-19].

We shall in this article only consider the work on light scattering from magnetic materials done at the Institute for Physical Problems, Academy of Sciences of the USSR (Moscow). In the course of the investigation light scattering from magnons was discovered in the antiferromagnetic CoCO_3 and the constants characterizing the magnon spectrum [6.20] were obtained. For the first time, the energy of the magnon dipole interaction for magnetic materials was experimentally discovered and measured. The optical observation of pumped spin waves in CoCO_3 enabled us to show that there is a "bottle-neck" in the AFMR relaxation process with energy being transferred [6.21]. Modulation of light under resonance conditions has also been observed in the ferromagnetic K_2CuF_4 [6.22], ferrimagnetic RbNiF_3 [6.23], and in the paramagnetic neodymium-gallium garnet, $\text{Nd}_3\text{Ga}_5\text{O}_{12}$ [6.24]. The intensities of the Stokes and anti-Stokes sat-

*

Also transliterated Jotikov.

ellites in RbNiF_3 were found to be substantially different and this anomaly has been explained. The first experiments on the parametric excitation of magnons [6.16] proved that the created magnons had a frequency of half the exciting microwave frequency. The dependence of the number of created magnons on the pumping power was also studied.

6.2. MAGNETOOPTICAL EFFECTS AND THE MECHANISM OF LIGHT SCATTERING IN MAGNETIC MATERIALS

The establishment of magnetic order in a crystal brings about a change in its optical properties. We shall only consider transparent crystals below. Therefore, by neglecting light absorption, we shall be interested in only two magnetooptical effects, namely circular birefringence, or the Faraday effect (φ_{MCB}), and linear birefringence (Ψ_{MLB}). General symmetry considerations impose certain limitations on the form of the tensors which correspond to these effects and describe the change in the dielectric permittivity of a magnetically ordered crystal. We shall also describe the magnetic order in ferromagnets and ferrimagnets by the magnetization vector \mathbf{M} , while in antiferromagnets we shall use two vectors, i.e. the magnetization $\mathbf{M} = \mathbf{M}_1 + \mathbf{M}_2$ and the antiferromagnetic vector $\mathbf{L} = \mathbf{M}_1 - \mathbf{M}_2$, where \mathbf{M}_1 and \mathbf{M}_2 are the magnetization vectors of the sublattices. The change in crystal permittivity due to magnetic ordering can be written down as an expansion in terms of the corresponding ordering vectors \mathbf{M} and \mathbf{L} . These expansions have the following form for ferromagnets, ferrimagnets and antiferromagnets:

$$\Delta\epsilon_{ik} = f_{ik\alpha}M_\alpha + g_{ik\alpha\beta}M_\alpha M_\beta \quad (6.1)$$

$$\Delta\epsilon_{ik} = f_{ik\alpha}L_\alpha + g_{ik\alpha\beta}L_\alpha L_\beta \quad (6.2)$$

where $i, k \rightarrow x, y, z$. In the absence of an external field, the linear term in (6.2) only occurs in antiferromagnets with weak ferromagnetism. The form of the expansion is determined by the crystal symmetry. But first we must allow for two general symmetry considerations (see, e.g. [6.25]):

1. If there is no absorption, the tensor ϵ_{ik} must be Hermitian, i.e.

$$\Delta\epsilon_{ik} = \Delta\epsilon_{ik}^* \quad (6.3)$$

2. The principle of kinetic coefficients symmetry imposes the following condition with respect to the magnetic field \mathbf{H} (or, similarly with respect to the vectors \mathbf{M} and \mathbf{L} , which, like \mathbf{H} , change sign for a time reversal operation):

$$\Delta\epsilon_{ik}(\mathbf{H}) = \Delta\epsilon_{ik}(-\mathbf{H}) \quad (6.4)$$

Conditions (6.3) and (6.4) lead to a distinction between the properties of the tensors $\Delta\epsilon_{ik}$, which have parts linear or quadratic in the components of the ordering vectors.

The part of $\Delta\epsilon_{ik}$ linear in M_α is a purely imaginary antisymmetric tensor,

$$(\Delta\epsilon_{ik})_1 = if_{ik\alpha}M_\alpha \quad (6.5)$$

This tensor describes the Faraday effect (Φ_{MCB}). In the simplest case of a cubic crystal, where the magnetization M_0 is directed along the z -axis, only two components of the tensor have nonzero values, namely $f_{xyz} = -f_{yxz} = -f$. Let us consider a plate of crystal whose planes are perpendicular to the direction of the magnetization (i.e. the z -axis). The plane of polarization of a light beam which passes through such a plate along the z -axis will be rotated through the angle

$$\Phi_{MCB} = \frac{\omega d}{2c} \frac{fM_0}{n} \quad (6.6)$$

where ω is the circular frequency of light, d is the plate thickness, c is the light velocity, and $n = \sqrt{\epsilon_{xx}^0}$ is the refraction index of the crystal. The Faraday effect results from the fact that the refraction circular right-handed (+) and left-handed (—) waves are different for light propagating in the magnetization direction:

$$n_\pm^0 = \epsilon_{xx}^0 \pm fM_0 \quad (6.7)$$

The part of $\Delta\epsilon_{ik}$ that is quadratic in M_α (or in L_α) is a real symmetric tensor

$$(\Delta\epsilon_{ik})_2 = g_{ik\alpha\beta}M_\alpha M_\beta \quad (6.8)$$

The tensor $g_{ik\alpha\beta}$ is symmetric in both the first and second pair of indices. Therefore, it can be more conveniently written in matrix form, $g_{ik\alpha\beta} = g_{lm}$ (where $l, m = 1, 2, \dots, 6$). The symmetry of the tensor $g_{ik\alpha\beta}$ results in additional magnetic terms both for non-diagonal components, as in the case of linear terms (6.5), and for diagonal components of the permittivity tensor ϵ_{ik} . Changes in the diagonal components lead to variations in crystal birefringence. The squares of antisymmetric tensor components (6.5), also contribute to the magnitude of magnetic birefringence (see, e.g. [6.26]).

Since we shall be presenting experiments with CoCO_3 we now consider the form of tensor (6.8) for this crystal in more detail. The CoCO_3 crystal is trigonal with D_{3d}^h group symmetry. Below $T_N = 18$ K CoCO_3 passes to an antiferromagnetic state with weak ferromagnetism [6.27]. The antiferromagnetic vector L_0 lies in a basal plane (perpendicular to the trigonal axis), the weak ferromagnetic vector M_D also lies in this plane and is perpendicular to L_0 . In the basal plane, anisotropy is practically absent. If a magnetic

field is imposed in the plane, the magnetization vectors of sublattices rotate so that $M_0 \parallel H$. Then $L \perp H$ and the magnetization vector M_0 depends on the field as follows:

$$M_0 = M_D + \kappa_1 H \quad (6.9)$$

where $4\pi M_D = 647$ Gs, and $\kappa_1 = 1.8 \times 10^{-3}$ emu.

When in the paramagnetic state, CoCO_3 is a uniaxial crystal with its optical axis along the trigonal one (z). At room temperature, the refraction indices are $n_0 = \sqrt{\epsilon_{xx}} = \sqrt{\epsilon_{yy}} = 1.855$, and $n_e = \sqrt{\epsilon_{zz}} = 1.60$.

Optical studies [1.28] indicated that there is no Faraday effect in CoCO_3 ($\Phi_{MCB} < 100$ deg/cm) at temperatures below T_N . Therefore, we only need to consider the form of the tensor $(\Delta\epsilon_{ik})_2$ from (6.8) to describe its magnetooptic properties in an ordered state. The tensor components are presented so as to distinguish which terms are independent of the direction of the vector L (isotropic contributions) and which are determined by components of L (anisotropic contributions) [1.28]:

$$\left\{ \begin{array}{l} \epsilon_{xx} = \epsilon_{\perp}^0 + \frac{1}{2} (g_{11} + g_{12}) L^2 + g^* L_z^2 + g_{14} L_z L_y + \frac{1}{2} g_{66} (L_x^2 - L_y^2) \\ \epsilon_{yy} = \epsilon_{\perp}^0 + \frac{1}{2} (g_{11} + g_{12}) L^2 + g^* L_z^2 - g_{14} L_z L_y - \frac{1}{2} g_{66} (L_x^2 - L_y^2) \\ \epsilon_{zz} = \epsilon_{\parallel}^0 + g_{31} L^2 + (g_{33} - g_{31}) L_z^2 \\ \epsilon_{yz} = \epsilon_{zy} = g_{44} L_z L_y + 2g_{41} (L_x^2 - L_y^2) \\ \epsilon_{xz} = \epsilon_{zx} = g_{44} L_z L_x + 2g_{41} L_x L_y \\ \epsilon_{xy} = \epsilon_{yx} = \frac{1}{2} g_{14} L_z L_x + g_{66} L_x L_y \end{array} \right. \quad (6.10)$$

Here $g^* = g_{13} - \frac{1}{2} (g_{11} + g_{12})$, $g_{66} = \frac{1}{2} (g_{11} - g_{12})$, and the x-axis is directed along a second order axis.

This tensor together with experimental data reveals the following two magnetooptic effects. First, there is a change in the magnitude of the main birefringence of the crystal. This change is determined (if $L_z = 0$) by the first terms of the expansion of the diagonal components, ϵ_{ik} . Second, and this is very important for our later discussion, if $L_x \neq 0$ or $L_y \neq 0$ then the CoCO_3 crystal becomes biaxial. In particular, birefringence arises for the light beam propagating along the z-axis. For the external field directed along the x-axis the difference between the refraction indices for waves polarized along the y-axis and the x-axis, respectively, will be:

$$n_y - n_x = \frac{g_{66}}{n_0} L_y^2 - \frac{g_{14}}{n_0} L_z L_y \quad (6.11)$$

The experimental value for this difference is 2.7×10^{-4} . This corresponds to the phase difference for the propagating waves, $\psi_{\text{LMB}} = 1500 \text{ deg/cm}$ (for $\lambda = 633 \text{ nm}$).

Let us turn to the mechanism of light scattering from magnetic excitations. The mechanism of direct interaction between the magnetization vector of the light wave and the spin oscillations that had been put forward by Bass and Kaganov [6.29] proved to be inefficient. In reality, the magnetic light scattering proceeds via virtual electro-dipole transitions which due to spin-orbital interactions can cause a change in the magnetic quantum number [6.30-32]. Thus as in the case of phonons scattering is determined by fluctuations in the electrical permittivity which arise from the magnetic ordering fluctuations owing to the above magnetooptic effects.

From the quantum viewpoint, the inelastic scattering of light is when one medium absorbs one photon ($h\nu^i$), emits another of a different energy $h\nu^s$, and as a result passes into a new quantum state. In so doing, a single elementary excitation is originated (or annihilated) in the medium. The frequency ν_q and the wave vector \mathbf{q} of this excitation are unambiguously determined by the conservation laws of energy and momentum:

$$h\nu = h\nu^i \pm h\nu_q, \quad \mathbf{K}^s = \mathbf{K}^i \pm \mathbf{q}, \quad (6.12)$$

where h is Planck's constant, and the superscripts s and i refer to the scattered and incident light, respectively. A “+” sign corresponds to the annihilation of a quasiparticle during scattering, i.e. to an anti-Stokes process, while a “-” sign corresponds to the origination of a quasiparticle, or a Stokes process. In BMS, the quasiparticle energy is much less than that of a light quantum, hence $|\mathbf{K}^i| = |\mathbf{K}^s|$. As a result, the magnitude and direction of \mathbf{q} are unambiguously determined by the scattering geometry given ν^i . One should take into account, however, the refraction index of the medium and this complicates the problem for anisotropic crystals.

The theory of light scattering is covered elsewhere (see, e.g. [6.25]), but to proceed further it is important to note that the intensity of the scattered light is proportional to the mean square of the permittivity fluctuations, $|\delta\epsilon_{ik}|^2$. The fluctuation amplitude $\delta\epsilon_{ik}$ is determined by the oscillation amplitude of the vectors $\mathbf{M}(\mathbf{r}, t)$ and $\mathbf{L}(\mathbf{r}, t)$ in a spin wave. In order to determine this amplitude we must linearize the expansion of $\delta\epsilon_{ik}$ [(6.1) or (6.2)] in terms of components of the vectors \mathbf{M}_i and \mathbf{L}_i , which are oscillating in the spin wave. In the simplest case of a cubic or uniaxial ferromagnet, every spin in the spin wave precesses in a circular cone. If the magnetization vector \mathbf{M}_0 lies along the z -axis, the spin wave will be described by the variables M_x and M_y :

$$|M_x| = |M_y| = M_\perp$$

Accordingly, the nonvanishing components of $\delta\epsilon_{ik}$ are:

$$\begin{aligned}\delta\epsilon_{xz} &= -ifM_y + g_{44}M_0M_x \\ \delta\epsilon_{zx} &= ifM_y + g_{44}M_0M_x \\ \delta\epsilon_{yz} &= ifM_x + g_{44}M_0M_y \\ \delta\epsilon_{zy} &= -ifM_x + g_{44}M_0M_y\end{aligned}\quad (6.13)$$

Auld and Wilson [6.33], Hu and Morgenthaler [6.34] and Le Gall and Jamet [6.35] all observed that scattering is due to both linear and quadratic magneto-optic effects. The incorporation of both effects results in an anomaly. Since the Faraday effect is described by an imaginary term, the intensity of scattering P_s appears to be different for the Stokes and anti-Stokes satellites. Namely,

$$P_s \sim (g_{44}M_0 \pm f)^2 M_\perp^2 \quad (6.14)$$

Here the “+” sign corresponds to the Stokes component, whereas the “−” sign to the anti-Stokes one in the scattering spectrum. Wettling, Cottam, and Sandercoc [6.36] demonstrated that in the case of scattering in YIG (yttrium-iron garnet) in addition to the above two magneto-optic effects one should take into account two other effects connected with absorption, i.e. magnetic circular dichroism ($\Delta\epsilon_{ik} = f_{ik\alpha}M_\alpha$) and magnetic linear dichroism ($\Delta\epsilon_{ik} = ig_{ik\alpha\beta}M_\alpha M_\beta$). We shall come back to this problem later when we discuss the investigation of BMS in RbNiF_3 .

An important topic concerns the relation between polarization of incident and that of scattered light. In order to elucidate the matter, let us use the expression for the electric vector of the scattered wave [6.25]:

$$\mathbf{E}^s \sim [\mathbf{K}^s [\mathbf{K}^s \mathbf{G}]] \quad (6.15)$$

where

$$G_i = \int \delta\epsilon_{ik} e_k^i \exp [-i(\mathbf{K}^s - \mathbf{K}^i) \mathbf{r}] dV \quad (6.16)$$

and \mathbf{r} is the radius-vector of the volume element of the scattering medium. Here e_k^i is a component of a unit vector characterizing the polarization of the incident light wave \mathbf{E}^i . If \mathbf{q} is the wave vector of a spin wave, then $\Delta\epsilon_{ik}$ can be written as $|\Delta\epsilon_{ik}| \exp(\pm i\mathbf{qr})$ so that

$$G_i \propto (|\Delta\epsilon_{ik}| e_k^i) \quad (6.17)$$

given that the conservation laws of energy and momentum are satisfied [see (6.12)]. By using (6.15) and (6.17) it is possible to get all the information concerning the relationship between the polarization of the incident and scattered waves. During scattering from a spin wave the light polarization, as a rule, appears to rotate through 90° .

6.3. APPARATUS AND SAMPLES

6.3.1. Apparatus

In order to investigate light scattering an experimental setup has been created which permits an investigation of the light spectrum scattered from thermally and microwave excited quasiparticles at $T \leq 2$ K for a broad range of magnetic fields from 0 to 30 kOe.

(A) For the spectral device we used a multi-pass high-contrast scanning Fabri-Perot interferometer (FPI) manufactured in the US by Burleigh. The interferometer is able to work in both the three and five pass modes, the contrast being either 5×10^6 or $\sim 10^8$, respectively. A detailed description of the multi-pass interferometer can be found in Sandercock [6.19].

A He-Ne laser with $\lambda = 632.8$ nm and an output power P of 30-50 mW and an Ar laser with $\lambda = 488.0$ and 514.5 nm and $P \simeq \simeq 200$ mW were used as the light sources.

The experiments were performed for three scattering geometries. Direct (or small-angle) light scattering enables us to study quasiparticles with a zero, or small, wave vector \mathbf{q} . In the cases of the 90° and 180° geometries, quasiparticles with a wave vectors of $|\mathbf{q}| \simeq \simeq 10^5$ cm⁻¹ were studied. The exact value of $|\mathbf{q}|$ was determined by the scattering geometry, the wavelength of the incident light, and the refractive indices of the sample.

A diagram of the setup to observe BMS using a triple-pass FPI is shown in Fig. 6.1. The same setup can be used to examine all three geometries indicated earlier. The laser light is focused onto the sample S by one of three lenses L_1 , L_2 , L_3 (depending on the geometry used). The scattered light is collected by the L_2 lens and focused by the L_4 lens onto the pinhole P_2 of the input collimator P_2-L_5 , whence the light passes to the FPI. The distance between the FPI mirrors is scanned by piezoelectric rods P. The figure shows the three-pass FPI with the corner cubes CC. The light from the FPI output is directed into the output collimator L_6-P_3 and having passed through the pinhole P_3 it hits a cooled photomultiplier PM. Thereafter, a conventional photon counter follows with a preamplifier PA whose output is connected to a multichannel analyzer which is a part of DAS-1 system. The analyzer is synchronized with a sweep oscillator that controls the piezoelectric rods. The DAS-1 system simultaneously and automatically adjusts the interferometer mirrors. The spectrum is projected onto the screen of the multichannel analyzer and can be recorded.

(B) Exciting quasiparticles with microwave power is performed by the conventional microwave technique. In order to apply a microwave field to the sample we used a simple microwave spectrome-

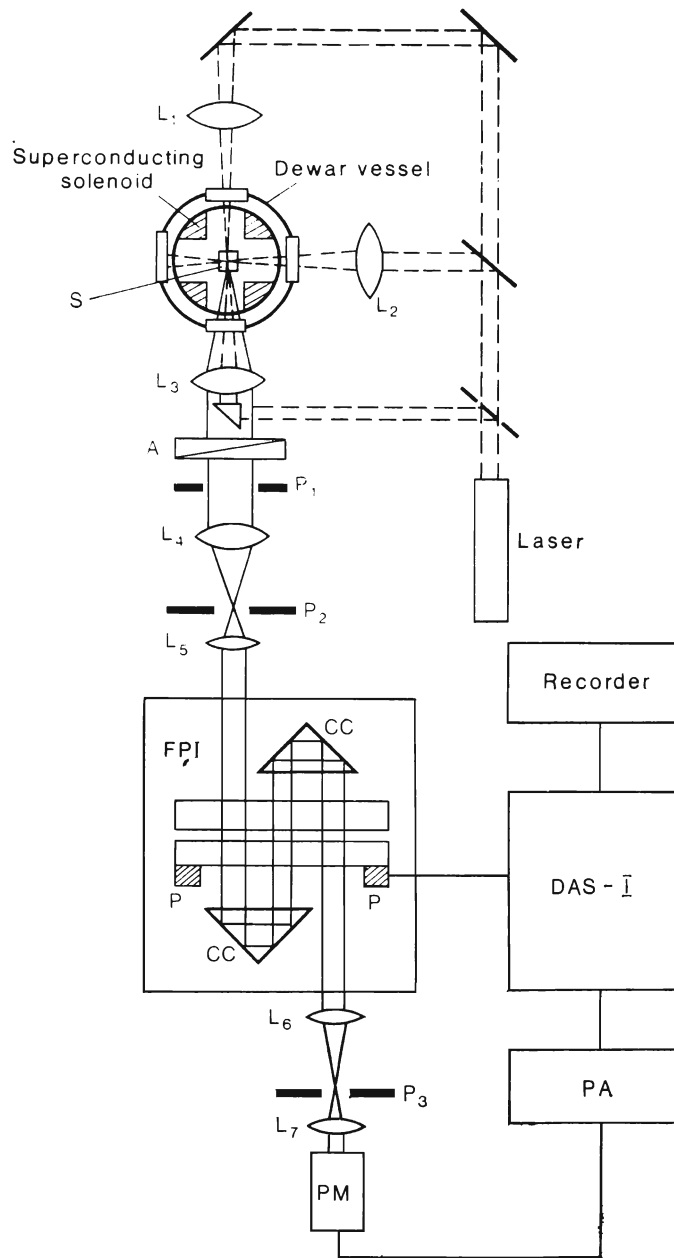


Fig. 6.1. Diagram of the optical part of the setup to observe BMS from thermal and pumped quasiparticles.

ter with direct amplification. We used a clystron with a generation frequency of $v'_1 = 36.2$ GHz, and two magnetrons running in a stationary mode at frequencies of $v_1 = 36$ GHz and $v_2 = 51$ GHz as the sources of the high frequency power. The maximum power in the experiments amounted to 500 mW. The sample was glued to a short-circuiting waveguide plunger. The sample was located in the antinode of the magnetic microwave component. The waveguide walls have special holes to pass light. The reflected microwave signal was detected by a crystal pick-up and applied either across the oscilloscope input or to the y -coordinate input of an xy -recorder, the x -coordinate receiving a signal proportional to the magnetic field strength. The input microwave power was monitored by a power meter in the second branch of a calibrated directional coupler. The following formula was used to calculate the microwave field amplitude inside the waveguide [6.37]:

$$h_{\text{mw}} = (4P/abz)^{1/2} \quad (6.18)$$

where P is the power in W, a and b the dimensions of the waveguide cross section in m, $z = 120 \pi \lambda_g / \lambda$ the waveguide impedance in Ω , λ_g the wavelength inside the waveguide, and λ the wavelength in free space. It should be noted that the wave attenuation inside waveguide was not taken into account.

(C) At low temperatures a metallic helium cryostat was used, which had four pairs of windows made from fused quartz and at 90° to one another. The experiments were performed at T from 1.7 to 2.0 K, and the sample was immersed into a bath with superfluid helium.

A magnetic field was produced using superconducting magnets equipped with special holes to pass through light. By using magnets with different designs a magnetic field would be established in three mutually perpendicular directions.

6.3.2. Samples

Depending on scattering geometry, several differently shaped crystal samples were used. In the direct scattering (modulation of light) test disks of diameters from 0.5 to 2.0 mm and thicknesses from 0.1 to 0.3 mm were usually used. This shape enabled the demagnetizing fields to be taken into account more precisely. Rectangular parallelepiped $1 \times 1.5 \times 2.0$ mm samples were prepared to study the 90° scattering. For the backscattering tests we used a special shape that enabled the light beams reflected from the back wall of the sample to swing out of the way.

The alignment accuracy of the samples was about $1-2^\circ$. Their surfaces were optically polished.

6.4. SPECTRA OF THERMAL MAGNONS IN CoCO_3

The BMS investigation of spin wave spectrum was performed with the CoCO_3 rhombohedral antiferromagnet, which possesses weak ferromagnetism. The spin wave spectrum for antiferromagnets with "easy plane" anisotropy contains a low frequency branch [6.38-39]. The AFMR data [6.40-41] show with a rather high accuracy that for CoCO_3 the gap in this spectral branch has a zero or very narrow width. The absence of a gap within this branch allows it to be investigated by BMS. Further on, we shall only be interested in the low frequency branch of the spin wave spectrum.

Because of the relatively high ferromagnetic momentum in CoCO_3 (see Sec. 6.2) a magneto-dipole interaction must be taken into ac-

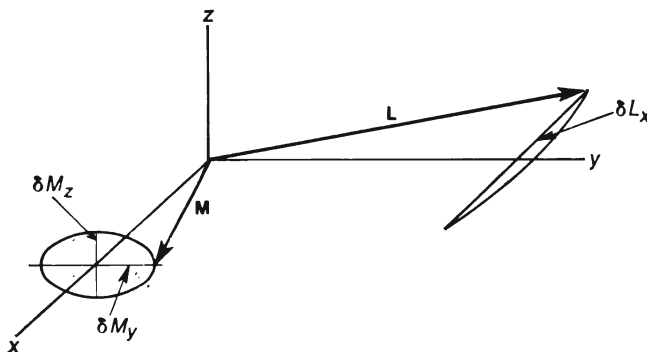


Fig. 6.2. Diagram of motion of the antiferromagnetism vector \mathbf{L} and magnetization \mathbf{M} for an easy-plane antiferromagnet in the low-frequency mode.

count when calculating the low frequency part of the spectrum. The dispersion law of this branch, with due account for the magneto-dipole interaction, was derived in [6.42-43] and has the following form:

$$\begin{aligned} v_q^2 = & \gamma^2 [H(H + H_D)(1 + 4\pi\kappa_{\perp} \cos^2 \theta) \\ & + 4\pi\kappa_{\perp}(H + H_D)^2 \sin^2 \theta \sin^2 \varphi] + \alpha^2(\theta\varphi) q^2 \end{aligned} \quad (6.19)$$

where \mathbf{q} is the magnon wave vector, γ is the gyromagnetic ratio, and θ and φ are the polar and azimuth angles of \mathbf{q} in the frame, where the z -axis is parallel to the trigonal axis and the x -axis is parallel to the field applied in the basal plane. A diagram of the oscillations of a spin system in the low frequency branch of spin waves is presented in Fig. 6.2. In the first approximation, these

oscillations can be described as swinging the \mathbf{L} vector in the basal plane and precessing the \mathbf{M} vector around the x -axis, \mathbf{L} and \mathbf{M} being mutually perpendicular. As a result, the low frequency spin waves are described by the oscillations δL_x and $\delta M_y, \delta M_z$.

A description of the light scattering from these spin waves can be done using the magnetic part of the dielectric permittivity tensor for CoCO_3 . The components of this tensor were given in Sec. 6.2 [see (6.10)]. By linearizing the components in the spin wave amplitude δL_x we get the expression for the components of the \mathbf{G} vector

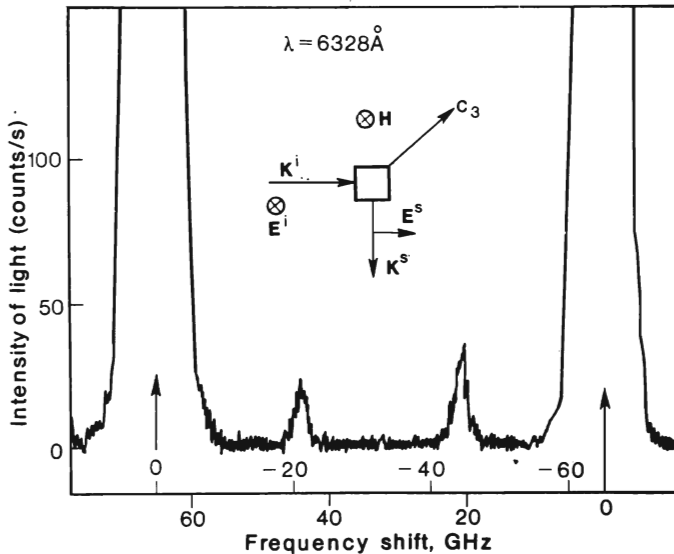


Fig. 6.3. A spectrum of BMS from magnons in CoCO_3 at $T \sim 2 \text{ K}$ [6.20].

that controls the components of the electrical vector of the light wave scattered due to anisotropic birefringence [see (6.15) and (6.17)]:

$$\begin{vmatrix} G_x \\ G_y \\ G_z \end{vmatrix} = \begin{vmatrix} 0 & g_{66}L_0\delta L_x & 2g_{11}L_0\delta L_x \\ g_{66}L_0\delta L_x & 0 & 0 \\ 2g_{11}L_0\delta L_x & 0 & 0 \end{vmatrix} \begin{vmatrix} E_x^i \\ E_y^i \\ E_z^i \end{vmatrix} \quad (6.20)$$

Here $L_0 = 2M_0$ is double the magnetization vector of the sublattices. An analysis of (6.20) reveals that the light's polarization rotates through 90° during the scattering from a spin wave. The light scattering from the magnons of the low-frequency branch of the

spin waves in CoCO_3 was investigated [6.20, 6.44, 6.45] for the wavelength $\lambda = 632.8$ nm at superfluid helium temperatures ($T \leq 2\text{ K}$). The magnons with the wave vector $|\mathbf{q}| = 2.5 \times 10^5 \text{ cm}^{-1}$ (90°-scattering) were studied when propagating along three rational directions: z -magnons along the axis C_3 ($\theta = 0^\circ$), x -magnons in the basal plane ($\theta = 90^\circ$, $\varphi = 0^\circ$), and y -magnons ($\theta = \varphi = 90^\circ$).

Figure 6.3 demonstrates a BMS spectrum for thermal z -magnons in CoCO_3 at the fixed external magnetic field. A change in the magnetic field changes the positions of the satellites corresponding to the scattering from magnons. The main experimental results are shown in Fig. 6.4 as the squares of the magnon frequencies versus the

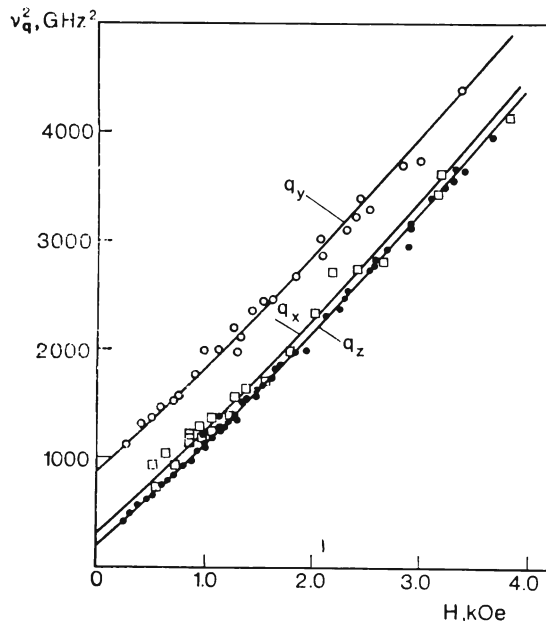


Fig. 6.4. Dependence of squared magnon frequency on the magnetic field strength for three directions of magnon propagation in the CoCO_3 crystal. q_z is the direction along the axis C_3 [111]; q_x , q_y are directions in the basal plane which are parallel and perpendicular to the magnetic field, respectively [6.20].

applied magnetic field for the three directions of the magnon wave vector \mathbf{q} . The solid curves in Fig. 6.4 are drawn according to (6.21). The figure illustrates a satisfactory agreement between the experimental data and the theoretical curves. These results provided the constants γ , H_D , α_x , α_y , α_z . It appeared (and it is consistent with the theory) that $\alpha_x = \alpha_y = \alpha_\perp = 1.2 \times 10^{-5} \text{ kOe} \cdot \text{cm}$ to within

the experimental error. The exchange constant $\alpha_z = \alpha_{\parallel} = 0.9 \times 10^{-5}$ kOe.cm. In the course of the BMS experiments in CoCO_3 all three branches ($q \parallel 0x, 0y, 0z$) of the low-frequency part of spin wave spectrum were detected. The agreement of the data with (6.19) lent support for the validity of the calculations of the dipole's contribution to the magnon energy for an easy plane antiferromagnet with weak ferromagnetism. It was found, in particular, that such an antiferromagnet differs from an isotropic ferromagnet in that in the former only spin waves propagating along the direction

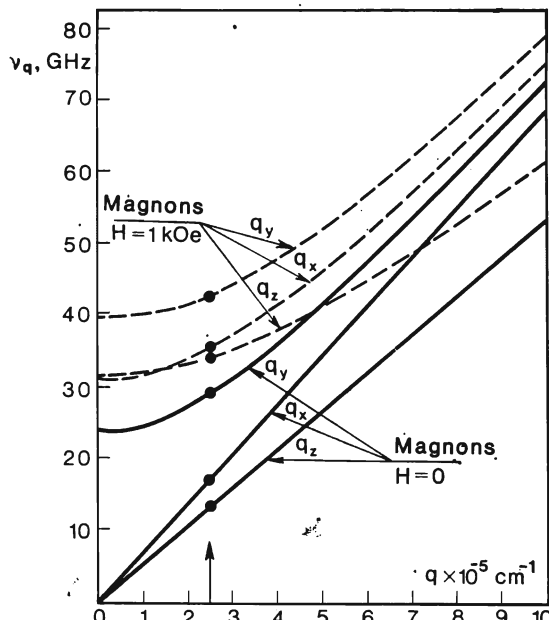


Fig. 6.5. Low-frequency spectrum, $v(q)$, for CoCO_3 . Solid curves correspond to $H = 0$ while dashed ones to $H = 1$ kOe. Points indicate experimental values obtained for $q = 2.5 \cdot 10^5 \text{ cm}^{-1}$.

normal both to the magnetic field and to the easy axis possess a higher energy. This is illustrated in Fig. 6.5, where two spin waves spectra $v_q(q)$ are shown for clarity. They are drawn according to (6.19) using the experimentally determined constants. The solid line is for the spectra given an external field $H = 0$ and the dashed line is for $H = 1$ kOe. As can be seen from the figure, the dipole-dipole interaction in the zero magnetic field results in the additional energy of magnons which propagate along the y -axis and having a spectrum with a gap of 24 GHz.

6.5. MODULATION OF LIGHT BY MAGNETIC RESONANCE IN MAGNETIC MATERIALS

6.5.1. General Remarks

In this Section we shall dwell on the spin systems of different magnetic materials (see Introduction) excited by a magnetic resonance. The studies were performed by the BMS method using direct scattering. As mentioned above, direct scattering enables spin waves with $q = 0$ to be investigated. The excitation of a uniform precession (resonance) in a substance is accompanied by an increase in the number of spin waves with $q = 0$ and frequency ν equal to that of the exciting microwave power source, ν_{res} . This in turn leads to an increase in the intensity of the light scattered from the quasiparticles. As a result, under resonance conditions, a direct scattering spectrum contains two intense satellites whose frequencies differ from that of the incident light by $\pm\nu_{\text{res}}$. However, the subjects of investigation include a conventional paramagnet which cannot be represented in the language of quasiparticles. Hence, for generality we shall offer a quasiclassical description of the phenomenon.

Let us consider two extreme cases, when light scattering is due to either Faraday effect or anisotropic magnetic birefringence only.

In the first case light scatters from oscillations of magnetic moment, the latter being spontaneous in ferri- and ferromagnets and induced by an external magnetic field, in paramagnets.

The experiments are performed with geometries where the direction of incident light is perpendicular to the magnetic field \mathbf{H} . In the absence of resonance, the optical system is aligned for the minimum intensity of the transmitted light. Under resonance conditions the magnetization vector \mathbf{M} precesses in phase with microwave field. A transverse magnetization component M_{\perp} , i.e. $M_{\perp} \perp \mathbf{H}$ (see Fig. 6.6), oscillating in the light propagation direction, changes the intensity of the transmitted light at the frequency $2\nu_{\text{res}}$, i.e. this component modulates the transmitted light at this frequency. An analysis of the transmitted light by means of an interferometer reveals two satellites with the frequencies $\nu^i \pm \nu_{\text{res}}$ in the spectrum. In order analytically to describe this phenomenon, a formula is available that was derived by Hanlon and Dillon [6.17]:

$$E^s = -\frac{1}{2} \Phi E_0^i \exp(-\alpha l/2) \{ \cos 2\pi (\nu^i + \nu_{\text{res}}) t + \cos 2\pi (\nu^i - \nu_{\text{res}}) t \} \quad (6.21)$$

where αl characterizes absorption in the sample and ν^i is the incident light frequency. This formula yields an intensity of satellites

which is proportional to the squared angle of Faraday rotation Φ and, consequently, to M_{\perp}^2 .

In the second case, light can scatter from oscillations of both ferromagnetic and antiferromagnetic vectors. The light scattering due to anisotropic magnetic birefringence was observed in CoCO_3 . Taking this compound as an example we shall describe the picture of scattering under antiferromagnetic resonance. Incident light propagated along the trigonal axis C_3 of the crystal. Such a geometry suggests only a magnetic birefringence in a plane perpendicular to

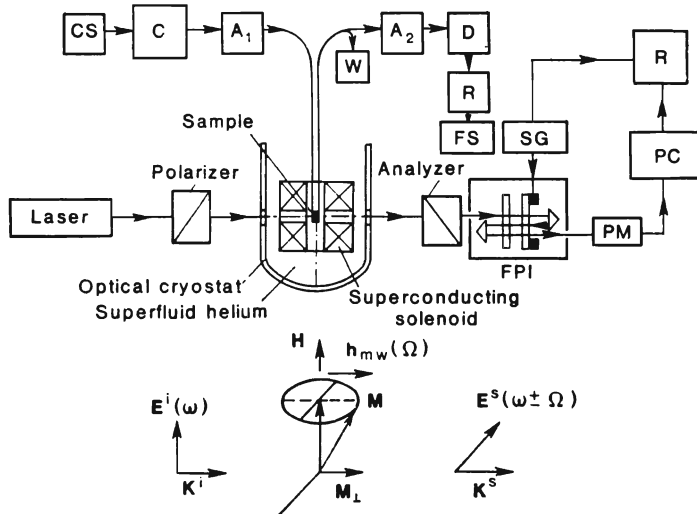


Fig. 6.6. Diagram of the experimental setup. PG—pulse generator, CS—klystron supply, C—klystron, A_1 , A_2 —attenuators, W—wavemeter, D—microwave detector, PM—photomultiplier, R—recorder, FS—field scanner, SG—scanning generator, PC—photon counter, FPI—Fabry-Perot interferometer. Below is given the scheme explaining modulation of light due to Faraday effect.

C_3 , i.e. in the basal plane. Positions of the principal axes of the tensor corresponding to a magnetic contribution into permittivity in this plane are governed by the position of the antiferromagnetic vector L . Position of the latter in the absence of AFMR is controlled by the direction of the magnetic field in the basal plane. Under a uniform resonance all spins of the sample oscillate in phase. An oscillation of the L vector is equivalent to that of the principal axes of the tensor about their equilibrium positions with the resonance frequency (see Fig. 6.2). Let us assume that in the absence of AFMR the entire optical system is compensated so that the photosensor detects a minimum light flux. When exciting a resonance at the fre-

quency v_{res} , the system will modulate the transmitted light at the frequency $2v_{\text{res}}$, which is to say that the components at the shifted frequencies, $v_0 \pm v_{\text{res}}$, (v_0 is the incident light frequency), are present in the spectrum of light transmitted through the crystal.

When describing light modulation, we assumed in both cases the optical system to be compensated for the minimum of the transmitted light in the absence of resonance. And yet this condition is not a rigid one. As can be seen from (6.21) and calculations for CoCO_3 [6.21], the spectrum of the light transmitted under resonance always contains additional satellites. Compensating the light signal at the incident light frequency facilitates an experimental detection of modulation and gives some insight into the phenomenon.

In addition to the two foregoing limiting cases situations are possible when light scattering is due to contributions from the two magneto-optic effects as well as from linear and circular dichroism. This point will be discussed in more detail, when describing the light modulation in RbNiF_3 .

The modulation depth or the ratio of intensity of the components observed in a spectrum to that of incident light enables us to estimate the angle of deviation of spins from the equilibrium position under resonance at the given absorbed power P . In the case of magnetically ordered substances this quantity is proportional to the number N_{res} of the excited spin waves with $q = 0$. By using the relation

$$P/hv_{\text{res}} = N_{\text{res}}/\tau \quad (6.22)$$

one can evaluate τ , the relaxation time of the spin system.

Now let us consider the results obtained for the above mentioned crystals.

6.5.2. CoCO_3

In this crystal, as has been mentioned above, light scattering is caused by anisotropic magnetic birefringence. The tensor for this case is given in Section 6.2, see Eq. (6.10). The low-frequency antiferromagnetic resonance in CoCO_3 is described by (6.19), where one has to put $q = 0$, $\varphi = 0$, $\Theta = \pi/2$. Figure 6.7 shows the spectrum of the light transmitted through a CoCO_3 crystal with the uniform spin precession excited in it under AFMR [6.46]. The presence of the satellites shifted by about ± 36 GHz indicates that the transmitted light is modulated at the frequency 72 GHz. It should be noted that the intensities of Stokes and anti-Stokes satellites are the same to within the experimental errors, (from 10 to 15%). The dependence of satellite intensities on the magnetic field strength H at the con-

stant supplied microwave power P reproduces the shape of the resonance absorption line. In turn, at $H = \text{const}$ the satellite intensities are proportional to the power P absorbed by the sample. In

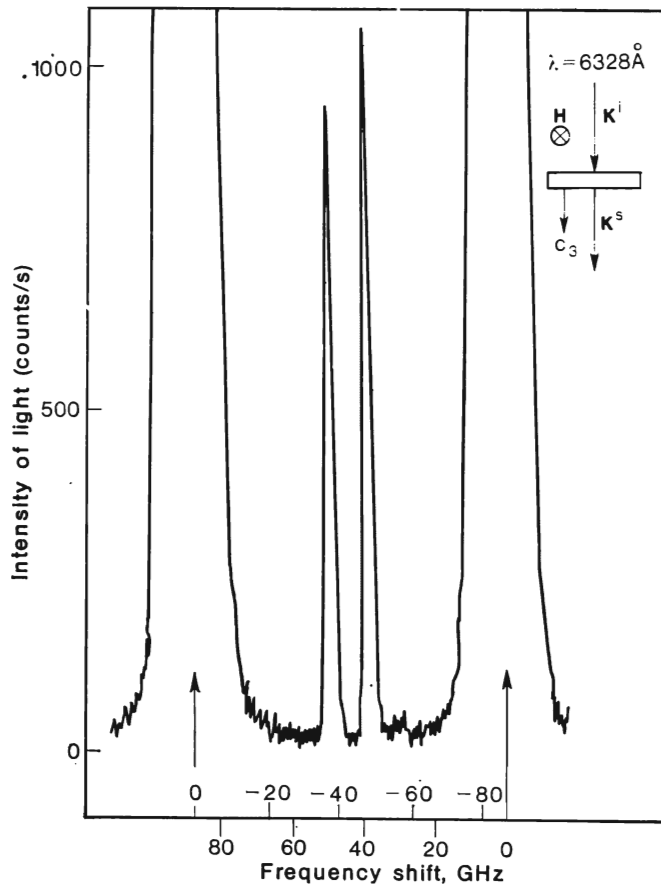


Fig. 6.7. Spectrogram of the light transmitted through the CoCO_3 crystal with uniform spin precession excited [6.46].

maximum of the microwave absorption line, the modulation depth is $10^{-4}\%$ at the supplied microwave power ~ 5 mW. Therefrom we can find out the number of the spin waves with $q = 0$, i.e. $N_0 = 2 \cdot 10^{14} \text{ cm}^{-3}$, as well as the relaxation time [see Eq. (6.22)]

$$\tau_0^* = 3 \cdot 10^{-10} \text{ s.}$$

6.5.3. K_2CuF_4

The compound K_2CuF_4 is a transparent quasi-two-dimensional ferromagnet ($T_c = 6.25$ K). The crystal K_2CuF_4 has a tetragonal symmetry. When in an ordered state, the magnetization vector lies in the plane perpendicular to a fourth order axis. In this crystal light modulation was investigated under the conditions of exciting a ferromagnetic resonance [6.22]. There were investigated two configurations, when light was directed either along the fourth order

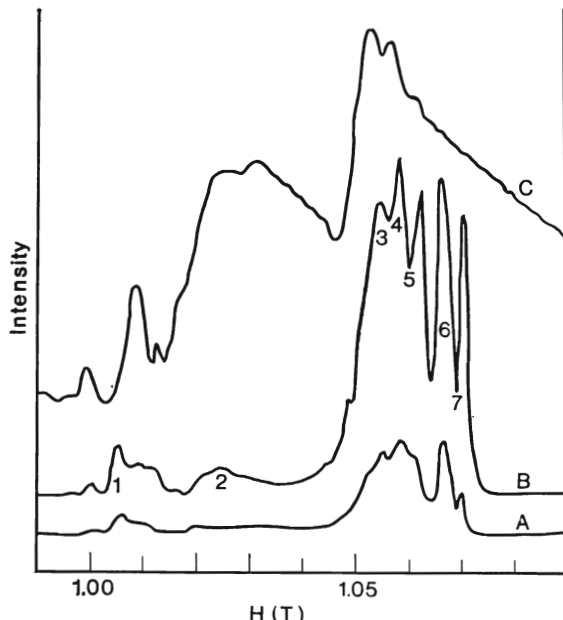


Fig. 6.8. Magnetic field dependence of the intensity of light scattered forward in K_2CuF_4 at the microwave pumping power 50 (A curve) and 150 mW (B curve) with the laser beam diameter 0.1 mm. Absorption microwave line (C curve) is given for comparison [6.22].

C-axis, or perpendicular to the latter, i.e. along the *a*-axis. The light modulation under FMR was detected in both cases. Intensities of the Stokes and anti-Stokes satellites in scattering spectrum had the same magnitude to within experimental error. From independent measurements [6.47] it is known that K_2CuF_4 exhibits a Faraday rotation that is significant, when compared to other magnetooptic effects. As follows from these data and from the fact that the BMS satellites have the same intensities, the light scattering in this crystal is governed by Faraday effect.

In the present crystal, as opposed to CoCO_3 , the shape of the resonance absorption line does not match the observed magnetic field dependence of satellite intensities. In Fig. 6.8 this dependence is presented for different values of the supplied microwave power along with the FMR absorption line. Such a difference in the shape of these functions can be explained by the fact that microwave power is absorbed by the entire sample whereas the focused light beam picks

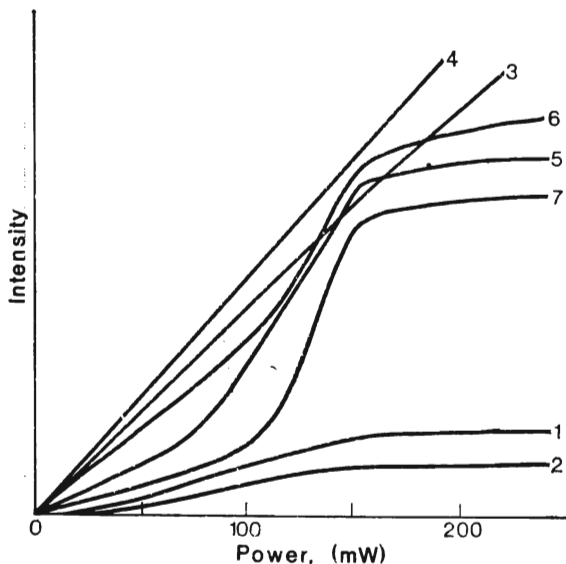


Fig. 6.9. Scattering intensity versus microwave pumping power for different components of the spectrum shown in Fig. 6.8. [6.22].

up information only from a small portion of the crystal. With a broad light beam (of the order of crystal dimension), the difference in shapes between B- and C-curves in Fig. 6.8 was diminished.

Also the dependences of the intensities of the Stokes and anti-Stokes satellites on the supplied microwave power at various magnetic field values corresponding to the maxima in Fig. 6.8 which describe different magnetostatic modes were recorded. The results are depicted in Fig. 6.9. It is possible to indicate three different intensity-power dependences, which the curves 1-2, 3-4, 5-7 (Fig. 6.9) correspond to. According to these types, the different relaxation mechanisms of magnetostatic modes and of homogeneous precession can be proposed. The curves 3-4, for example, could be explained by two-magnon relaxation on crystal defects and impurities. These

processes yield a dominating contribution into the relaxation under FMR. As a result magnons with $q < D^{-1}$ are generated where D is the minimum diameter of a defect. The estimates had shown that only the magnons with $q < 10^3 \text{ cm}^{-1}$ could be registered in this experiment. The curves 5-7 characterize a nonlinearity of FMR. At low microwave powers, the relaxation can be due to processes of fusion with thermal magnons. At high pumping power levels, when thermal magnons are lacking in number, the amplitude of magneto-resistance oscillations start to grow up to its saturation.

6.5.4. RbNiF_3 [6.23]

This crystal, as opposed to the two previous ones, possesses both Faraday rotation and magnetic birefringence which are closely related in magnitude.

As has been noted in Section 1.2, the question of the intensity ratio of the Stokes and anti-Stokes satellites in scattering spectrum was discussed in the number of papers [6.34-35]. The most general results were obtained by Wetling, Cottam, and Sandercock [6.36] in studying the BMS in YIG. The intensities under study were shown to be governed by different combinations of material magnetooptic constants. Generally, when all constants have comparable values, the intensities of satellites are different. If one of the magnetooptic constants is significantly larger than others, the intensities of satellites are the same. As we have seen before, the scattering spectra of CoCO_3 and K_2CuF_4 exhibit the Stokes and anti-Stokes satellites of the same intensity. The point is that in the case of CoCO_3 the dominating factor is the anisotropic magnetic birefringence, whereas in K_2CuF_4 it is the Faraday effect.

By virtue of the above features RbNiF_3 provides the second after YIG object to check the reasons for the difference in intensity between the Stokes and anti-Stokes components.

The crystal RbNiF_3 has a hexagonal symmetry. At $T_C = 139 \text{ K}$ it passes into a ferrimagnetic state. The magnetization vector \mathbf{M}_0 in RbNiF_3 in the absence of an external magnetic field lies in the basal plane perpendicularly to the hexagonal axis C_6 [6.48].

The excitation conditions of ferromagnetic resonance in RbNiF_3 were investigated theoretically and experimentally at $T \geq 77 \text{ K}$ by Golovenchits, Gurevich, and Sanina [6.49]. According to these authors [6.50] the low temperature experimental data can be described in a first approximation by the model of a uniaxial ferromagnet with anisotropy of the "easy-plane" type. The resonance frequencies ν for two directions of magnetic field, $\mathbf{H} \perp C_6$ and $\mathbf{H} \parallel C_6$, are described in the framework of this model by the well-known formulas (see, e.g.

[6.51]):

$$\mathbf{H} \perp C_6; \left(\frac{v^\perp}{\gamma} \right)^2 = [H + H_A + (N_z - N_x) M_s] [H + (N_y - N_z) M_s] \quad (6.23)$$

$$\mathbf{H} \parallel C_6; \left(\frac{v^\parallel}{\gamma} \right)^2 = [H - H_A + (N_x - N_z) M_s] [H - H_A + (N_y - N_z) M_s] \quad (6.24)$$

The formulas (6.23) and (6.24) were derived for an ellipsoidal sample under the assumption that coordinate axes coincide with the principal axes of the ellipsoid. And the axis $z \parallel C_6$, while the x -axis lies in the basal plane and coincides with \mathbf{H} if $\mathbf{H} \perp C_6$; N_x , N_y , N_z are the principal values of the tensor of demagnetization coefficients, M_s is the saturation magnetization and H_A the anisotropy field strength.

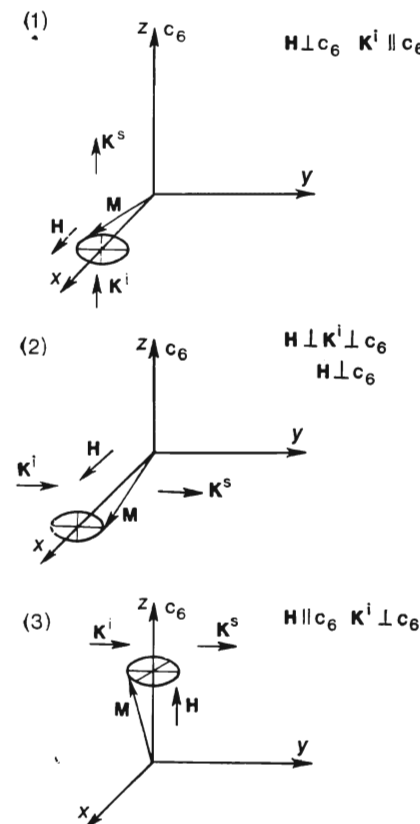


Fig. 6.10. Experimental geometry to observe modulation of light in RbNiF_3 .

light was perpendicular to the C_6 -axis. A modulating light by ferromagnetic resonance in RbNiF_3 was detected for the first and third geometries of the experiment at the incident light wavelengths,

According to these formulas, ferromagnetic resonance in RbNiF_3 at $v \approx 36$ GHz and $\mathbf{H} \perp C_6$ is observed in low fields: $H_{\text{res}} = 4.7$ kOe (low-field resonance), whereas for $\mathbf{H} \parallel C_6$ the field H_{res} is high enough and amounts to 32.8 kOe (high-field resonance).

In order to detect and investigate modulation of light by ferromagnetic resonance in RbNiF_3 , we performed experiments in the three geometries indicated in Fig. 6.10. The geometries (1) and (2) correspond to excitation of the low-field resonance, when $\mathbf{M} \parallel \mathbf{H} \perp C_6$. They are distinguished by the direction of light propagation: $\mathbf{K} \parallel C_6$ in case (1) and $\mathbf{K} \perp C_6$ in case (2). The geometry (3) corresponds to excitation of the high-field resonance (6.24), when $\mathbf{M} \parallel \mathbf{H} \parallel C_6$. Here

$\lambda = 488.0$, 514.5, and 632.8 nm. For the second geometry, the modulation of light was not observed.

The intensity ratio for the Stokes (P_S) and anti-Stokes (P_{AS}) satellites in scattering spectrum depends on geometry and incident light wavelength in the experiment. For $\lambda = 488.0$ nm and 514.5 nm under the first geometry, this ratio, $P_S/P_{AS} = 2.8$; under the third

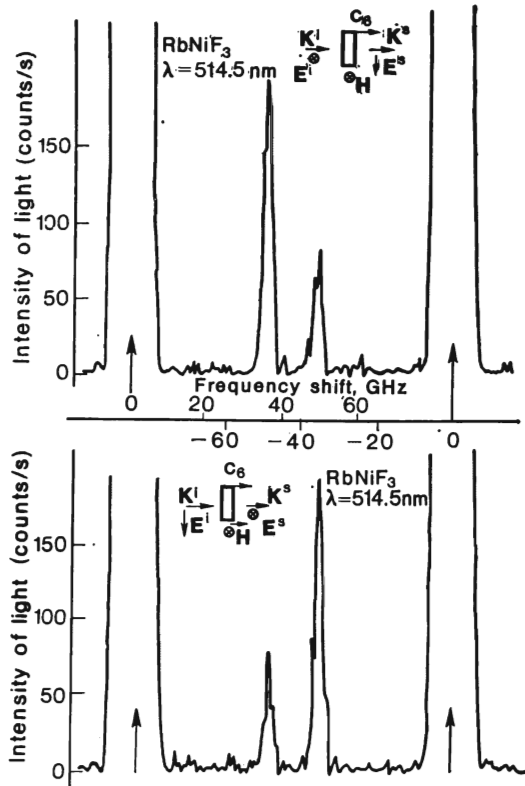


Fig. 6.11. Modulation spectrum in RbNiF_3 for two polarizations of \mathbf{E}^i .

geometry $P_S/P_{AS} \approx 1$. In the case of $\lambda = 632.8$ nm and the first geometry, $P_S/P_{AS} \approx 1.3$. The instrumental error when measuring this ratio is 10%. When rotating the polarization plane of incident light through 90° in all cases the value of the intensity ratio is reversed. Examples of recording the spectra at $\lambda = 514.5$ nm in the first experimental geometry for two polarizations of incident light are given in Fig. 6.11. Satellites in a scattering spectrum are observed in the range of magnetic fields corresponding to a FMR linewidth.

For a given intensity of incident light the field dependence of the intensities of satellites almost copies the shape of the microwave absorption line.

The experimental results indicate that the specific feature of the spectra of light modulated by ferromagnetic resonance in RbNiF_3 is a difference in intensities of the Stokes and anti-Stokes components in these spectra.

Let us consider this problem theoretically. Let us write out $\delta\epsilon_{ij}$, a magnetic part of the permittivity tensor for RbNiF_3 for the first geometry (Fig. 6.10), i.e. when a low-frequency resonance is excited in the sample: $\mathbf{H} \parallel x$ and $M_y = m_y e^{2\pi i v t}$, $M_z = m_z e^{2\pi i v t}$, and $M_x = M_0 = \text{const}$ (v is the FMR frequency and $\mathbf{K} \parallel z$). Here we shall take into account only linear in M_y and M_z contributions into the tensor components, since they are those which are responsible for the appearance in scattering spectrum of the satellites at the frequency $v^i \pm v$, where v^i is the incident light frequency:

$$\delta\epsilon_{ij} = \begin{pmatrix} 0 & if_{123}M_z + g_{66}M_sM_y & if_{321}M_y + g_{44}M_sM_z \\ -if_{123}M_z + g_{66}M_sM_y & 0 & 0 \\ -if_{321}M_y + g_{44}M_sM_z & 0 & 0 \end{pmatrix} \quad (6.25)$$

Here, as in Section 6.2, the coefficients f_{ijk} and g_{ij} describe the contributions into $\delta\epsilon_{ij}$ from Faraday rotation and linear magnetic birefringence, respectively. By means of the obtained $\delta\epsilon_{ij}$, (6.25) values and formulas (6.15), (6.17) one can find the scattered light intensity when the incident light is polarized along the x -axis: i.e. the vector \mathbf{E}^i has the components $(E_0^i \sin 2\pi v t, 0, 0)$. Here the scattered light is polarized along the y -axis. If the intensity of the Stokes satellite is denoted by P_S and that of the anti-Stokes one, by P_{AS} , the calculated results can be presented in the form:

$$\frac{P_S}{P_{AS}} = \left(\frac{f_{123}m_z + g_{66}M_sM_y}{f_{123}m_z - g_{66}M_sM_y} \right)^2 \quad (6.26)$$

When the incident light polarization is rotated through 90° , i.e. when the vector \mathbf{E}^i has the components $(0, E_0^i \sin 2\pi v t, 0)$, the expression (6.26) is replaced by

$$\frac{P_S}{P_{AS}} = \left(\frac{f_{123}m_z - g_{66}M_sM_y}{f_{123}m_z + g_{66}M_sM_y} \right)^2 \quad (6.27)$$

A similar analysis was performed for both the second and third geometries (Fig. 6.10) of the experiment. And in both cases the incident light polarization was supposed to be either parallel to magnetization [upper sign in (6.28) and (6.29)] or perpendicular to it [lower sign in (6.28), (6.29)]. For $\mathbf{K} \parallel y$ and $\mathbf{H} \parallel \mathbf{M} \parallel x$ (the second geo-

metry):

$$\frac{P_S}{P_{AS}} = \left(\frac{f_{321}m_y \pm g_{44}M_s m_z}{f_{321}m_y \mp g_{44}M_s m_z} \right)^2 \quad (6.28)$$

For $\mathbf{K} \parallel y$ and $\mathbf{H} \parallel \mathbf{M} \parallel z$ (the third geometry)

$$\frac{P_S}{P_{AS}} = \left(\frac{f_{321}m_y \pm g_{44}M_s m_x}{f_{321}m_y \mp g_{44}M_s m_x} \right)^2 \quad (6.29)$$

Thus, the calculation demonstrates that generally the intensities of the Stokes and anti-Stokes satellites in a spectrum of scattered light are different, and their ratio is reversed, when the incident light polarization rotates through 90° .

Based on (6.26-6.29) and using our experimental P_S/P_{AS} values for various geometries as well as the values of Faraday effect and magnetic birefringence from [6.52], we have calculated the ratios of coefficients of the tensor $\delta\epsilon_{ij}$ (6.25), namely:

$$f_{123}/g_{66}M_s = 0.75; \quad f_{321}/g_{44}M_s < 2 \cdot 10^{-2} \quad (6.30)$$

These values show the modulation of light for $\lambda = 514.5$ nm in the first geometry is due to both magnetic birefringence and Faraday effect. In the third geometry, modulation of light is predominated by magnetic birefringence.

The P_S/P_{AS} value for $\lambda = 488$ nm coincides with that for $\lambda = 514.5$ nm. When using $\lambda = 632.8$ nm, this ratio changes. RbNiF_3 is known to be characterized by strong absorption of light in red spectral region. As a result, linear and circular dichroism become significant and can change constants in the Faraday effect and magnetic birefringence. All this can lead to variations in the P_S/P_{AS} ratio. However, our experimental data are insufficient to calculate the magnetooptic constants at $\lambda = 632.8$ nm.

6.5.5. $\text{Nd}_3\text{Ga}_5\text{O}_{12}$ [6.24]

Up to now the point in question has concerned a modulation of light in magnetically ordered compounds. Of some interest for us was to observe the modulation of light in a conventional paramagnetic crystal with electron paramagnetic resonance (EPR) excited in it. The neodymium-gallium garnet (NdGG) was chosen as an object that remains to be paramagnet up to $T_N = 0.516$ K and becomes antiferromagnet below this point. This crystal has a large saturation moment ($4\pi M \approx 910$ Gs at $T = 4.2$ K and $\mathbf{H} = 50$ kOe) and a large Faraday effect constant at $T \leq 2$ K. At the temperature of $T = 1.8$ K we determined the Verdet constant, $B = 280$ deg/(cm · kOe).

The modulation of light was studied at the wavelength, $\lambda = 632.8$ nm. EPR was excited at the frequency, $\nu = 36$ GHz. Resonance saturation was not observed because of the broad EPR line width. Incident light propagated along the [111] crystal axis. The

spectrogram of the light transmitted through the NdGG crystal under EPR is given in Fig. 6.12. As in all foregoing cases, this spectrum contains satellites of a significantly lower intensity which are shifted relative the principal line by the resonance frequency, $\pm v_{\text{res}}$. Their intensity is about 10^{-8} of that of the incident light. This implies that the light transmitted through the crystal is modulated at

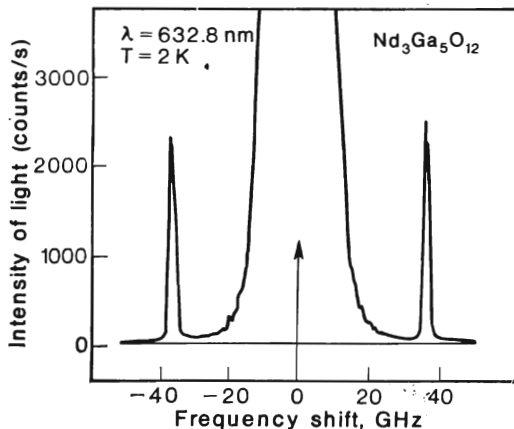


Fig. 6.12. Spectrum of light transmitted through the sample of $\text{Nd}_3\text{Ga}_5\text{O}_{12}$ with a paramagnetic resonance excited in it at the frequency $v_{\text{mw}} = 36 \text{ GHz}$ ($\lambda = 632.8 \text{ nm}$, $T = 2 \text{ K}$).

the frequency $2v_{\text{res}}$ and the modulation depth amounts to 5×10^{-8} . The modulation of light was observed within the entire microwave absorption line. The intensity of each satellite is proportional to the microwave absorption value under constant power input. As can be seen from Fig. 6.12, the intensities of the Stokes and anti-Stokes satellites in the scattering spectrum are the same. This suggests the scattering at $\lambda = 632.8 \text{ nm}$ to be controlled by a magnetooptic effect alone, i.e. the Faraday rotation.

The modulation depth enables determining the spin tilting angle under resonance conditions. Therefore, given the microwave power input, the transverse relaxation time can be found. We made such estimates and obtained the value of 10^{-11} s which agrees with the broad EPR line width.

6.6. MAGNON “BOTTLE-NECK” UNDER AFMR AND FMR

Let us consider relaxation processes in a spin system with FMR or AFMR excited. Here the microwave field directly excites uniform spin oscillations or, which is the same, spin waves with

$q = 0$. The energy of spins excited in resonance is transferred to other spin excitations, i.e. to the magnons with $q \neq 0$, via two-magnon, three-magnon, etc. processes with the relaxation times τ_0^1 (see the diagram in Fig. 6.13). Also possible is a process of the energy transfer from the spin waves with $q = 0$ directly to phonons with the relaxation time τ_0'' . Naturally, the relaxation is dominated by the process with the shortest time, τ_0^* . The transfer time of energy of uniform oscillations to phonons usually exceeds that to magnons. The

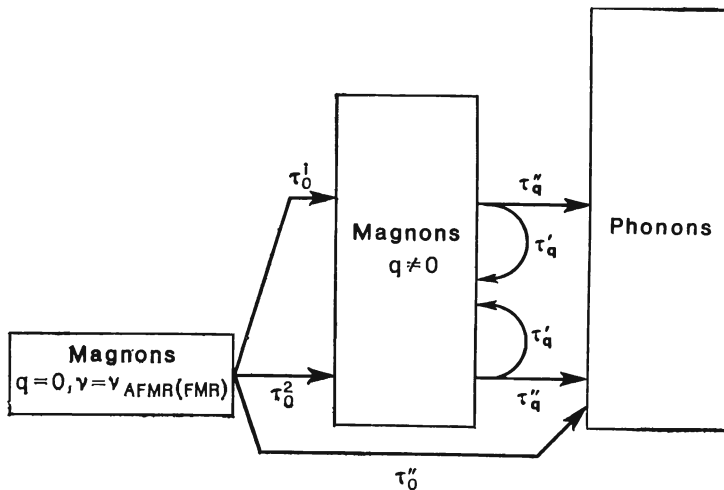


Fig. 6.13. Diagram of explaining magnon relaxation processes in magnetic materials.

magnons caused by relaxation which have particular energies and wave vectors relax either to a reservoir of the remaining spin waves with the time τ_q' or to a reservoir of phonons (to the lattice) with the relaxation time τ_q'' . Provided τ_q'' is much longer than τ_q' , an excess in the number of magnons over the thermal level corresponding to the lattice temperature occurs in the system of spin waves. The ratio of the total number N_q of the excess spin waves in the system to the number N_0 of the pumped spin waves with $q = 0$ will be governed by the ratio τ_q''/τ_0^* of the relaxation times. Once $\tau_0^* \sim \tau_q'$, the entire spin system will be overheated. If $\tau_0^* \ll \tau_q'$, then an isolated group of magnons with a particular v and q will be overheated. Such a situation is similar to the phenomenon in EPR called a phonon "bottle-neck" with the difference that magnons rather than phonons are overheated. The magnon "bottle-neck" was discovered by us in the antiferromagnetic crystal of CoCO_3 . A set of three runs were performed to study this phenomenon.

The first one, namely, the modulation of light under AFMR, has been discussed in the preceding Section. From this experiment we have determined the number $N_0 = 2 \times 10^{14} \text{ cm}^{-3}$ of spin waves with $q = 0$ excited by microwave power 5 mw and the relaxation time, $\tau_0^* = 3 \times 10^{-10} \text{ s}$.

In the next experiment the number N_q of the magnons with $q \neq 0$ excited under AFMR was determined [6.21]. An increase in the num-

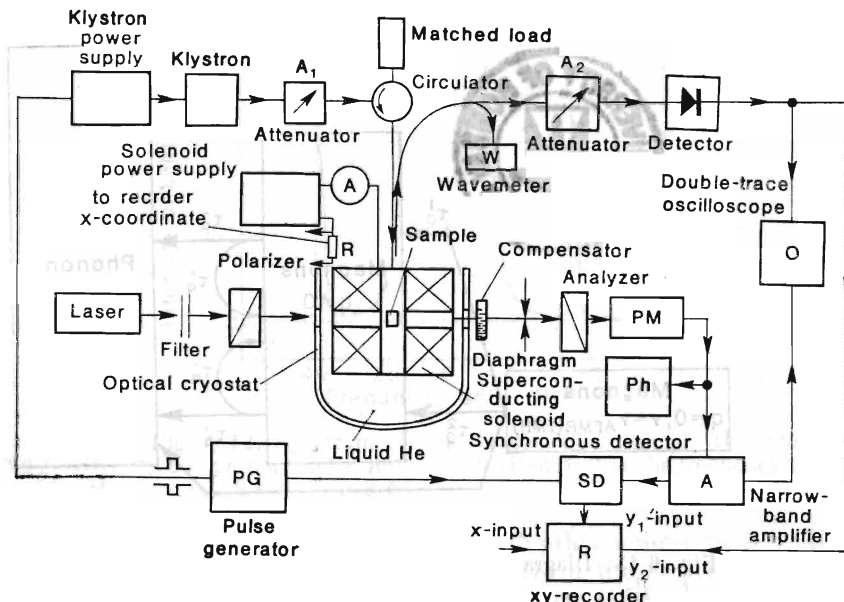


Fig. 6.14. Diagram of the experimental setup for optical observations of AFMR.

ber of spin waves results in a decrease in magnetization of sublattices of the sample under study. Since magnetic birefringence is proportional to the squared magnetization of the sublattices [see (6.8)], a decrease in magnetization is accompanied by a decrease in birefringence. Consequently, by measuring a change in birefringence under AFMR, it is possible to find out N_q .

A change in magnetic birefringence of light in a crystal was investigated when scanning the AFMR line by magnetic field. A diagram of the experimental setup is given in Fig. 6.14. The microwave part of the setup is similar to the previous one. However, in order to amplify optical signals, we used the modulation of microwave power by rectangular pulses with a repetition frequency from 1 to 20 kHz and a duty factor of 0.5.

The optical scheme to measure the light birefringence in a crystal, Δn , will be described here in more detail. A light beam ($\lambda = 632.8$ nm) from the He-Ne-laser passed through the system which consisted of a polarizer, a crystal to be investigated, a calcite Berek compensator and analyzer, and was incident on the photomultiplier PM. The output signal of the photomultiplier (the voltage drop across a photomultiplier load) could contain both a direct-current (dc) component due to incomplete compensation of light and an alternating-current (ac) component changing with the modulation frequency of klystron power. The dc component of the signal was measured by means of the digital voltammeter VA. The ac component of the light signal was amplified by the narrow-band amplifier U tuned for the klystron modulation frequency and then was applied either across the oscilloscope output \bar{O} or the recorder y_1 -coordinate unit via a synchronous detector. Thus, setup optical scheme permitted changes in the birefringence Δn to be measured both in a static and in a dynamic mode of operation. In the first case we used the method of direct compensation of path-length difference (by means of the Berek compensator) and in the second case the amplitude of the ac signal (at the instant a resonance occurs). The sensitivity to variations in Δn for the dc mode was from 10^{-5} to 10^{-6} and that for the ac mode was substantially higher i.e. from 10^{-8} to 10^{-9} (depending on sample thickness).

The main experimental results were obtained with a sample in the form of a thin disk 1.2 mm in diameter and 0.3 mm thick. The disk plane coincided with the crystal basal plane. The sample had the most narrow resonance line about 30 Oe (Fig. 6.15).

There were studied two cases: when the incident light polarization was coincident with the magnetic field direction and when the former was inclined at the angle of 45° to the latter. In both cases the polarizer and analyzer were crossed. In the first case, the ac optical signal was not detected down to the level of 5×10^{-6} of the incident light intensity. In the second case, the ac optical signal was absent under the conditions of a maximum compensation of the dc optical signal by means of a compensator at the instant the resonance occurs. This signal appeared however, at a certain incomplete compensation of the system due to a rotation of the compensator. Figure 6.15 shows records of both the ac light I_{\sim} at different compensator positions and microwave absorption signals when the AFMR line was scanned by magnetic field.

The optical signal shape is easily seen to fully match the curve of microwave absorption.

The amplitude and phase of the ac signal, I_{\sim} , vary with the path-length difference Γ for two orthogonal light polarizations in the sample and compensator (measured in radians). The phase of the ac light signal is scaled relative to the modulation phase of microwave

power by rectangular pulses. Figure 6.16 demonstrates relationships between the dc I_{\perp} (curve 2) and ac I_{\perp} (curve 1) (for the AFMR line peak) light signals and the path-length difference Γ , changed by means of the compensator. In fact, the figure depicts a variation in

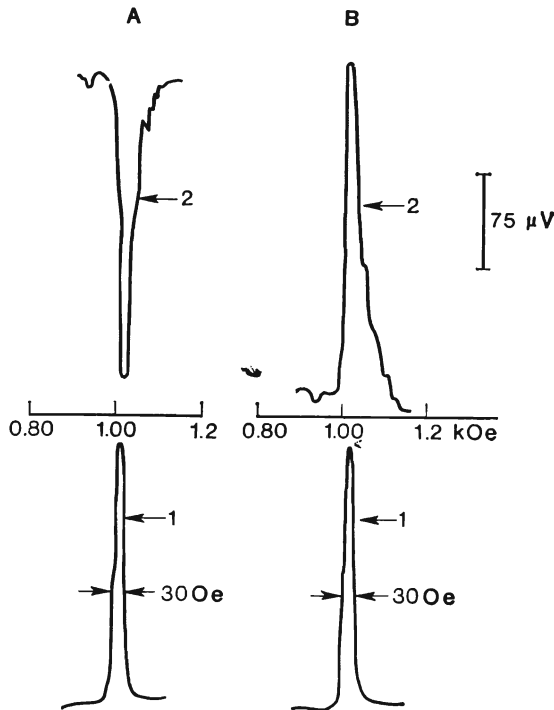


Fig. 6.15. An example of recording a microwave absorption line (curves 1) and alternating light signal (curves 2) under resonance in CoCO_3 at two path-length differences Γ : (A) $\Gamma = \pi/6$, (B) $\Gamma = 7\pi/6$.

the path-length difference, $\Gamma = 2\pi n$, measured from the value of Γ which corresponds to the minimum dc signal.

The experimental dependences obtained can be described by the relationships:

$$I_{\perp} = I_{\perp}^0 \sin(\Gamma/2) \quad \text{for curve 2} \quad (6.31)$$

$$I_{\perp} = I_{\perp}^0 \sin(\Gamma) \quad \text{for curve 1} \quad (6.32)$$

(The first formula agrees with the dependence of the transmitted light intensity on the compensator position in crossed polaroids de-

rived, e.g. in [6.53].) It can be seen from Fig. 6.16 that maxima in the amplitude I_{\sim} correspond to $\Gamma = 2\pi n + \frac{\pi}{2}$ or $2\pi n + \frac{3\pi}{2}$ and amount to 2×10^{-4} of the dc signal amplitude, I_{\perp}^0 . When a compensation or decompensation of light is complete, the ac light signal is absent. All results above were obtained by us at a modulation frequency of microwave power equal to 1 kHz. An increase in this frequency up to 20 kHz influenced the acquired data neither qualitatively nor quantitatively.

As can be seen from the above results, the conditions for observing the ac optical signal differ from those of modulation of light.

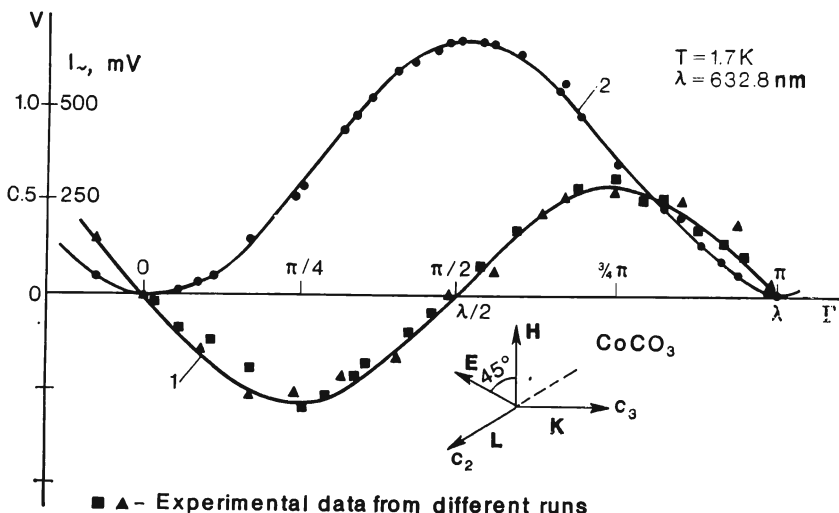


Fig. 6.16. Intensities of the dc I_{\perp} (curve 2) and ac I_{\sim} (curve 1) light signals versus the path-length difference Γ due to compensator and sample.

The modulation depth was maximized when incident light was of vertical polarization directed along the applied magnetic field, with a maximum compensation of the transmitted light. For these conditions, the ac optical signal I_{\sim} was totally absent. A large difference in values of the two observed effects should also be marked. Their intensities measured by the same absorbed microwave power are equal to $\frac{I_{\omega} \pm \Omega}{I_{\omega}} \simeq 5 \cdot 10^{-8}$ (the light modulation) and to $\frac{I_{0\sim}}{I_{0\perp}} \simeq \simeq 2.5 \cdot 10^{-4}$ (the optically detected AFMR). As seen they differ by a factor 10^4 . The performed comparison shows the detected ac optical signal under AFMR to be unconnected with uniform oscillations of magnetization. This can be explained if it is remembered that at the instant of resonance the magnetic birefringence of the entire sample

is decreased. Such a decrease is due to diminishing an L -component which is a perpendicular to magnetic field, when L oscillates about the equilibrium position. In turn, a decrease in the L -component is due to a growth in the total number of the spin waves which are excited under AFMR. According to the experimental data this number $N_q = 10^{17} \text{ cm}^{-3}$ (at $P = 5 \text{ mW}$) which corresponds to a relaxation time, $\tau_q = 1.5 \times 10^{-7} \text{ s}$.

Let us compare the results of two optical experiments for the number of spin waves excited under AFMR:

$$\frac{N_{q=0}}{N_q} = \frac{2 \times 10^{14}}{10^{17}} \sim 10^{-3}$$

This means that the total number of the spin waves created in a system under AFMR relaxation is about 1000 times more than the number of the spin waves with $q = 0$ corresponding to a uniform precession. In other words, an accumulation of energy in the spin system occurs at the instant of resonance, i.e. the spin system is overheated as compared to its equilibrium state.

Now we have been interested to find frequencies and wave vectors of the magnons due to relaxation. With this aim in mind we used the BMS technique. A sample was chosen where thermal spin waves were studied. The setup described above was used. The BMS was observed in the 90°-scattering geometry ($q = 2.5 \times 10^5 \text{ cm}^{-1}$). The magnons propagating along the x -axis (x -magnons) and z -axis (z -magnons) were studied. AFMR was excited at two pumping frequencies, $v_1 \approx 36 \text{ GHz}$ and $v_2 \approx 51 \text{ GHz}$. The sample was inserted into a waveguide and practically the whole spectrum of magnetostatic modes was excited because of large dimensions of the sample. This manifested itself in the AFMR line width of 600 Oe (instead of 30 Oe for thin samples). According to [6.42-43] this value corresponds to the limits of the spectrum of magneto-static modes. The experiments were performed at $T \leq 2 \text{ K}$. The same polarization conditions were fulfilled as in the case of thermal magnons observation.

The scattered light spectrum was experimentally investigated under AFMR excitation. For microwave power input at the frequency $v = v_{\text{AFMR}}$ a significant increase in the intensities of magnon peaks as compared to the thermal ones was found. Magnon amplification persists over a very narrow range of magnetic fields $\pm 25 \text{ Oe}$, although as has been indicated above the microwave absorption line width under AFMR is about 600 Oe. The frequency of the amplified magnons always coincides with that of AFMR. Figure 6.17 shows the spectrogram of light scattered from z -magnons for a microwave power input of about 5 mW in a field $H = 1014 \text{ Oe}$. Here the intensity of magnon peaks was augmented as compared to the thermal ones about 20 times. Increasing the pumped microwave power P results in building up the intensity of the amplified peaks I .

Judging by the result obtained, the predominating relaxation process of uniform precession is a two-magnon process, in which a magnon with the frequency ν_{AFMR} and $q = 0$, after scattering from an impurity or crystal defect, creates a magnon with the same frequency and non-zero wave vector.

In order to elucidate this situation, let us consider Fig. 6.18. The long-wave part of the CoCO_3 magnon spectrum is shown here and

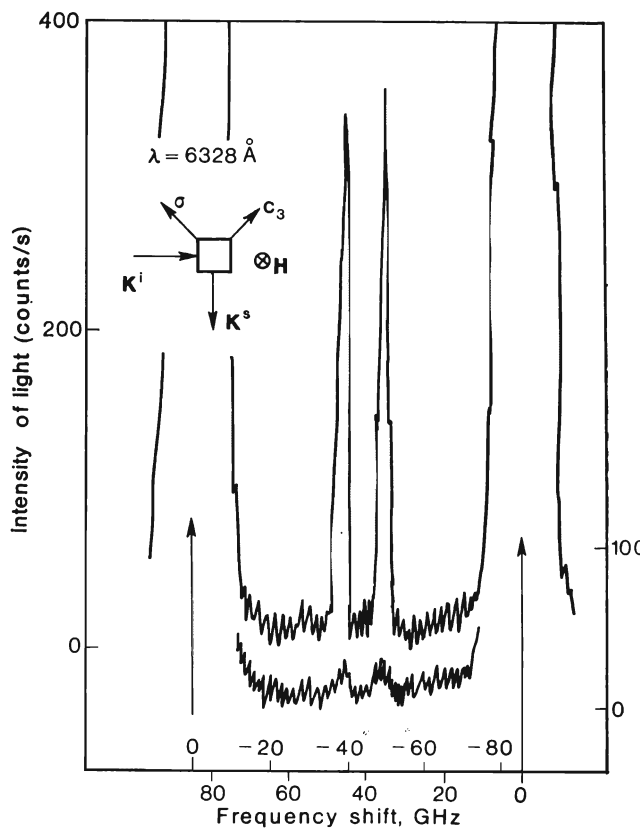


Fig. 6.17. Light scattering spectrum at 90° in CoCO_3 from thermal (lower curve) and excited under AFMR (upper curve) magnons.

ν_{MW} is the frequency of a microwave photon exciting AFMR. The latter has the form of the uniform precession with $q = 0$ as well as one of the magneto-static modes with q near zero. Every point in the region between the curves q_z and q_y corresponds to the magnon with a definite \mathbf{q} and ν . The curve q_z corresponds to $\mathbf{q} \parallel z$ and q_y to

$\mathbf{q} \parallel \mathbf{y}$. Upon changing magnetic field, this region shifts along the vertical axis (frequency axis).

Let us consider the case of z -magnons. In our experiment the strength of the magnetic field was selected to be such that the z -magnons with a frequency equal to the microwave one had a wave vector with modulus $q = 2.5 \cdot 10^5 \text{ cm}^{-1}$. Upon pumping the microwave power, the number of such magnons proved to be significantly larger

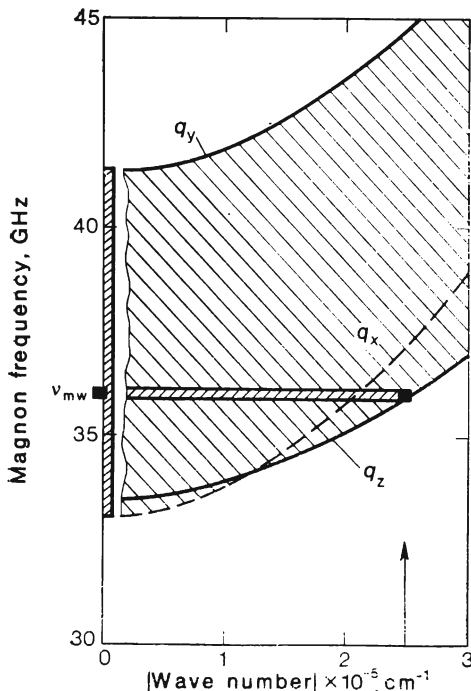


Fig. 6.18. Long-wave part of the spin wave spectrum in CoCO_3 for different directions \mathbf{q} and the magnons created under AFMR relaxation in a two-magnon process (horizontal dashed region).

than that of the thermal ones. Therefore we conclude that the excited AFMR magnons with $q = 0$ (or close to zero) and the frequency ν_{AFMR} relax mainly into the magnons with the same frequency and non-zero wave vector. These magnons are located in the horizontal dashed region in Fig. 6.18. The same considerations are also valid, when observing x -magnons.

The results of the first two experiments demonstrate that during relaxation of the magnons with $q \approx 0$ excited under AFMR, the reservoir of the spin waves with $q \neq 0$ accumulates magnons which

means it becomes overheated compared to the equilibrium state. This is due to the fact that the time of energy transfer from the group of the magnons with $v = v_{AFMR}$ and $q \neq 0$ to other magnons or phonons (Fig. 6.13) is much greater than the time τ_0^2 needed for magnons with $q \approx 0$ to relax. The phenomenon observed here is similar to that called the "bottle-neck" in EPR. The only difference is that in an antiferromagnet magnons are overheated rather than phonons.

The last optical experiment provided the answer to whether the entire system is overheated uniformly (due to a short τ_q') or the overheating concerns only a selected group of spin waves. The results show that only a group of magnons with a frequency of the exciting AFMR and different wave vectors that are controlled by the magnon spectrum for this frequency is overheated. Thus, in antiferromagnets we observed a classical "bottle-neck".

The similar experiments were performed with a two-dimensional ferromagnet K_2CuF_4 . In addition to modulation of light, the back-scattering due to the excitation of a ferromagnetic resonance was also investigated in this substance. The amplification of magnon peaks was observed similar to that found by us in $CoCO_3$.

6.7. LIGHT SCATTERING FROM PARAMETRICALLY EXCITED QUASIPARTICLES (MAGNONS AND PHONONS) IN $CoCO_3$

The BMS technique proved to be very efficient in detecting and studying parametrically excited quasiparticles, i.e. magnons and phonons [6.16, 6.54, 6.55].

Various nonlinear phenomena are known to occur in magnetically ordered substances placed inside intense high-frequency fields. The nonlinear phenomena, which will be discussed below, include processes of parametrically excited oscillations and premature saturation of resonance. Common to both processes is the presence of a certain threshold microwave field, $h_{mw} = h_{th}$, above which these processes do occur. Both processes take place in an external magnetic field, H .

A paramagnetic excitation of quasiparticles is such a process, when one high-frequency photon with $v_{mw} = v_p$ at $h_{mw} \geq h_{th}$ and a certain value of magnetic field (determined by the wave vector of quasiparticles) creates two quasiparticles with opposite values of the wave vector, q , and with the half-frequency of the photon, $v_{qp} = v_p/2$. In this process there can be created parametrically both magnons and phonons. This depends on the shape of the spectrum of quasiparticles in the given magnetic substance as well as on the value of magneto-elastic interaction and on the pumping frequency, v_p .

Another process takes place here, when a magnetic resonance (MR) or uniform precession is excited in a substance, i.e. when a microwave photon ν_{MR} creates a magnon with $q = 0$ and $\nu = \nu_{\text{MR}}$. Upon attaining a certain power level, the resonance comes to saturation (premature saturation of resonance). In the process the magnons with $q = 0$ and $\nu = \nu_{\text{MR}}$ are able to decay into two quasiparticles with $\nu_{\text{qp}} = \nu_{\text{MR}}/2$ and $\mathbf{q}_1 = -\mathbf{q}_2 \neq 0$. In the event that the magnon is the quasiparticle, the process is called the first order Suhl instability. As will be shown in the present Section, a quasiparticle with the frequency $\nu_{\text{qp}} = \nu_{\text{MR}}/2$ is liable to be a phonon, as well. The probability of realizing one or another version is governed, as in the case of parametric excitation of quasiparticles, by the kind of spectrum, value of magneto-elastic interaction, and ν_{MR} .

The investigation of nonlinear phenomena allows rich information to be obtained on the properties of magnetic materials. It opens up the possibilities to study relaxation channels of quasiparticles and relaxation times and to determine the spatial distribution of quasiparticles and the parameters of their spectrum. An important problem is the study of a stationary state of spin waves which is established at a high pumping power level, much higher than the threshold one.

Microwave techniques pertain to the commonly used methods of studying the nonlinear processes, when investigating a dependence of the absorbed microwave power on the power input, pumping frequency and magnetic field strength. These techniques provide many interesting experimental results in studying both ferromagnets and antiferromagnets. In addition, the theory of nonlinear processes was developed. The studies of the parametrically excited spin waves in magnetically ordered substances are reviewed in [6.56-57].

However, the microwave techniques available cannot supply all needed information about the processes. These techniques fail to clear up the question what quasiparticles (phonons or magnons) are excited in experiment, what direction they propagate in, and what wave vector \mathbf{q} correspond to. This is why a demand arose for investigating nonlinear processes by other techniques.

Next, the results will be described of studying parametrically excited magnons and phonons in CoCO_3 by means of the BMS technique. All the experiments were performed in the 90° -scattering geometry, as was the case with thermal magnons. The notations of Sec. 6.4 will be used. The samples were placed at the endface of a plunger which shortcircuits a waveguide.

6.7.1. Parametrical Magnons in CoCO_3

Next, the spectra of scattering from z -particles at the pumping frequencies $\nu_p = \nu_1 \sim 36$ GHz and $\nu_p = \nu_2 = 51.02$ GHz

as well as from x -particles at $v_p = v_s$ will be discussed. The results reveal that in the magnetic field corresponding (in accordance with the kind of magnon spectrum) to the existence of the magnons with $v = v_p/2$ at $q = 2.5 \cdot 10^5 \text{ cm}^{-1}$ the pronounced peaks of the frequency which differs from that of incident light by $\Delta v = v_p/2$ show on the spectrum of scattered light when the pumping power is switched on with $v = v_p$. In the absence of microwave pumping and with the same magnetic field strength the peaks of much lower intensity due to the thermal magnons with $v = v_p/2$ are evident. The intensity of scattering is governed by the number of scattering particles. It follows that an increase in the intensity of peaks caused by the microwave pumping will favour a large number of quasiparticles with $v = v_p/2$ and $q = 2.5 \cdot 10^5 \text{ cm}^{-1}$ being created at the given magnetic field strength. An illustration of this result is presented in Fig. 6.19 for z -particles.

In this figure curve 1 corresponds to a spectrum of scattering from the thermal magnons with $v = 25.5 \text{ GHz}$. Curve 2 with pronounced peaks corresponds to a scattering from the excited quasiparticles created by switching on the microwave power with $v_p = 51.02 \text{ GHz}$ at the same magnetic field strength.

When observing the process of scattering from the created quasiparticles the following polarization conditions always have to be satisfied: (a) $\mathbf{E}^i \perp \mathbf{E}^s$, where \mathbf{E}^i and \mathbf{E}^s are the electric field vectors of the incident and scattered light waves, respectively; (b) one of the vectors \mathbf{E}^i and \mathbf{E}^s lies in the scattering plane and another is perpendicular to it. In our experiment the vector \mathbf{E}^i was always parallel to the external magnetic field. Studying the influence of magnetic field strength on the position and intensity of the satellites, given test values of wave vector and pumping frequency, points to the existence domain of excited quasiparticles from ± 10 to $\pm 15 \text{ Oe}$ in magnetic field strength. Within this field range the frequency of the satellite differs from that of incident light by exactly half the pumping frequency to an accuracy of $\pm 0.5 \text{ GHz}$. The satellite intensity for x -particles versus magnetic field strength is depicted in Fig. 6.20.

Next, we investigated the influence of the microwave pumping power with $v = v_p$ on the intensity I of satellites with $\Delta v = v_p/2$ at a constant magnetic field level. Such a relation was found to have a threshold pattern. In other words, an increase in the intensity of satellites starts from a certain finite value of pumping power. Figure 6.21 demonstrates the correlation between the intensity of the satellites with $\Delta v = v_p/2$ and pumping power in a constant magnetic field for x -particles. The curve in Fig. 6.21 illustrates a threshold in this dependence. The experimental data obtained allowed us to determine the threshold values of power P_{th} and corresponding magnetic component h_{th} of the microwave field such that the

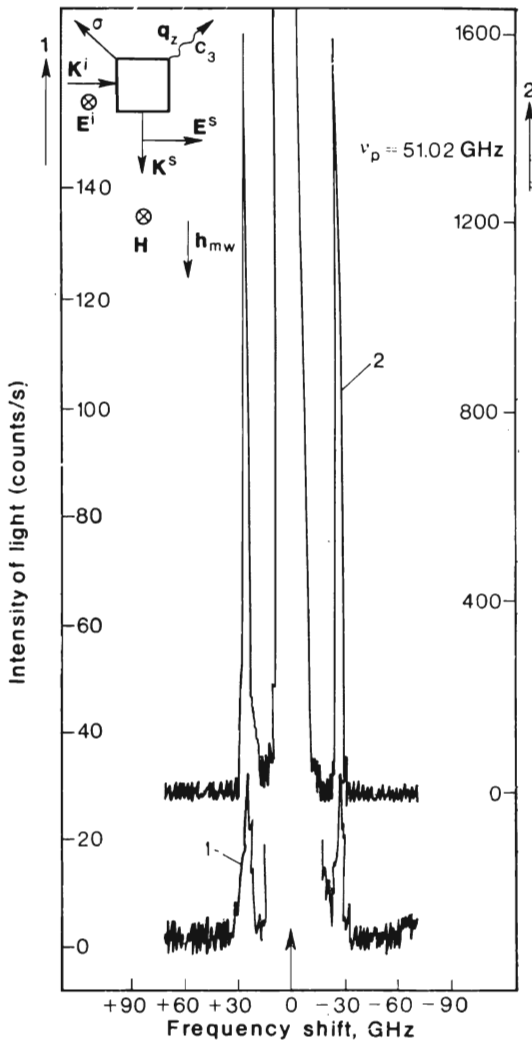


Fig. 6.19. Spectrum of light ($\lambda = 632.8$ nm) scattered at 90° in CoCO_3 ($T \leq 2$ K) from z -magnons: (1)—thermal magnons, (2)—parametrical magnons. The accumulation time of spectrum (1) amounts to 2000 s and that of (2) to 1000 s.

parametric excitation of quasiparticles sets in. These values are given in the Table 6.1.

The threshold values P_{th} and h_{th} given in Table 6.1 are in the range of estimates, since the accuracy of the applied microwave pow-

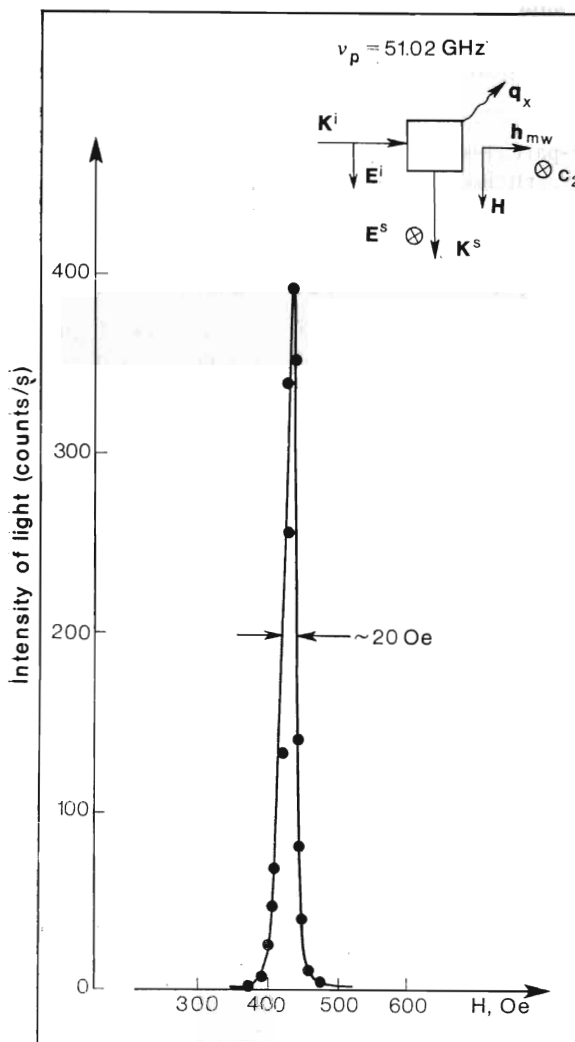


Fig. 6.20. Intensity of light scattered from parametric x -magnons versus the external magnetic field strength H in CoCO_3 ($T \leq 2 \text{ K}$).

er measurement was not so high in our experiments. The excess in the pumping power over the threshold value results initially in a linear growth of satellite intensity (see Fig. 6.21) and then the curve $I(\bar{P})$ is saturated and falls down. A deviation of $I(\bar{P})$ from the linear relationship for z -particles occurs at the pumping powers about

Table 6.1.

Quasiparticles	v_p , GHz	P_{th} , mW	h_{th} , Oe
z-particles	36.0	30.0	0.030
	51.2	60.0	0.045
x-particles	51.2	80.0	0.053

300 mW (or about 0.1 Oe) while for x -particles at about 100 mW (or about 0.06 Oe). The creation of excited quasiparticles should be, apparently, accompanied by the microwave power absorption in a

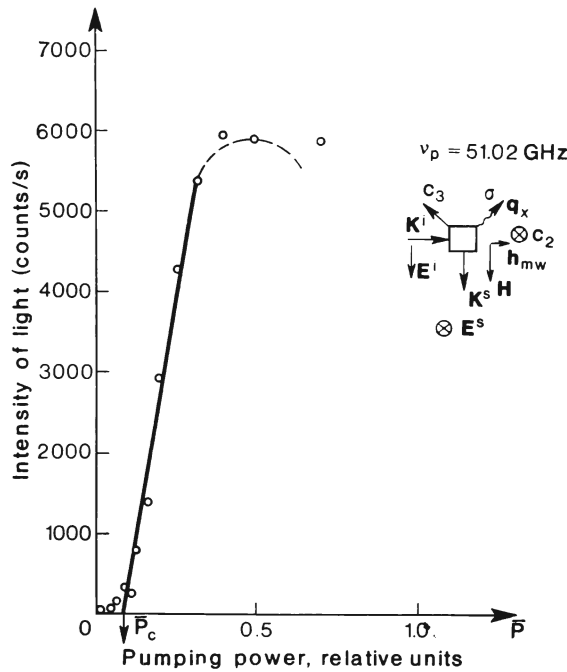


Fig. 6.21. Intensity of light scattered from parametric x -magnons versus the microwave power \bar{P} in CoCO_3 ($T \leq 2$ K).

certain range of magnetic field strengths. In our experiments, however, such an absorption was not found. The value of the absorbed power was likely to be too low while our technique used to detect the absorption of the power too rough.

The data obtained indicate that a number of quasiparticles in excess of the thermal level was created in a crystal under the action of microwave power. The creation of quasiparticles proceeds in a parametric way, since their frequency amounts to half-frequency of the pumping and the process of their excitation is of a threshold nature. The parametric x - and z -magnons are expected to be dealt with in this case. These result from the decay of one microwave photon

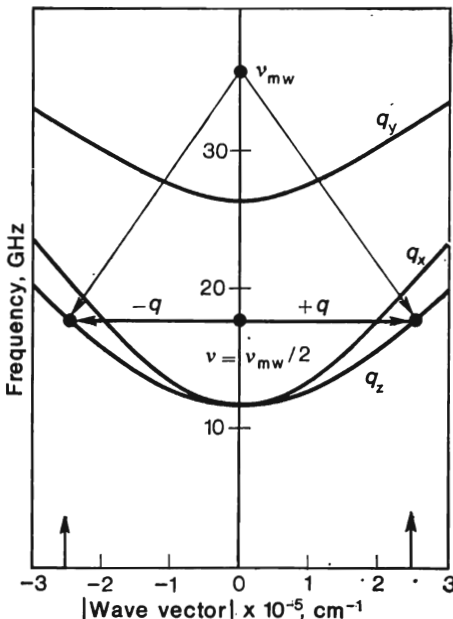


Fig. 6.22. Scheme for illustrating the parametric excitation of z -magnons with half-frequency of pumping in CoCO_3 at $v_p \approx 36$ GHz.

with $v = v_p$ into two magnons with opposite wave vectors and the microwave photon half-frequency $v = v_p/2$. The basis for such an assumption is formed by experimentally controlled conditions of observing the light scattering from these quasiparticles as well as by the fact that in the absence of microwave power and in the same magnetic field the thermal magnons with a frequency equal to $v_p/2$ can be observed (see Fig. 6.19). The parametrically excited quasiparticles are observed within a narrow range of magnetic field strength (see Fig. 6.20). This fact can be explained in more detail by means of Fig. 6.22. The latter shows the low-frequency part of the spectrum $v(q)$ for x -, y -, and z -magnons according to Sec. 6.4 at fixed magnetic field strength. In addition, this figure schematically shows the

process of decay of one microwave photon with $v = v_{\text{mw}}$ into two z -magnons with $v = v_{\text{mw}}/2$. The scheme indicates that at each value of the magnetic field strength in the given crystalline direction the magnons are created that possess fixed values of wave vectors. As discussed above the value of wave vector and direction of quasiparticle propagation as well as the frequency of exciting photon are preset by experimental conditions in our case. Only the magnetic field strength whose value can be varied arbitrarily serves as a free parameter. In so doing, the magnon spectrum has to be displaced within the (v, q) plane along the abscissa (v). In order to observe the light scattering from parametric magnons we have to select a value of magnetic field strength such that the frequency of the magnon investigated (x - or z -ones) with $q = 2.5 \times 10^5 \text{ cm}^{-1}$ amounts to half-frequency of the pumping as shown in Fig. 6.22 for a z -magnon. The scheme shows how a deviation from this field strength should result in violating the observation conditions. According to the theory the region that satisfies the conditions should correspond to a very narrow interval of magnetic field strengths. In experiment this interval ranges from 10 to 20 Oe (see Fig. 6.20). The value corresponds to the width of a really observed scattering line, which in addition to the true width is contributed by the response function of interferometer, line width of laser radiation, etc.

The parametric excitation of magnons in CoCO_3 was discovered in our experiments. The parametric magnons were directly observed which propagated along the C_3 -axis and across the basal plane of a crystal in the magnetic field direction. Their frequency was proven to be really equal to half-frequency of the pumping.

As to the y -particles propagating in basal plane transversally to magnetic field, pumping microwave sources should be used with wavelengths shorter than those of the sources we have to detect the parametric y -magnons in CoCO_3 .

Based on our experiments, it is believed that at a sufficiently high microwave power level parametric magnons are created in all directions.

As seen from Fig. 6.19, the intensities of the Stokes and anti-Stokes spectral components due to parametric magnons are practically the same. Since the experimental geometry in all runs was the same, the Stokes spectral component always corresponded to a scattering from the particles with one direction of the wave vector q whereas the anti-Stokes component—with an opposite direction. With this experimental fact in mind we can conclude that the same number of magnons with opposite wave vectors exists in the above-threshold state. This conclusion agrees with a conventional scheme of parametric excitation of magnons.

As has been mentioned above, we determined the threshold fields such that the parametric excitation of magnons occurs. And for x -

and z -magnons these values differ by 1.5 times (see Table 6.1), while z -magnons possess a lower threshold.

The dependence of the threshold microwave field strength h_{th} on the pumping frequency v_p , on the damping of magnons Δv_q , and other parameters was obtained theoretically by Ozhogin [6.58] for antiferromagnets of the "easy-plane" type under the conditions of parallel pumping, when $\mathbf{h}_{mw} \parallel \mathbf{H}$. This dependence has the following form:

$$h_{th} = \frac{v_p \Delta v_q}{\gamma^2 (2H_0 + H_D)} \quad (6.33)$$

where H_D is Dzyloshinskii's field, H_0 the field in which parametric magnons are observed, and γ the gyromagnetic ratio. For CoCO_3 we have $H_D = 27$ kOe and $\gamma = 5.8$ GHz/kOe.

In our experiments the parallel pumping conditions can be satisfied only when exciting x -magnons. If the parametric x -magnons are assumed to be created as a result of parallel pumping, then we can estimate the relaxation time of x -magnons in $\text{CoCO}_3 \tau = (2\pi \Delta v_q)^{-1}$ by means of formula (6.33) and the experimental threshold value (see Table 6.1). The estimate yields $\Delta v_q \simeq 0.7$ MHz and $\tau \simeq 0.2$ μ s. The magnon relaxation time in CoCO_3 agrees, by an order of magnitude, with those measured for MnCO_3 and CsMnF_3 [6.59-60]. It should be noted, however, that for the above compounds the magnon relaxation time strongly depends on the temperature. We did not study such a dependence for CoCO_3 . All our experiments were performed at a single temperature of about 1.8 or 1.9 K.

In our experiments parametric z -magnons are excited under the conditions of transverse pumping. Presently we know no formula to describe the relationship between the threshold field and relaxation time for the case under study. Therefore, the only conclusion that can be made is that the value of the threshold field is proportional to pumping frequency (see Table 6.1).

The comparison of the intensities of satellites in light scattering spectrum that correspond to thermal and parametric magnons enables us to determine the excess value F of the number of parametric magnons over the thermal level. Such an estimate is valid, if the observed width of a scattering peak coincides with the intrinsic line width Δv_q of a parametric magnon. However, as the above estimates have demonstrated, Δv_q amounts to 0.7 MHz. It is by a factor of 10^3 less than the width of an observed scattering line whose instrumental width is about 0.5 GHz. This means that the value obtained from the ratio of intensities should be multiplied by 10^3 to evaluate an excess of the number of parametric magnons over the thermal level. With this result in mind, we obtained as a maximum excess $F \simeq 6 \times 10^5$ in the following range of changing q determined

by the line width $\Delta\nu \simeq 0.7$ MHz:

$$\Delta q = \frac{1}{2} \frac{\partial q}{\partial \nu_q} \Delta \nu_q \simeq 20 \text{ cm}^{-1} \quad (6.34)$$

The estimate is valid for x -magnons. In the case of z -magnons the ratio of the satellite intensities of thermal and parametric magnons is about tenfold lower, hence for them $F \simeq 5 \times 10^4$.

Now we can easily determine the maximum number of magnons N_q in 1 cm^3 having $q = 2.5 \times 10^5 \text{ cm}^{-1}$ and $\Delta q \simeq 20 \text{ cm}^{-1}$ which contribute to light scattering:

$$N_q = n_q F \quad (6.35)$$

Here n_q is the number of thermal magnons which are collected from a q -plane controlled by an aperture of light beam.

For the occupation numbers, $n_0 = (e^{\hbar\nu_q/kT} - 1)^{-1} \simeq 2$, where $T \simeq 2 \text{ K}$, the number n_q amounts to 2×10^8 particles per cm^3 while N_q is in the interval from 10^{13} to 10^{14} particles per cm^3 .

The experimental dependence of satellite intensities corresponding to the scattering from parametric magnons versus the power input (see Fig. 6.21) enables us to evaluate a variation in the number of magnons N_q for the case of high pumping power level. An initial part of the curve in Fig. 6.21 shows that above the threshold N_q grows linearly with the difference $\bar{P} - \bar{P}_{th}$ or in other words

$$N_q = \left[\left(\frac{h_{mw}}{h_{th}} \right)^2 - 1 \right], \quad A = \text{const} \quad (6.36)$$

Such a relationship takes place for an excess over the threshold in the interval $1 \leq h_{mw}/h_{th} \leq 2$. An increase in the pumping power over the threshold value is known to result in a stationary state of a magnon system. One of the basic questions arising from the investigation of the state is the mechanism of limitations imposed on the number of parametric magnons [6.61]. Generally, two mechanisms are considered as follows: (a) the mechanism of nonlinear damping and (b) the phase mechanism. Each of them is characterized by its specific dependence of the number of parametric magnons N_q on the pumping field strength h_{mw} (see [6.56]), namely

$$N_q = \frac{K}{\eta} (h_{mw} - h_{th}) = B \left(\frac{h_{mw}}{h_{th}} - 1 \right) \text{ in the (a) case} \quad (6.37)$$

$$N_q = \frac{\tilde{\gamma}K}{S} \sqrt{\left(\frac{h_{mw}}{h_{th}} \right)^2 - 1} = C \left[\left(\frac{h_{mw}}{h_{th}} \right)^2 - 1 \right]^{1/2} \text{ in the (b) case} \quad (6.38)$$

Here K is the coefficient of coupling high-frequency magnetic field to a spin wave, η the nonlinear damping factor, S the amplitude of

the four-frequency process, $\tilde{\gamma}$ the conventional damping factor, and $B = Kh_{th}/\eta$, $C = \tilde{\gamma}K/S$.

We tried to compare the experimental result with those (6.37), (6.38) from the theory. Figure 6.23 illustrates the dependence of the relative number of particles on the excess h_{mw}/h_{th} of microwave field strength over the threshold. The coefficients A , B , and C [(6.36)-(6.38)] are adjusted in such a way as to make values of N_q for all

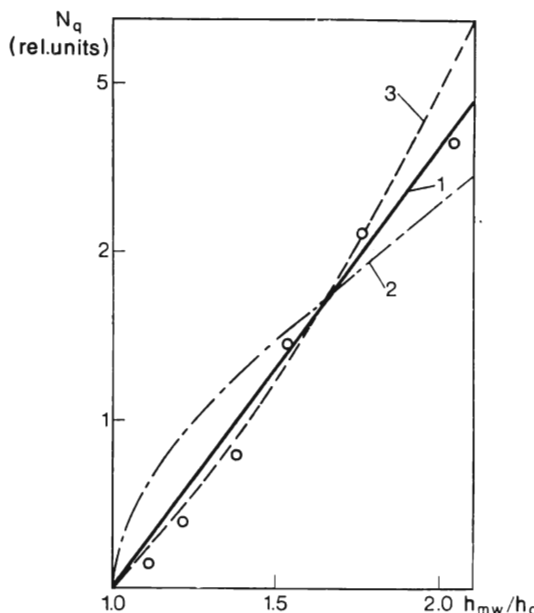


Fig. 6.23. The number of parametric magnons N_q versus the microwave field excess over threshold value h_{mw}/h_{th} . Curve 1 is drawn according to formula (6.37), curve 2 to (6.38), and curve 3 to (6.36). Experimental points correspond to Fig. 6.21.

three curves be the same at $h_{mw}/h_{th} = 1.65$. With the coefficient B in (6.37) properly fitted, the experimental results are seen to be sufficiently well described by the mechanism of nonlinear pumping. Yet the available spread of experimental points does not allow unambiguously discrimination between relations (6.36) and (6.37). The further growth of pumping power ($h_{mw}/h_{th} \geq 2$) leads to the saturation of the curve $N_q (P)$ and then to a decrease in the number of magnons. Such a behaviour is evidently caused by the sample overheating by microwave power.

6.7.2. Parametrical Phonons in CoCO_3

In this Section we shall dwell on the results obtained in studying the BMS from x - and y -quasiparticles excited at the pumping frequency $\nu_1 \simeq 36$ GHz.

6.7.2.1. BMS from Parametrical x -Quasiparticles

Investigation of BMS from x -quasiparticles with the microwave pumping at the frequency $\nu_p = \nu_1 = 35.02$ GHz has demonstrated that in the spectrum of scattered light the satellites occur

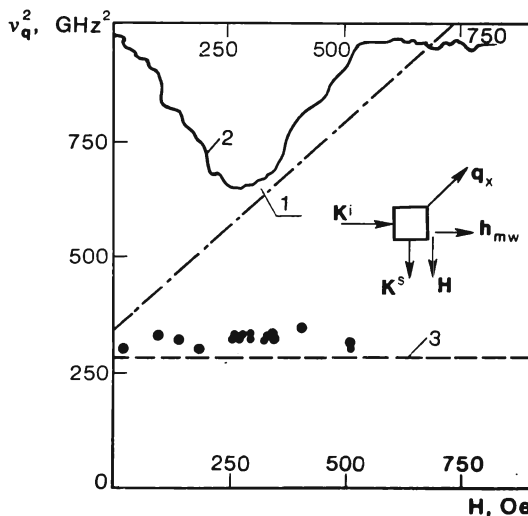


Fig. 6.24. The squared frequency ν_q^2 versus the magnetic field strength for thermal and pumped x -quasiparticles in CoCO_3 . Points correspond to the pumped-in quasiparticles. Curve 1 corresponds to the spectrum of thermal x -magnons, curve 2 to the absorption line of microwave power, curve 3 to transverse phonon frequencies in the basal plane at $T \sim 100$ K.

with frequencies differing from those of incident light by half-frequency of the pumping. Unlike the observing conditions of parametric magnons, these satellites exist over a wide range of magnetic field strength from 0 to 500 Oe. And their frequency is independent of the applied magnetic field strength in the interval (see Fig. 6.24). In this range of magnetic fields an extra absorbed microwave power is observed (curve 2 in Fig. 6.24). The dependence of satellite inten-

sities on the external magnetic field strength copies the shape of the curve describing the additional microwave absorption in a sample. Also, polarization conditions for observing these satellites differ from the foregoing case, since scattered light is depolarized.

The investigation of the dependence of the satellite intensity I on the power P of the applied microwave field resulted in a threshold to be in it. The value of the threshold microwave field is $h_{th} \simeq 0.09$ Oe.

The available experimental data enable one to assume that the presence of the intense satellites with $\Delta\nu = v_p/2$ in the spectrum of scattered light is due to the excitation of parametric phonons in the sample. This assumption is supported by the following experimental evidence:

(a) The excitation frequency of quasiparticles is independent of a magnetic field strength in the interval from 0 to 500 Oe. Due to this, the observed quasiparticles cannot be parametric magnons, since according to Sec. 6.7.1 the magnetic field conditions to excite these magnons are very stringent.

(b) The proximity of the quasiparticle frequency to that of transverse phonons propagating in the basal plane: the frequency $v_{ph} = 16.9$ GHz at $T = 100$ K and it differs from v_q by only 1 GHz. With decreasing temperature down to 2 K the phonon frequency is expected to increase up to 18 GHz. The excitation of parametric phonons may be explained in the following way.

The investigation of energy spectra of phonons [6.44] and magnons (Sec. 6.4) in CoCO_3 by the BMS technique have demonstrated that the frequency of x -magnons with $q \approx 0$ is close to that of transverse phonons propagating in the basal plane. In such a situation, the magnetoelastic interaction in a crystal can produce a coupling between two oscillation types, i.e. magnon-phonon interaction. When investigating the dispersion law for the quasimagnon branch, we detected no departure from the relationship described by formula (6.19) with magneto-elastic interaction neglected. This may indicate a small magnitude of the latter. Nevertheless, the experiments described in this Section show this interaction to exist. An excitation of phonons is believed to be due to the magneto-elastic interaction in a crystal in low magnetic fields (near the intersection point of branches) at the pumping frequency $v_p \sim 36$ GHz in CoCO_3 . Perhaps, the phonons have to be most intensively excited at the intersection point of magnon and phonon branches, i.e. at $H \simeq 0$. The sample though is subdivided into domains and the magnitude of actual field inside the domain depends on its dimensions and shape.

An analysis of equations for elastic oscillations obtained from a Hamiltonian with an added magneto-elastic interaction confirms our assumption of the parametric excitation of transverse phonons.

6.7.2.2. BMS from γ -Quasiparticles Excited Under AFMR [6.54-55]

When exciting an antiferromagnetic resonance in a sample at the frequency $\nu_{\text{AFMR}} = 36.2$ GHz in the spectrum of light

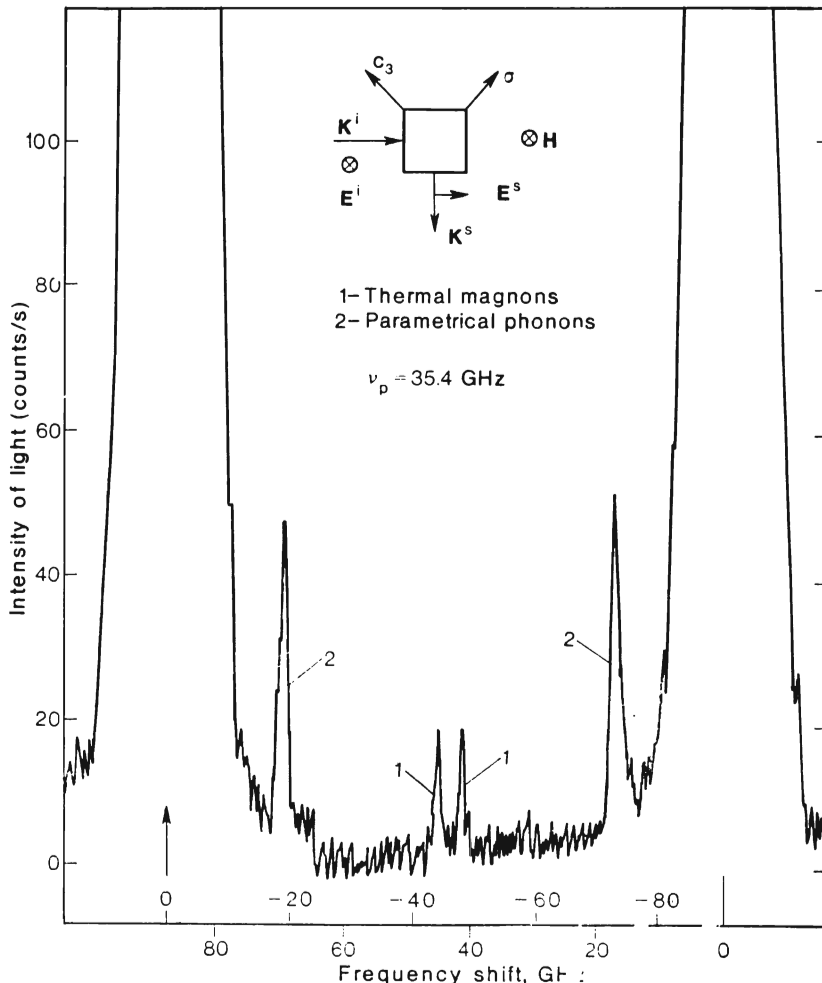


Fig. 6.25. Spectrum of light ($\lambda = 632.8$ nm) scattered at 90° in CoCO_3 ($T \leq 2$ K) from thermal γ -magnons (1) and parametrical γ -phonons (2) excited by microwave power at $\nu_p = 36.2$ GHz under AFMR.

scattered from γ -particles, extra peaks at the frequency $\nu_2 = \nu_{\text{AFMR}}/2 = 18.1$ GHz (curve 2 in Fig. 6.25) are discovered in

addition to thermal magnons (curve 1 in Fig. 6.25) whose frequency is established from the spectrum of y -magnons (see Fig. 6.25, $v_1 = 44.4$ GHz). The polarization conditions to observe the peaks match those for transverse phonons. Their frequency is close to a transverse y -phonon frequency measured at room temperature and equal to $v_{ph} = 16.9$ GHz. All these facts enable us to assume that in this experiment we observe the decay of magnons of the uniform

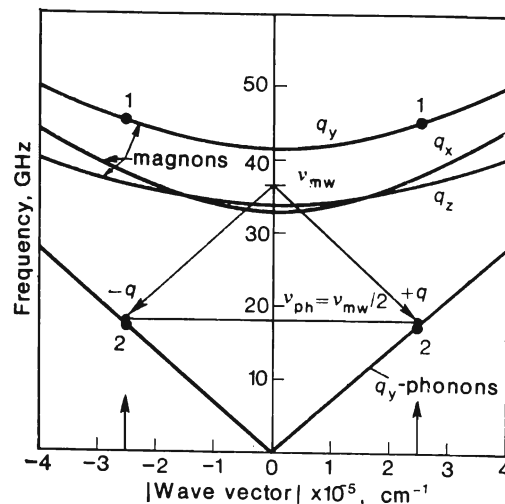


Fig. 6.26. Scheme illustrating the parametrical excitation of y -phonons in CoCO_3 under AFMR at $v_{\text{AFMR}} \simeq 36$ GHz.

precession with $q = 0$ into two parametrical phonons whose frequency is equal to half the AFMR frequency and $q = 2.5 \times 10^5 \text{ cm}^{-1}$. The decay scheme is shown in Fig. 6.26. Here is presented a low-frequency part of magnon spectrum in a magnetic field corresponding to the experimental conditions, and a part of the transverse y -phonon spectrum taken at room temperature. Peaks 1 in Fig. 6.25 correspond to points 1 in Fig. 6.26 while peaks 2 to points 2. The above mentioned decay process is due to a resonance saturation and has to be of a threshold character. In experiment, we observed the saturation of an absorption resonance line at the pumping power level used in the scattering studies.

A comparison of the intensities of light scattering from thermal y -phonons at $T \leq 300$ K and from parametrical y -phonons at $T \leq 2$ K (Fig. 6.25) allows to evaluate by how many the latter exceed the former.

This excess appears to be about 3×10^5 . Such an estimate is valid under an assumption of the true line width of a parametrical phonon to be about 1 MHz (by analogy to magnons, see 6.7.2.1).

The similar result was obtained by Wettling and Jantz with FeBO_3 [6.62].

Let us stress once more that the phenomenon discovered by us in CoCO_3 and by Wettling and Jantz in FeBO_3 [6.62] is a new type of instability under AFMR, this differing from the first order Suhl instability in that a magnon of uniform precession decays into two phonons rather than into two magnons of the half-frequency. Such a decay process is due to the magneto-elastic interaction in substance.

The parametrical excitation of phonons has been recently observed in FeBO_3 by means of microwave techniques as well [6.63]. The identification of particles by these techniques is less reliable. Studying the BMS from quasiparticles enables their type to be determined from the whole complex of observational conditions (i.e. frequency and wave vectors, polarization conditions, range of magnetic field involved in observation, etc.).

From the point of view of relaxation processes this phenomenon can be related to one of the kinds of a phonon "bottle-neck". As is seen, the relaxation of magnons with $q = 0$ excited under AFMR by means of high pumping powers can lead to an accumulation (as compared to the equilibrium value) of a phonon group with definite energies and wave vectors. The "bottle-neck" inhibits thermalizing these "hot" phonons and heating of the phonon spectrum.

References

- 6.1. G. S. Landsberg and L. I. Mandelstam, *Compt. Rend. Acad. Sci.* **187**, 109 (1928).
- 6.2. C. V. Raman and K. S. Krishnan, *Nature* **121**, 501 (1928).
- 6.3. I. L. Fabelinskii, *Light Scattering by Molecules*, Nauka, Moscow, 1965 (in Russian).
- 6.4. V. L. Ginsburg, *Proc. of 1st Sov.-Amer. Symp. on Theory of Light Scattering in Solids*, Vol. 2, 648, 1976 (in Russian).
- 6.5. L. I. Mandelshtam, *Journal of the Russian Physico-Chemical Society* **58**, 381, 1926 (in Russian).
- 6.6. L. Brillouin, *Ann. de Phys.* **17**, 88 (1922).
- 6.7. E. F. Gross, *Zs. Physik* **63**, 685 (1930).
- 6.8. P. A. Fleury, S. P. C. Porto, L. E. Cheesman, and H. J. Guggenheim, *Phys. Rev. Lett.* **17**, 84 (1966).
- 6.9. P. A. Fleury, S. P. C. Porto, and R. Loudon, *Phys. Rev. Lett.* **18**, 658 (1967).
- 6.10. P. A. Fleury, R. Loudon, and L. R. Walker, *J. Appl. Phys.* **42**, 1640 (1971).
- 6.11. J. R. Sandercock and W. Wettling, *Solid St. Comm.* **13**, 1729 (1973).
- 6.12. J. R. Sandercock, *Proc. Int. Conf. Light Scattering in Solids*, vol. 9, Flammarion, Paris, 1971.
- 6.13. R. E. Slusher, C.K.N. Patel, and P. A. Fleury, *Phys. Rev. Lett.* **18**, 77 (1967).

6.14. S. A. Altshuler, Yu. G. Nasarov, and A. Kh. Khasanov, *JETP Lett.* **33**, 508 (1981).

6.15. A. S. Borovik-Romanov, V. G. Zhotikov, N. M. Kreines, and A. A. Pankov, *JETP Lett.* **24**, 207 (1976).

6.16. V. G. Zhotikov and N. M. Kreines, *JETP Lett.* **26**, 360 (1977).

6.17. J. T. Hanlon and J. F. Dillon, Jr., *J. Appl. Phys.* **36**, 1269 (1965).

6.18. A. S. Borovik-Romanov and N. M. Kreines, *Physics Reports* **81**, 353 (1982).

6.19. J. R. Sandercock, in: *Topics in Applied Physics*, vol. 51, *Light Scattering in Solids III*. Ed. M. Cardona and G. Güntherodt, Springer-Verlag, 1982.

6.20. A. S. Borovik-Romanov, V. G. Zhotikov, and N. M. Kreines, *Sov. Phys. JETP* **47**, 1188 (1978).

6.21. A. S. Borovik-Romanov, V. G. Zhotikov, N. M. Kreines, and A. A. Pankov, *Sov. Phys. JETP* **43**, 1002 (1976).

6.22. A. S. Borovik-Romanov, N. M. Kreines, R. Laiho, T. Levola, and V. G. Zhotikov, *J. Phys. C* **13**, 879 (1980).

6.23. A. S. Borovik-Romanov, S. O. Demokritov, N. M. Kreines, and S. V. Petrov, *Sov. Phys. JETP* **86**, 2273 (1984).

6.24. A. V. Butashin, S. O. Demokritov, N. M. Kreines, and V. I. Kudinov, *JETP Lett.* **38**, 600 (1983).

6.25. L. D. Landau and E. M. Lifshits, *Electrodynamics of Continuous Media*, Pergamon Press, Oxford, 1960.

6.26. R. V. Pisarev, in: *Physics of Magnetic Dielectrics*, Nauka, Leningrad, 1974, p. 356 (in Russian).

6.27. A. S. Borovik-Romanov and V. I. Ozhogin, *Sov. Phys. JETP* **12**, 18 (1960).

6.28. A. S. Borovik-Romanov, N. M. Kreines, A. A. Pankov, and M. A. Talaev, *Sov. Phys. JETP* **39**, 378 (1974).

6.29. F. G. Bass and M. I. Kaganov, *Sov. Phys. JETP* **37**, 986 (1959).

6.30. R. J. Elliott and R. Loudon, *Phys. Lett.* **3**, 189 (1963).

6.31. J. R. Shen and N. Bloembergen, *Phys. Rev.* **143**, 372 (1966).

6.32. P. A. Fleury and R. Loudon, *Phys. Rev.* **166**, 514 (1968).

6.33. B. A. Auld and D. A. Wilson, *J. Appl. Phys.* **38**, 3331 (1967).

6.34. H. L. Hu and F. R. Morgenthaler, *Appl. Phys. Lett.* **18**, 307 (1971).

6.35. H. Le Gall and J. P. Jamet, *Phys. Stat. Sol. (b)* **46**, 467 (1971).

6.36. W. Wettling, M. G. Cottam, and J. R. Sandercock, *J. Phys. C* **8**, 211 (1975).

6.37. C. F. Pool, *Electron Spin Resonance*, Interscience Publ., New York, 1976.

6.38. A. S. Borovik-Romanov, *Sov. Phys. JETP* **36**, 539 (1959).

6.39. E. A. Turov, *Sov. Phys. JETP* **36**, 890 (1959).

6.40. E. G. Rudashevskii, *Sov. Phys. JETP* **19**, 96 (1964).

6.41. L. A. Prozorova, G. D. Bogomolov, Yu. F. Igonin, and R. S. Rusin, *Sov. Phys. JETP* **27**, 572 (1968).

6.42. V. I. Ozhogin, *Sov. Phys. JETP* **21**, 874 (1965).

6.43. V. G. Baryakhtar, M. A. Savchenko, and V. V. Tarasenko, *Sov. Phys. JETP* **22**, 1115 (1965).

6.44. A. S. Borovik-Romanov, V. G. Jotikov, N. M. Kreines, and A. A. Pankov, *Physica* **86-888**, 1275 (1977).

6.45. A. S. Borovik-Romanov, N. M. Kreines, and V. G. Jotikov, *Proc. USA-USSR Symp.*, Plenum Press, New York—London, 1979, p. 175.

6.46. A. S. Borovik-Romanov, V. G. Zhotikov, N. M. Kreines, and A. A. Pankov, *JETP Lett.* **23**, 649 (1976).

6.47. R. Laiho and T. Levola, *Solid State Comm.* **18**, 1619 (1976).

6.48. G. A. Smolenskii, V. M. Yudin, P. P. Syrnikov, and A. B. Sherman, *Fiz. Tverd. Tela* **8**, 2965 (1966).

6.49. Ye. I. Golovenchits, A. G. Gurevich, and V. A. Sanina, *JETP Lett.* **3**, 266 (1966).

6.50. Ye. I. Golovenchits, V. Sanina, and A. G. Gurevich, *Fiz. Tverd. Tela* **10**, 2956 (1968).

6.51. A. I. Akhiezer, V. G. Baryakhtar, and S. V. Peletinskii, *Spin waves*, Nauka, Moscow, 1967 (in Russian).

6.52. I. G. Sinii and R. V. Pisarev, *Fiz. Tverd. Tela* **12**, 114 (1970).

6.53. M. Born and E. Wolf, *Fundamentals of Optics*, Nauka, Moscow, 1972 (in Russian).

6.54. V. G. Zhotikov and N. M. Kreines, *Sov. Phys. JETP* **50**, 1202 (1979).

6.55. V. G. Zhotikov and N. M. Kreines, *J. M. and M. M.* **15**, 809 (1980).

6.56. V. E. Zakharov, B. S. L'vov, and S. S. Starobinets, *Usp. Fiz. Nauk* **114**, 609 (1974).

6.57. L. A. Prozorova, *Izv. Acad. Nauk SSSR, ser Fiz.* **42**, 1672 (1978).

6.58. V. I. Ozhogin, *Sov. Phys. JETP* **31**, 1121 (1970).

6.59. B. Ya. Kotyuzhanskii and L. A. Prozorova, *Sov. Phys. JETP* **35**, 1150 (1972).

6.60. B. Ya. Kotyuzhanskii and L. A. Prozorova, *Sov. Phys. JETP* **38**, 1233 (1973).

6.61. A. G. Gurevich, *Magnetic Resonance in Ferrites and Antiferromagnets*, Nauka, Moscow, 1973 (in Russian).

6.62. W. Wetling and W. Jantz, *Appl. Phys.* **19**, 175 (1979).

6.63. B. Ya. Kotyuzhanskii and L. A. Prozorova, *Sov. Phys. JETP* **56**, 903 (1928).

Author index

Abraham, B. H., 131
Abrikosov, A. A., 240
Adamenko, I. N., 85, 130
Aharonov, Y., 225, 239
Ahles, G., 219
Ahonen, A. I., 165, 173
Akhiezer, A. I., 292
Alekseevskii, N. E., 12, 13, 174, 218, 219
Almond, D. P., 131
Altshuler, B. L., 221, 225, 239
Anderson, A. C., 13, 85, 112, 131
Anderson, J. R., 220
Anderson, P. W., 133, 143, 172
Andreev, A. F., 11, 24, 27, 38, 43, 72, 74, 75, 77, 83, 87, 128, 130
Andres, K., 141, 172
Anufriev, Yu. D., 132, 172
Aschroft, N. W., 219
Atkins, K. R., 41, 76
Auld, B. A., 247, 291
Avron, J. E., 75
Azbel, M. Ya., 219

Babkin, A. V., 74, 75
Balian, R., 133, 143, 152, 172
Balkombe, R. J., 219
Baryakhtar, V. G., 291
Bass, F. G., 291
Bazan, Cz., 220
Becker, F. L., 130
Bergmann, G., 235, 240
Blount, E. J., 218
Bodensohn, J., 71, 72, 73, 76
Boldarev, S. T., 56, 76
Bol'shov, L. A., 75
Borovik-Romanov, A. S., 13, 133, 172, 173
Born, M., 292
Bowley, R. M., 76
Brekhovskikh, L. M., 76, 92, 230
Brillouin, L., 290
Brinkman, W. F., 161, 173
Bun'kov, Yu. M., 12, 132, 172
Burton, W., 18, 22, 24, 75
Butashin, A. V., 291

Castaing, B., 41, 71, 75, 76, 77
Challis, L. J., 130
Chernov, A. A., 18, 75, 76
Cohen, N. H., 217
Coleridge, P. T., 219
Corruccini, L. R., 133, 172
Crepeau, R. H., 76

Deegan, R. A., 220

Egorov, V. S., 13, 219
Elliott, R. J., 291
Eliashar, N., 220

Fabelinskii, I. L., 290
Falge, R. L., 240
Falikov, L. M., 219
Fal'kovskii, L. A., 92, 130

Farnell, G. W., 92, 130
Fawcett, E., 220
Fisher, D. S., 74, 75
Flerov, V. N., 240
Fleury, P. A., 241, 290
Folinsbee, J. T., 112, 131
Fomin, I. A., 133, 147, 156, 163, 172, 173
Fraasa, B. A., 76
Frossati, G., 172

Gershenson, M. E., 240
Gianetta, R. W., 172
Gibbs, J. W., 17, 75
Gijs, M., 240
Ginzburg, V. L., 219, 290
Golo, V. L., 167, 173
Goloventchits, Yu. I., 261, 291
Golub, A. A., 55, 76
Goodenouf, J. B., 220
Gordi, W., 220
Gordon, J. M., 240
Gostishchev, V. I., 219
Graebner, J. E., 220
Greywall, D. S., 76
Grilly, E. R., 76
Groff, R. P., 230, 239
Gross, E. F., 290
Gully, W. G., 172
Gurevich, A. G., 292
Gurevich, V. L., 130

Hakonen, P., 172
Halloran, M. H., 220
Hang, H., 85, 130
Hanlon, J. T., 242, 255, 291
Herring, C., 75
Herrmann, R., 131
Hikami, S., 240
Hu, H. L., 247, 291
Huber, T. E., 73, 75, 76

Iordanskii, S. V., 75, 76

JJackson, K. A., 75
Jones, C. K., 131

KKagan, Y., 240
Kaganov, M. I., 219
Kapitza P. L., 11, 130, 132, 172
Karine, D. P., 220
Keshishhev, K. K., 11, 74, 75, 76
Kesternich, W., 219
Khalatnikov, I. M., 11, 45, 76, 77, 82, 83, 130
Knizhnik, V. G., 38, 72, 76
Kompaneetz, D. A., 43
Konstantinov, O. V., 219
Korshunov, S. E., 77
Kosevich, A. M., 76
Koshino, S., 240
Kotyushanskii, B. Ya., 292
Kreines, M. N., 13, 241, 242

Krill, G., 240
 Kulik, I. O., 230, 240

Ladan, F. R., 230, 240
 Laiho, R., 291
 Laikhtman, B. D., 130
 Landau, J., 48, 52, 76
 Landau, L. D., 11, 17, 20, 32, 75, 76, 130, 291
 Landsberg, G. S., 241, 290
 Larkin, A. I., 240
 Lee, C. W., 240
 Lee, D. M., 133, 172
 Le Gall, M., 247, 291
 Leggett, A. J., 133, 143, 145, 156, 172
 Leib, E. H., 75
 Leiderer, P., 56, 62, 76
 Lifshitz, I. M., 21, 27, 75, 76, 77, 130, 174, 218, 249, 291
 Little, W. A., 130
 Loucks, T. L., 248
 Lounasmaa, O. V., 135, 172

Lüthi, B., 219
 Macfarlane, R. F., 126, 130
 Mandelstam, L. I., 241, 290
 Marchenko, V. I., 24, 35, 74, 75
 Marcus, S. M., 220
 Maria H. J., 73, 75, 76
 Mattheis, L. F., 219, 220
 Merkulova, V. M., 85, 130
 Meservey, R., 239
 Mezhov-Deglin, 55, 76, 77
 Meyers, L., 239
 Mills, N. G., 92, 130
 Morgan, V. N., 219
 Mott, G., 13, 85, 130
 Muller-Krumbhaar, H., 75

Niinikoski, T. O., 172
 Nizhankovskii, V. I., 12, 13, 174
 Nozieres, P., 41, 75

Osheroff, D. D., 76, 132, 133
 Ozhogin, V. I., 283, 291, 292

Pannetier, B., 240
 Parks, R. D., 226, 239
 Parker, R., 18, 75
 Parshin, A. Ya., 11, 15, 75, 76
 Peshkov, V. P., 56
 Peterson, R. E., 85, 130
 Pipman, J., 76
 Pippard, A., 188, 219
 Pisarev, R. V., 291
 Pitayevskii, L. P., 12, 77, 132, 172
 Pool, C. F., 291
 Press, F., 130
 Prozorova, L. A., 291, 292
 Puech, L., 75, 76

Raman, C. V., 241, 290
 Ramesh, S., 75
 Read, W. T., 76
 Reed, W. A., 219
 Rudashevskii, E. G., 291

Saan, W. F., 76
 Sandercock, J. R., 242, 248, 290
 Schoch, A., 131
 Scott, G. B., 220
 Shablo, A. A., 230, 231, 239
 Shahnikov, A. I., 49, 55, 74, 76
 Sharvin, D. Yu., 13, 221, 240
 Sharvin, Yu. V., 13, 221, 240
 Shen, J. R., 291
 Shoenberg, D., 219
 Sinii, I. G., 292
 Sinvani, M. M., 240
 Slusher, R. E., 290
 Slutskin, A. A., 13, 175, 218, 219
 Smolenskii, G. A., 291
 Stark, R. W., 218, 220
 Svatko, S. V., 55, 76

Takayama, H., 240
 Tandit, A. B., 219
 Taylor, P. L., 240
 Terrell, J. H., 218
 Testardi, I. R., 219
 Tripp, J. H., 219
 Truell, R., 131
 Tsymbalenko, V. L., 76
 Turov, E. A., 291

Urazakov, E. I., 92, 130
 Uwaga, M., 76

Victorov, I. A., 130
 Vlasov, K. B., 131
 Volasco, V. R., 131
 Volovik, C. E., 173
 Vol'skii, E. P., 219
 Voronkov, V. V., 18, 75
 Vos, J. E., 76

Watts, B. R., 218
 Weber, J., 92, 130
 Weeks, J. D., 74, 75
 Weiss, A., 85
 Wetting, W., 247, 261, 290, 291, 292
 Wheatley, J. C., 172
 Wilks, J., 76
 Wolf, P. E., 75
 Wyatt, A.F.G., 130

Zakharov, V. E., 292
 Zhotikov, V. G., 291, 292
 Zinov'eva, K. N., 11, 78, 130, 131

Subject index

Absorption of sound, 83
adatom, 28
aluminum, 191
coherent magnetic breakdown in, 191

Bath of ${}^4\text{He}$, 103
beryllium, 175
coherent magnetic breakdown in, 175
breakdown, 174
coherent magnetic, 174

Cadmium, 236
oscillation of magnetoresistance in, 236
capillary phenomena, in crystals, 45
chamber, measuring, 97
 CoCO_3 , 244
Brillouin-Mandelstam scattering in, 244, 257, 275
cryostat, optical, 47
crystal growth, 24
kinetics of, 24, 49
process of, 48
crystallization, 36
coherent, 36, 45
spectrum of, 62
waves in ${}^3\text{He}$, 40, 45
waves in ${}^4\text{He}$, 15, 38, 45, 55, 60

Debye, 27
law, 27
temperature, 37, 176
delocalization, 33
detector, lock-in, 65
dilution refrigerator, 97, 134, 135
dipole-dipole interaction, 144
Doppler effect, 37

Equation of Euler, 16
emitter, 99
effect of,
AAS, 225, 230
Brillouin-Mandelstam, 244
de Haas-van Alphen, 175, 178, 187, 197
Hall, 178, 184
Faraday, 243, 244
magnetooptical, 243
Raman, 241
errors, of measurement, 115

Fermi gas, 34
Fermi level, 176
Fermi liquid, 38, 40, 132
Fermi surface, 174, 192, 198, 212
flip-over, 30

Geometry, parallel-plate, 169
gold,
sample of, 104
comparison between theory and experiment, for, 126

Heat transfer between liquid helium and solid, 82

Interface, liquid-solid, 79
induction signal, in ${}^3\text{He-A}$, 149
interferometer of Fabri-Perot, 248

Kapitza resistance, 45, 73, 74, 82, 87, 95, 110
Kapitza jump, 95
 K_3CuF_4 , 259
kink, 18, 19, 20, 29
gas, 19
collisions, 30
Kossel's model, 17, 18, 28

Laser, He-Ne, 62, 248
lithium,
film, an experiment with, 226
oscillations of magnetoresistance in, 237
localization, weak electron, 221

Magnesium, 234
oscillations of magnetoresistance in, 234
magnetoresistance, 174
magnons,
Spectra of thermal, 251
"bottle-neck" of, 206
modulation of light by magnetic resonance.
255

NaF , crystal of, 92
 $\text{Nd}_3\text{Ga}_5\text{O}_1$, 265
niobium, 198
coherent magnetic breakdown, in, 198
NMR,
pulsed, 132, 133
pulsed, in ${}^3\text{He-B}$, 164

Ordering parameter, 133
oscillations, 221
of magnetoresistance, 221, 230
longitudinal, 230

Phase, ${}^3\text{He}$ superfluid, 132
phonons,
"bottle-neck" of, 290
parametrical in CoCO_3 , 286
thermal, passing across a liquid helium-solid interface, 92
photodiode, 64
pickups, 101
Poisson's ratio, 32
precession,
instability of homogeneous, 143, 156, 161
Larmor's, 145

Quantum crystal,
surface of, 27
quantum-rough,
state, 27
surface, 31
sound transmission through, 41

Rayleigh wave, 41, 43, 83, 87, 89
RbNiF₃, 257, 261
refrigerator,
dilution, 135
nuclear demagnetization, 141
relaxation, 143
Brinkman-Smith, 169
intrinsic, in superfluid ³He, 146
Riemann's function, 32
ruthenium dioxide, 212
coherent magnetic breakdown in, 212

Samples, 100
satellites,
Stokes and anti-Stokes, 245, 247
scattering,
Brillouin-Mandelstam, 241
of light, in magnetic materials, 243
Snell's law, 86
sound propagation through a liquid-metal
interface, 78
superfluidity, 132
surface,
of classical crystal, 16
energy, 16
structure at $T = 0$, 17
structure at $T \neq 0$, 22

Theory,
generalized acoustic, 83, 116
of Leggett-Takagi, 133
transducer, piezoelectric, 96
transition, texture, in ³He-B, 164
transmission, 94
of sound from liquid ⁴He into a metal, 94
tungsten, 105
sample of, 105
calculations for, 116
comparison of theory with experiment
for, 121

Ultralow temperatures, 134
equipment for producing, 134

Van der Waals interaction, 30, 32

Wulff construction, 16

X-ray experiments, 55

YIG,
Brillouin-Mandelstam scattering in, 247
Young's modulus, 30

To the Reader

Mir Publishers would be grateful for your comments
on the content, translation, and design of this book.

We would also be pleased to receive any other suggestions
you may wish to make.

Our address is:

Mir Publishers
2, Pervy Rizhsky Pereulok
1-110, GSP, Moscow, 129820
USSR

Low Temperature Physics

Edited by A. S. Borovic-Romanov

The authors of this collection are leading members of the staff at the Institute of Physics Problems of the Academy of Sciences of the USSR, Moscow. Three of them are Members of the Academy of Sciences. The Institute was founded fifty years ago by the great contemporary physicist P. L. Kapitza. Academician L. D. Landau another giant of our time, also worked at the institute. The institute is world famous for research in low temperature physics. This is a collection of six articles on the basic achievements of the Institute during the last few years. They include the discoveries of crystallization waves in helium and quantum magnetic breakdown. The collection is intended for scientists working in solid state physics and students interested in the latest advances of quantum physics of the condensed state.

Mir Publishers
2 Pervy Rizky Pereulok
1-11-, GSP Moscow 129820
USSR